(2)

Surgical Diagnostics, Guidance, and Intervention using Optical Coherence Tomography

by

Stephen Allen Boppart

M.S. E.E., University of Illinois at Urbana-Champaign (1991)
B.S. E.E., University of Illinois at Urbana-Champaign (1990)

Submitted to the
Harvard-MIT Division of Health Sciences and Technology
Medical Engineering and Medical Physics Program

in Partial Fulfillment of the Requirements for the Degree of
Doctor of Philosophy in Medical and Electrical Engineering
at the
Massachusetts Institute of Technology
May, 1998 [June 1998]

Signature of Author ______________________________
Harvard-MIT Division of Health Sciences and Technology
May 1, 1998

Certified by ______________________________
James G. Fujimoto, Ph.D.
Professor of Electrical Engineering
Thesis Supervisor

Accepted by ______________________________
Martha L. Gray, Ph.D.
J.W. Kieckhefer Associate Professor of Electrical Engineering
Chairman, HST Graduate Committee
Co-Director, Harvard-MIT Division of Health Sciences and Technology

Surgical Diagnostics, Guidance, and Intervention using Optical Coherence Tomography

by

Stephen Allen Boppart

Submitted to the Harvard-MIT Division of Health Sciences and Technology
on May 1, 1998 in partial fulfillment of the requirements for the degree of
Doctor of Philosophy in Medical and Electrical Engineering

ABSTRACT

Advances in biomedical imaging technology are rapidly becoming integrated into the surgical suite for image-guidance of interventional procedures. Clinical imaging modalities including computed tomography, magnetic resonance imaging, and ultrasound offer resolutions sufficient to guide placement of surgical instruments, but insufficient to resolve tissue and cellular microstructure. Optical coherence tomography (OCT) is a new high-resolution biomedical imaging modality based on the detection of backscattered near-infrared laser light from tissue. The compact fiber-optic based OCT technology is capable of micron-scale resolution real-time imaging in non-transparent highly-scattering tissue.

This thesis research investigates the use of OCT for high-resolution real-time surgical diagnostics, guidance, and intervention. The capabilities of OCT imaging of tissue microstructure are first demonstrated using *in vivo* developmental biology animal models. Morphological and functional imaging of normal and abnormal specimens is performed. High-resolution OCT permits *in vivo* imaging of cellular mitosis and migration providing insight into limits for cellular imaging and identification of neoplastic tissue in humans.

The fiber-optic based design of OCT has been integrated with optical surgical instruments including catheters, endoscopes, laparoscopes, microscopes, and hand-held surgical imaging probes. Using these devices, *in vitro* imaging of surgically-relevant human tissue is performed to determine diagnostic capabilities and limitations. High-speed interventional OCT imaging is used to guide placement of laser and radio-frequency thermal lesions in *in vitro* tissue and to assess dynamics during tissue ablation.

These results demonstrate the capabilities of OCT for use in the surgical suite. In addition, results suggest OCT may play a significant role in new methodologies of high-resolution image-guided surgical procedures.

Thesis Supervisor: James G. Fujimoto, Ph.D.
Title: Professor of Electrical Engineering and Computer Science

Acknowledgments

I would like to thank my thesis advisor, Dr. Jim Fujimoto, for believing enough in me to give me the opportunity to explore my ideas, and for providing the laboratory space and equipment to accomplish my goals. I appreciate the frequent opportunities to attend scientific conferences, present my research, and interact with experts in my field. The critical reviews of my research and my scientific writings, by both Dr. Fujimoto and Dr. Mark Brezinski, have helped mature my professional skills which I will utilize the remainder of my career. I thank them and the rest of my thesis committee, Drs. Tom Deutsch and Erich Ippen, for their guidance in shaping my research and thesis.

My understanding of medicine and the culture of clinical medicine has been enhanced by my interactions with Drs. Mark Brezinski and James Southern. I appreciate their time in sharing with me their experiences, knowledge, and advice from which I learned valuable lessons for my future in biomedical research. I especially thank Dr. Brezinski for his medical insight and for bringing this insight into the optics laboratory to shape the direction of OCT in medicine.

My research would not have progressed this far if it had not been for the daily interactions with former post-doc Brett Bouma and fellow graduate students Gary Tearney, Boris Golubovic, Costas Pitris, and Igor Bilinsky. I shall long appreciate the technical gifts I have seen in them, the comic relief and the camaraderie that was shared, our lunch-time group meetings, and the lingering taste of truck food. I enjoyed working closely with visiting scientist Dr. Juergen Herrmann and medical student Parth Patwari. I wish them both well. I thank Drs. Joe Izatt and Mike Hee for getting me started in the Ultrafast Optics Group, Eric Swanson for his technical contributions to OCT, and Cindy Kopf for helping to lighten my paperwork load.

Most importantly, I appreciate the support and love from my wife and family. Had it not been for Marni's patience and strength during the years we were separated because of our career paths, I would not have had the opportunity to pursue my goals at MIT, nor experience the comfort of being happily married to my best friend. My accomplishments are as much for myself as they are for my mother, father, and family. I thank my grandfather, John Boppart, for defining morality for me and for demonstrating the rewards of what persistent hard work can bring. I thank my father for raising me as an engineer and my mother for my compassion. I will forever be indebted to my sister Loreene for giving me life and appreciation for what I once took for granted. To my family and friends, I extend my appreciation for the interest and support of my life's endeavors and will continue to try to explain just exactly what I do and why it is important.

Lastly, I would like to thank my friends and colleagues from Brooks Air Force Base, Drs. Don Farrer, Pat Roach, Ben Rockwell, and the many others, for helping me establish new paths through uncharted Palace Knight waters and for helping me keep my head above a rising tide. I am grateful for the unending support from Betty Ferguson, the Palace Knight Program, and the Air Force Office of Scientific Research. They have provided me with the means by which this research could be accomplished.

I would like to believe that I am solely responsible for what is presented in this thesis. Rather, it represents a culmination of experience, input, guidance, enthusiasm, and passion from everyone I have come in contact with throughout my life. I say this to not only share the rewards which this research may bring, but also to share responsibility for that which I may be accused.

Dedication

This thesis is dedicated to my friend, Hector, who reminds us that engineers cannot fix everything.

The front line of research is almost always in a fog. It is instruments that function as our eyes, allowing us to gather map-points in the fog, to construct a picture of the world in the form of a map, and ultimately to penetrate those obscuring mists.

-Stephen S. Hall, *Mapping the Next Millennium*

Contents

Chapter 1

Introduction

Chapter 2

Optical Coherence Tomography

Chapter 3

Beam Delivery Instruments

Chapter 4

Imaging Tissue Microstructure

Chapter 5

Image Characterization for Surgical Diagnostics

Chapter 6

Surgical Guidance

Chapter 7

Surgical Intervention

Chapter 8

Summary and Conclusions

Chapter 1

Introduction

1.1 Overview

Advances in imaging technology have historically had major influences on medicine. Ever since Roentgen first visualized the bones of his hands using newly discovered x-rays[1], the potential to visualize within the human body has led to improvements in patient diagnostics and treatment with a subsequent improvement in patient mortality and morbidity. The two seemingly disparate fields of engineering and medicine will continue to be tightly interrelated in the future as high-technology advances our ability to peer into the body less invasively and with higher resolution. No field of medicine is more aligned for improvements in technology than the field of surgery. Viewed objectively, the art of surgery is rather archaic and still relies primarily on invasive procedures with rather large incisions. The recent success of minimally invasive surgery (MIS) has, in part, been due to patient demands for smaller incisions, shorter hospital stays, and reduced morbidity. Along with the minimally invasive approach to surgery comes the necessity for visualizing inside the body, often at remote sites. In this thesis, I describe a state-of-the-art advance toward improving medical imaging in surgery. Optical coherence tomography (OCT) is applied for surgical diagnostics, guidance, and intervention to advance the state of technology and patient care within the surgical suite.

1.2 The Surgical Suite

The surgical suite is the ultimate proving grounds for OCT. It is a rather hostile environment which presents additional challenges for imaging modalities. The sterile surgical field requires that all instruments be frequently sterilized with high temperatures and pressures. Often the surgical field is small, making it difficult to integrate additional surgical instruments into the field. The number of instruments available and the frequency at which the surgeon must switch between instruments must be kept to a minimum. Finally, the presence of blood and other body fluids can quickly obscure the viewing and imaging capabilities of optical instruments. Still, the need for the surgeon to visualize the tissue he or she is operating on is essential and imaging modalities which enable better visualization will attract attention. Imaging modalities such as computed tomography (CT), magnetic resonance imaging (MRI), ultrasound (US), and microscopy are techniques which play a role in surgery, both in and out of the operating room. Minimally invasive or keyhole surgery utilizes multiple small incisions through which imaging and mechanical instruments are passed. These MIS instruments can be flexible, such as the endoscope for examining the upper and lower gastrointestinal tract, or rigid, such as the laparoscope for trans-abdominal access. Because the surgeon does not have full visualization as in the open surgical field, imaging instruments play a critical role.

1.3 Imaging Modalities

The integration of imaging modalities into the surgical suite has been fueled by improvements in visualization and the additional information that can be obtained from the tissue. Imaging modalities can either directly acquire an *en face* image of the tissue as in microscopy or endoscopy, or indirectly assemble an image of the tissue structure based on measured properties. Examples of this indirect form include the detection of sound reflections in ultrasound, fluorescence in spectroscopy, or backscattered light in OCT. It is clear that the continual improvements in imaging techniques will benefit patient care. The next generation of MIS technologies will begin to incorporate multiple modalities into a single instrument. The integration of endoscopic ultrasound has already occurred and efforts are underway to incorporate the magnetic resonance technology into MIS devices[2]. No doubt, optics and laser-based techniques will be integrated as well.

Prime examples of cutting-edge MIS technology and the integration of multi-modality imaging include endoscopic ultrasound and the miniaturization of ultrasound transducers that permit their placement at the tips of endoscopes and laparoscopes. Studies have shown that sonographically guided laparoscopy and mediastinoscopy can be used to identify sub-surface morphology[3] which normally would be detected by palpation, but is no longer palpable due to the remote operative site. This innovation also illustrates the powerful concept of image-guided surgery which relies on real-time imaging capabilities for intra-operative guidance of procedures. This area appears ripe for technological insight as is demonstrated by the intense interest in open-magnet MR imaging at the Brigham and Women's Hospital in Boston. Excitement has been generated internationally in not only the medical community, but also in the engineering and computer science communities as well. Perhaps neurosurgery will experience the greatest impact from open-magnet MRI-guided procedures. Removing small pathologic tissue deeply positioned in critically sensitive structures such as the brain is an ideal application. Near real-time feedback is necessary to reduce collateral damage.

The remainder of this section will describe the major imaging modalities and techniques that are incorporated into surgery and surgical planning. Comparisons will be made between methods of image generation, imaging parameters, instrument design, and economic factors. Consideration will be given to both clinical and research instruments as imaging performance often varies between these systems. This will provide a basis for an objective assessment of OCT and its role in surgery.

1.3.1 Computed tomography

Computed tomography (CT) has been primarily used to plan surgical procedures and guide placement of needle biopsies. Current CT technology uses x-rays emitted from a source in a fan-like pattern. Multiple detectors arranged in a similar fan-like pattern are positioned opposite the source. The patient is positioned between the source and detector array which rotate around the patient to collect projection data from angles over 360°. Images are then reconstructed using algorithms based on the source and detector geometry. Image contrast is based on the x-ray attenuation properties of the tissue. Highly attenuating bone appears white while low attenuating air and fluid appears black in CT images. Tissue discrimination is poorest between soft-tissues with similar x-ray attenuation coefficients. Iodine or barium-based contrast agents which increase x-ray attenuation can be administered to localized specific organ systems such as the gastrointestinal tract. X-ray radiation is ionizing and represents a hazard at high energies or accumulated doses.

The resolution of CT is determined by the detector array, number of angular projections acquired, and the algorithms used to reconstruct the image. Within a single plane, 0.5-1.0 mm resolutions are possible[4], multiple planes are acquired by stepping the patient through the source-detector plane in increments as small as 5-10 mm. The density resolution on the exposed film is 2-3% and dependent on the radiation dose, x-ray energy, and slice thickness[4]. Depth of imaging, at least in the human body, is not restricted due to the ease at which x-rays pass through tissue. The field-of-view is large ($\approx$ 1 m) representing the bore-size between the source and detector array. Image acquisition times of 50 ms per planar scan have been improved in recent years with helical-scanning methods and algorithms. The patient is continuously translated through a rotating source-detector pair rather than stepping and repeating the image acquisition process[5]. Acquisition of 3-D data sets is straightforward by translating the patient through the source-detector plane. The size of the CT instrument is large, often requiring a separate room to house the device and to limit x-ray exposure to medical personnel. Instrument costs are expensive, in the range of $500,000-$750,000 dollars[6]. Still, CT has become a standard for whole-body or organ imaging and scanners are found in every major hospital.

Research applications of x-rays have been applied to microscopic applications. The shorter wavelengths of x-rays ($\approx$ 1 nm) compared to those of visible wavelengths (300-700 nm) allow higher resolutions. Configured with a single source and detector which are scanned over specimens, x-rays have been used to image *in vitro* insects[7] and more recently individual live bacteria with 200 nm resolutions; high enough to resolve bacterial DNA[8].

1.3.2 Magnetic resonance imaging

Magnetic resonance imaging (MRI) is ideally suited for whole-body or organ imaging. Because the technique relies on the detection of the electron spin from hydrogen atoms, excellent contrast between soft, water-based tissues can be obtained, a limitation for CT imaging. One significant advantage of MRI is the many modes of operation and image contrast mechanisms. Images can be weighted according to spin relaxation mechanisms (T_1 and T_2), chemical-shifts, bulk flow, and spectroscopic functional information. Contrast agents such as gadolinium can be given intravenously to identify the vasculature. In the past, MRI was solely used for diagnosis and planning prior to surgery. The powerful idea of image-guided surgery have produced an open-magnet MRI machine which permits the surgeon to stand next to the patient[9]. The surgical field lies within the uniform magnetic field of the instrument allowing three-dimensional MRI data to be acquired during the surgical procedure.

The resolution of MRI is dependent on the magnetic field strength that can be generated within the tissue. Most clinical MRI machines have a 1.5 T magnet and provide 0.5-1 mm resolution within an imaging plane[10]. The depth of imaging is governed by the dimensions of the uniform magnetic field that is established within the bore of the magnet. Bores are large enough to pass a prone patient, permitting whole-body or organ imaging. Image acquisition times have been reduced to 50 ms and 3-D volumes are readily acquired by translating the patient through the magnet bore. The instrument size is equivalent to that for a CT scanner. However, extra precautions are necessary surrounding the magnet to prevent the introduction of metal instruments which are attracted toward the strong magnetic field. Statistics from 1995 estimate 3900 commercial MRI machines in operation in the U.S.[11] since the introduction in the early 1980's. The instrument costs for MRI machines exceed those of CT scanners. Clinical 1.5 T machines cost approximately $1.6 million dollars[11].

Engineering improvements in the MRI technology have enabled high-resolution research systems for MRI microscopy. Resolutions as high as 12 μm have been demonstrated on *in vivo Xenopus laevis* (African clawed frog) tadpoles during development[12,13]. However, to attain these resolutions, 7 T field strengths were needed across small (≈ 1 cm) magnet bores. Acquisition times are prohibitively slow with three-dimensional volumes of developing tadpoles requiring 2 hrs. The use of gadolinium contrast agents can be used to label blood flow within mouse embryos and striking sequences of vascular development in the mouse have been demonstrated[14].

1.3.3 Ultrasound imaging

Ultrasound (US) is routinely used in an outpatient setting, particularly in obstetrics and gynecology because the fetus can be safely imaged. Ultrasound image-guidance is used for the placement of needles for biopsy. Ultrasound imaging relies on the detection of reflected acoustic waves from biological tissue. Contrast within US images is generated by differences in acoustical impedance within tissue. The use of air-filled albumin-coated microspheres has recently been used to increase ultrasound backscatter contrast in echocardiography[15-17]. An US transducer made from piezoelectric materials functions both as an acoustic pulse emitter and receiver. The transducer can be swept in an arc, collecting adjacent depth information to form an image, or multiple transducers can be positioned within a phased array. The phased array permits multi-location imaging without moving parts by controlling constructive and destructive interference patterns of pulses within the tissue. Engineering of US transducers has permitted a reduction in size. Transducers less than 3 mm have been placed on the tips of endoscopes and laparoscopes to develop multimodality instruments for the imaging of subsurface tissue structures[3]. Transducers have been placed within rotating catheters for intravascular ultrasound (IVUS) imaging of atherosclerosis and stenosis in the human coronary artery[18].

Most clinically available instruments today operate at 10-20 MHz with high-frequency US considered to be 30 MHz and higher. These acoustic frequencies provide 100-200 μm resolutions at depths of tens of centimeters[19]. The resolution is governed by the frequency of the acoustic wave. Higher frequencies do not penetrate as deeply into tissue and therefore a trade-off exists, much like in optics, between image resolution and depth of imaging. The field of view in US is dependent on the translation of the transducer ranging from several millimeters to tens to centimeters. Clinical instruments acquire images at video-rates (30 frames/s). Three-dimensional US imaging is performed by translating the transducer along a third axis and assembling a series of 2-D slices to form the 3-D data set. The instrument size is compact compared to CT and MRI and can fit on a small cart. The US waves are delivered to the patient via a small hand-held probe containing the transducer. Costs for US instruments range from $30,000-$150,000, relatively affordable for most hospitals and clinics[6]. A major limitation of US imaging is the requirement of an index-matching medium between the transducer and the sample to be imaged. The placement of a gel or medium during laparoscopic or endoscopic exam is problematic and impractical if large areas are to be imaged.

Ultrasound backscatter microscopy is a research field utilizing extremely high frequency transducers (>100 MHz) to image microstructure at the expense of depth of penetration[20]. Human myocardial cells have been imaged with 1.7 μm resolutions using a 600 MHz transducer[21]. However, a fixed 5 μm-thick tissue section was used as the sample as penetration was poor. Currently, these resolutions are not available in any clinical instrument. Ultrasound backscatter microscopy using 40-100 MHz transducers providing 17-30 μm axial and 33-94 μm lateral resolution has been applied clinically for imaging skin in humans and the progression of melanoma in the mouse animal model[22,23].

1.3.4 Microscopy

Light microscopy has been well established in the surgical suite, particularly for microsurgery of vessels[24] and nerves[25], and for delicate procedures of the central nervous system[26]. Surgical microscopes and loupes magnify the tissue under examination to allow avoidance and recognition of injury, prompt visualization of abnormal changes, and the practice of delicate surgical techniques using fine microsurgical instruments and suture materials. Resolutions as high as 1 μm can be achieved under high magnification. Depth of visualization, however, is limited to the optical scattering properties of the tissue. Except for the transparent structures of the eye, only surface features can be visualized. Contrast between tissue types can be enhanced with dyes, such as toluidine blue, which selectively attaches to dividing cells. The field-of-view is limited by the magnification. The 5-10X magnification of surgical microscopes and loupes provides a field-of-view of several centimeters. Because microscopy is considered a visualization technique rather than imaging, statistics on acquisition times and 3-D imaging are not applicable. Surgical microscopes occupy a significant amount of space within the surgical suite. Counter-weighted positioning systems allow placement over the operating table. The costs associated with a surgical microscope approach and exceed $100,000 depending on the complexity of the optics and positioning systems[6].

The bench-top light microscope is the standard for clinical and research biological investigations with resolutions of approximately 1 μm. Light microscopy coupled with differential tissue staining properties enables the histopathological visualization of tissue constituents down to the cellular and subcellular levels. The use of selected stains permit specific identification of cells. Hematoxylin and eosin are the most commonly used stains which color the nucleic acid within cell nuclei (DNA) purple while staining collagen and connective tissue pink. Without the use of stains, no contrast would exist within tissue slices at visible wavelengths for light microscopy observation.

The confocal microscope[27] has revolutionized the way in which biological samples are visualized. The confocal microscope utilizes a point source illumination, either white-light or a laser, and collection through a pin-hole aperture placed confocally to the source. Light arriving from outside of the objective lens focal plane is spatially rejected by the pin-hole aperture. This reduces the axial point-spread function to 0.5 to 1 μm and permits optical sectioning of biological specimens. Fluorophores can be attached to specific cells or subcellular constituents which can later be excited by an incident laser source. Recent advances utilizing ultrafast lasers[28] have demonstrated two- and three-photon confocal microscopy[29-31]. By utilizing the high peak powers that are confined to the focus, a further reduction in the axial point spread function is possible. In addition, because longer wavelengths in the near infrared (IR) are used, deeper penetration into tissue is possible. Real-time confocal microscopy has been a challenge, but successes have revealed fascinating sequences of calcium dynamics in fertilized oocytes[32,33].

1.4 Minimally Invasive Surgery

Minimally invasive surgery (MIS) is a relatively new methodology that has contributed significantly to patient care by reducing the morbidity and mortality that is associated with more invasive procedures. By reducing the size of the surgical access site, patient recovery time and risk of infection are likewise reduced. Because of this, MIS procedures are becoming the standard for many surgical procedures. The increase in MIS procedures has, in turn, resulted in advancements in instrument design and optical and non-optical imaging technology for specific tissue or organ system access[34]. Examples include the rigid laparoscope for abdominal or pelvic access, the flexible bronchoscope or endoscope for respiratory or gastrointestinal systems, and the small rigid arthroscope for access into joint spaces. Recent advancements have begun to take advantage of synergistic benefits from multiple imaging modalities integrated into a single MIS instrument[3,35,36]. Common to all instruments, both mechanically and optically, are design features which permit entry via narrow incisions or natural body openings.

1.4.1 Endoscopy

Endoscopy is a well-established technique used primarily for visualizing tortuous internal body lumens and cavities. Endoscopic instruments are flexible, consisting of either coherent fiber bundles for relaying or a micro-CCD (charge-coupled device) camera located at the distal end of the device for capturing surface images of tissue. Instruments range from 0.5-2 cm in diameter and from 10 cm to over 1 m in length. Manual manipulation at the proximal end is translated to the distal end with cables enabling directional control of the imaging field-of-view. The surgical uses of endoscopes include the resection of polyps from the colon[37] and for investigating tumors of the lung during video-assisted thoracic surgical (VATS) procedures[38]. Endoscopes can be made extremely small in diameter permitting the passage into individual vessels (angioscopy) for the repair of valves[39].

Contrast in acquired images is dependent on the illuminating wavelengths (typically white-light from an arc lamp), surface optical properties of the tissue, and the dynamic range of the CCD. The resolution is limited to the pixel size of the CCD, generally 1-5 μm. Visualization depth into tissue is limited to surface features as in microscopy. The field of view is dependent on the magnification which, in turn, is non-linearly dependent on the distance from the tissue. This presents one limitation for assessment of scale during the procedure. The instrument light source and control unit can fit on a small cart with interchangeable, steralizable endoscopes for each application. Costs for the light source and controller are around $50,000 plus $10,000-$12,000 for each endoscope[6].

1.4.2 Laparoscopy

Laparoscopy is becoming the standard for cholecystectomy, tubal sterilization, puncture and aspiration of ovarian cysts, diagnostics for abdominal disorders[40], staging intra-abdominal malignancies[41], and many others. Laparoscopy has even been found to be significantly more sensitive and more accurate than either US or CT for detecting intra-abdominal metastases[42].

Unlike the flexible endoscope, the laparoscope is a rigid instrument approximately 2-10 mm in diameter and 10-40 cm in length. The rigid design permits the use of glass optical relay elements to relay the image from the distal end to the proximal end[43] where it is observed with either the human eye or digitized with a CCD camera and displayed on a monitor. The imaging performance, instrument size, and device costs are comparable to those for endoscopy.

The hallmark MIS procedure is laparoscopic cholecystectomy which is now a gold standard because of its high success rate, efficiency at which the procedure can be performed, and the decreased morbidity. Since the introduction of the technique[44] in the U.S. in 1989, the number of surgeons adopting the procedure reached 80% in 1992 and is approaching 100% today[45]. The widespread dissemination and acceptance of this procedure has occurred with a rapidity that has never been seen before. Perhaps the largest collection of statistics has been assembled by the Connecticut Laparoscopic Cholecystectomy Registry[46] which surveyed 97% of the hospitals in Connecticut from May 1, 1990 to September 30, 1991. In 1989, before the first laparoscopic procedure, 5786 open cholecystectomies were performed. In 1991, 4389 out of 7462 (58.8%) procedures were performed laparoscopically. Overall, there was a 29% increase in the number of cholecystectomies (both open and laparoscopic). Mortality decreased from 1.5% to 1.1% and was statistically significant ($p<0.05$). The mean hospital stay was reduced from 9 to 3 days and the cost of the procedure fell from $10,295 (1989 dollars) to $7,576 (1991 dollars). Technical complication rates fell with increasing experience. The 5.3% rate in the surgeon's first 10 cases fell to 0.98% after the 75th procedure. These results helped quantify what many had observed. The introduction of this MIS procedure resulted in increased frequency of surgery without an increase in surgical mortality.

1.5 Optical Coherence Tomography

Optical coherence tomography (OCT)[47,48] is a relatively new imaging technology compared to those previously described. OCT is based on the detection of backscattered optical radiation from biological tissue and is somewhat analogous to ultrasound B-Mode imaging except optical rather than acoustical reflections are detected. Cross-sectional images of tissue microstructure are generated based on the optical backscatter characteristics of the specimen rather than the acoustic properties as in ultrasound. Contrast in OCT images is generated by scattering inhomogeneities or changes in index of refraction within tissue. There have been no published reports of the use of contrast agents for OCT, although melanin granules and air-filled microspheres may be effective.

OCT performs optical ranging within tissue utilizing low-coherence interferometry to localize the position within the specimens from which the backreflection originated. Imaging depths range from 1-3 mm in highly scattering tissue. Micron-scale axial and transverse resolutions are possible within two-dimensional cross-sectional images. Two-dimensional images can be acquired spatially at given intervals to produce three-dimensional volumes. Three-dimensional volumes can be acquired over time to produce four-dimensional volume sequences of dynamic tissue changes. The field-of-view is limited by the beam scanning range, typically < 5 mm. OCT images have high signal-to-noise (SNR) ratios around 110 dB by utilizing optical heterodyne detection originally implemented in optical communication techniques. Video-rate acquisition times (30 frames/s) can be achieved, depending on the image size. Because OCT is fiber-optic based, the personal computer-driven device is compact, portable, and readily integrated into existing medical and surgical optical instruments including microscopes, endoscopes, laparoscopes, and hand-held optical imaging probes for beam delivery. Cost estimates for an OCT instrument range between $30,000-$50,000. The non-contact, non-invasive nature of OCT, coupled with resolutions exceeding those of clinical instruments, makes this technique extremely promising for applications in biomedical imaging. A comparison of OCT with existing imaging modalities and techniques is summarized in Table 1-1.

TABLE 1-1: Comparison of Imaging Modalities and Visualization Techniques.

	Resolution	Imaging Depth	Field of View	Speed	Device Size	Costs	Notes
Clinical CT	0.5-1.0 mm	full body	full body	50 ms	room size	>$500K	ionizing radiation
Research CT (x-rays)	200 nm	cm	cm	seconds	cart	research costs	ionizing radiation
Clinical MRI	0.5-1.0 mm	full body	full body	50 ms	room size	>$1 mil	expensive
Research MRI	12 µm	1 cm	1 cm	10 min	bench top	research costs	slow acquisition
Clinical US	100-200 µm	30 cm	20 cm	video rate	cart	$50K	tissue contact
Research US	2 µm	50 µm	mm-cm	15 s	bench top	research costs	tissue contact
Light Microscopy	1 µm	<100 µm	mm-cm	video rate	bench top	$10K-$100K	surface imaging
Confocal Microscopy	0.5-1 µm	<300 µm	mm	video rate	bench top	$50K-$150K	limited imaging depth
Endoscopy	5 µm	<100 µm	cm	video rate	cart	>$50K	surface imaging variable magnification
Laparoscopy	5 µm	<100 µm	cm	video rate	cart	>$50K	surface imaging variable magnification
OCT	2-15 µm	3 mm	mm-cm	4-8 fps	cart	$30K-$50K	imaging in highly scattering tissue

1.5.1 Historical overview

Optical ranging measurements were first performed using optical time domain reflectometry (OTDR) which relied on the optical time-of-flight of ultrashort laser pulses[49]. One of the first applications for OTDR was for diagnostics of concatenated fiber-optic components or long optical fiber transmission lines[50]. In 1986, OTDR was demonstrated by Fujimoto, *et. al.*[51,52] for the first time in biological tissue. Reflected pulses from ocular tissue were correlated with pulses from a reference optical delay line in order to determine the time delay, and hence the position, of the reflection. The approach to optical ranging provided high axial resolutions (15 µm) in cornea and skin, but suffered from low detection sensitivity of 70 dB, was expensive, and complex. In addition, axial resolution was determined by the temporal pulse width, requiring the maintenance of a 30 fs pulse for 10 µm axial resolution.

The frequency domain analog to OTDR, called optical coherence domain reflectometry (OCDR) was subsequently developed for optical ranging. Low-coherence interferometry was implemented to provide equivalent resolutions as OTDR without the need for complex mode-locked laser sources necessary to generate femtosecond optical pulses. The techniques of low-coherence reflectometry was first applied to diagnosing optical waveguide properties and finding faults in fibers[53,54]. Rather than using short pulses of light, OCDR used light with short temporal coherence. Therefore, continuous-wave laser sources with broad spectral bandwidths (short coherence lengths) could be used with equivalent axial resolutions. The development of the super-luminescent diode (SLD) in the 1980s made it possible to integrate a fiber-coupled SLD with a fiber-optic coupler (beam splitter) for the construction of a compact fiber-based instrument. Utilizing optical heterodyne detection, dynamic ranges of 120 dB (detection of 10^{-12} of the incident power) were possible with axial resolutions up to 10 μm.

In 1988, the first biological application of OCDR was performed by Fercher *et. al.*[55] in the transparent tissue of the eye. The longitudinal ranging capabilities were demonstrated by measuring *in vivo* human eye lengths[56,57] and *in vitro* corneal incision depths[58]. Optical coherence tomography was proposed by Huang, *et. al.*[48] in 1991 as the two-dimensional extension of OCDR. By assembling adjacent axial profiles acquired using OCDR, two-dimensional images could be constructed representing the optical backscatter from within tissue. These techniques have analogues in ultrasound. The single axial profile acquired with OCDR is equivalent to the ultrasound A-scan while the OCT image is equivalent to the B-scan.

1.5.2 OCT in ophthalmology

OCT imaging in the *in vivo* human eye was first performed by the Fujimoto group[59] in 1993. Advancements in faster acquisition rates and the integration of the OCT instrument with a slit-lamp biomicroscope used in ophthalmology enabled real-time imaging of the retina in human subjects[60]. Studies imaging anterior eye structures were also performed and assessments for clinical potential were made[61]. The high-resolution cross-sectional OCT imaging of the retina provided unprecedented detail which suggested a use for diagnosing a wide range of retinal and anterior eye diseases[61,62]. Clinical studies were begun in collaboration with the New England Eye Center of Tufts University School of Medicine. To date, over 5000 patients have been diagnostically imaged and followed for response to treatment and therapy. OCT images of macular pathologies have been strongly correlated with corresponding fundoscopic photographs and fluorescein angiography. OCT has been shown to be effective for diagnosing and following macular holes, retinal detachment, epiretinal membranes, macular edema, and age-related macular degeneration[63-67]. The ability of OCT to image and quantify retinal nerve fiber layer thickness has been shown[68]. Thinning of the nerve fiber layer is an early indication of glaucomatous changes within the eye. Current studies are attempting to demonstrate that the axial resolution of OCT is sufficient to detect early changes in thickness and to diagnostically monitor progression and treatment of glaucoma[69].

1.5.3 Optical biopsy with OCT

The term "optical biopsy" associated with OCT refers to the non-excisional imaging of biological structure, *in vivo*, at resolutions that approach those of histology. Non-excisional imaging is in contrast to excisional biopsy in which the tissue sample is removed, fixed, sectioned, stained, and observed using light microscopy. Other optical research groups have used the term optical biopsy in regard to the detection of spectroscopic information from tissue. This data, however, may not necessarily be in the form of an image, but may represent spectral data characteristic of specific tissue types. The term "optical biopsy" may be a misnomer for the medical community given that a biopsy has been traditionally defined as the physical resection of tissue. The concept, however, is powerful because tissue removal can often become nontrivial in surgical settings, particularly in MIS. This technique would enable images of tissue microstructure for the diagnosis of disease without having to physically remove tissue. For sensitive tissues of the nervous and cardiovascular systems where the physical resection of tissue could prove detrimental to the patient, an "optical biopsy" would offer the surgeon a nondestructive means of diagnosing tissue pathology.

The first demonstration of an OCT optical biopsy from an *in vitro* coronary artery was performed by Huang, *et. al.*[48] in 1991. This highly scattering tissue presented challenges compared to the transparent structures of the eye. The low-power, 800 nm wavelength, SLD used for this study did not permit deep imaging penetration. Imaging penetration was improved with the use of longer wavelengths in the near infrared[70] and with higher-power broad bandwidth sources[71]. Penetration in highly scattering, non-transparent tissue is possible with OCT because multiply-scattered photons, which travel longer pathlengths than corresponding photons in the reference arm of the interferometer, are rejected. The human skin was the most accessible highly scattering *in vivo* tissue available. Researchers were able to penetrate 1 mm with up to 10 μm resolution and identify architectural structures corresponding to the epidermis, dermis, sweat glands and hair follicles[72,73]. At the same time, studies were being performed to characterize OCT imaging in highly scattering tissue[72,74] and to utilize OCT to determine optical properties of tissue such as absorption and scattering coefficients and the index of refraction[75-77].

Investigational studies were and continue to be performed in highly scattering tissue samples throughout the human body including the gastrointestinal, urinary, respiratory tracts and cardiovascular and nervous systems. Advancements in high-power broad bandwidth mode-locked laser sources along with the engineering and development of beam delivery devices described in this thesis have permitted the *in vivo* optical biopsy of the gastrointestinal and respiratory tracts of a rabbit[78]. Since the demonstration of imaging in highly scattering tissue, the number of investigators pursing OCT and OCT-related research has grown at a tremendous rate with *in vivo* human studies already being performed in the gastrointestinal, reproductive, and urinary tracts[79]. Not limited to biological tissue, OCT has been used for the non-destructive evaluation of composite and ceramic materials for structural defects[80,81] and as a technique for high-density multi-layer optical data storage[82,83]. The blossoming level of interest in this technology serves not only as a motivating factor for further research, but also as a testament to the future potential for improvements in patient care.

1.6 Scope of thesis

The goal of this thesis is to investigate a previously unexplored potential of OCT in biomedical imaging: the use of OCT in surgery for diagnostics, guidance, and intervention. The high-resolution, high-speed imaging capabilities of OCT are ideally suited to interface with the surgical environment and advance the state of technology within the surgical suite. The compact, portable, and fiber-optic based instrument can be readily integrated into existing surgical instruments or provide new minimally-invasive devices for *in vivo* imaging. The non-contact nature of performing an optical biopsy enables imaging and diagnostics of tissue structure, particularly in the sensitive regions of the cardiovascular and nervous systems. Real-time surgical guidance using OCT can avoid vessels and nerves during incisions or be used to rapidly locate suspect regions of tissue for further investigation. Finally, OCT can be used to guide surgical interventions such as the delivery of high-power laser radiation for tissue ablation or to monitor the process of radio-frequency ablation. OCT has the potential for improving a surgeon's ability to visualize tissue which will subsequently improve patient outcome.

The fundamental operating principles and theory behind OCT will be described in Chapter 2. Evaluation of low-coherence light sources and axial scanning mechanisms will be considered along with the necessary modifications for high-resolution and high-speed OCT imaging. Other embodiments of coherence-domain optical imaging including frequency-scanning OCT and spectral radar will be discussed. Descriptions, designs, and performance of beam delivery instruments will be discussed in Chapter 3. Chapter 4 demonstrates the fundamental capabilities of OCT imaging in *in vitro* and *in vivo* biological structures using developmental biology animal models. Correlations are made between OCT images and corresponding histological preparations to define how biological structures are represented in OCT images.

Functional imaging is performed to demonstrate high-speed capabilities and high-resolution cellular imaging is explored as precursors to cellular imaging in humans. Not only will these developmental biology studies define and demonstrate OCT imaging capabilities for use in the surgical suite, but they will also establish, for the first time, the use of OCT in the field of developmental biology and as a new *in vivo* microscopy technique. Characterizing OCT images for surgical diagnostic information is described in Chapter 5. This is followed in Chapter 6 by an exploration of the surgical tissue environment in which OCT will function to guide surgical procedures. Monitoring surgical interventions with OCT is demonstrated in Chapter 7. Finally, thesis research results are summarized, conclusions are made, and future studies are described in Chapter 8.

Chapter 2

Optical Coherence Tomography

2.1 Introduction

Optical coherence tomography represents a high-resolution imaging technique that could significantly impact the approach to surgery. The compact, non-invasive, non-contact nature of this optical technique minimizes the changes that would have to occur in the surgical setting. The concept of image-guided surgery is well recognized with the use of ultrasound, CT, and MRI as imaging modalities. However, the high-resolutions of OCT offer a new level of surgical precision not offered by other imaging modalities. Surgical guidance can approach the level of cellular resolutions which would reduce the amount of collateral damage to normal tissue. Adaptability to minimally-invasive instruments will permit surgical guidance with demonstrated reductions in patient morbidity and mortality as a result of smaller incisions, faster recovery times, and fewer post-operative complications. Understanding the principles and limitations of OCT will establish a framework on which surgical diagnostics, guidance, and intervention can be built.

2.2 System Overview

OCT is based on the principle of low-coherence interferometry using an optical heterodyne detection scheme to detect small levels of backscattered light from within tissue. The OCT technology can be modularized to simplify the understanding of the components and how each interacts within the system. In addition, since the development of this imaging technique, technical advancements have improved various modules of the overall system and these will be addressed individually in later sections. In general, the OCT system can be represented by the block diagram in Figure 2-1. A light source is coupled into a single-mode optical fiber which is one arm of a fiber-optic 50:50 coupler used as a Michelson interferometer. The sample arm of the interferometer consists of a beam-delivery instrument which acts at the interface between the OCT instrument and the sample to be imaged. The beam-delivery instrument also includes transverse scanning mechanisms to translate the imaging beam. Instrument designs are discussed in detail in Chapter 3. The reference arm of the interferometer includes a mechanism to perform an optical path-length delay for axial (depth) scanning of the detection envelope through the sample. Backreflections from both the reference and sample arms are recombined at the detector where the optical signal is converted into an electrical signal current. This signal is filtered and processed resulting in the amplitude of the backscattered intensity from one localized region within the tissue sample. All of the scanning and data acquisition is under computer control.

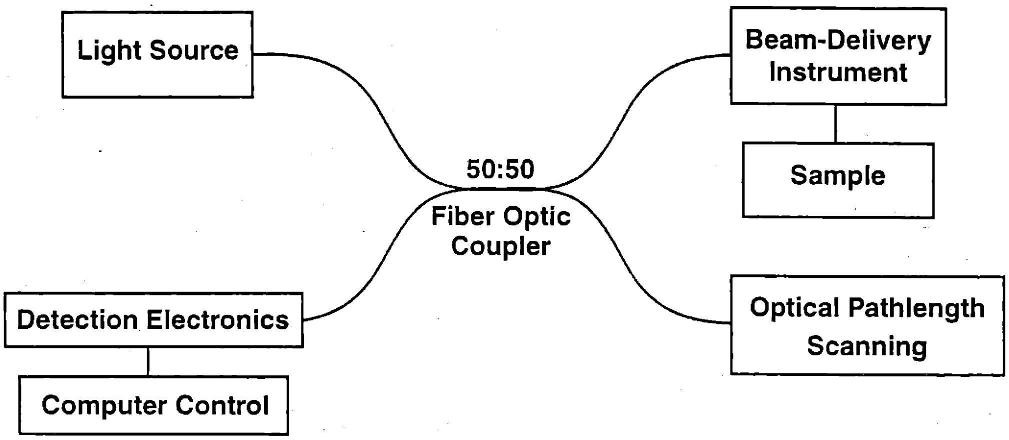

FIGURE 2-1: Modular OCT system.

2.3 Interferometry

Interferometry is the process which begins by splitting a single optical wave into two using a beamsplitter. Optical delays are then introduced in each of the waves. Finally, the two waves are recombined and the intensity of the superposition is measured. The Michelson interferometer uses a single element to both split and recombine the waves. A schematic of the interferometer is shown in Figure 2-2. If one first assumes the light source emits monochromatic plane waves, then the complex amplitude of the incident electromagnetic wave propagating in the z direction has the form

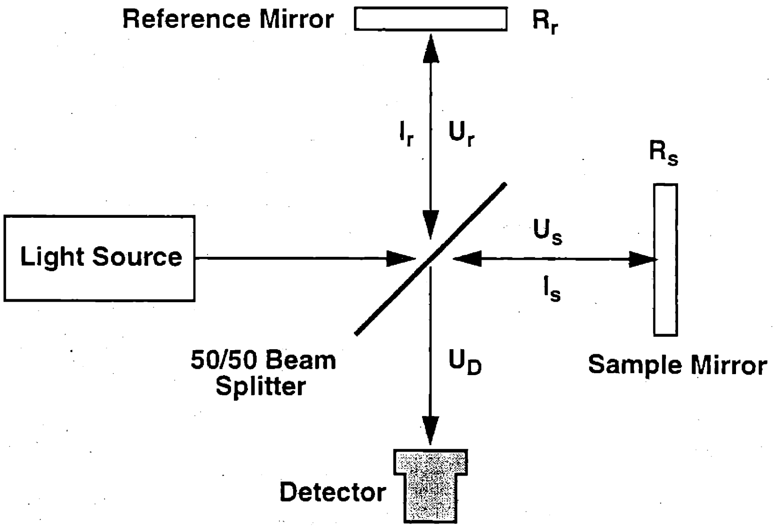

FIGURE 2-2: Michelson interferometer. $U_{r,s}$ and $I_{r,s}$ refer to the optical field and intensity, respectively, in the reference and sample arms.

$$U(\vec{r}) = 2A_0\exp(-jkz). \tag{2-1}$$

This wave is split equally by the beamsplitter. The two waves in the reference and sample arms travel distances l_r and l_s, respectively, before undergoing a reflection and returning. The two fields are summed at the detector

$$U_D(\vec{r}) = U_r(\vec{r}) + U_s(\vec{r}) = \frac{1}{2}A_0R_s\exp(-j2kl_s) + \frac{1}{2}A_0R_r\exp(-j2kl_r) \tag{2-2}$$

where R_s and R_r represent the reflectivities from the sample and reference arms, respectively. The intensity at the detector is the magnitude squared of the summed fields given by

$$I_D = |U_D(\vec{r})|^2 = \frac{1}{4}|U_r(\vec{r})|^2 + \frac{1}{4}|U_s(\vec{r})|^2 + \frac{1}{4}U^*{}_r(\vec{r})U_s(\vec{r}) + \frac{1}{4}U_r(\vec{r})U^*{}_s(\vec{r}) \tag{2-3}$$

or

$$I_D = \frac{1}{4}I_r + \frac{1}{4}I_s + \frac{1}{2}\sqrt{I_rI_s}\cos\Delta\phi \tag{2-4}$$

where $\Delta\phi$ is the phase difference between the fields from the reference and sample arms. This phase difference can be expressed in terms of pathlength difference

$$\Delta\phi = 2k\Delta l \tag{2-5}$$

where $k = 2\pi/\lambda$ and $\Delta l = l_r - l_s$, the difference in the arm lengths. If the reference arm mirror is moved at a constant velocity v_M, the pathlength mismatch becomes a linear function of time

$$\Delta l(t) = 2v_Mt. \tag{2-6}$$

The moving mirror will induce a Doppler-shift in the returning light with a frequency $f_D = 2\ v_M/\lambda$. The intensity at the detector is then

$$I_D(t) = \frac{1}{4}I_r + \frac{1}{4}I_s + \frac{1}{2}\sqrt{I_rI_s}\cos(2\pi f_Dt). \tag{2-7}$$

The first two terms in Equation (2-7) represent a DC component to the detector signal. The last term is an AC cosine component whose amplitude depends on the relative phase between the two arms.

If the source contains more than one wavelength, it is considered polychromatic and has a lower degree of coherence. The complex wavefunction from this source can be represented as a sum of monochromatic waves

$$U(\vec{r}, t) = \frac{1}{\pi}\int_0^\infty U_\omega(\vec{r})\exp(j\omega t)d\omega \tag{2-8}$$

where $U_\omega(\mathbf{r})$ can be determined by obtaining the Fourier transform of $U(\mathbf{r},t)$. The degree of temporal coherence in the complex wavefunction stated above is determined by its autocorrelation function

$$G(\tau) = \langle U^*(t)U(t+\tau)\rangle \tag{2-9}$$

where τ represents a time delay. The autocorrelation function can be normalized by dividing by the autocorrelation function $G(\tau = 0)$ thereby allowing a measurement of coherence that is insensitive to the intensity of the fields. The absolute value of the normalized autocorrelation function $g(\tau)$ is bounded between 0 and 1. For a given position and time, the normalized autocorrelation of the waves from the two arms of the interferometer is given by

$$g_{rs} = \frac{\langle U_r^* U_s\rangle}{\sqrt{I_r I_s}} \tag{2-10}$$

which then enters into the interference equation as

$$I_D = \frac{1}{4}I_r + \frac{1}{4}I_s + \frac{1}{2}|g_{rs}|\sqrt{I_r I_s}\cos(2\pi f_D t). \tag{2-11}$$

The term $|g_{rs}|$ will vary between 0 and 1 depending on the polarization, dispersion, and phase differences between the two arms; parameters which affect the coherence of the light returning from the reference arm and the sample.

The autocorrelation function in Equation (2-9) is related to the spectral density function $S(\omega)$ by the Fourier transform

$$S(\omega) = \int_{-\infty}^{\infty} G(\tau)\exp(-j\omega\tau)d\tau. \tag{2-12}$$

The relation in Equation (2-12) is known as the Wiener-Khinchin theorem[84,85]. The Fourier transform relation implies that for low-coherence light, the autocorrelation function will be narrow and the spread of wavelengths about a center wavelength will be broad. Therefore, high axial spatial resolution can be achieved by using sources with broad spectrums. The interference signal at the detector is proportional to the interference by each monochromatic component. Incorporating the source spectrum $S(\omega)$ yields

$$I_D \propto Re\left\{\frac{1}{2\pi}\int_{-\infty}^{\infty} S(\omega)\exp(-j\Delta\phi)d\omega\right\}. \tag{2-13}$$

The medium in the arms of the interferometer through which the light propagates will affect the relative phase difference $\Delta\phi$ in Equation (2-5) and consequently the detected intensity in Equation (2-13). For the case where the medium is uniform, linear, and non-dispersive, the propagation constant k is equal in both arms. The constant can be Taylor-series expanded to first order to give

$$k_s(\omega) = k_r(\omega) = k(\omega_0) + k'(\omega_0)(\omega - \omega_0) \tag{2-14}$$

where $\omega = 2\pi\nu$ and ω_0 is the center frequency. Inserting this into Equation (2-5) and (2-13) gives a photocurrent

$$I_D \propto Re\left\{\exp(-j\omega_0\Delta\tau_p)\frac{1}{2\pi}\int_{-\infty}^{\infty} S(\omega-\omega_0)\exp(-j(\omega-\omega_0)\Delta\tau_g)d(\omega-\omega_0)\right\} \tag{2-15}$$

where the phase delay mismatch $\Delta\tau_p$ is

$$\Delta\tau_p = 2\Delta l\frac{k(\omega_0)}{\omega_0} = 2\Delta l \cdot v_p \tag{2-16}$$

and the group delay mismatch $\Delta\tau_g$ is

$$\Delta\tau_g = 2\Delta l k'(\omega_0) = 2\Delta l \cdot v_g. \tag{2-17}$$

The light propagating from the source will experience group velocity dispersion (GVD) from the optical fiber, other lenses or optical components, and the specimen. The effect of these dispersive elements will be to broaden the autocorrelation function, resulting in a decrease in the axial point spread function or axial resolution. To examine the effect of GVD on the photocurrent at the detector, the propagation constants k_r and k_s are Taylor series expanded to second order around the center frequency ω_0

$$k_s(\omega) \approx k_r(\omega) = k(\omega_0) + k'(\omega_0)(\omega-\omega_0) + \frac{1}{2}k''(\omega_0)(\omega-\omega_0)^2. \tag{2-18}$$

Note that k_r and k_s are only approximately equal because of differences between each arm. If the length over which GVD is mismatched between the two arms is L_M, then the effect of GVD is added to the phase difference in Equation (2-5) to give

$$\Delta\phi(\omega) = k(\omega_0)\cdot 2\Delta l + k'(\omega_0)(\omega-\omega_0)\cdot 2\Delta l + \frac{1}{2}\Delta k''(\omega_0)(\omega-\omega_0)^2\cdot 2L_M \tag{2-19}$$

where $\Delta k''(\omega_0)$ represents the change in GVD between the reference and sample arms. By increasing or decreasing the amount of GVD in the interferometer arms, it is possible to fully balance the dispersion and minimize the width of the autocorrelation function; thereby maximizing the axial resolution of the OCT system. The photocurrent obtained by propagating light from a polychromatic source through dispersive a medium is given by

$$I_D \propto Re\left\{\exp(-j\omega_0\Delta\tau_p)\frac{1}{2\pi}\int_{-\infty}^{\infty} S(\omega-\omega_0)\exp\left(-j\frac{1}{2}\Delta k''(\omega_0)(\omega-\omega_0)^2\cdot 2L_M\right) \times \right. \tag{2-20}$$
$$\left. \exp(-j(\omega-\omega_0)\Delta\tau_g)d(\omega-\omega_0)\right\}.$$

The effect of the dispersive medium on the polychromatic light is to broaden the autocorrelation function and to induce asymmetry due to chirp (time-dependent frequency variations).

If the source spectrum can be represented by a Gaussian power spectral density given by

$$S(\omega) = \sqrt{\frac{1}{2\pi\sigma_\omega^2}}\exp\left(\frac{-(\omega-\omega_0)^2}{2\sigma_\omega^2}\right) \tag{2-21}$$

with σ_ω being the standard deviation and $2\sigma_\omega$ being the width of the Gaussian distribution, then the autocorrelation function also has a Gaussian profile. The signal current at the detector is then represented by

$$I_D \propto \exp\left(-\frac{\Delta\tau_g^2}{2\sigma_\tau^2}\right)\cos(\omega_0\Delta\tau_p) \tag{2-22}$$

where the temporal standard deviation σ_τ is inversely proportional to the standard deviation of the source spectrum

$$\sigma_\tau = \frac{1}{\sigma_\omega}. \tag{2-23}$$

Two standard deviations of the temporal Gaussian envelope $2\sigma_\tau$ represents the coherence length or axial resolution of the OCT system which will be thoroughly defined in Section 2.7.1.

Non-Gaussian light sources may broaden the autocorrelation function and increase the presence of sidelobes. In addition, the presence of noise or ripple on the source spectrum will elevate the noise floor of the autocorrelation function. These effects are shown in Figure 2-3. The source spectrum in the left column is Fourier transformed using the FFT to produce the autocorrelation functions displayed on linear and logarithmic scales. The FFT of the Gaussian spectrum is another Gaussian function. On a logarithmic scale, this would be a parabolic function without sidelobes. The sidelobes which are a factor of 10^{-5} below the peak are due to the truncation of the Gaussian spectrum. Two Gaussian profiles were separated by 30 nm and added together to produce the rectangular Gaussian profile. A wider spectral bandwidth of the rectangular Gaussian produces a narrower autocorrelation function but with the presence of elevated sidelobes. The sidelobes are approximately a factor of 10^{-1} below the peak, sufficiently close to become evident during OCT imaging at regions that differ greatly in index of refraction such as the air-tissue interface. Within tissue, the change in index is less significant reducing the effects from the elevated sidelobes. The additional sidelobes a factor of 10^{-4} below the peak are due to the truncation of the rectangular Gaussian spectrum. A noisy Gaussian spectrum was generated by multiplying the Gaussian profile with a random frequency sinusoidal function. This spectrum produces an autocorrelation function with an elevated noise floor but without the presence of large sidelobes.

2.4 Low-Coherence Light Sources

The low-coherence light source represented by the box in Figure 2-1 is optimally selected based on its center wavelength, spectral bandwidth, spectral profile, output power, and compact design. Each of these parameters will be discussed for the sources used in this thesis research.

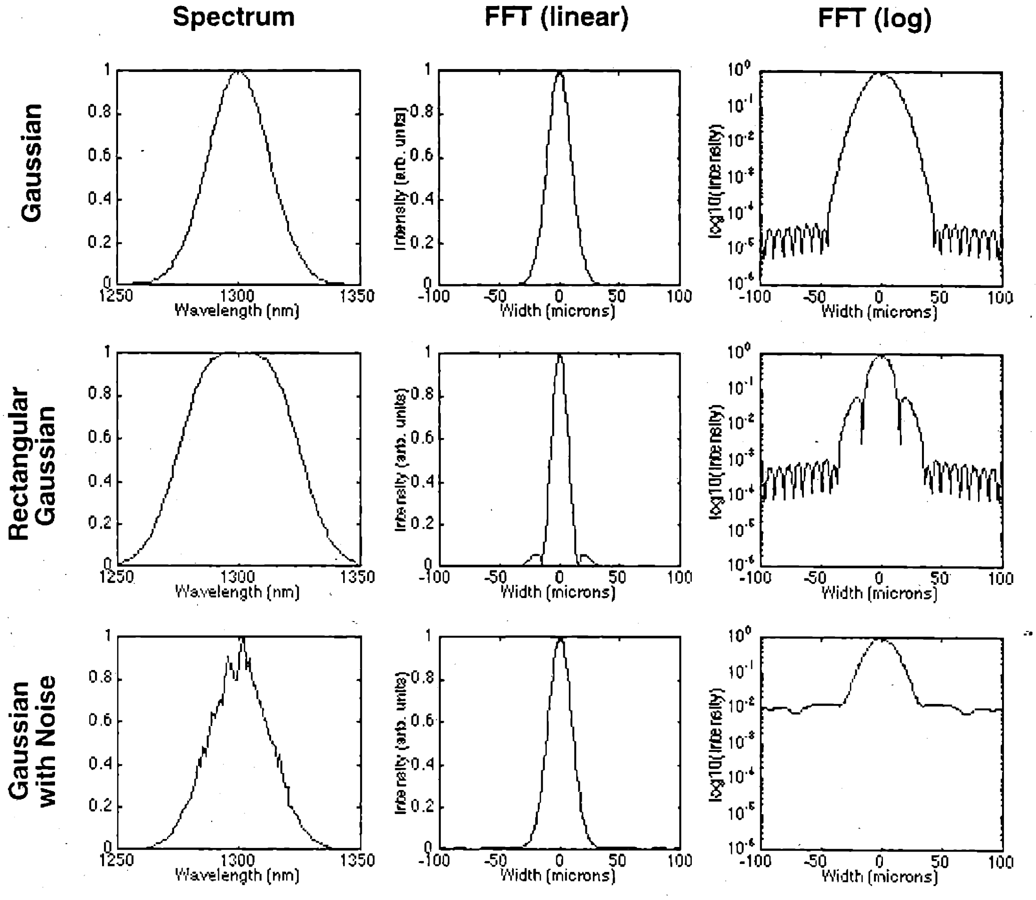

FIGURE 2-3: Non-Gaussian source spectrum effects on autocorrelation function envelope.

2.4.1 Super-luminescent diodes

Super-luminescent diodes (SLDs) are extremely compact, solid-state, fiber-coupled devices that provide low-coherence light for OCT imaging. A superluminescent diode is constructed in a similar manner as laser diodes except the end facets are angle-cleaved to prevent lasing. Typical center wavelengths are 800, 1300, and 1500 nm used in the telecommunications industry. Bandwidths in the range of 30-50 nm permit axial resolutions of 15-25 µm. Output powers have been in the range of 300-1000 µW which is sufficient for most OCT systems at slow acquisition rates. With a recent interest in developing compact gyroscopic guidance systems, manufacturers have increased production of SLDs. However, SLDs designed for gyroscopes have 10-30 nm spectral bandwidths which are sufficient for only moderate 25-75 µm resolution OCT imaging.

Recently, commercial devices using an amplified SLD with spectrum-shaping filters have produced outputs at $\lambda_0 = 1310$ nm, $\Delta\lambda = 40$ nm, and output powers of 18 mW (AFC Technologies, Inc.). This spectral bandwidth produces a coherence length of 19 µm. By modifying the spectrum-shaping filters and reducing the output power to 9.5 mW, it is possible to achieve $\Delta\lambda = 80$ nm at $\lambda_0 = 1310$ nm. This source is capable of 9.5 μm axial resolution with reasonable output powers. Ongoing research in SLD source development with an expanding market for OCT will continue to improve performance.

2.4.2 Kerr-lens modelocked lasers

Increased output powers and broader spectral bandwidths are possible with the use of solid-state crystals in Kerr-lens modelocked (KLM) lasers[28]. The disadvantages, however, include increased complexity, cost, and size of the source. A general schematic of a KLM oscillator is shown in Figure 2-4. The titanium:sapphire ($Ti:Al_2O_3$) KLM laser has become a reliable laser source for generating ultrashort optical pulses in the femtosecond regime[86,87]. As schematically shown in Figure 2-4, the $Ti:Al_2O_3$ crystal is pumped by a continuous wave (cw) argon laser at 514 nm. Dispersion is compensated within the laser cavity by adjusting the position of the prisms to permit longer or shorter pathlengths through the dispersive glass. This dispersion compensation is also used to balance the dispersion between the two arms of the OCT interferometer. With a center wavelength at 800 nm, output powers near 400 mW, and spectral bandwidths of 145 nm, this source was used for high resolution OCT imaging by a number of investigators[88,89]. Free-space axial resolutions as high as 1.9 μm have been achieved.

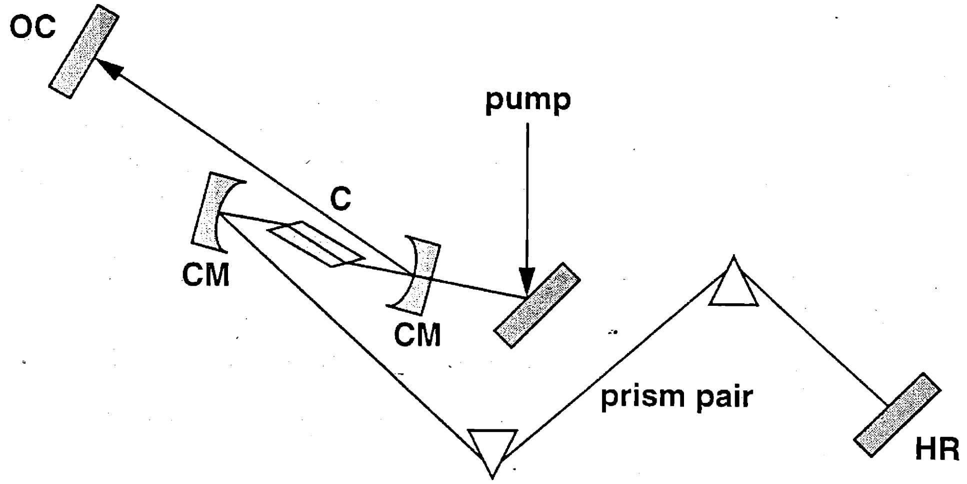

FIGURE 2-4: Schematic of KLM oscillator. Abbreviations: C, crystal; CM, curved mirror; HR, high reflector; OC, output coupler.

Because longer wavelengths scatter less and permit deeper imaging penetration in biological tissue, a solid-state KLM laser using a Cr^{4+}:forsterite crystal was developed by Bouma, *et. al.*[90] for OCT imaging. Cr^{4+}:forsterite oscillators pumped by a cw Nd:YAG have achieved pulse durations less than 25 fs by several groups[91,92]. Using a diode-pumped Nd:YAG pump laser with 6 W output power at 1.06 μm, a KLM Cr^{4+}:forsterite laser has been constructed. Output from this source is 300 mW at 1280 nm center wavelength[90]. A spectral bandwidth of 50 nm results in a 15 μm coherence length. The stability of the pump source eliminates the need for dual-balanced detection which was required for shot-noise-limited detection with the $Ti:Al_2O_3$ source. The high output powers from this laser permit higher image acquisition rates while maintaining high signal-to-noise ratios (SNRs). Scanning speed and SNR limitations will be covered in Section 2.7. The use of this laser permits high-speed *in vivo* imaging of tissue morphology which is necessary for any viable surgical application.

The spectral and temporal output characteristics of the KLM laser are related through the Fourier transform. Therefore, the frequency bandwidth $\Delta\nu$ and the pulse duration τ_p cannot vary independent of one another. The minimum duration-bandwidth product is

$$2\pi \cdot \Delta\nu \cdot \tau_p \geq 2\pi \cdot S_p \tag{2-24}$$

where S_p is a constant dependent on the pulse shape. For a Gaussian pulse, $S_p = (2 \ln 2) / \pi \approx 0.441$. Using the proportionality relation

$$\frac{\Delta\nu}{\nu} = \frac{\Delta\lambda}{\lambda} \tag{2-25}$$

which is equal to

$$\Delta\nu = \frac{c \cdot \Delta\lambda}{\lambda^2}, \tag{2-26}$$

Equation (2-24) can be written as

$$\Delta\lambda \geq \frac{S_p \lambda^2}{\tau_p c}. \tag{2-27}$$

Therefore, for a 25 fs Gaussian pulse from a Cr^{4+}:forsterite KLM laser operating at $\lambda = 1280$ nm, the Fourier-transform limited spectral bandwidth would be 96 nm. This corresponds to a coherence length and axial resolution of 7.5 μm.

To further broaden the output spectrum from this laser, and therefore increase axial imaging resolutions, the high peak output powers are used to induce self-phase modulation (SPM) within an optical fiber[93-95]. Self-phase modulation was induced in a single-mode Corning SMF-DS™ CPC3 dispersion-shifted fiber[90]. Spectral broadening due to self-phase modulation is illustrated in Figure 2-5. SPM in standard SMF-28 single-mode fiber with a zero group velocity dispersion point around 1.3 μm interferes with the output spectrum broadening the autocorrelation function and raising the level of the sidelobes. Using SMF-DS single-mode dispersion-shifted fiber with a zero group velocity dispersion point at 1.55 μm, the spectrum is broadened to 127 nm with an autocorrelation function that has reduced side lobes. The coherence length was 5.7 μm FWHM. This laser was used to acquire all of the high-resolution images in this thesis. In addition, its high-output powers were used to acquire the majority of the high-speed images as described in the following chapters. Although high-resolution and high-speed OCT imaging can be performed with this laser source, this source in its current state of development does not represent a reliable, compact, and cost-effective option for clinical or surgical applications. Studies have investigated the use of compact cavity designs for mode-locked solid-state lasers[96]. Ongoing research will continue to investigate compact and reliable sources with output characteristics suitable for OCT imaging.

2.4.3 Fiber lasers

Fiber sources may offer broad spectral bandwidths at high output powers in simple and compact geometries. Rare-earth doped fibers (REDFs) can be diode-pumped and output single-mode beam profiles ideal for coupling into a clinical or surgical-based OCT instrument. Pumping of the REDF results in fluo-

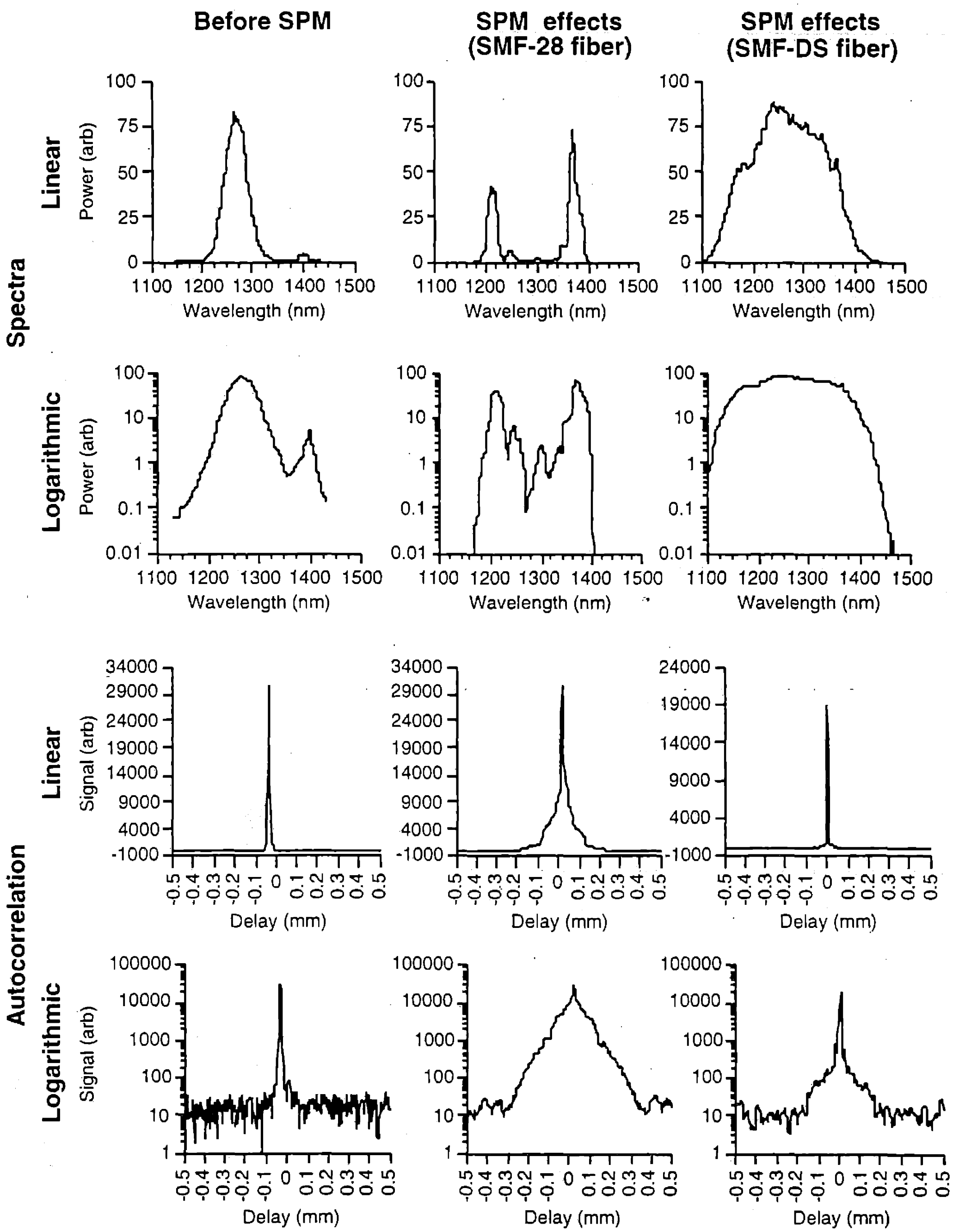

FIGURE 2-5: Output from KLM Cr^{4+}:forsterite laser[90]. Plots illustrate spectrum and autocorrelation function on both linear and logarithmic vertical axes. Output is shown prior to SPM, after SPM using standard SMF-28 single-mode fiber, and after SPM using SMF-DS single-mode dispersion-shifted fiber.

rescence within the fiber which is amplified by spontaneous emission along the fiber length. During amplification, spectral narrowing and lasing occurs. Angle-cleaving the fiber ends and reducing the degree of feedback within the device suppresses lasing and produces outputs of broad bandwidth superfluorescence.

Fibers doped with neodymium, praesodymium[97], ytterbium[98], erbium[99], and thulium[100], among others, have been investigated as possible sources for OCT imaging[101]. Thulium-doped fiber with emissions at 1.8 µm offers the most promise. The 1.8 µm wavelength is in a region of low water absorption between a sharp peak around 1.6 µm and increasing absorption after 2.0 µm. The fiber was pumped with 500 mW of 785 nm output from a $Ti:Al_2O_3$ laser. An asymmetric but near-Gaussian spectrum with a 80 nm bandwidth produced a coherence length of 18 µm. A comparison between OCT imaging at 1.8 µm and 1.3 µm of *in vitro* calcified aortic plaques shows similar image penetration with few effects due to high sidelobes in the autocorrelation function[100]. The current state of development for most of the REDF sources, however, is limited by narrow, non-Gaussian spectrums, low output powers, and unavailable or expensive pumping diodes.

2.5 Axial Scanning Mechanisms

In the OCT system, a mode-locked laser, superluminescent diode, or other suitable broad-bandwidth optical source is used and coupled to the interferometer. The reference arm illustrated in Figure 2-1 must incorporate some means of varying the optical pathlength between the two arms of the interferometer. Only when the optical pathlengths of the sample and reference arms are equal to within the source coherence length is optical interference detected. Thus, by varying the reference arm path length, depth resolved interferometric profiles of the samples optical properties can be obtained. Although varying the reference arm path length is not difficult at slow velocities, doing so becomes increasingly difficult when performing linear axial scanning at rates fast enough for high-speed *in vivo* OCT imaging. This section describes and compares mechanisms by which axial scanning may be performed.

2.5.1 Galvanometer retroreflector

The simplest mechanism is the mechanical displacement of a reference arm mirror mounted on a computer-controlled galvanometer. Linear translation of a flat mirror or the sweep of a mirrored retroreflector in a small arc enables linear velocities up to tens of millimeters per second at frequencies less than 100 Hz. The length and mass of the mirror mount determine the maximum frequency before mechanical resonances affect the linear displacement. Custom drive waveforms can be used to minimize resonant oscillations from rapid changes in direction of the reference arm mirror. The galvanometer-mounted retroreflector used to acquire images in this thesis operated at a linear translation velocity of 30 mm/s. Therefore, a 300 x 300 pixel, 3 x 3 mm image required approximately 30 s to acquire.

The linear translation velocity imparts a Doppler-shift in the reflected light. This Doppler-shifted frequency beats with the frequency of the light returning from the sample arm. Detection electronics discussed in Section 2.6 will explain how this Doppler-shifted frequency is used in optical heterodyne detection.

2.5.2 Piezoelectric displacement

Piezoelectric crystalline materials have the property of producing mechanical forces proportional to applied electrical charges. The basis of this effect is an asymmetrical crystalline structure. Polycrystalline ferroelectric ceramics such as lead-zirconate-titanate (PZT) are preferred for their optimum expansion or displacement[102,103].

The first use of piezoelectric materials to vary the optical pathlength of the OCT reference arm was described by Sergeev, *et. al.*[104]. Tens of meters of optical fiber were wound around a piezoelectric cylinder. Although the change in radius of the cylinder was on the order of microns, this change over the wound optical fiber resulted in a path length change of ≈ 3 mm. By rapidly varying the drive waveform to the piezoelectric material, rapid axial scanning could be performed.

A modified design incorporating four piezoelectric stacks was used to displace two hemi-cylinders[101]. Forty meters of single-mode optical fiber were wound around the hemi-cylinders. A custom 0-60 V, 600 Hz, triangular waveform was used to drive the four PZT stacks. A custom waveform was necessary to compensate for the hysteresis effects due to temperature, displacement, and the material itself. Displacement of 10 μm resulted in a reference arm pathlength change of 3 mm. A high power of 400 W was necessary to drive the four PZT stacks. This significant demand was only feasible in the laboratory setting.

Stretching the optical fiber induced a birefringence mismatch between the two arms of the interferometer resulting in variations in detector signal amplitude[105]. To reduce this mismatch, Faraday rotators were inserted into each arm of the interferometer. Faraday rotators will rotate the polarization of the incident light in a non-reciprocal manner[106]. The Faraday rotators are designed for one wavelength. The use of broad bandwidth light results in incomplete correction of polarization mode dispersion. This reduces the contrast of the interference fringes and broadens the coherence length by a factor of two[101]. The use of PZT stacks enabled acquisition of 1200 axial scans per second or 300 x 300 pixel OCT images in 250 ms. This axial scanning method was used to acquire *in vivo* high-speed images of a beating *Xenopus laevis* (African frog) tadpole heart[107].

2.5.3 Optical delay line

Techniques for obtaining optical delays have evolved from the development of autocorrelators for determining the temporal shape of an ultrafast optical pulse[108]. Spinning mirrors and rotating cubes have been used to rapidly alter the pathlength and delay an optical pulse[109,110]. Scan velocities > 20 m/s at 400 Hz repetition rates are possible, but nonuniform delay rates and varying dispersion during cube rotation require additional compensation to linearize scanning.

Phase control of the optical field is an effective method for producing a scanning optical delay[111]. Based on the Fourier transform property

$$f(t-t_0) \leftrightarrow F(j\omega)\exp(-j\omega t_0) \tag{2-28}$$

which states that if the original spectrum $F(j\omega)$ is shifted in phase by $-\omega t_0$, then the function in time will be delayed by t_0. This technique has been used to temporally shape ultrafast pulses by spatially filtering the optical spectrum at the Fourier transform plane of a lens once the spectrum has been dispersed by a grating. A second lens-grating pair is used to perform an inverse Fourier-transform resulting in a modified temporal profile of the ultrafast pulse[112,113].

The diagram in Figure 2-6 illustrates an optical delay line developed by Tearney, *et. al.*[114] that has been used for high-speed OCT imaging. This configuration represents a folded geometry where the incident optical spectrum is spread by the grating, Fourier transformed by the lens, and incident on a galvanometer scanning mirror. The angular scanning of the mirror imparts a sweeping wavelength-dependent phase shift. The returning field is inverse Fourier transformed and re-coupled back into the single-mode

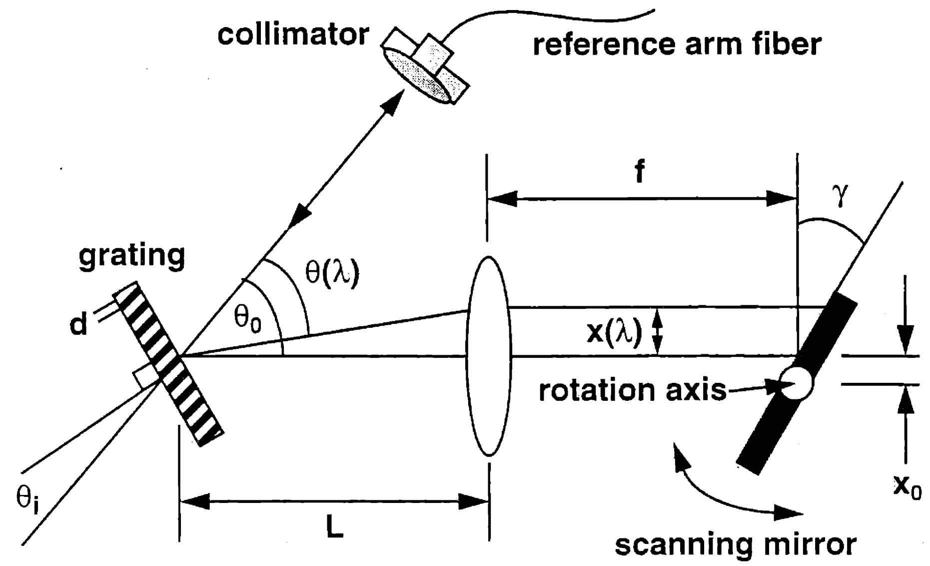

FIGURE 2-6: Optical delay line for high-speed OCT imaging[101].

fiber of the interferometer reference arm. The swept wavelength-dependent phase shift in the frequency domain corresponds to a swept time delay in the time domain. The folded geometry not only doubles the time delay, but also conveniently re-couples the light back into the interferometer.

The phase delay produced by the scanning galvanometer mirror in Figure 2-6 can be written as

$$\phi(\lambda, t) = \frac{4\pi f\gamma t}{\lambda}\left[\theta_0 - \operatorname{asin}\left(\frac{\lambda}{d} - \sin\theta_i\right) + \frac{x_0}{f}\right] \tag{2-29}$$

where the variables are defined in Figure 2-6. This phase delay reduces to

$$\phi(\lambda_0, t) = \frac{4\pi\gamma t x_0}{\lambda_0} \tag{2-30}$$

when the rotation angle γ changes linearly with time[101]. Therefore, the modulation frequency used in heterodyne detection of OCT is

$$f_g = \frac{2\gamma x_0}{\lambda_0}. \tag{2-31}$$

One advantage of this optical delay scheme is the independence of the phase and group delays. The total group delay for the double-pass configuration in Figure 2-6 is given by

$$l_g(\gamma) = \frac{2f\lambda_0\gamma}{d\cos\theta_0}. \tag{2-32}$$

For small mirror scan angles, this group delay is linearly dependent on the angle γ. The group delay can be varied to perform axial scanning and OCT imaging at different rates while the phase modulation remains matched to the center frequency of the detection filter used for demodulation[101].

This optical setup enables flexible control over both the modulation frequency and dispersion compensation. Arbitrary modulation frequencies may be obtained by varying the offset x_0 of the center wavelength λ_0 from the center axis of rotation of the scanning mirror as shown in Equation (2-30). The group velocity dispersion of the double-pass grating compressor has been analyzed by Fork, *et. al.*[115], and described by

$$\left.\frac{d^2\phi}{d\omega^2}\right|_{\omega_0} = -\frac{\lambda_0^3(L-f)}{\pi c^2 d^2}\frac{1}{\sqrt[3]{\cos\theta_0}}. \qquad (2\text{-}33)$$

Dispersion compensation is varied by adjusting L, the separation between the grating and the lens. For L > f, the optical delay line contributes negative dispersion while for L < f, positive dispersion is added. This adjustment allows dispersion balancing between the two arms of the OCT interferometer.

For high-speed OCT imaging, the galvanometer scanning the mirror in the optical delay line was driven with a 1 kHz triangular waveform. This enabled 2000 scans per second because scanning was performed for both the rising and falling portions of the waveform. The 3° rotation of the mirror enabled axial scan lengths of 3 mm. High-speed image acquisition rates were dependent on the number of horizontal pixels in the OCT image. Images of 256 x 256 pixels were acquired in 8 frames per second. Real-time acquisition, considered to be 30 frames per second, is possible for images with 67 horizontal pixels.

2.6 Detection Electronics

The signal current generated by the photoelectric conversion at the detector represents the axial point spread function of the OCT system modulated by a sinusoid as shown in Equation (2-11). The modulation frequency is the beat frequency between the backreflections from the sample and the Doppler-shifted reflections from the reference arm. For the galvanometer-scanning retroreflector in the reference arm, the Doppler-shifted frequency is

$$f_D = \frac{2v_M}{\lambda_0} \qquad (2\text{-}34)$$

where v_M is the velocity of the retroreflecting mirror. The optical pathlength variations between the reference and sample arms map the spatial distributions of optical backscatter from within the tissue into the signal current which is a function of time. The detection electronics module in Figure 2-1 extracts the envelope of the interferometric signal, the peak of which represents the intensity of optical backscatter from the spatial position within the tissue. The block diagram for the detection electronics is shown in Figure 2-7. The detection electronics were developed and constructed by Swanson, *et. al.*[59]. The transimpedance amplifier converts the detector signal current into a voltage which is then bandpass-filtered around the Doppler modulation frequency f_D. The interferometric signal, which has been separated from both the DC component and the noise, is then demodulated and low-pass filtered to extract the envelope. The amplitude of the envelope is stored in an array representing the spatial position within the image.

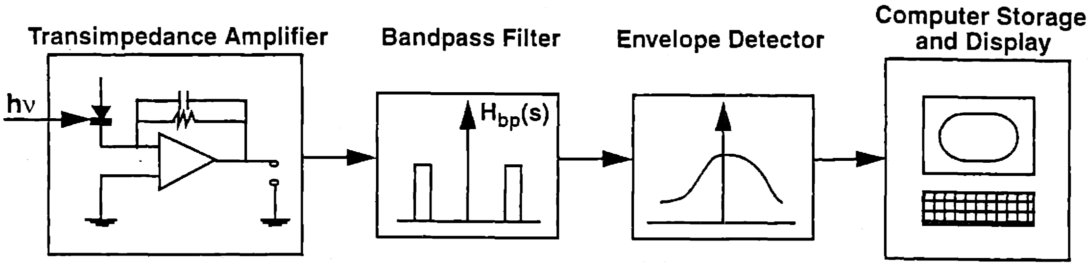

FIGURE 2-7: Block diagram of detection electronics.

The transimpedance amplifier circuit in Figure 2-8 converts the photon-generated current i(t) into a

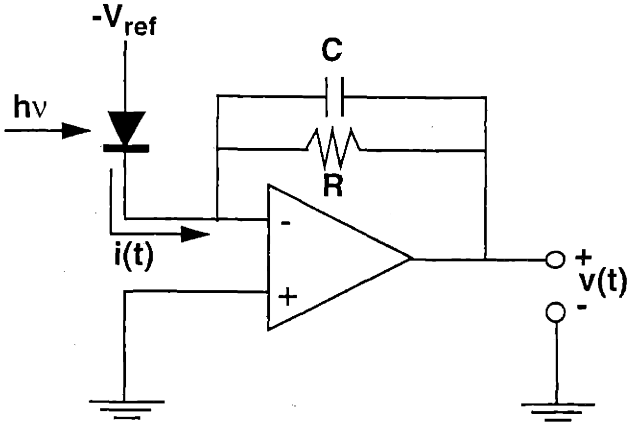

FIGURE 2-8: Transimpedance amplifier.

voltage v(t) according to Ohm's Law, v(t) = i(t) R. The resistor and capacitor provide feedback and stabilize the amplifier. The gain of amplifier is determined by the resistance R and a single pole at

$$\omega_c = \frac{1}{RC} \tag{2-35}$$

above which the gain will roll off at 20 dB/decade.

The voltage v(t) is then bandpass filtered to separate the interferometric signal from the noise. Two types of bandpass filters were used depending on the Doppler-shifted modulation frequency. For frequencies less than 100 kHz, such as those generated with the galvanometer-scanning retroreflector, two active Sallen and Key filters were cascaded to shape the pass-band. The cascade filter shown in Figure 2-9 con-

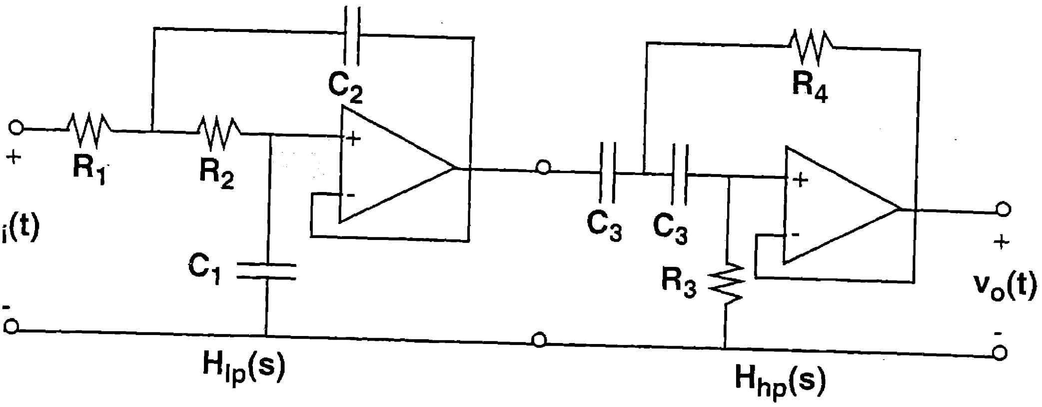

FIGURE 2-9: Active Sallen and Key cascade filter.

sists of a low-pass filter with transfer function $H_{lp}(s)$ followed by a high-pass filter with transfer function $H_{hp}(s)$. The overall transfer function $H_{bp}(s)$ is the product of the two and can be described in terms of the undamped natural frequencies ω and the quality factors Q for the low- and high-pass filters:

$$H_{bp}(s) = H_{lp}(s) \cdot H_{hp}(s) = \frac{\omega_{lp}^2}{s^2 + \frac{\omega_{lp}}{Q_{lp}}s + \omega_{lp}^2} \cdot \frac{\omega_{hp}^2 s^2}{s^2 + \frac{\omega_{hp}}{Q_{hp}}s + \omega_{hp}^2} \tag{2-36}$$

where

$$\omega_{lp} = \frac{1}{\sqrt{R_1 R_2 C_1 C_2}} \tag{2-37}$$

$$\omega_{hp} = \frac{1}{C_3\sqrt{R_1 R_2}} \tag{2-38}$$

$$Q_{lp} = \sqrt{\frac{C_2}{C_1}} \tag{2-39}$$

$$Q_{hp} = \frac{1}{2}\sqrt{\frac{R_1}{R_2}}. \tag{2-40}$$

Bode plots of magnitude and phase were generated to predict the frequency response using values of $R_1 = R_2 = 3.16$ kΩ, $R_3 = 68.1$ kΩ, $R_4 = 681$ Ω, $C_1 = 100$ pF, $C_2 = 0.01$ μF, $C_3 = 470$ pF. The center frequency of 50 kHz corresponds to the Doppler-shifted frequency induced by the retroreflector velocity of 32.5 mm/s. The bandwidth of 16.6 kHz with a roll off of 40 dB/decade outside of the bandpass will be important for bandwidth selective Doppler imaging in Section 5.4.2.

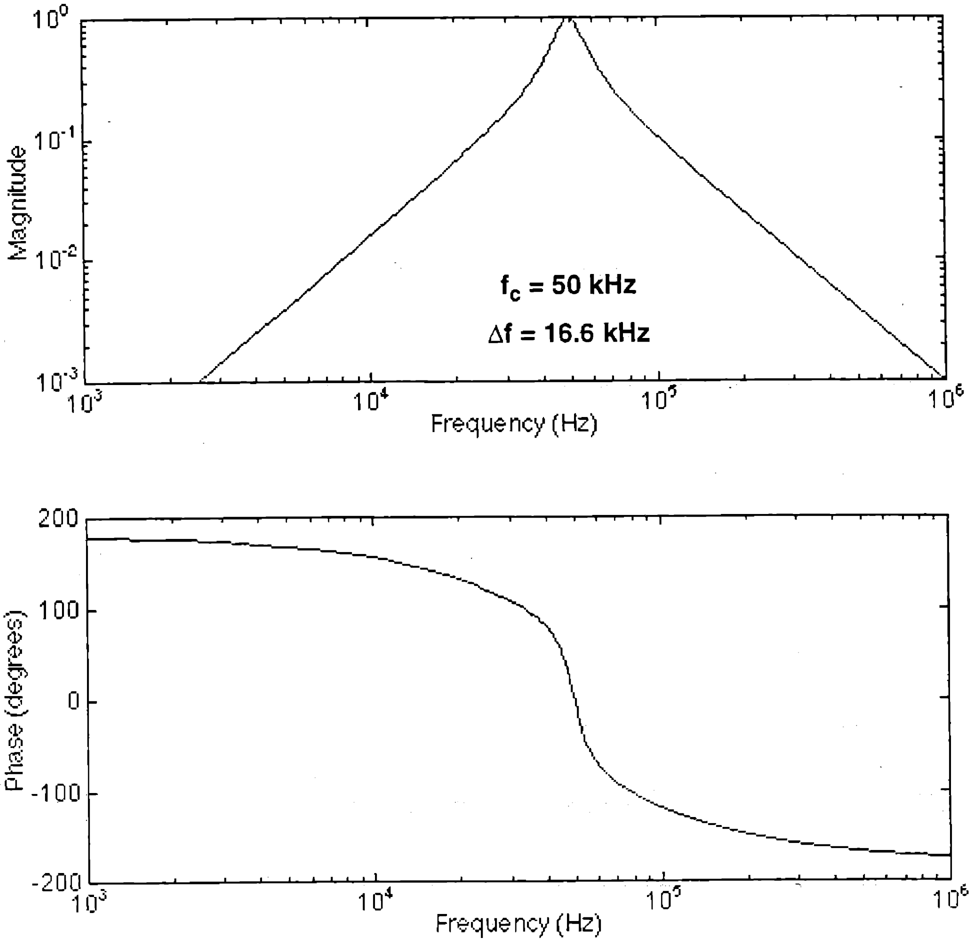

FIGURE 2-10: Frequency response of Sallen and Key cascade.

For modulation frequencies above 100 kHz, the slew rate of the operational amplifiers will limit the frequency response. Therefore, a passive Butterworth filter is used for bandpass filtering when performing high-speed OCT imaging with the optical delay line (Section 2.5.3). The circuit diagram of a fourth order Butterworth filter is shown in Figure 2-11. The frequency response of the transfer function $H_{bp}(s)$ using component values $R_1 = 826\ \Omega$, $R_2 = 2606\ \Omega$, $C_1 = 437$ pF, $C_2 = 152$ pF, $L_1 = 346\ \mu$H, $L_2 = 91\ \mu$H is shown in Figure 2-12. Lateral adjustment (x_0) of the rotating mirror in the optical delay line places the modulation frequency at the center frequency (750 kHz) of this filter to maximize SNR and utilize the full bandwidth (475 kHz). Outside of the pass-band, the frequency response falls off at ≈ 40 dB/decade.

Following bandpass filtering, the voltage v(t) is demodulated using envelope detection. Envelope detection can be modeled in Figure 2-13 as rectification by a diode followed by low-pass filtering. The diode conducts only during the rising part of the interferometric signal, charging the capacitor to the peak value. If the time constant $\tau = RC$ is long compared to the modulation frequency, then the output voltage

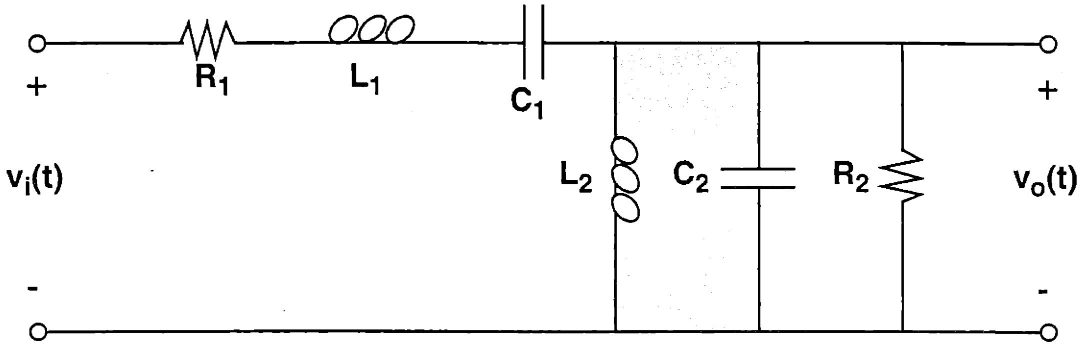

FIGURE 2-11: Passive fourth-order Butterworth bandpass filter.

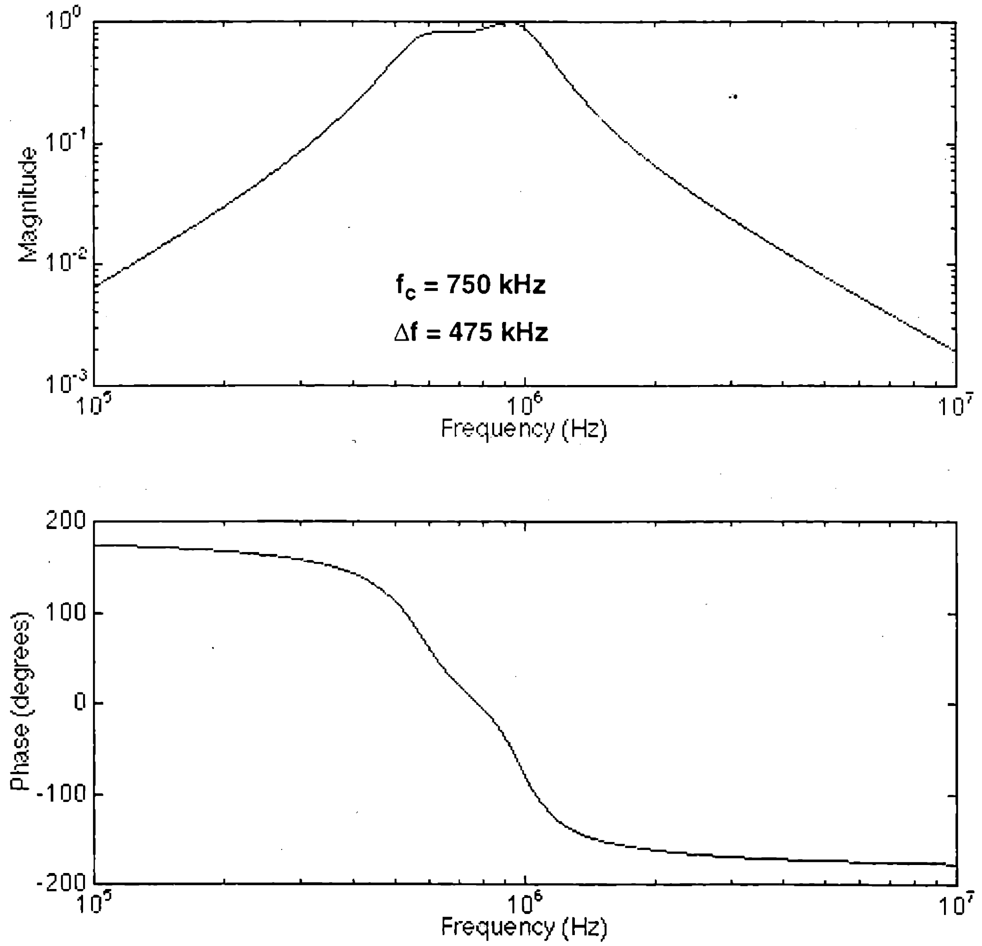

FIGURE 2-12: Frequency response of passive Butterworth bandpass filter.

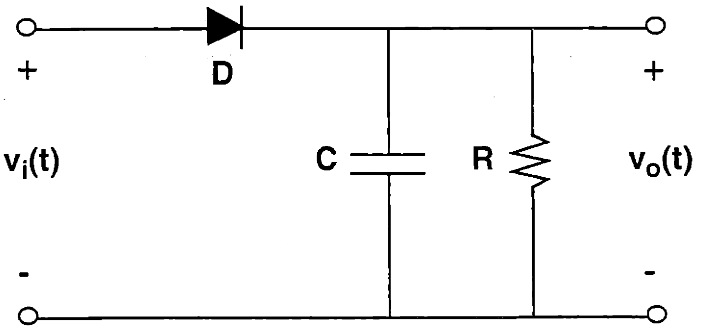

FIGURE 2-13: Envelope detection circuit.

$v_0(t)$ will follow the envelope of the interferometic signal. In practice, this envelope detection was performed with an AD637 or AD606 High Precision Wideband RMS-to-DC Converter (Analog Devices) for linear or logarithmic demodulation, respectively.

For image acquisition using the slower, galvanometer-based scanner in the reference arm, the analog output voltage $v_0(t)$ is digitized using a 12-bit A/D converter and stored in a computer. For each sweep of the reference arm pathlength, one waveform $v_0(t)$ is obtained, representing one axial profile of optical backscatter. Two-dimensional OCT images are constructed by assembling adjacent axial profiles. The base-ten logarithm of the 2-D image data is obtained to improve visibility of the full dynamic range of the data. A false-color or gray-scale table is assigned and the image is displayed on the computer.

Image acquisition at higher rates (4-8 fps), using the optical delay line to vary the pathlength difference between the reference and sample arms, requires a system for rapid acquisition, display, and storage. An *in vivo* OCT (IVOCT) system was developed by Tearney, *et. al.*[101,107] and used to perform high-speed OCT imaging. The IVOCT system is synchronized by a computer-controlled master clock. The clock controls the image acquisition by a frame grabber, the reference arm scanning by the optical delay line, and the transverse scanning by the sample-arm beam delivery instrument. As the optical backscatter intensity data is continuously acquired, the data is video-formatted for display as either 512 x 256 or 256 x 256 pixel images (4 and 8 fps, respectively). Images can be displayed in either rectangular coordinates or in polar coordinates if acquisition is performed with the radial-imaging catheter (described in Section 3.6). Images are simultaneously displayed on the computer screen and a second video monitor for real-time recording on analog super-VHS (SVHS) video tape. Options in the custom-designed software permit digital storage of screen images as well.

High-speed image acquisition is performed using the AD606 High Precision Wideband RMS-to-DC Converter for base-ten logarithmic demodulation followed by capture and display using an 8-bit variable-rate frame grabber. The PCI bus 8-bit frame grabber has sufficient dynamic range to capture all levels of the demodulated signal. Using an Apple Computer Power Macintosh 8500/120 to control the IVOCT system, image data is transferred directly from the frame-grabber memory to the computer memory using direct memory access. Both frame-grabber and computer bus speeds are sufficient to accommodate real-time video-rate (30 fps) acquisition.

2.7 System Performance

The performance of the OCT system is dependent on fundamental optical, electrical, and statistical parameters. These performance parameters and limitations will be described in this section.

2.7.1 Resolution

Gaussian optics will be used to define the resolution and optical parameters of OCT. The propagation of a Gaussian beam through beam delivery instruments in Chapter 3 will be used to compare optical properties and imaging performance. Therefore, a thorough description of the Gaussian beam is provided.

The complex amplitude of the Gaussian beam is given by[116]

$$U(\vec{r}) = \frac{C}{jz_R}\frac{w_0}{w(z)}\exp\left(\frac{-\rho^2}{w^2(z)}\right)\exp\left(-jkz - jk\frac{\rho^2}{2R(z)} + j\zeta(z)\right) \tag{2-41}$$

where z_R is the Rayleigh range, $\rho = x^2 + y^2$, and the other parameters are defined as

$$w(z) = w_0\sqrt{1 + \left(\frac{z}{z_R}\right)^2} \tag{2-42}$$

$$R(z) = z\left[1 + \left(\frac{z_R}{z}\right)^2\right] \tag{2-43}$$

$$\zeta(z) = \mathrm{atan}\left(\frac{z}{z_R}\right) \tag{2-44}$$

$$w_0 = \sqrt{\frac{\lambda z_R}{\pi}}. \tag{2-45}$$

The parameter w_0 is the minimum Gaussian beam radius defined as $1/e \approx 0.368$ down from the peak of the normalized optical field $U(\mathbf{r})$ or $1/e^2 \approx 0.135$ down from the peak of the normalized beam intensity $I(\mathbf{r}) = |U(\mathbf{r})|^2$. The transverse resolution in OCT is typically defined by the minimum spot size diameter d of the Gaussian beam which is $2w_0$. The spectral bandwidth and coherence length of the source are typically defined in terms of the full width half maximum (FWHM). For a normalized Gaussian beam, the FWHM is related to the beam diameter d by

$$FWHM = \sqrt{\ln 2}\cdot d_{1/e} = \sqrt{\frac{\ln 2}{2}}\cdot d_{1/e^2}. \tag{2-46}$$

All of the beam parameters in Equations (2-42) to (2-45) are dependent on the Rayleigh range z_R and the wavelength λ. The Rayleigh range is defined as the distance from the minimum beam radius w_0 at $z = 0$ to where the radius has increased by a factor of the square root of 2 at $z = z_R$. The confocal parameter b or depth of focus of the Gaussian beam is defined as

$$b = 2 \cdot z_R = 2\frac{\pi w_0^2}{\lambda_0} \tag{2-47}$$

and represents the region in which the beam area lies within a factor of 2 of its minimum. The confocal parameter is an important factor in OCT imaging because over this region, the transverse resolution is assumed relatively constant. The converging and diverging Gaussian beam above and below the region defined by the confocal parameter will have larger spot size diameters, and hence, poorer transverse resolution. The dependency of the confocal parameter on the spot size diameter and the wavelength is illustrated in Figure 2-14. The wavelengths represented are visible (550 nm) and those for which SLDs are currently available. For a given spot size diameter, shorter wavelengths will diverge less, providing a longer region of uniform transverse resolution. The difference between visible and near IR wavelengths must be considered when designing beam delivery instruments through which both wavelengths are propagated.

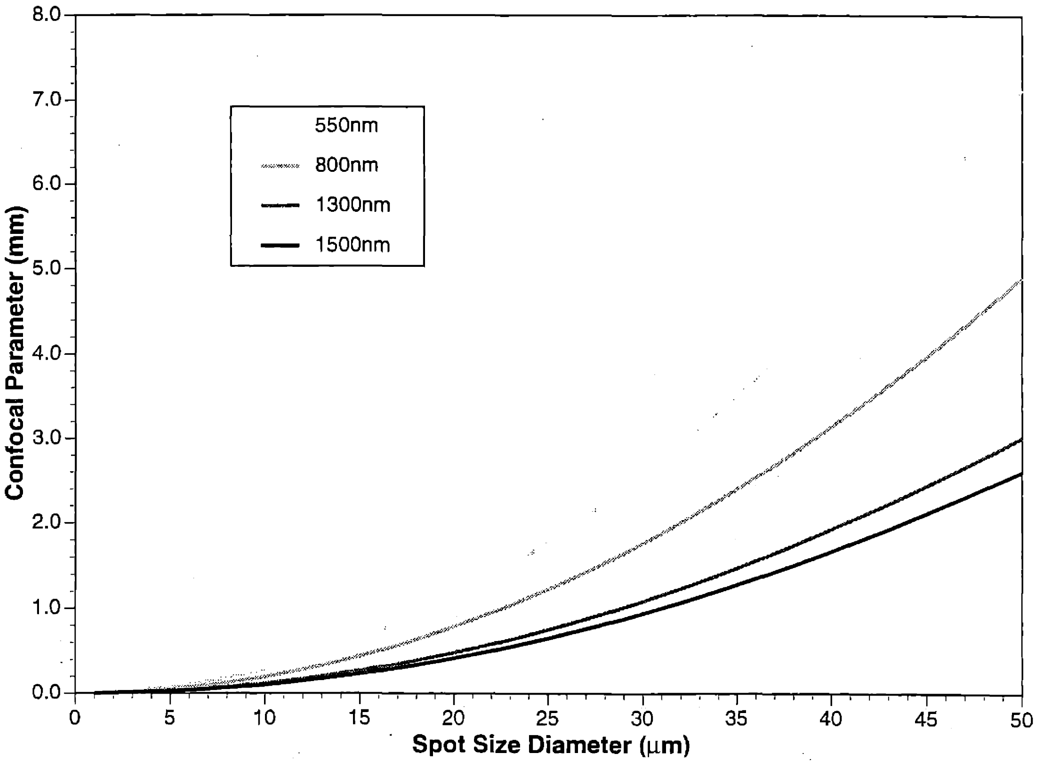

FIGURE 2-14: Confocal parameter dependence on spot size diameter and source wavelength.

Far from the minimum beam waist, when z >> z_R, the beam diameter increases approximately linearly with z which defines a half-angle θ_0 given by

$$\theta_0 = \frac{2}{\pi} \cdot \frac{\lambda_0}{2w_0}. \tag{2-48}$$

Smaller spot size diameters will produce a more highly diverging beam as illustrated in Figure 2-15.

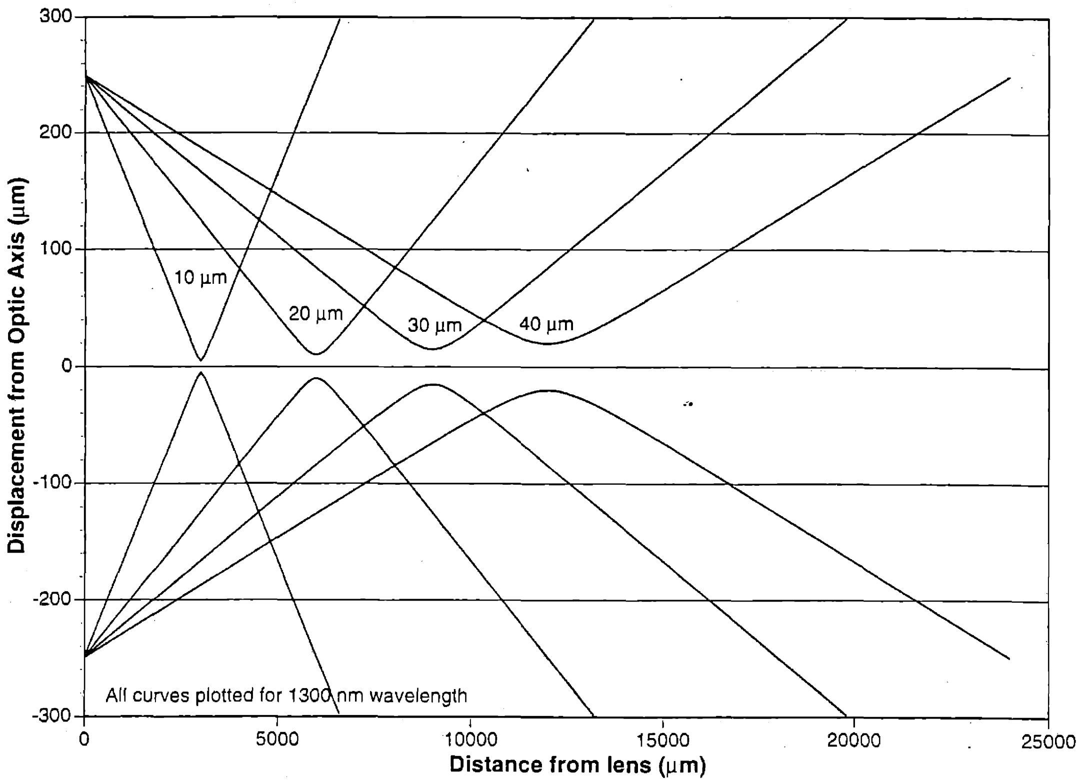

FIGURE 2-15: Gaussian beam diameters as a function of minimum spot size diameter and distance from lens.

Assuming constant beam diameters incident on the focusing lens, this figure also demonstrates the shift of the focus toward the lens for smaller spot size diameters or equivalently, higher NA lenses.

In OCT, the transverse and axial image resolutions are independent. For measurements of spectral bandwidth and coherence length, the FWHM of a Gaussian beam is used. The axial resolution or coherence length Δl_c in free-space is governed by the center wavelength λ_0 and the spectral bandwidth $\Delta\lambda$ of the source

$$\Delta l_c(air) = \frac{2\ln 2}{\pi}\left[\frac{\lambda_0^2}{\Delta\lambda}\right]. \tag{2-49}$$

A plot illustrating the dependence on the coherence length on the center wavelength and spectral bandwidth is shown in Figure 2-16. Shorter wavelengths require less spectral bandwidth to achieve a given coherence length. Therefore, to maximize the axial OCT resolution, shorter wavelength sources with broad spectral bandwidths are desired. However, shorter wavelengths are scattered more in biological tissue (see Section 5.2).

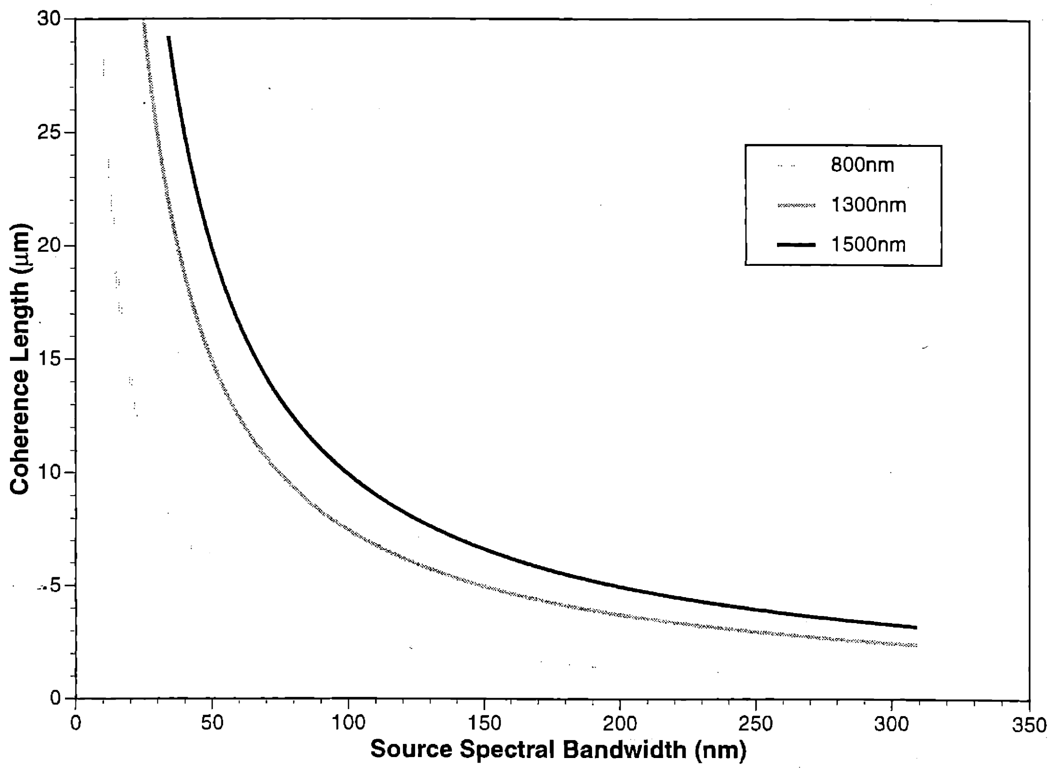

FIGURE 2-16: Coherence length dependence on source wavelength and spectral bandwidth.

A confocal OCT limit can be defined which is dependent on the confocal parameter b and the coherence length of the source Δl_c

$$\text{confocal OCT limit:} \quad b \leq \Delta l_c. \tag{2-50}$$

Above this limit, which is typically encountered in low-resolution OCT imaging, the confocal parameter is much larger than the coherence length. Translation of the reference arm mirror sweeps the coherence envelope through the confocal parameter. The number of non-overlapping envelopes (defined by FWHM) within the confocal parameter is then determined by

$$\frac{b}{\Delta l_c} = \frac{2\pi w_0^2}{\lambda_0 \Delta l_c}. \tag{2-51}$$

Below this limit, at high transverse resolutions, the confocal parameter will be less than the coherence length. Therefore, reference arm scanning alone is insufficient for axial imaging because the majority of the scan positions will lie outside of the confocal parameter. An axial translation of the beam focus must subsequently be employed. Within the confocal OCT limit, as in high NA confocal microscope systems, the confocal parameter will determine the axial resolution while the transverse resolution will remain as the spot size diameter d.

The use of OCT can further increase axial resolution in highly scattering tissue as was shown in a study by Izatt, *et. al.*[117]. A similar confocal imaging limit was defined for optical coherence microscopy (OCM). OCM is the use of coherence gating in OCT to further reject out-of-focus light when using high NA objectives and imaging in highly scattering media. Assuming the source spectrum is Gaussian, the axial point spread function in OCT and OCM decreases exponentially compared to the geometric decrease in single-mode confocal microscopy. This results in improved optical sectioning when the focal plane is dominated by light scattered from other planes. In terms of the scattering MFP of tissue, confocal microscopy is limited to 0-5 MFP while OCM extends the imaging depth to 5-15 scattering MFPs; down to the quantum noise sensitivity limit.

The axial OCT resolution will change when the imaging beam is propagated through tissue or other material with an index of refraction that is different from air. The axial resolution in tissue with an average index of refraction n_t will be scaled by the inverse of the index

$$\Delta l_c(tissue) = \frac{\Delta l_c(air)}{n_t} \tag{2-52}$$

because of the change in the wavelength of the light propagating through the tissue. The transverse resolution, which is determined by the spot size diameter d of the focused beam within the tissue, will change in a more complicated manner. For an incident beam diameter D on a lens of focal length f, the spot size diameter in air is

$$d_a = 2w_0 \approx \frac{4}{\pi}\lambda_0\frac{f}{D} = \frac{2}{\pi}\lambda_0 \cdot \frac{1}{\tan\theta_a} \tag{2-53}$$

where θ_a is the half-angle of the incident beam on the tissue[116]. Similarly, the spot size diameter in tissue is given by

$$d_t = \frac{2\lambda_t}{\pi\tan\theta_t}. \tag{2-54}$$

Using Snell's Law, the two half-angles θ_a and θ_t are related by

$$\tan\theta_t = \frac{\sin\theta_a}{n_t\sqrt{1-(\sin\theta_a/n_t)^2}} \tag{2-55}$$

and the spot size diameter in tissue d_t in terms of the NA ($\sin\theta_a$) and the tissue index n_t is therefore

$$d_t = \frac{2\lambda_0}{\pi} \cdot \frac{\sqrt{1-(\sin\theta_a/n_t)^2}}{\sin\theta_a}. \tag{2-56}$$

The ratio of the transverse resolution in tissue to the transverse resolution in air is then

$$\frac{d_t}{d_a} = \frac{\sqrt{1-(\sin\theta_a/n_t)^2}}{\cos\theta_a}. \tag{2-57}$$

To verify Equation (2-57), two limits can be examined

$$\lim_{n_t \to 1}\left(\frac{d_t}{d_a}\right) = 1 \tag{2-58}$$

and

$$\lim_{\theta_a \to 0}\left(\frac{d_t}{d_a}\right) = 1. \tag{2-59}$$

Hence, from Equation (2-58), as the tissue index approaches that of air ($n = 1$), the spot sizes in air and in tissue will become equal. Equation (2-59) reflects the NA of the focusing optics. As the beam becomes collimated ($\theta_a = 0$) the spot sizes in air and in tissue will again become equal.

When the confocal parameter is much larger than the coherence length, the confocal parameter should be chosen to closely match the imaging penetration depth (typically 1-2 mm), however, because an inverse relationship exists between the confocal parameter (depth of field) and the transverse image resolution, there will be a loss in transverse resolution. For imaging at high transverse resolution, when $b \approx \Delta l_c$, large depths of field are not feasible. Therefore, the spot size diameter should be chosen to closely match the coherence length providing pixel dimensions that are comparable in both the axial and transverse dimensions. To image in depth, the short confocal parameter requires additional mechanisms to shift the focus of the lens axially through the tissue while simultaneously positioning the coherence imaging volume to maintain overlap. This technique is called focus tracking and is discussed in Section 3.2.

Typical free-space axial resolutions for the SLD-based OCT systems range from 15-20 μm. The broader spectral bandwidths of the KLM lasers permit axial resolutions as high as 5.1 μm for the Cr^{4+}:forsterite and 1.9 μm for the Ti:Al_2O_3 sources. Transverse resolutions are governed by the beam-delivery instrument optics and are typically 30 μm for *in vitro*, SLD-based imaging. At 1300 nm wavelengths, this results in a 1.1 mm confocal parameter. For high-resolution imaging, it is more important to closely match the transverse resolution with the axial resolution. A spot size diameter of 9 μm at the Cr^{4+}:forsterite center wavelength of 1280 nm gives a confocal parameter of 100 μm.

2.7.2 Noise

Noise within the OCT system arises from the optical source and the detection electronics. The term, quantum noise, can be used to describe these contributions. In addition to the statistical fluctuations of the source, the statistical nature of converting a photon into an electron generates its own noise, called shot noise. Each photoelectron in a quantum detector will produce a current impulse given by

$$i = e\frac{v}{x} = \frac{e}{\tau} \tag{2-60}$$

where v is the free electron velocity and x is the distance it travels before recombining; giving a lifetime τ. If $i_D(t)$ is the detector current produced by the optical photons, then the Fourier transform of this current is described by

$$I_D(\omega) = e\left[\frac{\sin(\omega\tau/2)}{\omega\tau/2}\right]. \tag{2-61}$$

Therefore, the process of detecting a photon produces a current pulse whose frequency components are spread over a band according to the spectral density function

$$S_D(\omega) = \frac{e}{\pi T}\left[\frac{\sin(\omega\tau/2)}{\omega\tau/2}\right]^2\Bigg|_{\tau\to 0} \to \frac{e}{\pi T} \tag{2-62}$$

where T represents the sampling interval.

The finite temperature within the detection electronics contributes to thermal noise. The maximum power that can be transferred from a blackbody at a temperature T in a bandwidth Δv can be described as

$$P = \frac{hv}{\exp\left(\frac{hv}{kT}\right) - 1}\Delta v. \tag{2-63}$$

A current generator defined to transfer this power would be, in terms of squared rms current,

$$\overline{i_n^2} = \frac{4}{R}\left[\frac{hv}{\exp\left(\frac{hv}{kT}\right) - 1}\right]\Delta v \cong \frac{4kT}{R}\Delta v \tag{2-64}$$

which shows that only the resistive components will accept or generate power and hence, produce thermal noise. Capacitors and inductors will affect the bandwidth Δv, but will not contribute to the thermal noise.

In practice, OCT detection is optimal if operating within the shot-noise limit. By choosing the proper transimpedance gain and reference arm power, shot-noise will exceed the contributions from thermal noise. A low-frequency noise contribution, called 1/f noise, may arise from within the semiconductor material of the detector or from the mechanical oscillations of optical mounts and components. This noise is avoided by modulating the OCT signal current above the dominant low-frequency (< 10 kHz) components of this noise source.

2.7.3 Dynamic range

The contributions of shot, thermal, and 1/f noise result in a decrease in signal-to-noise ratio (SNR) and dynamic range (DR). The maximum SNR possible, assuming shot-noise dominates the thermal noise, is defined as

$$SNR(dB) = 10\log\left[\eta_{qe}\frac{\langle P_s\rangle}{h\nu}\frac{1}{2\Delta\nu}\right] \qquad (2\text{-}65)$$

where η_{qe} is the quantum efficiency and $<P_s>$ is the time-averaged signal power. Experimentally, the SNR is determined by measuring the peak signal from a mirror placed in the sample arm and dividing by the variance of the signal when the sample arm is blocked. The SNR is represented in units of decibels because of the high sensitivity of the optical heterodyne detection. For the slow-scanning, amplified SLD-based OCT system, theoretical SNRs as high as 126 dB are possible (η_{qe} = 0.8, $<P_s>$ = 5 mW, $\Delta\nu$ = 3 kHz).

The SNR alone does not specify the dynamic range of the OCT system. Although a SNR of 120 dB implies that a signal 10^{-12} of the sample arm power can be detected, the signals returning from the tissue do not approach the magnitude of the incident power. Therefore, the dynamic range is more accurately stated as the difference between the SNR and the maximum signal detected returning from the sample. Maximum backreflections from tissue are typically -45 to -55 dB giving a dynamic range of approximately 70 dB.

The dynamic range may be further limited by the digitization of the analog signal. For an n-bit A/D converter, the dynamic range DR, in decibels, would be limited to

$$DR(dB) = 10\log(2^n). \qquad (2\text{-}66)$$

Current 12-bit A/D converters are therefore restricted to a dynamic range of 36 dB resulting in loss of data during the scaling process. The use of a base-ten logarithm demodulator circuit enables a larger dynamic range of 60-80 dB.

The SNR in Equation (2-65) is linearly dependent on the signal power. This was empirically demonstrated by measuring the SNR and acquiring images of the same tissue for various sample arm powers using the galvanometer scanning retroreflector in the reference arm and the amplified SLD source. The effect of SNR on image quality is shown in Figure 2-17 by acquiring images of *in vitro* human uterus. For SNR less than 100 dB, image penetration is poor for this highly scattering tissue. The vertical lines in each image indicate the location of an axial scan obtained for comparison between images. This comparison is shown in Figure 2-18. With a relatively constant peak signal from the tissue surface, the noise floor elevates with decreasing SNR. From these axial plots, it is obvious that with lower SNR, the DR is reduced. There is also a shift in depth of the tissue surface for lower SNR. Images were acquired over time with decreasing sample arm powers. This shift is due to dehydration of the tissue over time.

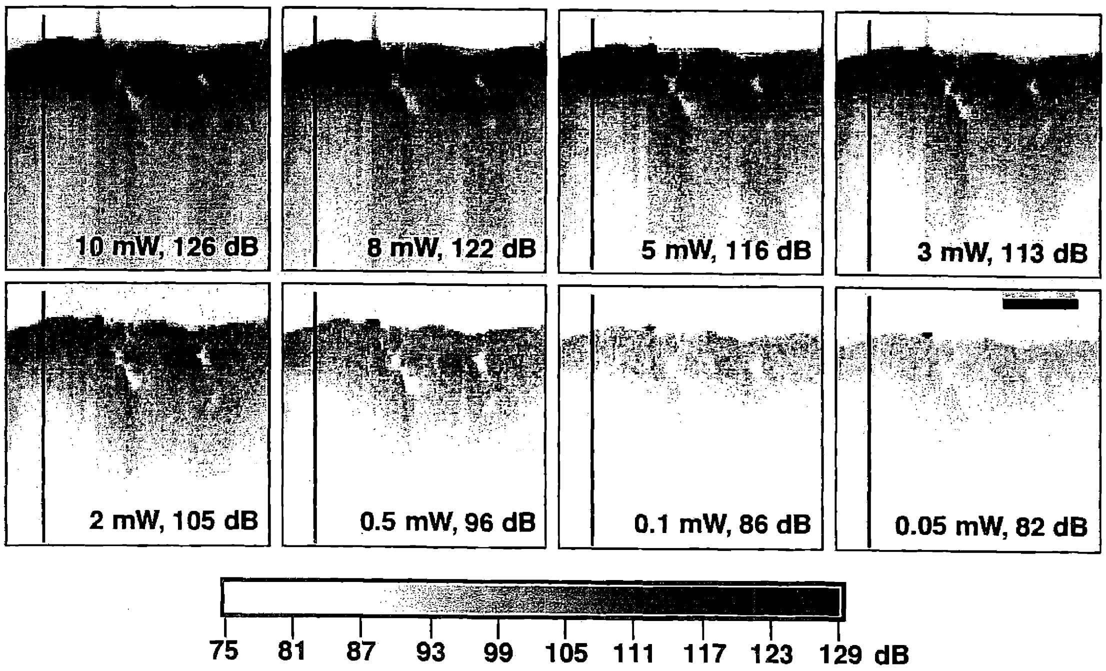

FIGURE 2-17: Effect of SNR on image contrast and quality. Images acquired from the same location on *in vitro* human uterus. Vertical lines in each image indicate location of axial scan used for comparison. Bar represents 1 mm.

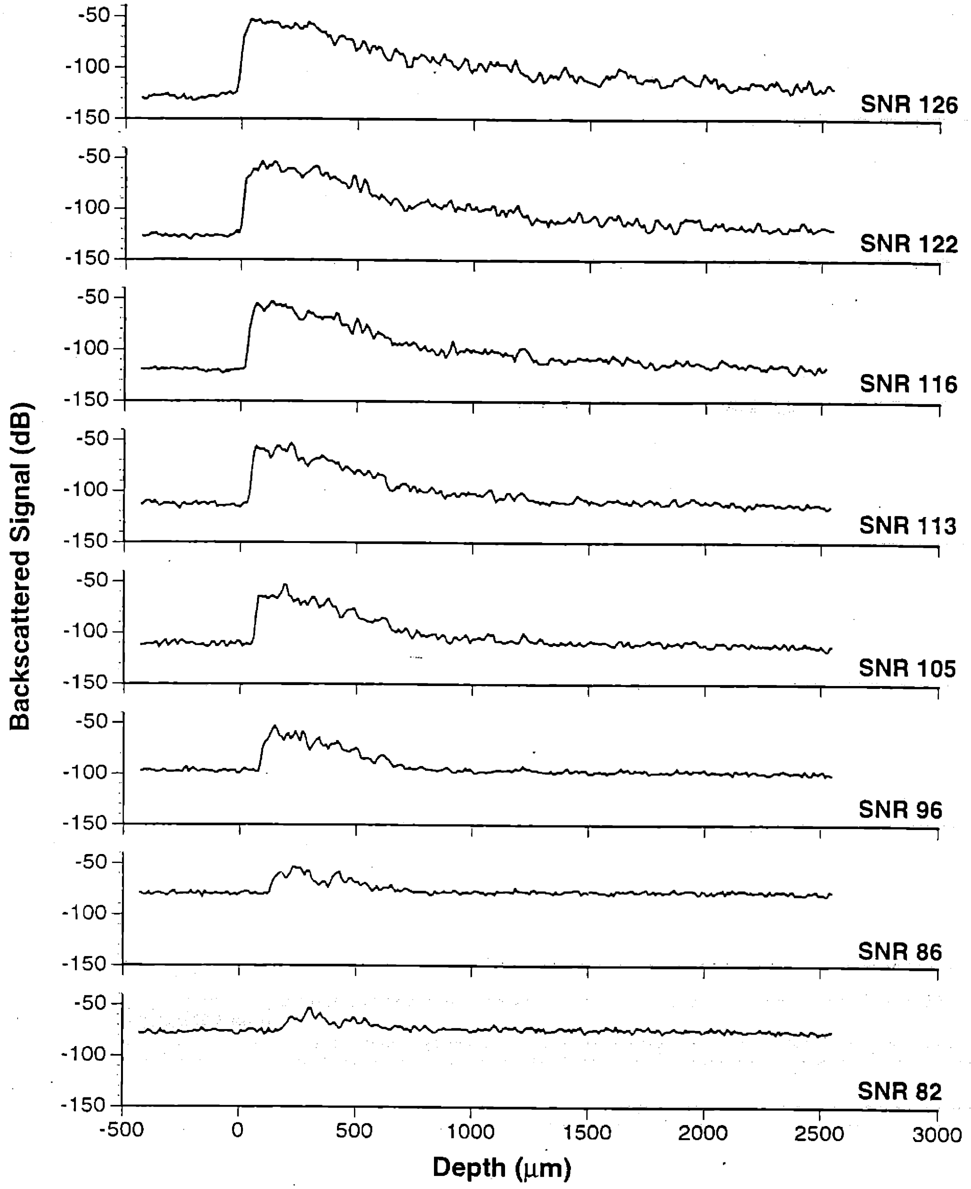

FIGURE 2-18: Axial scan comparison between images of varying SNR. Axial scans were acquired from images shown in Figure 2-17 and illustrate elevation of noise floor and subsequent reduction of dynamic range with decreasing SNR.

2.7.4 Scanning speed

Increasing the scanning speed during OCT imaging will reduce the period of time the beam is positioned over a region of tissue. Hence, the power delivered to this region will be decreased resulting in a lower SNR as defined in Equation (2-65). The power on the sample, the SNR, and the detection bandwidth $\Delta\nu$ are related by

$$\frac{SNR \cdot \Delta\nu}{\langle P_s \rangle} = \text{constant} \tag{2-67}$$

where the detection bandwidth $\Delta\nu$ in terms of scanning speed S_s and source parameters is defined as

$$\Delta\nu = 2S_s \cdot \frac{\Delta\lambda}{\lambda^2}. \tag{2-68}$$

These two equations imply that scanning speed will linearly increase the bandwidth of the OCT signal. To maintain the same SNR, the power delivered to the sample must also be linearly increased. In addition to scanning speed, improvements in axial resolution, which can be obtained using shorter wavelengths λ and broader source spectrums $\Delta\lambda$, also increase the required detection bandwidth.

2.7.5 Image representation

The beam spot size and coherence length are used to determine pixel dimensions within an image and to ensure that sampling is greater than the Nyquist limit. The Nyquist sampling theorem states that if sampling is performed at greater than twice the highest frequency contained in the data, then the original signal (backscatter properties) can be accurately recovered. The number of non-overlapping spot size diameters (NOSSDs) in the X and Y direction is given by

$$NOSSD = \frac{\text{X or Y Scan Length}}{\text{Spot Size Diameter}} \tag{2-69}$$

and the number of non-overlapping coherence lengths (NOCLs) in the Z (depth) direction is given by

$$NOCL = \frac{\text{Z (depth) Scan Length}}{\text{Coherence Length}}. \tag{2-70}$$

Therefore, to ensure sampling above the Nyquist limit, the acquired OCT image for given X, Y, and Z scan lengths must have the following number of pixels:

$$pixels_{X,Y} \geq 2 \cdot NOSSD \tag{2-71}$$

$$pixels_Z \geq 2 \cdot NOCL. \tag{2-72}$$

The index of the tissue specimen must be considered to correctly scale the Z (axial) image dimension. Accurately determining the index of refraction for biological specimens is difficult because of its heterogeneous nature and the dependency on the state of hydration of the tissue. Several methods have been proposed for using OCT to determine the index of refraction of tissue, both *in vitro* and *in vivo*[75,77]. By comparing the measured tissue thickness from an image $z_{measured}$ with the actual tissue thickness z_{actual}, an average index of refraction could be determined by

$$n_{avg} = \frac{z_{measured}}{z_{actual}}. \tag{2-73}$$

This average index of refraction is typically close to that of water (n = 1.33), which is often the main constituent of tissue. Because of the slower propagation velocity of light within tissue, the axial OCT image dimensions do not coincide with the free-space distance the reference arm pathlength has varied. Therefore, for accurate image representation, the axial image dimension must be scaled by a factor of $1/n_{avg}$ where n_{avg} represents the average index of refraction for the tissue being imaged defined by Equation (2-73).

2.8 Spectral Radar

Spectral radar is an OCDR technique based on spectral interferometry. Like OCT, a source with a broad spectral bandwidth is coupled to an interferometer. Reflections from the sample and stationary reference arm will optically interfere at the receiver, which is an optical spectrum analyzer. The optical spectrum will consist of fringe profiles, the contrast of which is proportional to the reflection coefficients within the sample and the period of which is proportional to the relative distance between the sample and the reference reflections. Using Fourier analysis, the axial profile of the sample reflectivity can be obtained.

According to Bail, *et. al.*[118], the spectrometer will measure the interference signal I(k) in terms of the wavenumber $k = 2\pi/\lambda_0$. The interferometric signal is given by

$$I(k) = S(k)\left[1 + 2\int_0^{\infty} a(z)\cos(2knz)dz + \int_0^{\infty}\int_0^{\infty} a(z)a(z')\exp(-i2kn(z-z'))dzdz'\right] \tag{2-74}$$

where S(k) is the spectral density function and a(z) is the backscattering amplitude with respect to depth. Aside from the DC term in Equation (2-74), the second term encodes the depth information and the third term describes the mutual interference between all the of the backscattered waves from the sample. The inverse Fourier transform of I(k) will give

$$\Im^{-1}(I(k)) = \Im^{-1}(S(k)) \otimes \left(\delta(z) + \frac{1}{2}\hat{a}(z) + \frac{1}{8}AC(\hat{a}(z))\right) \tag{2-75}$$

which represents the convolution of the source spectrum with a delta function, the scattering amplitude, and the autocorrelation of the scattering amplitude[118]. From this, the scattering amplitude can be bandpass filtered out and used to construct an image of the sample reflectivity.

The imaging depth is limited by the resolution of the spectrometer because large optical pathlength differences between the two interferometer arms will cause high frequencies in the detected spectrum. The depth for detection is given by

$$\Delta z = \frac{1}{4n}\frac{\lambda_0^2}{\delta\lambda} \tag{2-76}$$

where λ_0 is the center wavelength of the source, n is the index of refraction of the sample, and $\delta\lambda$ is the wavelength resolution of the spectrometer[118]. As with OCT, the spatial resolutions are governed by the coherence length of the source, the scattering properties of the sample, and the beam focussing optics. Acquisition time to acquire and process a single axial scan is ≈ 100 ms, which is comparable to the galvanometer retroreflector scanning in OCT. Spectral radar has been used for 3-D imaging and surface profilometry of human skin[119]. With a dynamic range of 79 dB, imaging depths were limited to less than 600 μm. However, this was sufficient to determine the hydration state of skin and to differentiate between normal skin and a melanoma[119,120].

Without having to scan the reference arm to collect axial depth reflectivity profiles, spectral radar potentially can be performed at high acquisition rates. The computational time necessary to extract the profile will become shorter as faster processors become available, making spectral radar a potentially viable alternative to OCT.

2.9 Frequency Scanning OCT

Both OCT and Spectral Radar perform optical ranging in the coherence domain (OCDR). Similar optical ranging can be performed in the frequency domain (OFDR) by scanning the source wavelength rather than scanning the optical pathlength. A frequency-tunable optical source is coupled to the interferometer. With a stationary reference arm mirror, the photodetector receives signals from the sample and reference reflections and detects any optical interference. The slight time delay between the arrival of these two signals, combined with the frequency tuning, results in a beat signal. The sample reflectivity can then be derived by taking the Fourier transform of the detector signal current. There are several methods for performing a wide frequency sweep including mechanically or electronically tuned external cavity lasers[121], current or temperature tuned semiconductor lasers[122-124], multi-section semiconductor lasers, and broad-band amplified spontaneous emission sources combined with tunable optical filters.

The Fourier transform of an OFDR photocurrent from an infinitely tuned optical source can be convolved with the Fourier transform of a square emission spectrum which reflects the finite tuning range of the source. The spectral density function of this convolution is[125]

$$S_{OFDR}(f) \sim (1+R_s)\left[\frac{\sin(\pi f\Delta T)}{\pi f\Delta T}\right]^2 + 2R_s\left[\frac{\sin(\pi(f\pm f_b)\Delta T)}{\pi(f\pm f_b)\Delta T}\right]^2 . \tag{2-77}$$

where R_s is the reflectivity from the sample, f_b is the beat frequency between the two arms of the interferometer, and ΔT is the measurement time. The spectral density function is composed of three squared sinc functions, one at the tuned source frequency f and two separated from the source frequency by f_b, the beat frequency.

Assuming the minimum detectable frequency change is inversely proportional to the measurement window[126], $\Delta f_{min} = 1 / \Delta T$, then the smallest resolvable separation of two backscatterers is

$$\Delta z_{min} = \frac{1}{4}\frac{\lambda_0^2}{\Delta\lambda_{max}} \tag{2-78}$$

where λ_0 and $\Delta\lambda_{max}$ are the center wavelength and maximum tuning range of the optical source[125].

Rapid wavelength scanning of a cw Cr^{4+}:forsterite laser has been used as a tunable source for OFDR ranging, imaging, and 3-D surface profiling[125,127]. Tilting of the high-reflector cavity mirror over 0.61° at frequencies up to 1 kHz continuously tuned the laser wavelength from 1200 to 1275 nm. Axial resolutions of 15 µm were achieved with a SNR of 70 dB. This technique is attractive for biological imaging, as is spectral radar, because ranging can be performed without physically scanning the reference arm pathlength. The use of tunable cw solid-state lasers may require less technical knowledge for operation and maintenance compared to solid-state KLM sources used for high-resolution OCT. However, the system complexity is shifted from the laser source to the signal processing required to extract the sample reflectivity profiles. Significantly more computing power is required to rapidly perform FFT calculations at acquisition rates comparable to current OCT imaging. Future research in OFDR techniques may make this a viable option for imaging in biological tissue.

Chapter 3

Beam Delivery Instruments

3.1 OCT Imaging Beam

The sample arm of the OCT Michelson interferometer is comprised of two components: a single-mode optical fiber[128] and a mechanism to scan the low-coherence light on the specimen for imaging. The optical fiber can be of arbitrary length, with the only requirement being that optical pathlengths in the sample and reference arms of the interferometer be matched. This chapter will focus on the means by which the OCT imaging beam is delivered to the tissue of interest. Mechanisms vary considerably depending on the particular application. Although delivery of the OCT imaging beam to the tissue may be rather straightforward, the engineering of scanning mechanisms to translate or displace a focused beam through a specimen represents a challenge. A simple, reliable, and compact displacement mechanism is necessary for the instrument to be integrated into the surgical suite.

The single-mode, spatially coherent optical beam exiting from the OCT sample arm fiber must be focused to a spot within the tissue specimen by the optics of the beam delivery instrument. The axial and transverse resolutions are determined by the Equations (2-49) and (2-56). A stationary focused beam in tissue only enables single axial backscatter profiles to be acquired. In order to obtain a multi-dimensional OCT image, the focused optical beam must be translated through the specimen or, alternatively, the specimen must be translated beneath a fixed optical beam. Numerous mechanisms exist for translating the optical beam in either the forward, lateral, or radial direction. Mechanisms include mechanical, optical, and acoustical means among others. Designs for beam delivery instruments will be discussed in the following sections including ABCD matrix representation of the optical components. Based on the optical design, magnification, field-of-view (FOV), and image and pixel dimensions will be determined.

3.2 Research Microscope

3.2.1 Introduction

Research microscopes are commonly used for laboratory investigation of biological specimens as well as small, microscopic, material samples. The principle advantage of integrating OCT with a microscope is to allow the precise positioning of the imaging beam on the specimen or sample, particularly when the specimen is on the microscopic scale (100-1000 μm). High magnifications imply short confocal parameters or depths-of-field for the microscope objectives. The numerical apertures (NA) for these objectives range from 0.3 to 1.0 and higher. In such a device, focus tracking is critical. Focus tracking permits the coherence envelope of the OCT source to be continuously aligned with the focal region of the microscope objective and hence, collect image information only within the confocal parameter (the region of highest and relatively constant transverse resolution). As the sample is translated under the beam or the beam is translated through the sample, inhomogeneities in the index of refraction of the sample will displace the predicted location of the coherence envelope as well as vary the beam parameters and focusing properties of the OCT imaging beam. The focal depth in the specimen is not simply related to any mechanical tracking parameter. Thus, custom waveforms must be generated to position the focus within the specimen. A high speed dynamic feedback system can be used to compensate as imaging is performed.

The use of high NA objectives is necessary for high transverse resolution in OCT images. Schmitt, *et. al.* has found that the use of high NA objectives significantly improves image contrast within OCT images. Aside from reducing the size of the diffraction-limited spot, the increase in NA improves multiple-scatter rejection by reducing the average size of the speckle[129]. Additionally, high NA objectives smooth the depth-dependent attenuation in OCT images due to the large illumination region. This is most noticeable in media with clusters of large backscattering particles which shadow underlying regions. Thus, shadowing effects are less significant when using higher NA objectives.

3.2.2 OCT research microscope designs

The general research microscope design used in these OCT studies is diagrammed in Figure 3-1.

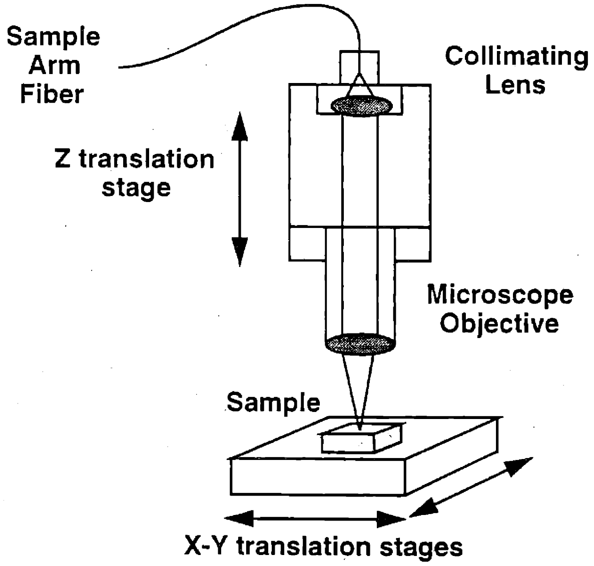

FIGURE 3-1: General research microscope design. Microscope objective is interchangeable to vary spot size diameter (transverse resolution) and confocal parameter.

The sample arm output is collimated and then focused by a microscope objective lens coated for the source wavelength to reduce backreflection artifacts. The Z-translation stage controls the depth of the focus in the specimen while the X-Y translation stages are used to scan the specimen and collect 2-D or 3-D images.

The beam path through the general research microscope design in Figure 3-1 can be represented by optical components and dimensions given in Figure 3-2. The ABCD ray matrix formulation is used to determine the output ray height y′ and angle θ′ for a given input ray height and angle (y, θ). In matrix form, this is written as

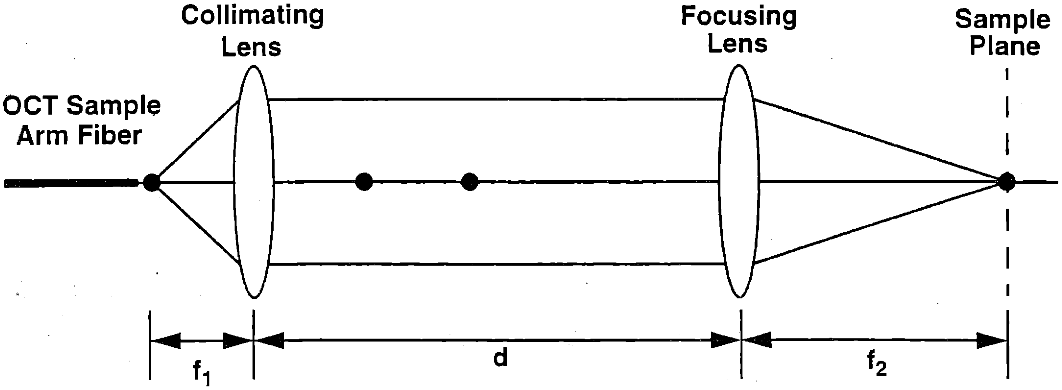

FIGURE 3-2: Research microscope beam path.

$$\begin{bmatrix} y' \\ \theta' \end{bmatrix} = \begin{bmatrix} A & B \\ C & D \end{bmatrix} \begin{bmatrix} y \\ \theta \end{bmatrix}. \tag{3-1}$$

The representation of these cascaded elements is given by

$$\begin{bmatrix} A & B \\ C & D \end{bmatrix} = \begin{bmatrix} \dfrac{-f_2}{f_1} & 0 \\ \dfrac{d}{f_1 f_2} - \dfrac{1}{f_1} - \dfrac{1}{f_2} & \dfrac{-f_1}{f_2} \end{bmatrix}. \tag{3-2}$$

The magnification of the system, given by the A matrix element, is determined by the ratio of the focusing and collimating lenses. The negative sign implies image inversion. Similarly, the angular magnification is given by the D matrix element. Because this system remains fixed and the specimen is translated beneath a stationary OCT imaging beam, the system FOV is dependent on the distance the specimen is translated.

The ABCD matrix is also useful to describe the propagation of a Gaussian beam through the optical system. The q parameter is defined as

$$\frac{1}{q} = \frac{1}{R(z)} - \frac{j\lambda}{\pi w^2(z)} \tag{3-3}$$

where R(z) and w(z) were defined in Equations (2-42) and (2-43). The q parameter is bilinearly transformed by the optical system giving the output q′ as

$$q' = \frac{Aq + B}{Cq + D}. \tag{3-4}$$

In this optical system, the output from the single-mode fiber core will therefore be magnified by $-f_2/f_1$ at the sample plane. For a spot side diameter $2w_0$ in the sample plane, the number of non-overlapping spot size diameters (NOSSDs) is given by the total scan length divided by $2w_0$.

The research microscope was implemented using a fiber-optic collimator and single-lens microscope objectives with low NAs. Longer confocal parameters were selected for depth-priority scanning. With f_1 = 5 mm, f_2 = 15 mm and 4.5 mm, and d = 10 cm, the 9 μm core of the single-mode fiber was magnified (demagnified) producing spot size diameters of 27 μm and 8.1 μm, respectively. For an X scan length of 5 mm and a 27 μm diameter spot size, NOSSD = 185.

In the previous microscope design, scanning is performed with depth priority. That is, the beam is positioned at one location via a two-dimensional scanning mechanism while the effective path length between the sample and reference arms of the interferometer is varied in order to collect data in depth (z direction). The scanning mechanism then repositions the beam and another axial depth scan is performed. Imaging can also be performed with transverse priority by keeping the reference arm position fixed during a single transverse scan and then stepping the reference arm (coherence envelope) in depth as subsequent transverse scans are acquired. In a three-dimensional mode, this is equivalent to the optical sectioning characteristics of a confocal microscope. The advantage of transverse priority scanning is a potential increase in speed. Rapid transverse scanning can readily be performed with galvanometers and mirrors. The axial position of the coherence envelope, determined by the position of the reference arm mirror, cannot be varied as quickly. OCT was not integrated with high NA microscope objectives, transverse-priority scanning, or focus-tracking for this thesis.

3.3 Surgical Microscope

3.3.1 Introduction

OCT can be integrated with existing surgical or dissecting microscopes to permit simultaneous OCT imaging at an arbitrarily oriented tomographic plane with *en face* visualization. Dissecting or stereo microscopes are typically binocular microscopes with long working distances (low NA) and large confocal parameters. They are frequently used in the research environment for low magnification of large samples that cannot be placed on the stage of a high-magnification, high NA microscope. Surgical microscopes with long working distances and long depths-of-fields are utilized in microsurgical techniques to enable the surgeon to visualize small structures such as arteries, veins, tendons, and nerves. Use of these microscopes is critical during procedures involving the reattachment of severed limbs as well as the reconstruction of delicate structures around the face, head, and neck.

In all of these microsurgical procedures, visualization of the small structures is crucial for success. Because most surgical microscopes only provide the *en face* surface profile of tissue and structures, the integration of OCT for sub-surface, cross-sectional imaging of these structures offers an improved degree of visualization and information. If the object to be imaged has dimensions that are difficult to view with the naked eye, then positioning the optical imaging beam on the sample will be equally difficult. Use of an integrated stereo microscope will enable the user to view the precise scan location on the sample. Because most surgical and stereo microscopes offer accessory ports for the attachment of CCD video cameras, the *en face* view and the position of a visible aiming beam coincident with the near infrared imaging beam can be captured and stored on either video tape or digitized and stored on computer storage media.

3.3.2 OCT surgical microscope designs

One design of an OCT surgical microscope is illustrated in Figure 3-3. The optical fiber from the sample arm is inserted into a collimator. The collimated beam is directed through a pair of orthogonal galvanometer scanners[130] before passing through a focusing lens. The orthogonal scanners enable the imaging beam to be scanned in arbitrary patterns on the specimen. This arbitrary pattern also enables the acquisition of multiple cross-sectional planes for 3-D image acquisition. As the beam is converging to a focus, a beamsplitter mounted at 45° redirects the near infrared imaging beam and the visible aiming beam downward and coincident with the viewing axis of the microscope. The beam splitter is coated to reflect the imaging and aiming beam wavelengths while allowing other visible wavelengths to transmit. The focusing lens will focus the imaging and aiming beams at two different locations. Since the visible aiming beam is only used to trace the location of the imaging beam, its focal position is relatively insignificant as long as the beam diameter is small (≈ 1 mm).

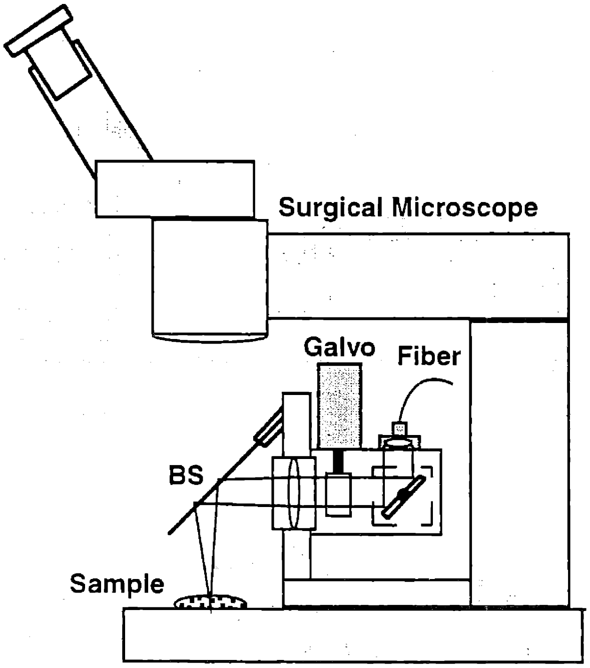

FIGURE 3-3: OCT surgical microscope. The OCT imaging beam is aligned with the viewing axis of the surgical microscope and scanned in arbitrary patterns with a pair of orthogonal galvanometers.

The beam path through the surgical microscope is diagrammed in Figure 3-4. The beam path is similar to that of the research microscope except galvanometer scanning mirrors have been added between the collimating and focusing lenses. The ABCD matrix is identical to the one given in Equation (3-2) with a

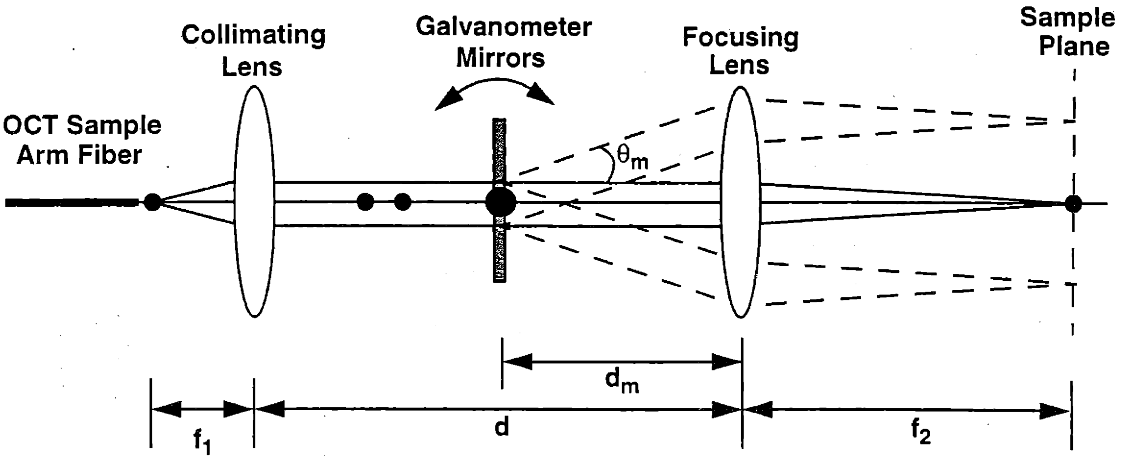

FIGURE 3-4: Beam path through surgical microscope.

magnification of $-f_2/f_1$ and an angular magnification of $-f_1/f_2$. Assuming a collimated beam is reflected by the scanning mirrors at a distance d_m from the focusing lens, it can be shown that the output ray position y' is equal to

$$y' = f_2 \cdot \theta_m. \tag{3-5}$$

Therefore, X or Y scan length on the specimen can be increased by increasing the focal length f_2 or the mirror angle θ_m. Increasing f_2 will provide a greater working distance and confocal parameter at the expense of transverse image resolution.

The FOV in this system is limited by the aperture of the focusing lens. For a focusing lens diameter D_{L2}, and using the paraxial approximation $\tan\theta \approx \theta$ (θ in radians), the FOV is equal to

$$FOV = 2\theta_m = \frac{D_{L2}}{d_m} \tag{3-6}$$

and the maximum X and Y scan length is given by

$$2y'_{max} = \frac{f_2 D_{L2}}{d_m}. \tag{3-7}$$

The number of NOSSDs within this maximum scan length is determined by the magnification of the system and the spot size diameter in the specimen

$$NOSSD = \frac{f_2 D_{L2}}{2 w_0 d_m}. \tag{3-8}$$

The surgical microscope described in Figure 3-3 was constructed for simultaneous OCT imaging and microscope visualization of the scan location and the specimen. Orthogonal galvanometers placed at d_m = 50 mm permitted high-speed *in vivo* OCT imaging of dynamic or rapidly moving specimens. A 1280 nm Cr^{4+}:forsterite beam had a 3.7 mm diameter at the focussing lens (f_2 = 75 mm, D_{L2} = 23 mm). After the focusing lens, the converging beam was reflected downward onto the specimen by a dichroic beam splitter which permitted the near IR wavelengths to be reflected while passing the visible wavelengths. The beam was focused to a 33 μm diameter spot. The maximum X or Y scan length was 34.5 mm permitting NOSSD = 1045.

3.4 Forward-Imaging Hand-Held Probe

3.4.1 Introduction

Forward-imaging devices overcome a limitation of side-imaging devices; permitting data to be collected before introducing the device into tissue[131]. This concept also permits the image-guided placement of the device in surgery and for monitoring interventional procedures such as tissue incision, resection, and laser surgery. While flexible endoscope or catheter-based imaging is necessary for internal lumens deep within the body, rigid laparoscopic and hand-held devices are suitable for regions accessed during minimally invasive or open-field surgical procedures, respectively. OCT beam delivery can be implemented in a hand-held device that performs forward-directed optical imaging of biological specimens or material samples[132]. The ability to have forward-directed imaging in an instrument no larger than a pen offers the advantages of data and image acquisition at locations remote to the OCT interferometer, electronics, and computer. The combination of OCT with a hand-held probe can be a powerful imaging technology for surgery because it enables the cross-sectional imaging of internal tissue microstructure *in situ*. Thus, it may be possible to guide surgery near sensitive structures such as nerves or blood vessels and identify abnormal pathology such as the margin between tumor and normal tissue.

A hand-held probe has applications in the medical field, materials investigation, and the military[133]. The medical field can utilize its compact profile in the open-field surgical setting to image sub-surface tissue morphology prior to disrupting, incising, or resecting the tissue. A forward-directed imaging probe offers the advantage that no portion of the instrument has to come in contact with the tissue prior to obtaining imaging data. This is in contrast to devices that image in the radial or transverse direction. Here, the catheter or device must be inserted into the tissue prior to obtaining an image. Within the open-surgical field, space is at a premium. Therefore, an additional instrument must be compact and easily manipulated by the surgeon. For medical applications not involving open-field surgery, the hand-held probe can be used to access any external region of the human body or any external orifice. For OCT imaging to occur, the fiber path lengths between the sample and reference arms must be matched or otherwise compensated for dispersion. Because long fiber lengths can be contained within small volumes, the sample arm, to which is connected the hand-held probe, can be of any reasonable length. Therefore, a hand-held probe can be used to image any external region of the human body while the patient stands, sits, or lies in a bed. In addition, because of the use of micro-optics, the distal portion of the device can be made very small and able to be inserted short distances into body orifices and canals such as the external ear canal, nasal passage, or mouth.

The compact nature of the OCT instrument coupled with the small hand-held probe permits the entire system to be portable for materials investigation around a factory or at remote job sites. The concept of a pen-like device requires little training in its use and alignment as this style has been readily adopted in technologies such as pen-style bar code readers. Finally, a compact profile and portability are attractive options for military medical imaging at forward battlefield locations where in-field assessment and potential treatment of injuries take place.

3.4.2 OCT hand-held probe designs

GRIN Lens Probe

One implementation of a forward-imaging hand-held probe is shown in Figure 3-5. This design utilizes a piezoelectric cantilever to displace a fiber and GRIN (GRadient INdex) lens unit in an arc. The overall dimensions of this device are no larger than a standard ink pen, making the instrument fit comfortably in the operator's hand. A digital photograph of the probe is shown in Figure 3-6. The cylindrical enclosure is made of a protective and insulating plastic that shields the cantilever, fiber, and lens from contaminants and liquids. The use of an insulating plastic material also prevents possible injury to the user which could result from electrical shorting between the piezoelectric cantilever and the user's hand.

The GRIN lens used in this device contains an optical index profile given by

$$n = n_0\left(1 - \frac{x^2 + y^2}{2h^2}\right) \tag{3-9}$$

where n_0 is the index at the center of the GRIN lens and 1/h is a measure of the rate of decrease of the index n with increasing distance from the axis[134]. The ABCD matrix for a GRIN lens of length l is given by

$$\begin{bmatrix} A & B \\ C & D \end{bmatrix} = \begin{bmatrix} \cos\left(\frac{l}{h}\right) & \frac{h}{n_0}\sin\left(\frac{l}{h}\right) \\ -\frac{n_0}{h}\sin\left(\frac{l}{h}\right) & \cos\left(\frac{l}{h}\right) \end{bmatrix}. \tag{3-10}$$

For the case l/h = π/2, the ABCD matrix is identical to that of a thin lens with focal length h/n_0 and free-space distances of h/n_0 on either side of the thin lens[134]. The beam path through the optical system of the GRIN lens probe is diagrammed in Figure 3-7. The dotted line through the GRIN lens represents an arbitrary ray path. The actual ray path is dependent on the length of the GRIN lens l, the index profile n, and the h parameter. The ABCD matrix representation is given by

$$\begin{bmatrix} A & B \\ C & D \end{bmatrix} = \begin{bmatrix} 1 & l_w \\ 0 & 1 \end{bmatrix} \begin{bmatrix} \cos\left(\frac{l_G}{h}\right) & \frac{h}{n_G}\sin\left(\frac{l_G}{h}\right) \\ -\frac{n_G}{h}\sin\left(\frac{l_G}{h}\right) & \cos\left(\frac{l_G}{h}\right) \end{bmatrix} \begin{bmatrix} 1 & \frac{l_c}{n_c} \\ 0 & 1 \end{bmatrix} \tag{3-11}$$

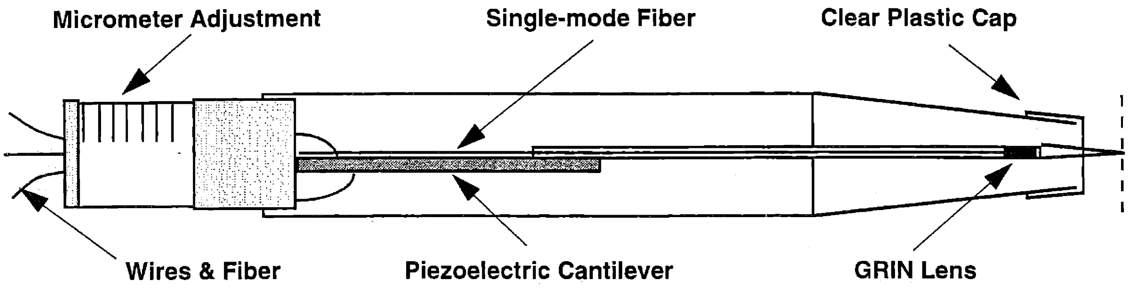

FIGURE 3-5: Hand-held surgical probe - GRIN lens design. Piezoelectric cantilever laterally scans beam focus from GRIN lens through tissue.

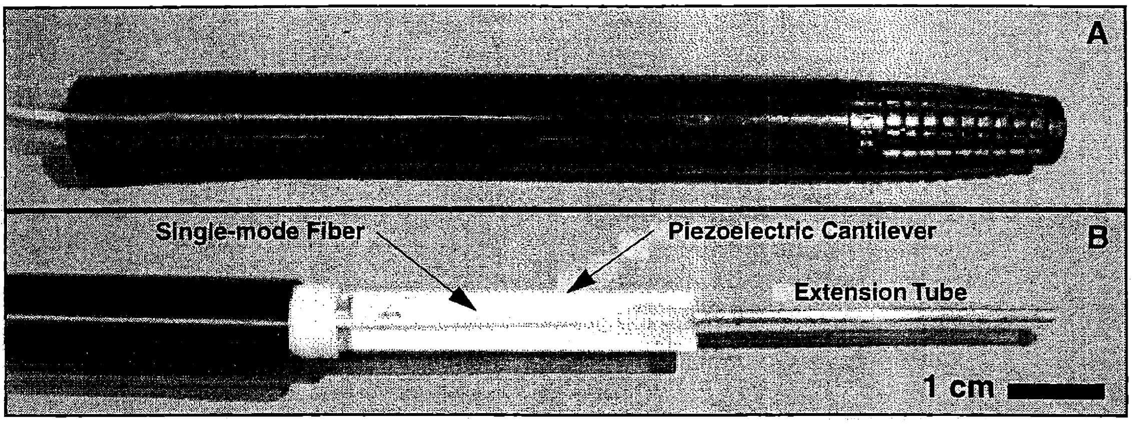

FIGURE 3-6: Hand-held surgical probe. A) Pen-like assembly with plastic housing. B) Exposed cantilever and extension tube. The GRIN lens is located at the distal end of the extension tube.

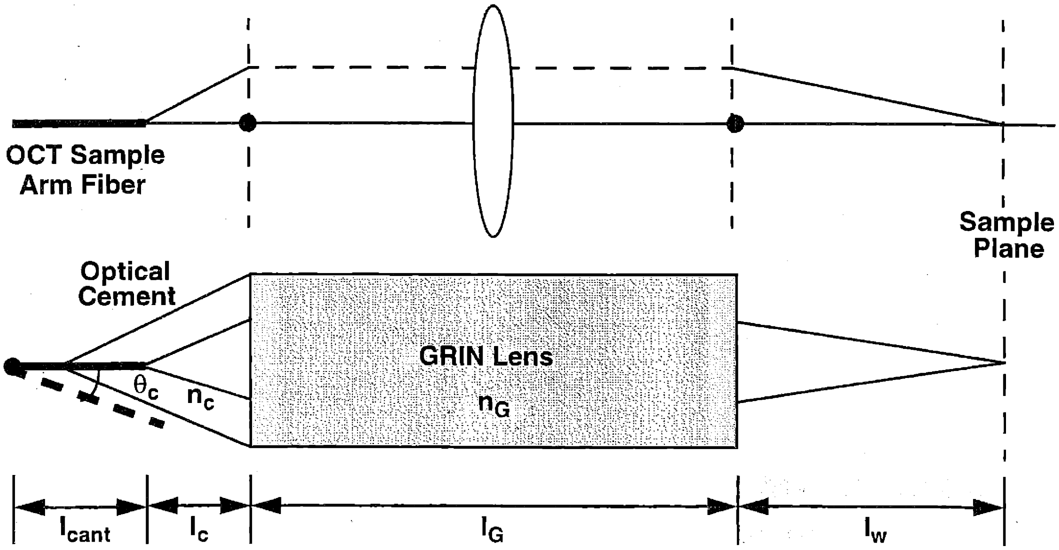

FIGURE 3-7: Beam path of GRIN lens probe.

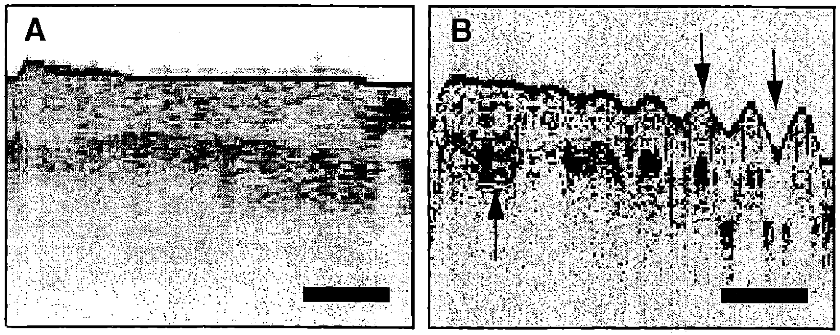

FIGURE 3-8: Scanning characteristics of GRIN lens probe. A) Low (0.1 Hz) and B) high (8 Hz) frequency scanning. Images are of *in vivo* human skin. Significant artifacts are noted during high frequency scanning (arrows). Bar represents 500 μm.

which for simplicity, has not been reduced. The transverse and angular magnification for this optical system are equal and given by

$$\frac{y'}{y} = \frac{\theta'}{\theta} = \cos\left(\frac{l_G}{h}\right) - \frac{l_c n_G}{n_c h}\sin\left(\frac{l_G}{h}\right). \tag{3-12}$$

The spot size diameter at the focus of the GRIN lens can be calculated from the ABCD matrix elements by

$$2w_0 = \sqrt{\frac{4\lambda z_f^2}{\pi}(A^2 + B^2/z_f^2)} \tag{3-13}$$

where z_R is the Rayleigh range and z_f is the position of the fiber output.

In this optical design, the FOV is limited by the displacement of the piezoelectric cantilever. The cantilever is a piezoelectric bimorph material centered within the probe barrel to allow bending displacement during scanning. The proximal end of the cantilever is fixed to a micrometer to vary the location of the imaging beam focus with respect to the distal end of the probe and with respect to the tissue specimen or sample. To increase the lateral displacement of the beam, a tube is fixed at the end of the cantilever. This increases the distance of the GRIN lens from the bending cantilever and linearly increases the displacement. The tube also protects the small lens and single-mode fiber. To reduce the degree of optical backreflections which would occur from the normal-incident faces of the fiber and GRIN lens, the fiber can be angle-cleaved and the GRIN can be angle-polished. The fiber is attached to the GRIN lens using ultraviolet-cured optical cement.

The distal end of the cylindrical enclosure has a clear plastic cap that is removable after contact with biological tissue. This cap serves four major purposes: 1) to allow the probe to be placed in contact with the tissue specimen or material sample thereby fixing the GRIN lens focal plane at a fixed distance within the specimen, 2) on contact, motion artifacts are minimized because the probe can move with the tissue or sample, 3) the clear plastic permits the user to visualize where scanning is occurring when a visible aiming beam is coincident with the OCT imaging beam, and 4) the replaceable cap maintains cleanliness and avoids transmission of bacteria or viruses between patients.

The only interconnections required with the use of this design include the single optical fiber and two wires necessary to drive the piezoelectric cantilever. The cantilever was a 6.4 x 38.1 mm lead zirconate titanate double plate flexing element manufactured by Morgan Matroc, Inc. The two transverse expander plates are bonded together so the applied voltage deforms the plates in opposite directions[102]. The advantage of this design is the ability to generate large motions, with low forces, for modest electrical excitation. Typically, voltages of several hundred volts are necessary to displace the cantilever. The displacement, ΔD, of the cantilever is related to the applied voltage, V, by

$$\Delta D = \frac{3dVL^2}{t^2} \tag{3-14}$$

where d is the piezoelectric charge constant defined as strain developed/applied field or 274×10^{-12} m/V for this material, t is the cantilever thickness and L is the length[103]. The cantilever used to construct these devices had a theoretical displacement of 1.27 mm when 300 V were applied. The limit for the applied voltage depends largely on the material properties of the piezoelectric, the duration the voltage is applied, and the operating temperature[135]. Under dynamic conditions, the piezoelectric response is complex. Of practical importance is the resonance frequency f_r of the cantilever which determines the maximum frequency at which OCT imaging can be performed with linear translations. This is calculated from

$$f_r = \frac{Nt}{3L^2} \tag{3-15}$$

where N is a material-specific frequency constant equal to 1420 Hz-m. For this cantilever, a resonant frequency of 173 Hz was considered adequate for OCT imaging. Maximum scan length in the sample plane is determined by the angle of the cantilever θ_c and the distance from the pivot point to the GRIN focus given by

$$2y'_{max} = 2 \cdot (l_{cant} + l_c + l_G + l_w) \cdot \theta_c \tag{3-16}$$

where θ_c is in radians. The number of NOSSD is found by dividing Equation (3-16) by the spot size diameter in the sample plane.

The hand-held probe design in Figure 3-5 was constructed for OCT imaging. A measured cantilever displacement of 1 mm was possible with a 0-300 V ramp waveform applied to the piezoelectric. This displacement was increased to 2 mm by the addition of a 38 mm extension tube to increase the cantilever arm length. The extension tube housed a single-mode optical fiber and a 0.7 mm dia, 0.25 pitch, 8° angle-polished GRIN lens[136]. The GRIN lens was fixed 290 μm from the tip of an 8° angle-cleaved fiber with UV-cured optical cement. The faces of the GRIN lens and fiber tip were angled to reduce internal backreflections which would saturate the detector. The faces were oriented parallel to maximize coupling between the optical elements. This produced a 31 μm diameter spot (the transverse resolution), which corresponds to a 1.2 mm confocal parameter, at a working distance of 3 mm from the GRIN lens. Only 65 NOSSDs can be acquired in the 2 mm scan length. Because of the fixed magnification and relatively small transverse scan length, this design is somewhat limiting.

This design permitted image acquisition at slow rates as shown by the *in vivo* image of human skin in Figure 3-8A. However, the addition of the extension tube lowered the frequency at which resonance occurs. When this design was operated at 8 Hz, nonlinear axial and lateral translation resulted as shown by the artifacts in Figure 3-8B. The GRIN lens design has the advantage that it is a compact single-unit assembly but has the disadvantage of having a fixed magnification and transverse scan length.

Telescope Probe Design

A second probe design in Figure 3-9 permits variable magnification by scanning a cleaved fiber tip in the focal plane of the first lens (L_1) in a telescope. The beam is collimated and then focused by a second lens (L_2) which effectively relay-images the fiber tip onto the object or specimen. Displacement of the fiber tip in the transverse direction results in a transverse displacement of the beam focus in the object plane. The working distance is set by the focal length of the second telescope lens (L_2). The advantages of this design include low mass on the piezoelectric cantilever permitting higher translation velocities and interchangeable magnification via different lenses. The interchangeable cap and lens are disposable and serve to protect the remainder of the probe from liquids and contaminants.

The beam path for the telescope probe design is shown in Figure 3-10. The ABCD matrix for the telescope probe is identical to the ABCD matrix for the research microscope described in Equation (3-2). The transverse magnification is determined by the ratio of the focal lengths of the two lens $-f_2/f_1$ and the

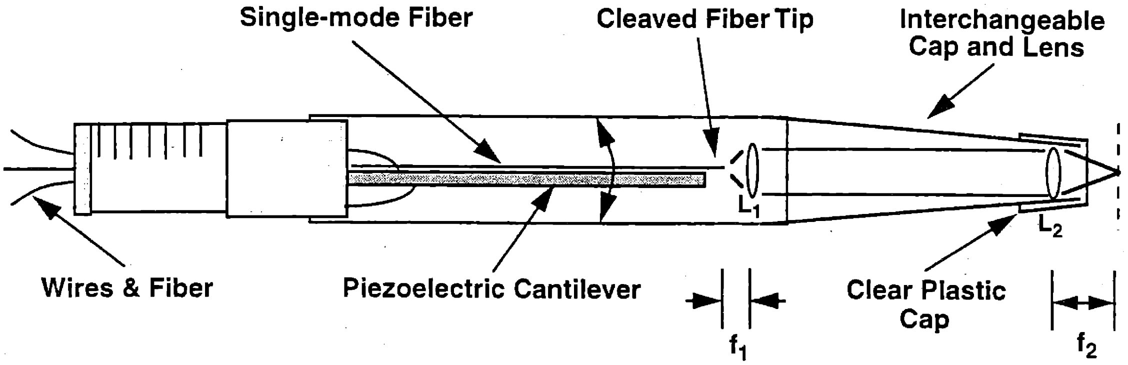

FIGURE 3-9: Hand-held surgical probe - telescope design. The piezoelectric cantilever displaces a fiber tip in the tissue image plane of a telescope which results in a magnified displacement and mode size on the tissue.

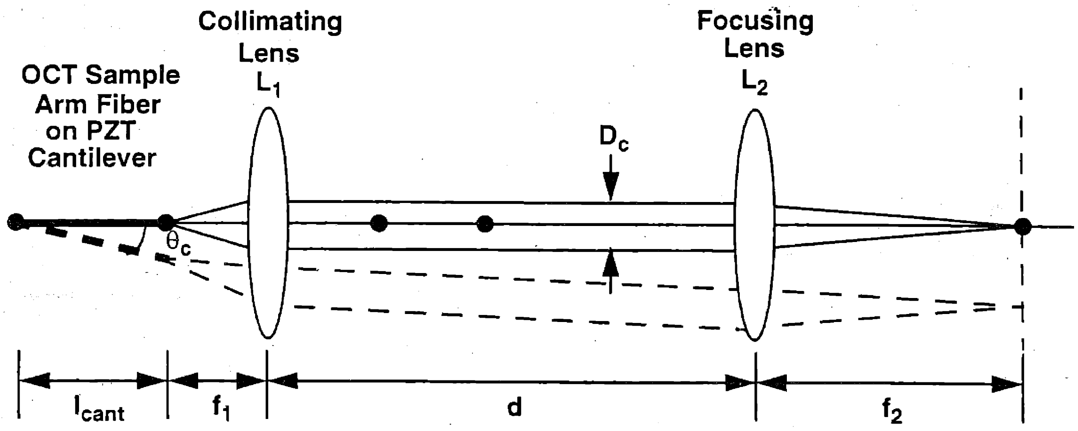

FIGURE 3-10: Beam path of telescope probe design.

angular magnification is given by the reciprocal $-f_1/f_2$. Unique to Figure 3-10, however, is the transverse displacement of the fiber tip by the PZT cantilever. From the ABCD matrix, the transverse output ray position y′ is only dependent on the input ray position y and scaled by the magnification

$$y' = -\frac{f_2}{f_1} \cdot y. \tag{3-17}$$

The FOV of this system is limited by the apertures of the collimating (L_1) and focusing (L_2) lenses. If the collimating and focusing lenses are far apart as shown in Figure 3-10, the focusing lens diameter (D_{L2}) will be the limiting aperture. Using a single ray in the ABCD matrix representation, the maximum cantilever angle θ_c is given by

$$\theta_c = \frac{D_{L2}}{2l_{cant}}\left(1 - \frac{d}{f_1}\right). \tag{3-18}$$

Assuming the fiber tip is in the focal plane of the collimating lens, the collimated beam diameter D_c will be

$$D_c = \frac{2\lambda f_1}{\pi w_0}. \tag{3-19}$$

This will reduce the maximum cantilever angle because of the finite beam diameter D_c to

$$\theta_c = \frac{D_{L2} - D_c}{2l_{cant}}\left(1 - \frac{d}{f_1}\right). \tag{3-20}$$

To minimize the aperture effects from the focusing lens (L_2), the focusing lens should be placed as close to the collimating lens (L_1) as possible. The collimating lens diameter D_{L1} then becomes the limiting aperture. The beam exiting the single-mode fiber will diverge with a half-angle α. The maximum θ_c before aperture effects from the collimating lens is given by

$$\theta_c = \frac{D_{L1}}{2f_1} - \alpha \tag{3-21}$$

which limits the maximum scan length to

$$2y'_{max} = 2\left(f_2\alpha - \frac{f_2}{f_1}D_{L1}\right). \tag{3-22}$$

This design has different optical characteristics than the GRIN lens design in Figure 3-5. The previous design has resolution and depth of field determined by a fixed GRIN lens magnification with the maximum scan length determined directly by displacement. The design in Figure 3-9, however, has resolution and depth of field determined by the fiber mode size and the numerical aperture of the lenses. Both the mode size exiting the fiber and the transverse displacement are scaled by the magnification of the two-lens optical system. In this case, the number of NOSSDs can be increased by decreasing the spot size.

The telescope probe design of Figure 3-9 was constructed using aspheric lenses with focal lengths $f_1 = 4.5$ mm ($D_{L1} = 4.1$ mm) and $f_2 = 18$ mm ($D_{L2} = 5.7$ mm) with a magnification of 4. The lens separation d was minimized without contacting the lenses. Assuming an NA of 0.15 for the single-mode fiber, $\alpha = 9°$ and $\theta_c(\text{max}) = 26°$. At maximum applied voltage to the PZT cantilever, the angular displacement of 0.8° was far less than $\theta_c(\text{max})$ and no limiting aperture effects were present. The long length of the cantilever arm l_{cant} relative to the transverse displacement resulted in only a 3 μm deviation of the fiber face from the focal plane of the collimating lens and was considered negligible. These calculations do not incorporate effects due to aberrations which may limit the off-axis distance of the beam. Empirical studies using a CCD camera to image the beam at the object plane have shown that the beam profile remains relatively focused at fiber displacements of 533 μm off-axis. At larger displacements the profile degrades to levels unacceptable for imaging. On-axis, the spot size diameter at the focus was 32 μm and the scan length was 3.8 mm; giving 119 NOSSDs.

A comparison was made between the GRIN lens and telescope probe designs at an 8 Hz scanning frequency. These are shown in Figure 3-11. Images in Figure 3-11A & B were acquired from the cuticle of a human finger. The finger nail is located on the right. The gross image artifacts in Figure 3-11A are a result of higher frequency transverse resonant oscillations in the cantilever as the imaging beam is scanned. These artifacts are reduced substantially in Figure 3-11B when using the telescope probe design. The lower mass on the cantilever is responsible for this improvement. The images in Figure 3-11C & D are of a calibrated metal grid composed of 129 μm metal lines and 43 μm open slits. Differences between the probe designs are striking. The decreasing size of the metal lines from left to right in Figure 3-11D, however, implies that the cantilever displacement is not uniform. This non-uniformity appears minimal and can be compensated.

The use of the hand-held probe in the surgical setting offers simple integration with existing surgical devices such as a scalpel. Because the forward-directed imaging probe is comparable in size to a surgical scalpel, the two can be attached in a manner which permits forward-directed imaging prior to incision and at arbitrary angles with respect to the surgical blade. Several design options exist which can direct the light more closely to the tip of the scalpel. For instance, a small fold mirror between the scalpel and probe could angle the beam more closely to the tip. Also, the scalpel blade could be rotated 90° with respect to the axis of imaging and the probe could be located below the scalpel so that the cutting axis is imaged prior to incision. Images obtained with the probe will permit the surgeon to view tissue sub-structure, avoid sensitive tissues, assist in determining locations of tumors, and identify tumor margins prior to resection. In addition, OCT may be configured to perform laser Doppler velocimetry prior to incision. Images can be generated which detect and display any sub-surface movement, such as flowing blood, which would indicate the presence of an artery or vein.

Alternatively, high-power continuous wave (cw) lasers or high-energy pulsed lasers can be integrated with the OCT imaging system to replace the surgical scalpel. These concepts have been demonstrated in the past as feasible means of thermally incising, coagulating, or mechanically disrupting biological tissues. High power or high energy laser light can effectively be delivered with single-mode or multi-mode optical fibers[137].

The designs discussed and shown for the hand-held probe all utilized a single piezoelectric cantilever for forward-directed imaging. An additional design would allow the internal scanning mechanism to rotate about the axis of the instrument. This would permit linear scanning at arbitrary angles. Multiple axes can be incorporated to allow two- and three-dimensional scanning. In place of piezoelectric cantilevers, a small pair of orthogonal galvanometers could be incorporated to direct the imaging beam off of rotating mirrors. This design would permit rapid two- and three-dimensional scanning.

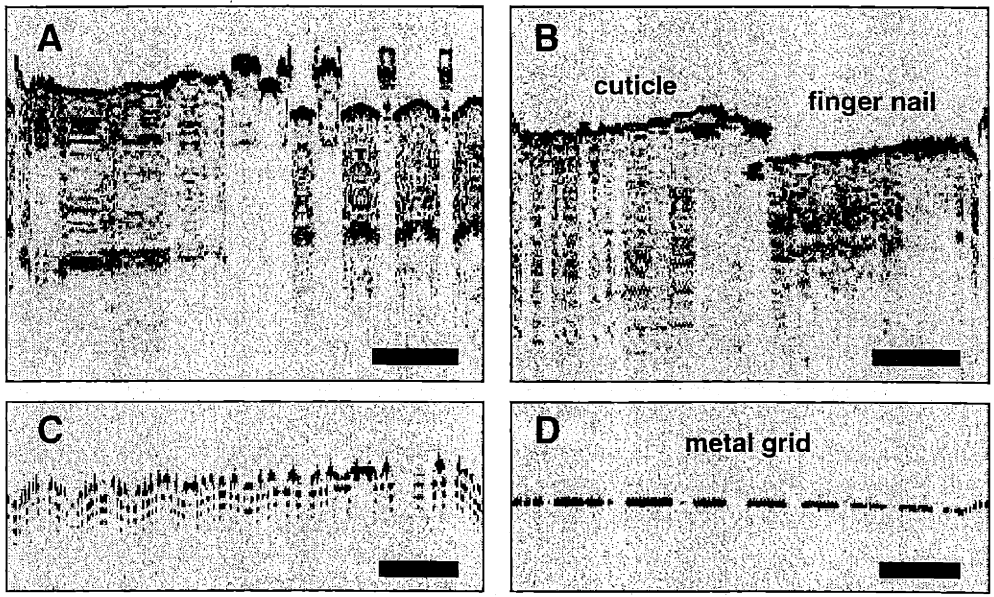

FIGURE 3-11: Comparison of GRIN lens (A,C) and telescope probe (B,D) imaging performance at 8 frames per second. Images in A,B were acquired from *in vivo* human finger nail. Images in C,D acquired from a calibrated metal grid. Bar represents 250 μm.

3.5 Forward-Imaging Laparoscope

3.5.1 Introduction

The design of the forward-scanning hand-held probe represents a method of transverse displacement that is modular in design. Using the probe described in Section 3.4 to transversely displace a focus in a forward-imaging plane is useful in other optical instruments such as a rigid endoscope or laparoscope. A laparoscope is a rigid optical device that is used in medical applications to visualize magnified tissue surfaces at remote internal sites. The concept of laparoscopic surgery has contributed to minimally invasive surgery; the idea that surgical procedures can be performed without large incisions and without exposing internal tissues as occurs during open-field surgical procedures. The laparoscope consists of a rigid cylindrical tube 1-2 cm in diameter and 10-50 cm in length. The proximal end contains optics that permit the operator to visualize the tissue surface located at the distal end. Alternatively, a CCD camera can be mounted at the proximal end with the *en face* image of the tissue appearing on a video monitor. Optics contained within the laparoscope relay the image of the tissue in the object plane to an image plane at the proximal end. Additionally, there are white-light fiber-optic bundles that run parallel to the imaging optics to provide illumination of the tissue surface. Typical laparoscopic surgical procedures involve inflating the human abdominal cavity with a gas to provide space to visualize internal organs and to manipulate various surgical instruments within the cavity. The laparoscope is especially well suited for OCT imaging because it preserves the transverse spatial mode character of the optical beam. The integration of forward-directed OCT imaging with a laparoscope design offers the possibility of sub-surface imaging of intra-abdominal and other internal organs and structures[132]. Sub-surface imaging can significantly complement the *en face* imaging that is currently performed with laparoscopes and white-light illumination. Additionally, the *en face* imaging significantly complements the sub-surface OCT imaging by allowing the user to simultaneously visualize the OCT scan location at a remote internal site.

3.5.2 OCT laparoscope designs

The general optical design of a laparoscope is shown in Figure 3-12. A single relay element in standard form can be described by a series of biconvex lens shown in Figure 3-13. The relay system consists of a train of one or more identical stages; each providing unit magnification as the image is transferred. A conventional system of thin bi-convex lenses requires that each stage be telecentric in both its object and

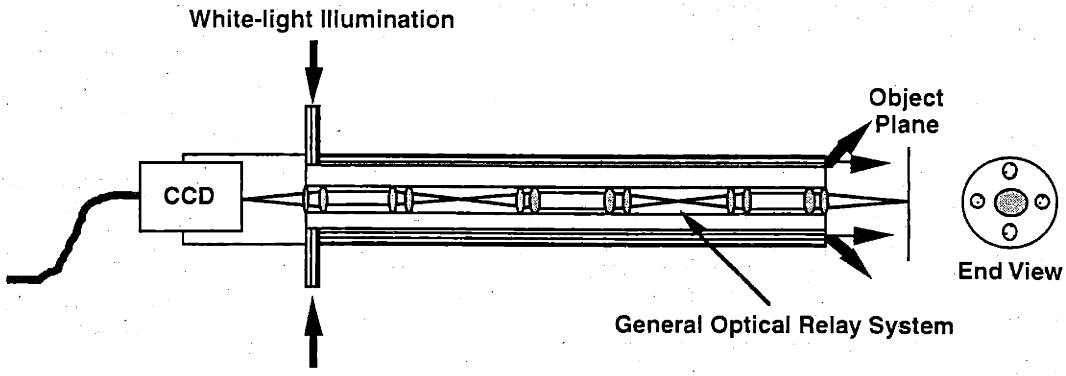

FIGURE 3-12: General laparoscope design.

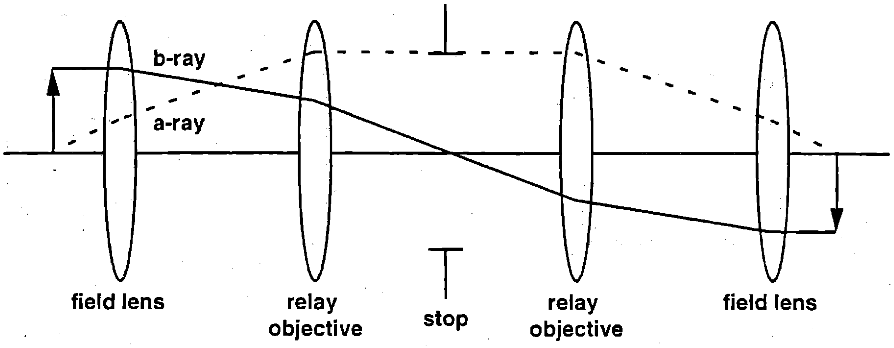

FIGURE 3-13: Biconvex lens relay element.

image spaces. Notice the b-ray enters and exits with zero slope. In this design, the medium between the field lens and the relay objective lens is air. This free space is replaced with a glass rod in the Hopkins relay system[138] shown in Figure 3-14. The advantages of this modification include increased light throughput and reduced vignetting or distortion of the image[43]. Because of these advantages, most modern laparoscopes are of this design. In fact, the enabling technology for laparoscopy is attributed to the use of CCD cameras and these design and image quality improvements.

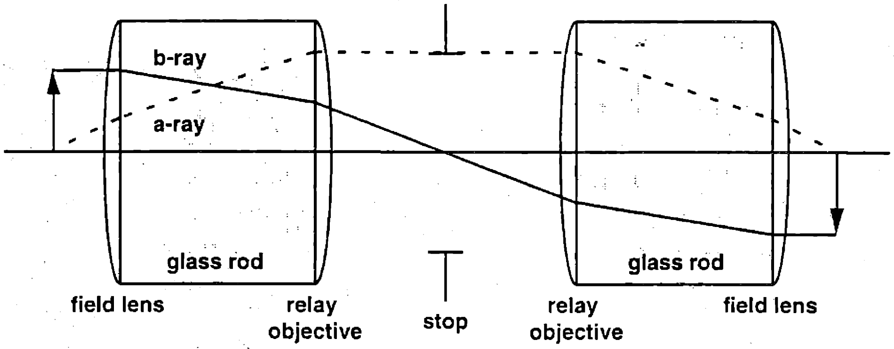

FIGURE 3-14: Hopkins relay element. Glass has replaced the free-space between the field lens and the relay objective resulting in increased light throughput and reduced vignetting or distortion of the image.

Alternatively, it is possible to construct a relay system with a single radial GRIN rod[136]. The ray path is sinusoidal with a full period, $P = 2\pi / \gamma$, defined as the pitch. The γ is a material parameter specific for each lens. Figure 3-15 illustrates how a rod lens (≈ 0.45 pitch) can be used as one stage in a relay system. Rod lenses are typically defined by their pitch length. An integral pitch length rod lens will relay a non-inverted image from one face to the other. In terms of the l/h parameter described in Section 3.4.2, a 1 pitch rod corresponds to $l/h = \pi$. In this case, a beam which is focused into the proximal end of the rod lens will be focused at the distal end as if the rod was of zero length. For rod lenses that are m/2 pitch lengths, where m is an odd integer, the image at the opposite rod face will be inverted. For rod lenses of other pitch lengths, the system resembles a focusing lens with free-space object and image distances. Hence, these rod lenses have image and object planes located finite distances away from the end faces. Typically, non-integral pitch length rod lenses are used in conjunction with additional focusing or collimat-

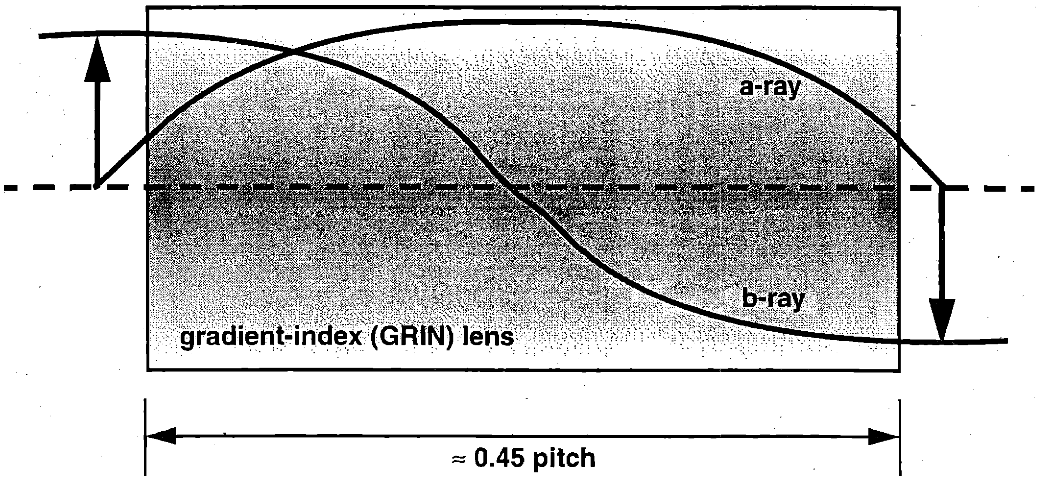

FIGURE 3-15: GRIN lens relay element. Radial index gradient produces sinusoidal beam propagation through lens.

ing lenses. These lenses can be small standard lenses or additional GRIN lenses which can be attached directly to the rod lens. Additional magnification and image-viewing optics may be necessary at the proximal end of the rod. The GRIN relay is the easiest rigid relay system to color-correct[43]. However, the manufacturing process of GRIN lenses is somewhat problematic because ions must be diffused radially into the rod to establish an index gradient. This process is variable and matching lenses to specifications is difficult. Overall, as this fabrication technology improves, GRIN lens relay designs are likely to be incorporated into clinical laparoscopes largely because of their simple design, fewer optical components, and comparably high optical quality.

A rigid OCT laparoscope design is shown in Figure 3-16. A single rod lens was used to relay both

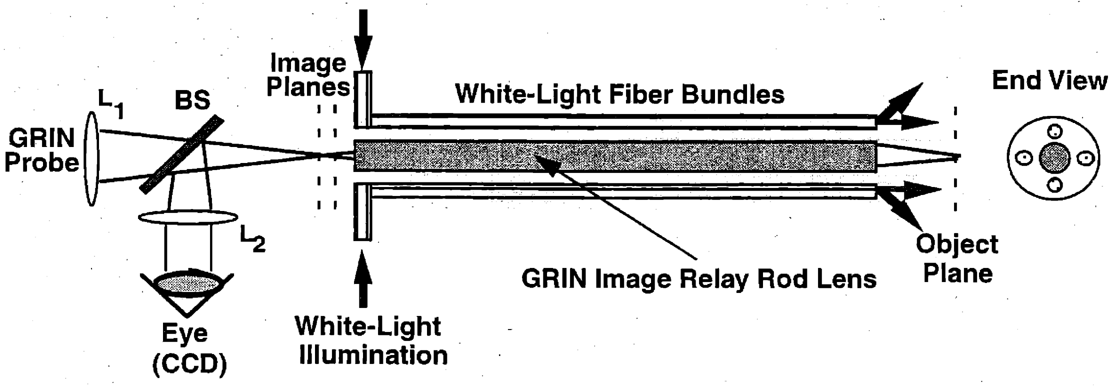

FIGURE 3-16: OCT laparoscope. A single GRIN rod lens was used to relay the scanning focus of the OCT imaging beam to the tissue as well as relay the surface image of the tissue back to the CCD camera.

the OCT imaging beam and the *en face* image of the tissue. The two are separated at the proximal end of the device by a beamsplitter. The path of the OCT imaging beam through the laparoscope is diagrammed in Figure 3-17. The sample arm fiber and GRIN lens on the left represent the GRIN lens hand-held probe

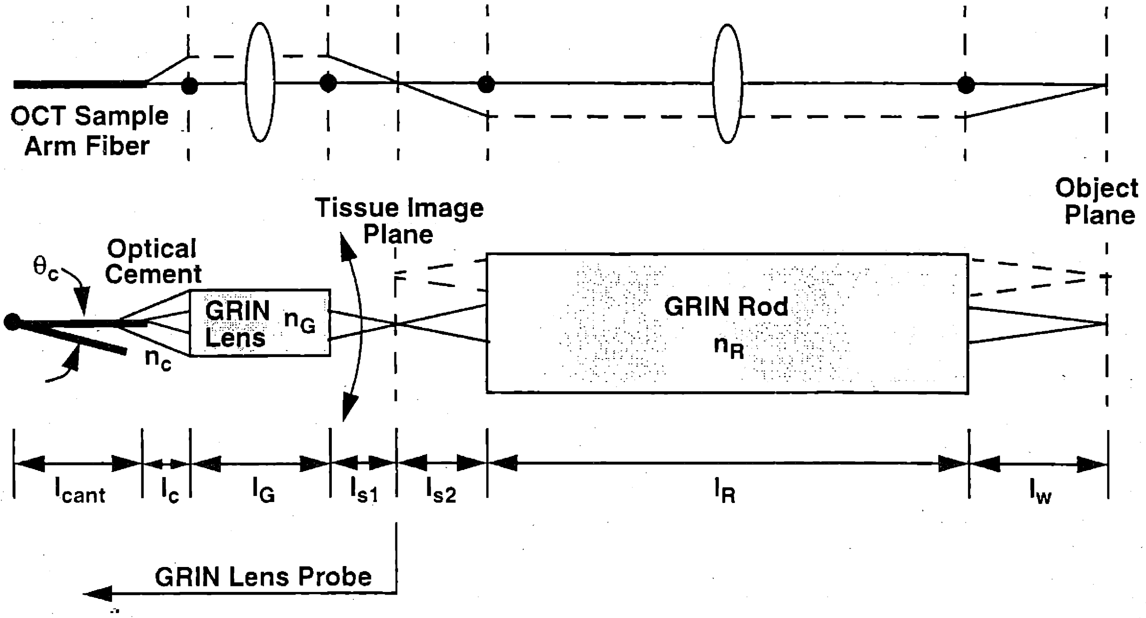

FIGURE 3-17: Beam path through OCT laparoscope.

which was described in Section 3.4.2. The object plane of the probe is placed at the tissue image plane of the GRIN rod to relay image the OCT beam to the tissue. The PZT cantilever displaces the focus in the tissue image plane which scans the focus on the tissue. The cascaded ABCD matrices for this optical system are given by

$$\begin{bmatrix} A & B \\ C & D \end{bmatrix} = \begin{bmatrix} 1 & l_w \\ 0 & 1 \end{bmatrix} \begin{bmatrix} \cos\left(\frac{l_R}{h_R}\right) & \frac{h_R}{n_R}\sin\left(\frac{l_R}{h_R}\right) \\ -\frac{n_R}{h_R}\sin\left(\frac{l_R}{h_R}\right) & \cos\left(\frac{l_R}{h_R}\right) \end{bmatrix} \begin{bmatrix} 1 & l_{s1}+l_{s2} \\ 0 & 1 \end{bmatrix} \begin{bmatrix} \cos\left(\frac{l_G}{h_G}\right) & \frac{h_G}{n_G}\sin\left(\frac{l_G}{h_G}\right) \\ -\frac{n_G}{h_G}\sin\left(\frac{l_G}{h_G}\right) & \cos\left(\frac{l_G}{h_G}\right) \end{bmatrix} \begin{bmatrix} 1 & \frac{l_c}{n_c} \\ 0 & 1 \end{bmatrix} \qquad (3\text{-}23)$$

which for simplicity, have not been reduced. Although the resultant ABCD matrix is complex, magnification can be determined by assuming that the GRIN lens and rod are equivalent to a thin lens with regions of free space on either side. For a thin lens, magnification depends on the position of the object and image planes. Therefore, the magnification of the GRIN rod is

$$M_R = -\frac{o}{i} = -\frac{l_w + h_R/n_R}{l_{s2} + h_R/n_R} \qquad (3\text{-}24)$$

and similarly, the magnification for the GRIN lens is

$$M_G = -\frac{o}{i} = -\frac{l_{s1} + h_G/n_G}{l_c + h_G/n_G}. \tag{3-25}$$

The overall magnification of the laparoscope is the product of these two

$$M = M_G \cdot M_R. \tag{3-26}$$

The FOV for the laparoscope is limited by the input aperture or acceptance angle of the GRIN rod. The NA of the GRIN rod is given by

$$NA = \sin\theta_a \approx n_R a \gamma \tag{3-27}$$

where a is the rod radius and γ is a measure of the pitch length. To avoid aperture effects, the displacement of the GRIN lens focus must remain within the acceptance angle θ_a of the GRIN rod. Under the paraxial approximation, $\tan\theta \approx \theta$, this relation is given by

$$\theta_c \cdot (l_{s1} + l_G + l_c + l_{cant}) \leq \theta_a \cdot l_{s2}. \tag{3-28}$$

The maximum scan length in the tissue image plane is determined by $\theta_a l_{s2}$ which is magnified by the GRIN rod to give the scan length on the tissue. Because the GRIN rod magnifies both the spot size diameter at the tissue image plane and the scan length, the number of NOSSDs will be the same at either plane and given by $\theta_a l_{s2} / 2w_0$ where $2w_0$ is the spot size diameter at the tissue image plane.

Because most commercial parameters for GRIN rod lenses are specified at 550 nm, calculations were performed[139] to determine optical parameters at 1300 nm, a typical OCT imaging wavelength. The gradient index profile within the rod for 550 nm and 1300 nm is shown in Figure 3-18. The small difference in index profile resulted in small variations in pitch length between the two wavelengths as shown in Figure 3-19.

The rigid OCT laparoscope shown in Figure 3-16 was constructed using a 2.68 mm diameter, 19.5 cm long, rod lens ($n = 1.57$) with a nominal pitch length of 3/2 for visible wavelengths. The index gradient of a rod lens is a function of wavelength so for 1280 nm, the rod pitch length is less than the nominal value of 3/2. Thus, an object at a distance of ≈ 10 mm from the distal end face of the rod lens yields an image plane at 10 mm from the proximal end face. Magnification of -3.1 for the GRIN lens and -1.04 for the GRIN rod gave an overall magnification of 3.22. Assuming a 9 μm diameter fiber core, the predicted spot size diameter at the tissue is 29 μm. A 33 μm diameter spot size was measured from the 1.3 mm confocal parameter and is in close agreement. Beam scanning at the proximal end was performed using a piezoelectric cantilever with an attached fiber and GRIN lens, similar to the hand-held probe described in Section 3.4.2. The focal plane of the PZT mounted GRIN lens was placed in the image plane of the rod lens which relay-imaged the beam onto the specimen at a working distance of ≈ 10 mm from the distal face. The 2 mm displacement of the focus from the GRIN lens was the maximum scan length permissible before aperture effects from the GRIN rod, which had an acceptance angle $\theta_a = 5.8°$. The scan length at the tissue image plane was only slightly magnified by the GRIN rod ($M_G = -1.04$). For a maximum scan length of 2 mm on the tissue and $2w_0 = 33$ μm, NOSSD = 60.

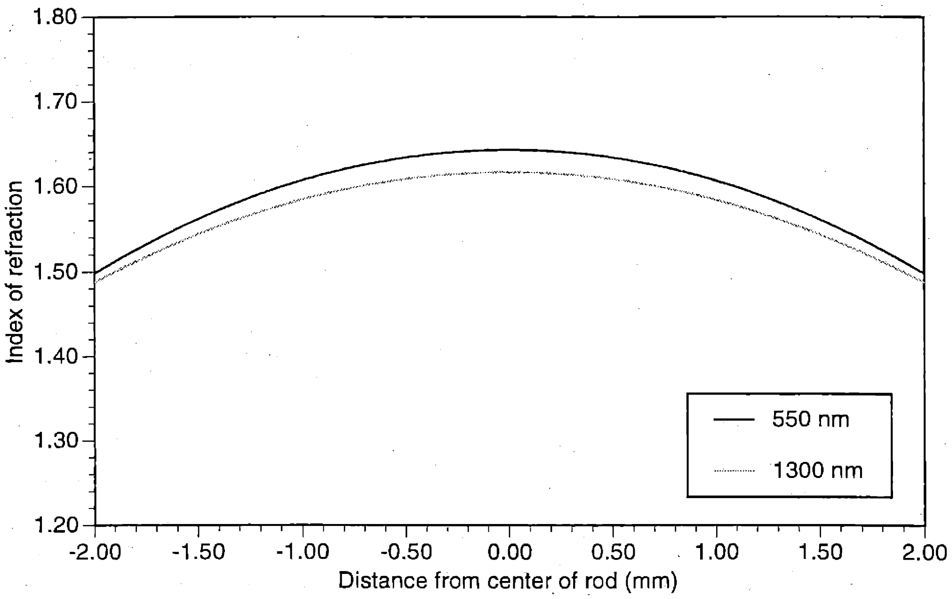

FIGURE 3-18: Gradient index profiles in rod lens. Visible (550 nm) and OCT imaging (1300 nm) wavelengths were chosen for comparison.

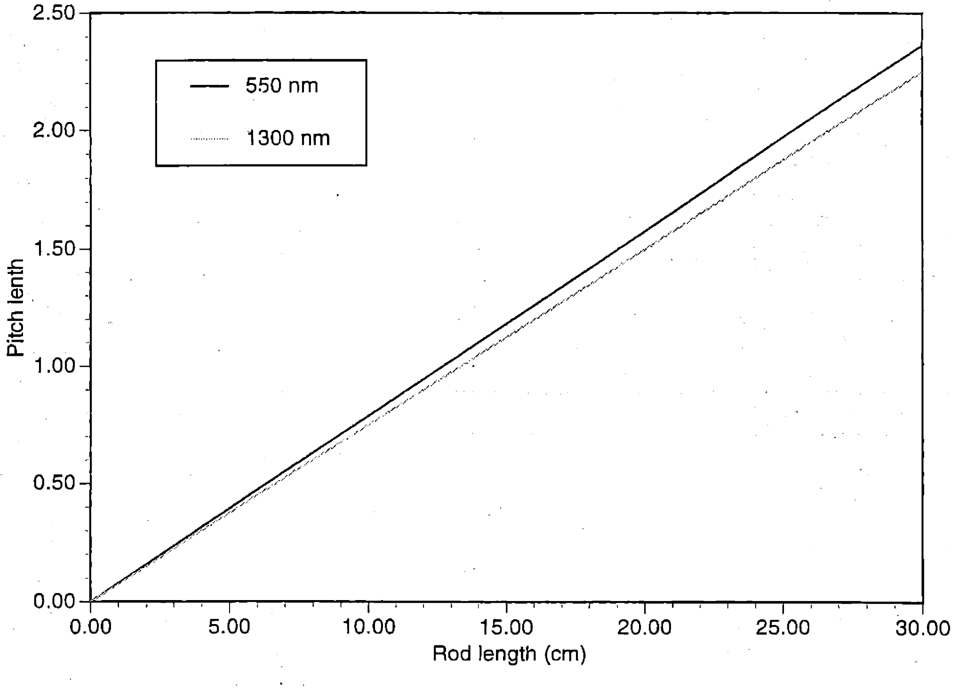

FIGURE 3-19: Pitch length variation of rod lenses. Between visible (550 nm) and OCT imaging (1300 nm) wavelengths, pitch length variations are minor and can be compensated.

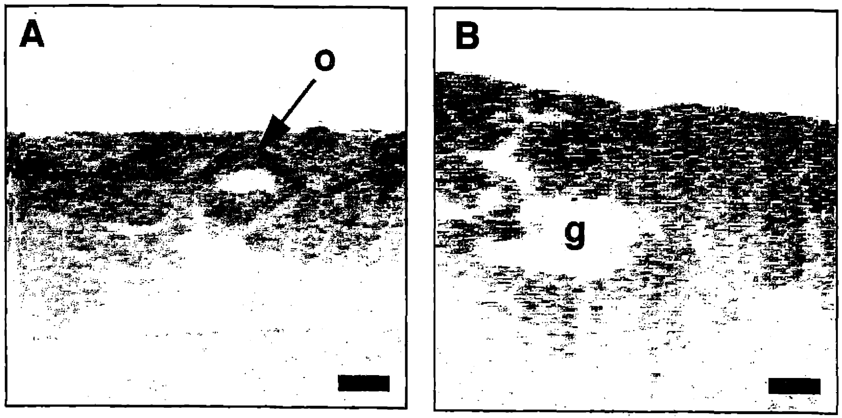

FIGURE 3-20: Images acquired with OCT laparoscope. A) Human ovary with mature oocyte (o). B) Gland (g) in secretory endometrium of human uterus. Bar represents 250 μm.

A beamsplitter was placed between the GRIN and rod lens to permit the simultaneous visualization of the rod lens object plane with a CCD micro-camera containing a 1/3-inch array. Because of chromatic dispersion in the rod lens, the image planes for the near-IR and visible wavelengths are displaced from each other. However, this effect can be compensated by using separate focusing elements for the visible beam path versus the IR scanning beam path. A 3.6 mm focal length camera-mounted lens was used as L_2 in Figure 3-16 to relay the visible image plane onto the CCD array while the GRIN lens focal plane was placed at the near-IR image plane of the rod lens. Two representative images of *in vitro* human tissue acquired with the OCT laparoscope are shown in Figure 3-20. The dynamic *en face* imaging of these specimens provided rapid localization of surface features. When the specimens were placed at the 10 mm working distance for OCT imaging, the tissue did not have striking surface features apart from the location of the coincident visible aiming beam.

This integrated laparoscope design has the potential to combine the ability to visualize intra-abdominal contents or other internal body structures via minimally invasive surgical procedures with sub-surface OCT imaging of architectural morphology.

3.6 Radial Scanning Catheter

3.6.1 Introduction

When imaging is to be performed in tortuous lumens of the body, such as the gastrointestinal, respiratory, or urinary tract, or within the vascular system, a rigid imaging system is impractical. A flexible device is required. Because such a device is used in lumens, imaging of the luminal wall is the prime region of interest. The endothelium that lines the majority of body lumens is a region of active cell division and often a site of neoplastic changes. Hence, a device that is capable of imaging this area at high-resolution would be useful for directing surgical therapy.

3.6.2 OCT catheter designs

The distal end of the OCT catheter should be kept as small as possible to permit insertion into small lumens. The number of optical components should be minimized and the drive mechanism should be located at the proximal end. Forward-imaging is difficult to accomplish in a small catheter design. Therefore, general design concepts were modeled after ultrasound catheters used for intravascular imaging[18,140,141]. These designs rotated a distal ultrasound transducer enclosed in a stationary plastic sheath to acquire a radial cross-section of the lumen.

Utilizing optical components, a simple, inexpensive design was constructed which did not rely on a distal transducer. The original design for the OCT catheter has been described and demonstrated in previous thesis research[101] and experimental studies[78,142-144]. Modifications to this original design were made and are shown in Figure 3-21 and Figure 3-22. Specific modifications will be discussed later in this section.

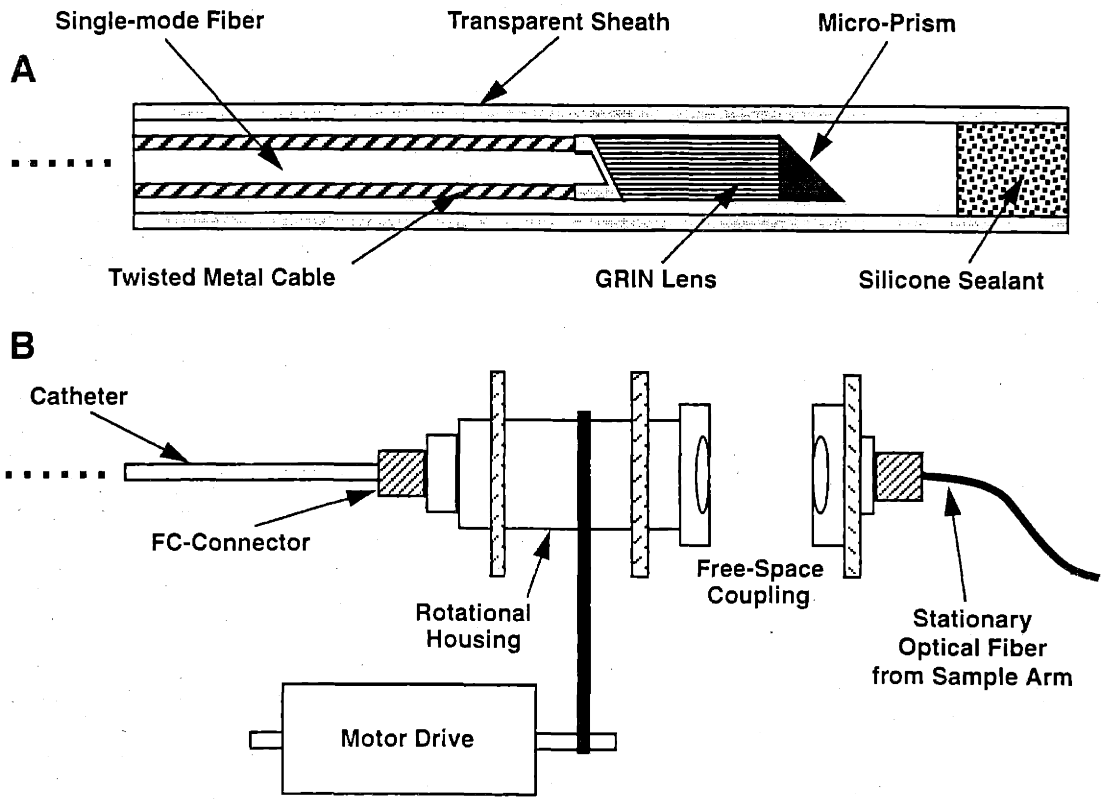

FIGURE 3-21: Modified OCT catheter and optical coupling. A) Modified catheter designed with short working distances for radial imaging of small vessels and lumens. B) Free-space optical coupling permits catheter rotation without optical backreflections from coupler.

The optical system of the OCT catheter is similar to that of the GRIN lens probe design with the addition of a right-angle prism. The beam path is shown in Figure 3-23. The dotted line through the GRIN lens represents an arbitrary ray path since the actual ray path depends on the length of the GRIN lens and the index profile. The ABCD matrix cascade is represented by

$$\begin{bmatrix} A & B \\ C & D \end{bmatrix} = \begin{bmatrix} 1 & l_w \\ 0 & 1 \end{bmatrix} \begin{bmatrix} 1 & \frac{l_p}{n_p} \\ 0 & 1 \end{bmatrix} \begin{bmatrix} \cos\left(\frac{l_G}{h}\right) & \frac{h}{n_G}\sin\left(\frac{l_G}{h}\right) \\ -\frac{n_G}{h}\sin\left(\frac{l_G}{h}\right) & \cos\left(\frac{l_G}{h}\right) \end{bmatrix} \begin{bmatrix} 1 & \frac{l_c}{n_c} \\ 0 & 1 \end{bmatrix} \tag{3-29}$$

where, again for simplicity, the matrices have not been reduced. The transverse and angular magnifications are equal and described in Equation (3-12). The spot size diameter at the focus can be calculated from the matrix elements as described in Equation (3-13).

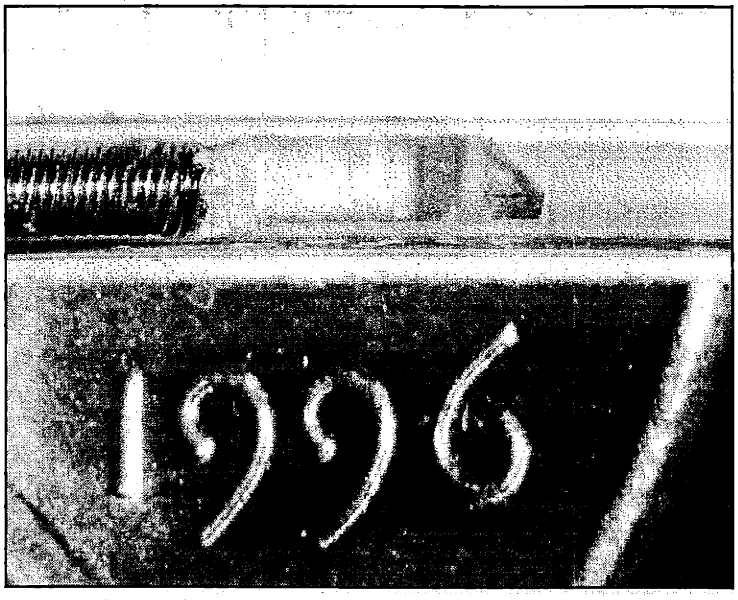

FIGURE 3-22: Photograph of OCT catheter on penny.

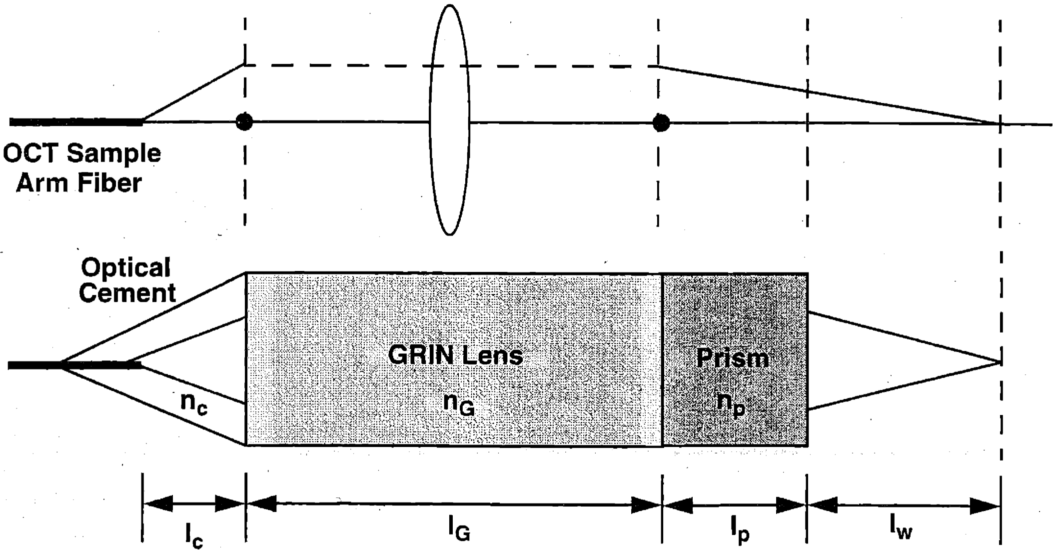

FIGURE 3-23: Beam path through OCT catheter.

The FOV for the radial imaging catheter is over 360° with a circumferential distance dependent on the working distance of the catheter (distance from the outer catheter sheath to the beam focus). Consider the diagram in Figure 3-24. The radial-imaging catheter, with a radius c, lies at the center of the region to be imaged. The focus of the beam is swept around the catheter at a larger radius r. If we let s_{over} represent the degree of oversampling in the transverse dimension, and p_x equal the pixel size, then the relation

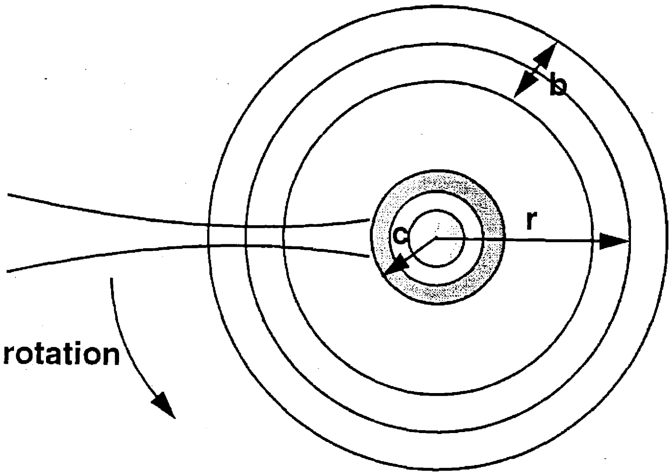

FIGURE 3-24: Radial scanning parameters. Confocal parameter of catheter is rotated about the center axis of catheter for imaging lumens. Variables: b, confocal parameter; c, outer catheter radius; r, beam focus radius.

$$\frac{2\pi r}{p_x} = \frac{2w_o}{s_{over}} \tag{3-30}$$

can be obtained. If the catheter is to be used for small lumens which may come in contact with the external catheter sheath, then it is desirable to have the inner limit of the confocal parameter at the catheter sheath (c). Hence, r = b/2 where b is the confocal parameter or twice the Rayleigh range as defined in Equation (2-47). Substituting for r in Equation (3-30) reduces to

$$w_o = \frac{\lambda \cdot pix}{s_{over}\pi^2} \quad \text{or equivalently,} \quad pix = \frac{s_{over}\pi^2 w_o}{\lambda} \tag{3-31}$$

which determines either the resolution or the number of transverse pixels needed for s_{over} times oversampling. The Nyquist limit governs that $s_{over} \geq 2$. For large confocal parameters, satisfying the requirement of two-times oversampling at the focus may not ensure that two-times oversampling occurs at the outer edge of the confocal parameter. This is a result of the transformation of the OCT image from a Cartesian coordinate system to a polar coordinate system. To ensure adequate oversampling within the confocal parameter, r should equal b rather than b/2.

Obtaining high resolution imaging at long working distances from the catheter is limited by the numerical aperture and wavelength

$$\text{spot size diameter} = 2w_o \equiv \frac{4\lambda f}{\pi D} \tag{3-32}$$

where f is the focal length of the lens and D is the diameter of the beam incident on the lens. Solutions to the engineering problem of permitting high imaging resolutions within large lumens include incorporating mechanisms for adaptive focus positioning, varying, and tracking. This would permit radial imaging at large working distances with low transverse resolution to screen large areas of tissue. Once suspicious areas are located, the beam parameters could be modified and the catheter approximated to the area of interest to permit high-resolution imaging at short working distances. Integrating a short working distance catheter with a quadrant balloon catheter can be used to control the position of the catheter with respect to the lumen wall. The major disadvantage is imaging can only be performed over a small angle rather than a full 360°.

New catheters were constructed to permit shorter imaging working distances. Previous catheter designs utilized GRIN lenses with working distances of 5 mm. Although earlier catheters were suitable for the larger lumens of the gastrointestinal and respiratory tracts, they would not permit imaging of small lumens, such as vessels, because the lumen wall lies outside of the confocal parameter. Therefore, radial imaging catheters were constructed using a GRIN lens with a 2 mm working distance and a 27-30 μm diameter spot size (confocal parameter of 0.9-1.1 mm). This permitted the acquisition of 524 NOSSDs around the circumference swept out by the catheter focus.

The second modification in catheter design was a refinement of the optical coupling between the rotating catheter and the fixed sample-arm fiber. Previous designs utilized contact-coupling within an FC fiber connector. Despite the addition of index matching oil within the coupling, significant backreflections resulted in saturation of the detector and poor OCT image quality. A free-space optical coupling was implemented as shown in Figure 3-21. Rotational variations were less than 5%. Single pass optical power loss was 46%.

The optical performance of this modified catheter design was demonstrated by measuring the free-space point-spread-function from the inner surface of calibrated holes within an aluminum block. The series of images is shown in Figure 3-25. The point-spread-function (PSF), measured at FWHM, varied from 48.4 μm just outside the catheter sheath to 24.6 μm at the focus to 60.5 μm 3 mm away from the catheter sheath. The images in Figure 3-25 also demonstrate several artifacts that occur during imaging. For smaller hole diameters, multiple backreflection artifacts from the close proximity to a highly reflective object are produced as illustrated by the arrow in the 2.0 image. Non-uniform catheter rotation and rapid catheter movement produces shifted image features as shown by the arrows in the 4.0 and 4.4 images. Detector saturation from a highly reflecting surface is approached in the 5.6 image. Similar artifacts have also be reported in intravascular ultrasound imaging[145].

The lumen sizes within the human body range from the 5 μm diameter capillary to the > 6 cm diameter distended colon. The outer catheter diameter determines the minimum lumen size which may be investigated, but the range of 1-60 mm body lumen diameters require further engineering of catheter designs if a single catheter is to be used. Optical beam focusing characteristics constrain the resolution, depth-of-field, and number of pixels necessary for OCT imaging.

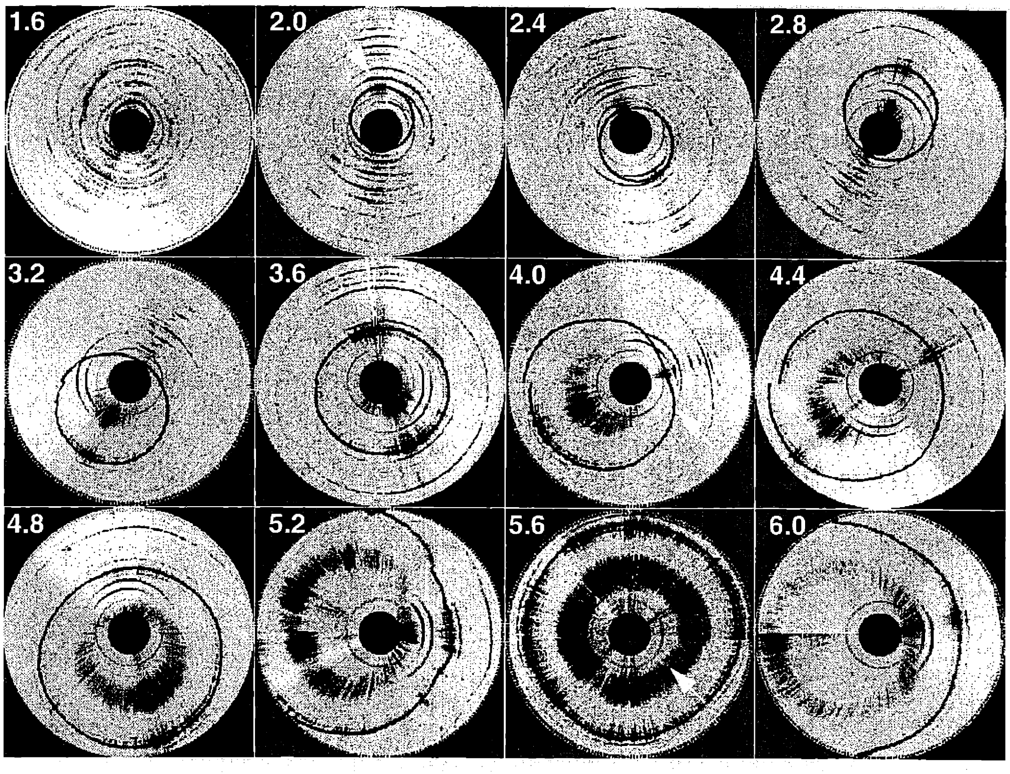

FIGURE 3-25: Catheter images of calibrated hole diameters. Numbers refer to hole diameter in millimeters. Arrow in image 2.0 illustrates backreflection artifact from highly reflective surface. Non-uniform and slow catheter rotation artifacts are shown in 4.0 and 4.4, respectively. Detector saturation is approached in image 5.6.

3.7 Summary

The results from both the theoretical calculations of the optical systems and the experimental investigations of instrument performance reveal both advantages and disadvantages for each beam delivery instrument. The research microscope relies on fixed lens and beam positions, enabling the use of high-quality, aberration-free objective lenses. High NA objectives permit high transverse resolutions at the expense of depth of field. The FOV or scan length is only limited by the translation stage travel distance. This instrument is ideal for a laboratory bench-top delivery system and could be fully integrated with existing light and confocal microscope designs.

The surgical microscope design permitted large 34.5 mm scan lengths (FOVs) in both the X and Y directions at high acquisition speeds. Colinear alignment with the viewing axis of the surgical microscope permitted simultaneous high-magnification visualization of the scan location. Achieving large working distances while maintaining a small spot size diameter was difficult. The current design permitted a 33 μm diameter spot at a working distance under the dichroic beamsplitter of 6 cm, sufficient for manipulating tissue specimens. The maximum number of NOSSDs was 1045.

Two optical designs for a hand-held surgical probe were constructed. The GRIN lens design had a fixed magnification dependent on the GRIN lens parameters and the GRIN-fiber separation. The focal spot was transversely displaced by a PZT cantilever. The cantilever displacement limited the scan length on the tissue to 2 mm. With a 31 μm spot size diameter, only 65 NOSSDs could be acquired. This design was compact, but suffered from mechanical resonances and nonlinear displacement during high-speed scanning. The telescope probe design minimized high-speed imaging artifacts by reducing the mass on the cantilever. Magnification was variable, determined by the ratio of the focal lengths of the two lenses. Both the scan length and spot size were scaled by this magnification resulting in a finite number of NOSSDs in an image. Experimentally, scanning a 33 μm spot over a 3.8 mm scan length implied NOSSD = 115. In order to increase this number, the cantilever displacement must be increased. The spot size at the fiber face is a fixed dimension.

The laparoscope permitted imaging at a remote location through a small-diameter GRIN rod. Using the GRIN probe to displace the focal spot in the tissue image plane of the GRIN rod, displacement was relayed to the tissue surface. The near-unity magnification of the GRIN rod implied a 1:1 mapping of the scan length in the tissue image plane. The NA of the GRIN rod limited the FOV or scan length to ≈ 2 mm in this device. A 33 μm spot size diameter permitted acquisition of 60 NOSSDs. The focal spot size can be reduced and the number of NOSSDs subsequently increased by implementing a design similar to the telescope probe where a bare fiber face is translated at the tissue image plane. However, this may restrict the space for inserting a beam splitter for simultaneous visualization of the tissue surface.

The optical design of the radial imaging catheter is similar to the GRIN probe with the addition of a right-angle prism. As with the GRIN probe, the magnification of the catheter is fixed. The FOV is over 360° as the catheter is rotated. The circumferential scan length is determined by the working distance, which is also fixed. The NA of the GRIN lens determined the focal spot size. Smaller spot sizes will subsequently decrease the working distance. Hence, new short-working distance catheters were constructed for imaging lumens that were approximately the diameter of the catheter sheath, such as in the vascular system. A working distance of 2 mm and a spot size diameter of 30 μm permitted NOSSD = 524. An engineering challenge remains to construct a catheter to permit high resolution imaging in large lumens.

These optical system designs for beam delivery instruments represent fundamental methods for scanning the OCT imaging beam. Further refinements are necessary to increase resolution, scan length, and scanning speed in a compact, rugged instrument. Integration with existing optical instruments will require adaptive modification depending on the specific optical system. However, the combination of the unique imaging abilities of OCT with standard visualization of tissue will represent an advance in imaging tissue microstructure.

Chapter 4

Imaging Tissue Microstructure

4.1 Introduction

Prior to integrating OCT in the surgical suite, fundamental OCT imaging of biological structure must be demonstrated. OCT images must be at sufficient resolutions to differentiate tissue microstructure. Images must reveal morphological differences that distinguish normal tissue from abnormal. Imaging at cellular resolutions in human tissue is the ultimate objective for identifying early neoplastic changes within tissue. High-speed OCT imaging must be demonstrated in order to reduce or eliminate motion artifacts while imaging *in vivo*. In this chapter, these imaging characteristics will be demonstrated and defined using well-characterized *in vivo* animal models.

4.2 *In Vivo* Developmental Biology Animal Models

Developmental biology is a research field that has exploded within recent years due to advances in molecular biology techniques. The field seeks to answer fundamental questions of how a single fertilized egg can develop into a multi-cellular, complex, organism. Developmental processes are all directed via the expression of genes within the animal genome. If the expression of the genetic program is understood, then researchers can determine when and why failure occurs, and how failure can be avoided. Aside from the inherent quest for this scientific knowledge, the research has long-ranging clinical applications to humans such as gene therapy, cloning research, and the treatment of genetic diseases.

The field of developmental biology utilizes several common animal models ranging from prokaryotic bacteria and eukaryotic yeast to increasingly more advanced nematodes (worms, *Caenorhabditis elegans*), fish (zebra fish, *Brachydanio rerio*), insects (fruit fly, *Drosophila*), amphibians (African frog, *Xenopus laevis*), birds (chicks) and small mammals (mice, rats). The lower species on the evolutionary tree are preferred for their ease of care and handling and their rapid reproductive cycles. Mice and rats are preferred for their close homology to humans. The single-cell yeast even has a significant degree of homology to humans, a rather humbling fact. The advancements in molecular biology techniques have permitted researchers to site-specifically modify the genomes of these animal models. By modifying the genome and observing how mutations are expressed within the developing organism, locations and functions of specific genes can be determined. OCT can be applied to developmental biology to observe the expression of genes *in vivo*, in ways previously unavailable to this research community.

The small organisms utilized in developmental biology research are ideal animal models for demonstrating the high-resolution, high-speed imaging capabilities of OCT[146]. These models are ideal due to their small size, ease of care and handling, variations in optical transparency, intact *in vivo* functioning organ systems and high cellular mitotic rates. Common animal models, namely amphibians and fish, are used in a series of experiments which not only define a novel imaging modality for biological microscopy, but also illustrate and define the limits for OCT imaging in surgical applications.

4.3 Identification of Tissue Morphology

Improved imaging of morphological changes has the potential for offering new insight into the complex process of embryonic development. Imaging embryonic morphology that results from cellular differentiation is important for the understanding of genetic expression, regulation, and control. Several well-recognized imaging technologies are currently used to provide structural information about microscopic specimens. These include magnetic resonance imaging, computed-tomography, ultrasound, and confocal microscopy (CM). High-resolution magnetic resonance imaging has been used to produce *in vivo* cross-sectional images of early *Xenopus laevis* development[12] with resolutions of 12 µm. Because the static and gradient magnetic fields required to obtain these resolutions are orders of magnitude greater than those found in most clinical systems, this modality represents a costly and technically challenging option that requires considerable skill from its operator in order to achieve high-resolution images. High-resolution computed-tomographic imaging of fixed insect specimens revealed internal microstructure with 8-12 µm resolution, yet required an elaborate microfocusing instrument and complex image reconstruction algorithms[7]. Ultrasound backscatter microscopy utilizing high-frequencies (40-100 MHz) is capable of 50 µm resolutions to depths of 4-5 mm and has been applied to the analysis of early embryonic development in the mouse[147]. To effectively image with ultrasound, probes require contact with the tissue.

The invention of the confocal microscope[27] and laser-scanning confocal microscopy has produced a revolution of understanding of biological systems and their development largely due to the ability to selectively visualize biological specimens, cells, and sub-cellular constituents[148]. Transverse resolutions of 0.5 µm with 1 µm optical section thicknesses are possible[149]. Although CM is superb for optically sectioning a specimen, imaging depths are still limited to less than 500 µm in nontransparent tissue[150]. Recent advances in CM have successfully shown that *in vivo* confocal imaging is possible. Examples include the imaging of calcium dynamics in sea urchin eggs[32] as well as *Xenopus* oocytes[33] during fertilization. Obtaining *in vivo* images is difficult, however, due to the toxicity of the products that are released when the fluorophores are excited by the incident laser radiation, the image acquisition time, and the maintenance of sub-micron specimen position. These limitations prevent biologists from imaging structure at later developmental stages or in highly scattering, optically opaque specimens. Currently, internal morphological changes occurring in later stages can only be studied with histological preparations at discrete time-points.

An *in vivo* means of imaging morphology is frequently needed to help identify the expression of genes. Furthermore, observing and tracking morphologic changes throughout development is useful for characterizing all aspects of genetic expression which take place. Here, OCT can perform high-resolution, non-contact, cross-sectional tomographic imaging *in vivo* with the potential to analyze the morphological changes in both semi-transparent and highly scattering specimens during normal and abnormal development. OCT tomographic imaging is performed on several of the commonly used animal models in order to establish baselines and demonstrate domains of application for this technology[146]. To verify image representation of morphology, OCT images are correlated with standard histological observations of the specimen, the current gold-standard for identifying morphological features during development.

Optical coherence tomography has the ability to image specimens that are opaque to visible light because it utilizes wavelengths of light in the near-infrared region. Although most tissues appear opaque under visible light, they are relatively non-absorbing in the near infrared. Imaging depth is therefore limited by attenuation from optical scattering rather than absorption. A 1300 nm super-luminescent diode light source in the interferometer enables imaging to depths up to 3 mm with an optical power of only 160 μW incident on the specimen. This imaging depth is sufficient for imaging many anatomical features of interest in most developing embryos. For these studies using the SLD, the free-space longitudinal spatial resolution was 16 μm (as determined by the 50 nm optical bandwidth of the low coherence light source) and the transverse resolution was set to be 30 μm (as determined by the spot size of the light beam). Within the specimen, a longitudinal resolution of ~12 μm is determined by dividing the free-space resolution by the measured average index of refraction of the specimen[77], $n = 1.35$.

The transverse resolution for the following OCT images was 30 μm with a corresponding confocal parameter of 1.1 mm. The SNR was 109 dB. The fact that OCT uses low coherence light and detects light at selected echo time delays greatly discriminates against the detection of light which is multiply scattered. While confocal microscopy discriminates against unwanted light using spatial coherence, the technique is still sensitive to multiply scattered photons which degrade image quality[117].

Imaging studies were performed on several standard biological animal models commonly employed in developmental biology investigations. OCT imaging was performed in *Rana pipiens* tadpoles (*in vitro*), *Brachydanio rerio* embryos and eggs (*in vivo*), and *Xenopus laevis* tadpoles (*in vivo*). Tadpoles were anesthetized by immersion in 0.05% Tricaine until they no longer responded to touch. Specimens were oriented for imaging with the optical beam incident from either the dorsal or ventral sides. After imaging, specimens for histology were euthanized in 0.05% Benzocaine for 30 min until no cardiac activity was observed. Specimens were then fixed in 10% buffered formalin for 24 h, embedded in paraffin, sectioned, and stained with hematoxylin and eosin.

In order to facilitate the registration between OCT images and corresponding histology, numerous OCT images were first acquired at desired anatomical locations in 25-50 μm intervals. Serial sectioning at 20 μm intervals was performed during histological processing. Following light microscopic observations of the histology, OCT images from the same transverse plane in the specimen were selected based on correspondence to the histological sections.

To illustrate the ability of OCT to image developing internal morphology in optically opaque specimens, a series of cross-sectional images were acquired *in vitro* from the dorsal and ventral sides of a Stage 49 (12 day)[151] *Rana pipiens* tadpole. The plane of the OCT image was perpendicular to the anteroposterior axis. Figure 4-1 shows representative OCT images displayed in gray-scale. The gray-scale indicates the logarithm of the intensity of optical backscattering and spans a range of approximately -60 dB to -110 dB of the incident optical intensity. These images (7x3 mm, 500x250 pixels, 12-bit) were each acquired in 40 s.

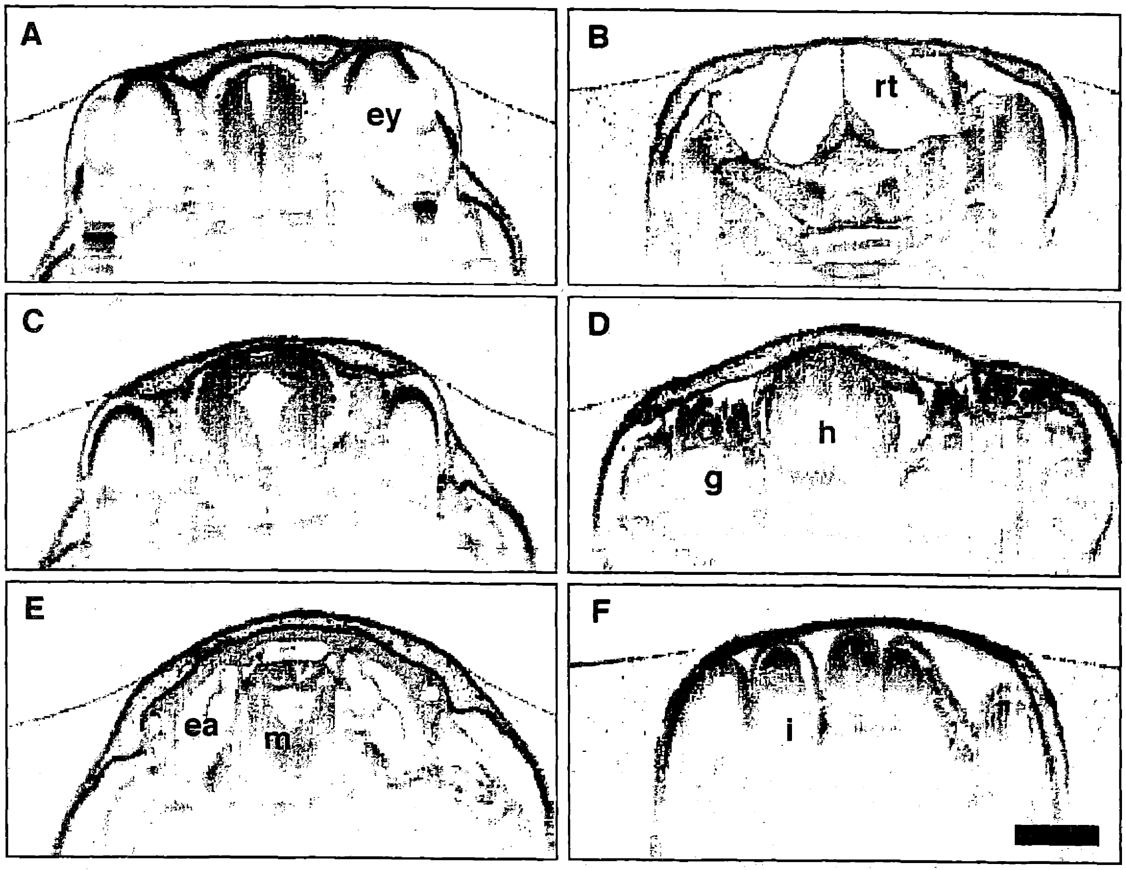

FIGURE 4-1: *Rana pipiens* tadpole. Images in left and right columns acquired from the dorsal and ventral sides, respectively. Abbreviations: ea, ear; ey, eye; g, gills; h, heart; i, intestinal tract; m, medulla; rt, respiratory tract. Bar represents 1 mm.

Features of internal architectural morphology are clearly visible in the images. Identifiable structures in Figure 4-1E include the midbrain, fourth ventricle of the brain, and medulla as well as the ear vesicle. The horizontal semicircular canal and developing labyrinths are observed. Internal morphology not accessible in one orientation due to the specimen size or shadowing effects can be imaged by reorienting the specimen and scanning in the same cross-sectional image plane. The images in Figure 4-1B, D, & F were acquired with the OCT beam incident from the ventral side to image the ventricle of the heart, internal gills, and gastrointestinal tract. The image of the eye (Figure 4-1A) differentiates structures corresponding to the cornea, lens, and iris. The corneal thickness is on the order of 10 µm and can be resolved due to the differences in index of refraction between the water and the cornea. By imaging through the transparent lens, the incident OCT beam images several of the posterior ocular layers including the ganglion cell layer, retinal neuroblasts, and choroid. The thicknesses of these layers were measured from the corresponding histology using a microscope with a calibrated reticule. The thicknesses of the ganglion cell layer, retinal neuroblasts, and choroid were 10 µm, 80 µm, and 26 µm, respectively, and demonstrate the high imaging resolution of the OCT system.

To confirm the *in vivo* resolution of OCT, regions of the anterior chamber and the retinal layers of the eye globe were magnified and measured from the OCT image. Figure 4-2A & B illustrate that as the cornea-lid and iris-cornea structures converge, two distinct layers could no longer be resolved when they were separated by less than 15 µm. The thickness of the retinal ganglion cell layer approaches the resolution limit of OCT and is measured in Figure 4-2C to be 14 µm. These measurements confirm the *in vivo* resolution predicted by dividing the free-space resolution of the OCT instrument by the measured index of refraction of the specimen.

Retinal layers are not imaged throughout the entire globe because of shadowing effects from the highly backscattering iris and sclera which attenuates the transmission of light to deeper structures directly below. A sharp vertical boundary demarcates the regions where light is transmitted through the lens and where light is shadowed. Variation of the specimen orientation will vary the shadow orientation and permit the imaging of different internal structures.

OCT image contrast results from the different optical backscattering properties between different structures. Tissue structures are differentiated according to their varying degrees of optical backscattering while the fluid-filled cavities within the specimen have low backscattering. The cartilaginous skeletal system of the tadpole appears highly scattering and is clearly identified in Figure 4-1A. As light propagates deeper through the specimen, a larger percentage of the incident beam is either scattered or absorbed. Hence, less signal is available from deeper structures and the shades of gray become lighter as the signal-to-noise ratio is reduced. Morphology located directly below a highly backscattering structure can be shadowed from the structure above. These effects are analogous to attenuation and shadowing observed in ultrasound. If the biological specimen is relatively homogeneous, the signal attenuation with depth can be compensated by simple image processing techniques. However, because the morphology of the specimens used in this study are highly complex, the application of these techniques is problematic.

Figure 4-3 shows corresponding *Rana pipiens* histology taken from the same axial plane as the OCT images. The neural retina, choroid, and sclera along with the anterior ocular structures in Figure 4-3A confirm the morphology observed in Figure 4-1A. The muscular ventricle of the heart in Figure 4-3B is well correlated with the corresponding OCT image in Figure 4-1D. Finally, in Figure 4-3C, the multiple coils of the gastrointestinal tract confirm observations made from the OCT image in Figure 4-1F.

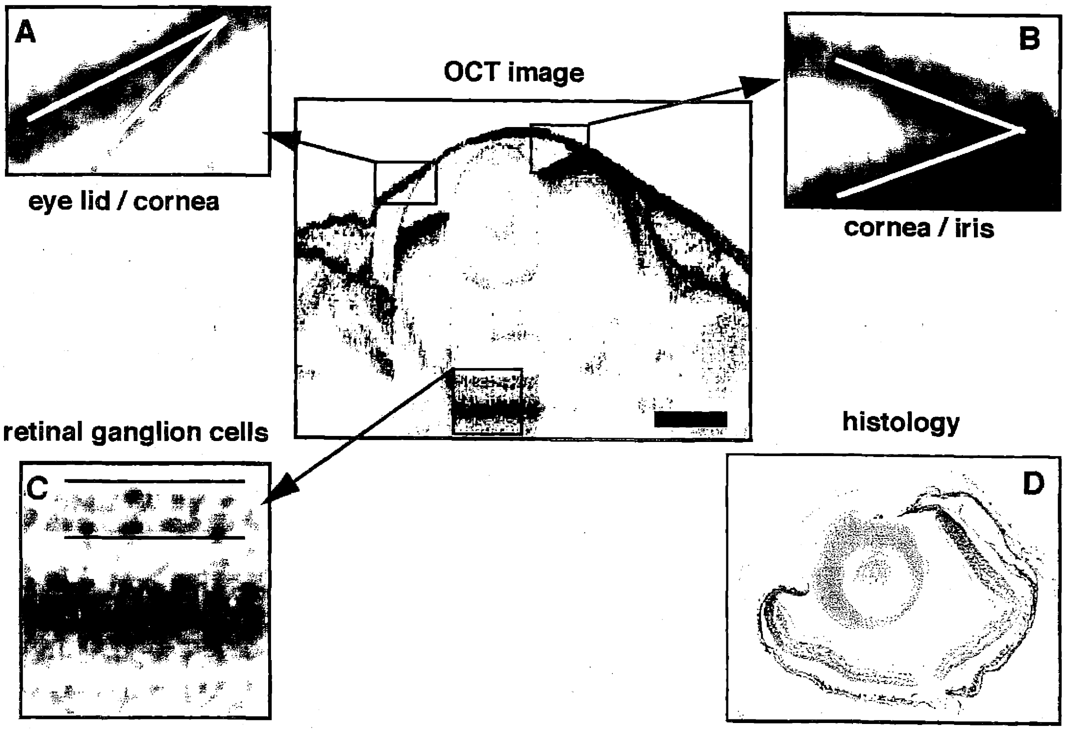

FIGURE 4-2: Verification of *in vivo* OCT resolution. Convergence of eye lid/cornea and cornea/iris structures as well as thickness of retinal ganglion cell layer confirm *in vivo* resolution of OCT. Bar represents 500 μm.

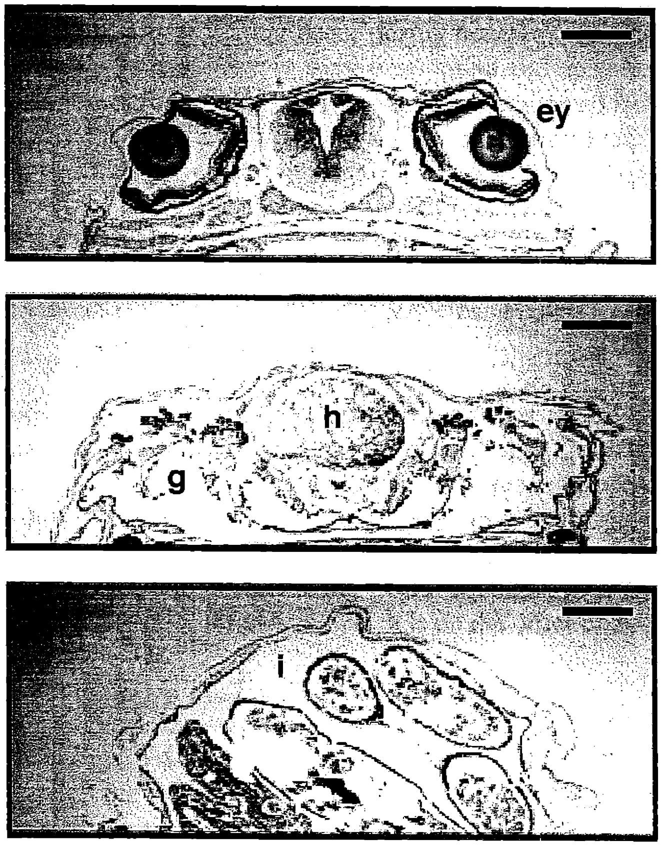

FIGURE 4-3: *Rana pipiens* histology. OCT images in Figure 4-1 strongly correlated with histological observations shown here. Abbreviations: ey, eye; g, gills; h, heart; i, intestinal tract. Bar represents 1 mm.

There is a strong correlation of the tissue architectural morphology between OCT images and the histology. However, it is important to note that OCT images tissue properties in a completely different manner than histology. Histology relies on the differences in the transmission of light through stained tissue while OCT relies on differentials in optical backscattering. The 10-15 μm resolution of OCT for the previous images does not permit the imaging of subcellular features.

To understand the complex processes that occur during neural development, a means of visualizing these micron-scale changes is necessary, often in semi-transparent and opaque specimens. OCT was used to image developing neural morphology in *Xenopus laevis* (African clawed frog) specimens[152]. A sagittal section through a *Xenopus* brain is shown in Figure 4-4. This image (2x6 mm, 250x500 pixels) was acquired in 40 s and represents a 30 μm-thick (spot size) optical slice of the specimen. This image shows high-resolution detail of internal brain morphology. Structure corresponding to the cerebellum, choroid plexus, and medulla oblongata are identified as well as a longitudinal section of the nasal tube and olfactory nerve as it enters the nasal placode. The white internal regions correspond to the low-backscattering cerebral spinal fluid within the lateral, third, and fourth ventricles. Posteriorly, a longitudinal section of the spinal cord is observed.

The vertical labelled lines in Figure 4-4 correspond to planes where cross-sectional OCT images were acquired from this same specimen. These images (1.5x1.5 mm, 200x200 pixels), each obtained in 15 s, are shown in Figure 4-5 and were acquired perpendicular to the anteroposterior axis of the specimen. These represent a normal developing *Xenopus* nervous system. In each image, distinct regions of the brain can be identified. Figure 4-5A shows the paired cerebral hemispheres of the telencephalon and the two lateral ventricles. Figure 4-5D illustrates the narrowing of the aqueduct of Sylvius connecting the diocoel with the rhombocoel. The posterior choroid plexus, which is on the order of 50-100 μm, is clearly resolved in the fourth ventricle in Figure 4-5G.

Following imaging, the specimen was histologically prepared for comparison with OCT images. One comparison is shown in Figure 4-6. The correlations between the OCT image and the histological preparation are strong, although the resolution of this diode-based OCT system does not permit the imaging of individual cell due to the limited spectral bandwidth of the super-luminescent diode light source. Instead, OCT performs well at imaging larger tissue and organ morphology; structure that is often too large to image *in vivo* with confocal microscopy. Note, however, the presence of preparation artifacts indicated by the arrows in Figure 4-6B. The top arrow indicates the displaced outer membrane of the embryo. The bottom arrow points to neural tissue which has been separated from the surrounding structure. These artifacts are most likely the result of dehydration of the tissue during processing or dislocations from sectioning and are relatively common. The OCT image in Figure 4-6A closely preserves the *in vivo* orientation and can be used to identify questionable artifacts found in the histology. The arrows in the OCT image point to the *in vivo* location where histological processing artifacts occurred. OCT images have their own specific artifacts based on the optical properties of the tissue and include the attenuation of signal with increasing depth and shadowing of deeper morphology from backscattering structures.

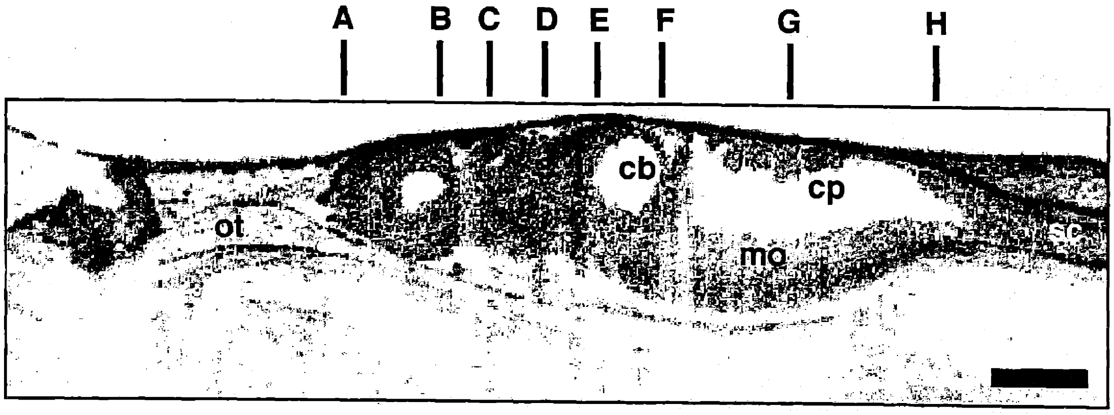

FIGURE 4-4: Sagittal section of *Xenopus laevis* neural tube. Labelled lines correspond to cross-sectional images in Figure 4-5. Abbreviations: cb, cerebellum; cp, choroid plexus; mo, medulla oblongata; ot, olfactory tract; sc, spinal cord. Bar represents 500 μm.

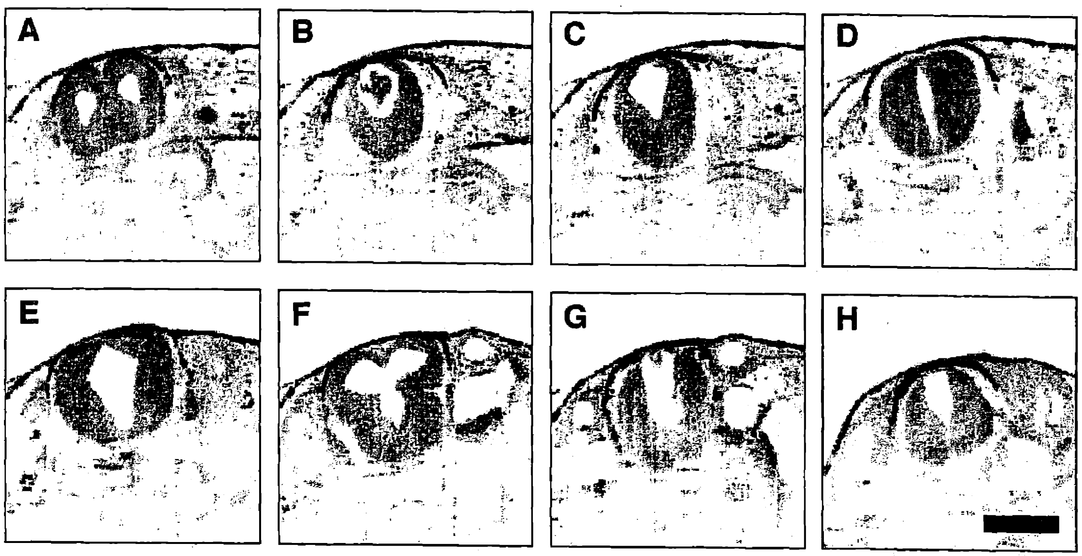

FIGURE 4-5: *Xenopus* neural tube cross-sections. Images correspond to labelled lines in Figure 4-4. Bar represents 500 μm.

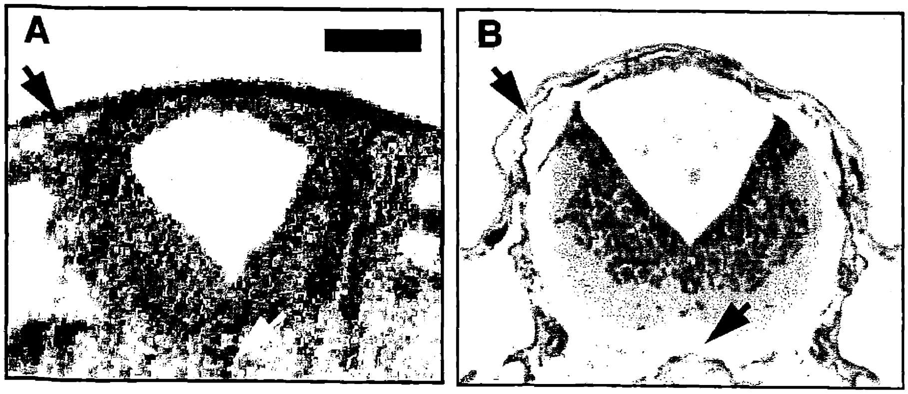

FIGURE 4-6: *Xenopus* neural tube histology. Arrows in B indicate preparation artifacts and can be compared to the *in vivo* image in A. Bar represents 250 μm.

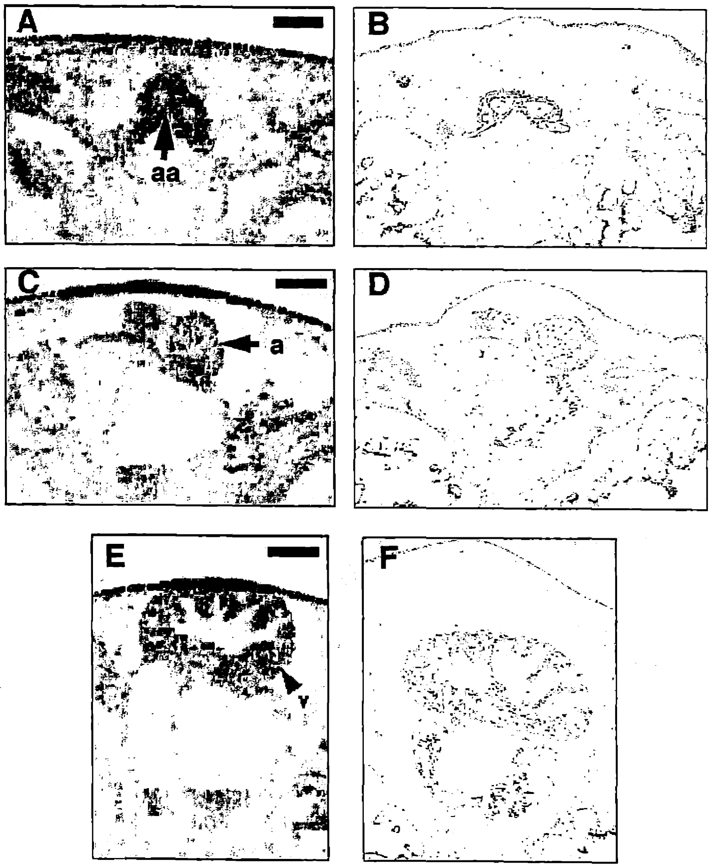

FIGURE 4-7: *Xenopus* cardiovascular histology. Excellent correspondence exists between the OCT images in the left column and the histology in the right column. Abbreviations: a, atrium; aa, arteries; v, ventricle. Bar represents 250 μm.

The developing cardiovascular system presents a technical challenge because of the inherent dynamic motion. A comparison was first made between *in vitro* acquired OCT images and the corresponding histology (stained with hematoxylin and eosin) from a stage 47 (7 day) specimen. In Figure 4-7, representative data from three different cross-sectional planes are shown from the same specimen which illustrate the strong correlation throughout various regions of the developing cardiovascular system. The OCT image in Figure 4-7A (histology, Figure 4-7B) is a cross-sectional image of the two major branches of the ventral aorta anterior to the bifurcation. The muscular walls, as thin as 3-4 cell layers, are clearly distinguished from the larger lumens and surrounding tissue. However, in Figure 4-7A, the smaller arterial lumens were not clearly identified on the OCT image. Using a light microscope with a calibrated reticule, the lumens of these smaller arterial cross-sections were measured to be 8-15 μm. This diameter is below the 16 μm resolution of the diode-based OCT system. In Figure 4-7E, the internal trabeculae carneae network and papillary muscles of the ventricular wall are easily identified in the OCT image and histology.

Figure 4-8 is a selection from 22 cross-sectional images that were acquired from a stage 47 (7 day) *Xenopus* tadpole. This sequence demonstrates the ability of OCT imaging to delineate fine cardiovascular microstructure along the axis of the embryo and maintain registration between images for three-dimensional reconstruction. These OCT scans were acquired at planes perpendicular to the anteroposterior axis of the embryo. The image most anterior to the heart (Figure 4-8A) includes two branches of the ventral aorta leaving the heart, one of which is noted by the arrow. Figure 4-8B was acquired 200 μm posterior and coplanar to Figure 4-8A. This image shows the bifurcation of the ventral aorta as it exits the truncus arteriosus. Other cardiac structures noted in the three chamber amphibian heart include an atrium, shown in Figure 4-8D, and the ventricle indicated in Figure 4-8F. Both atria and the ventricle can be identified in many of the images in this sequence. The pericardial sac is also readily apparent in Figure 4-8B-H.

The presence of histological processing artifacts are common as seen in Figure 4-3, Figure 4-6 and Figure 4-7. High-quality histology, especially serial sectioning, is often difficult, time consuming, and costly. It is especially difficult to histologically prepare the large numbers of specimens typically needed for genetic and developmental studies. The OCT technology offers a promising alternative for rapidly accessing changes in architectural morphology. Because the position of the OCT optical beam on the specimen is precisely controlled by micron stepping motor stages and galvanometric scanners, the registration of the OCT images with respect to the specimen is precisely established. Repeated serial OCT sectional images can easily be acquired to construct a three-dimensional representation of specimen morphology in analogy with MRI. In contrast, in histology, alignment of sectioned planes is often difficult and not repeatable. The major discrepancy in registration between OCT images and histology occurs as the result of small discrepancies in the tilt angle of the image planes rather than axial (anterior-posterior) registration.

A number of comparisons and contrasts can be drawn between the OCT images and histological preparations. Histology with light and electron microscopy offers unprecedented resolution on the cellular and subcellular level. OCT does not have comparable resolution but has the ability to rapidly and repeatedly perform imaging *in vivo*. Histological images have artifacts due to tissue dehydration, shrinkage, and stretching during processing. OCT images have artifacts which arise from optical attenuation with depth, shadowing, and refractive index effects. The axial distances measured in OCT images represent the echo time delay of light and thus, in order to convert this information into physical dimensions, it is necessary to know the index of refraction of the tissue. The index of most tissues varies between 1.35 and 1.45, thus, possible errors in longitudinal range can be on the order of only 5-10% if the index is unknown.

In addition to axial scale changes, the index of refraction also produces refraction of light rays when they traverse boundaries with different index. This effect is most significant at the proximal boundary of the specimen where the OCT beam is incident on the specimen from air. This refraction effect can cause

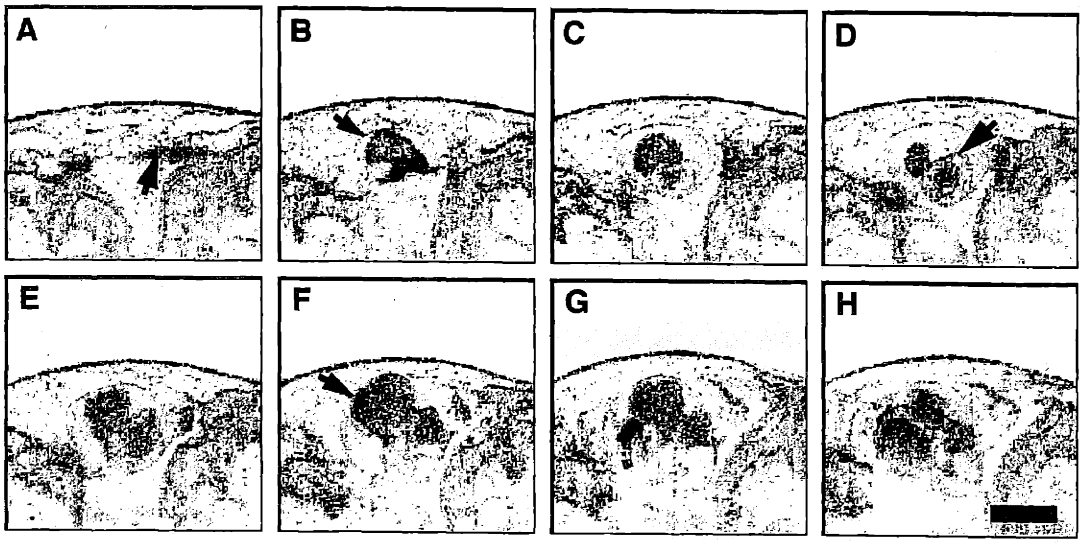

FIGURE 4-8: OCT cross-sections of *in vitro Xenopus* heart. Arrows indicate A) branch of ventral aorta, B) pericardial sac, D) atrium, F) ventricle. Bar represents 500 μm.

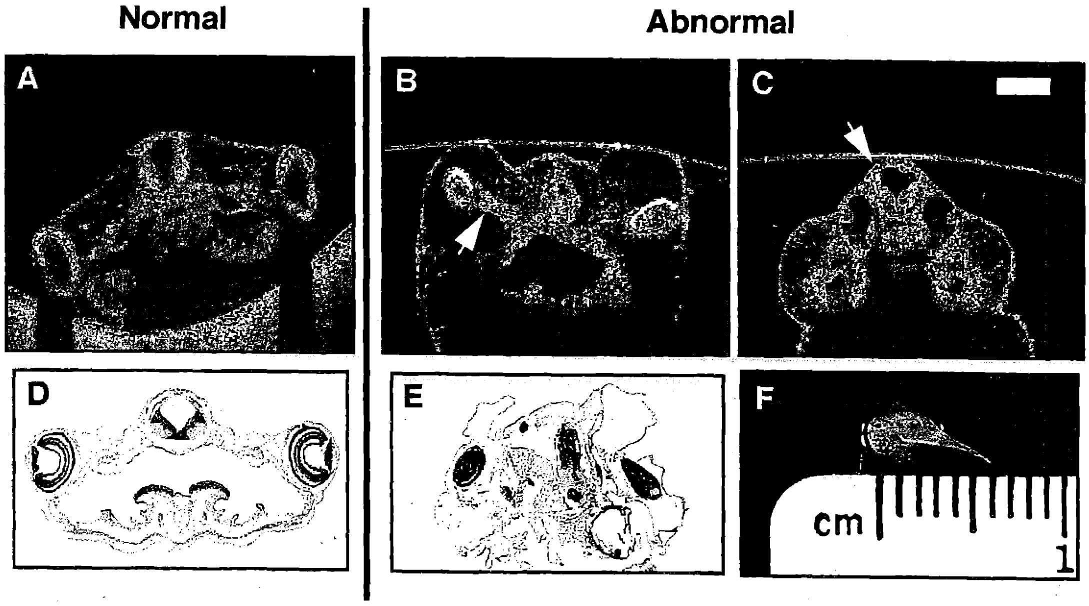

FIGURE 4-9: Identification of abnormal *Xenopus* development. Normal specimen in A with corresponding histology in D can be compared to an abnormal specimen in B,E. Arrow in B indicates longitudinal section of left optic nerve and ocular muscles. Subtle neural tube abnormality is shown in C. Bar represents 500 μm.

internal features to appear as if they are angularly displaced. Refraction depends on the mismatch of the index across a boundary and is negligible if the light enters the tissue perpendicular to the boundary and becomes larger when the light ray is more oblique. These errors can be minimized by either partially or fully submerging the specimens in liquid which produces refractive index matching. It is important to note that these same scale uncertainties and refractive effects are also present in ultrasound imaging. However, if measurements are performed in a consistent manner, these effects are considered part of the baseline. The diagnostic power of the imaging technique is not compromised because it relies on detecting deviations from the baseline.

The image scale and distortion effects are actually present in both ultrasound and MRI images although they arise from slightly different physics principles. Histology, to some extent, suffers from similar problems in obtaining measurements from preparations due to tissue preservation, dehydration, and sectioning. Tissue configuration following preparation may not always reflect the *in vivo* orientation making quantification difficult. Despite the artifacts in both techniques, these artifacts are reproducible and can be perceived as the baseline. The differences in calibrating histopathology against real tissue dimensions usually does not compromise its diagnostic utility.

4.3.1 Morphological abnormalities

The application of OCT in surgery is advantageous if the technique is sensitive enough to detect subtle changes in tissue microstructure compared to a normal baseline. This is demonstrated using developmental biology animal models by distinguishing internal structural abnormalities from normal morphology[146]. Figure 4-9A-F compare and contrast *in vivo* morphology between both normal and abnormal *Xenopus* using OCT images (3x3 mm, 300x300 pixels) and corresponding histology. These developmental abnormalities are believed to be spontaneous and not the result of mutagenic agents. The normal *Xenopus* OCT image (Figure 4-9A) correlates well with histology (Figure 4-9D). The neural tube shows normal formation as well as symmetrically placed and correctly oriented eyes. Internal gills are observed in both OCT and histology. Shadowing of the clay-lined dish is evident below the highly scattering ocular structure. In striking contrast, the abnormal specimen (Figure 4-9B & E), at the same stage, has an irregularly shaped neural tube and abnormally large orbits which contain small, poorly formed optic cups. The optic cups are oriented asymmetrically. In this image plane, a longitudinal section of the left optic nerve and ocular muscles are noted by the arrow in Figure 4-9B. An OCT image acquired more posterior in the abnormal specimen reveals the continuation of the poorly formed neural tube with morphological variations occurring on the scale of 50 μm (Figure 4-9C). These images show that both gross and microscopic structural differences are clearly identifiable.

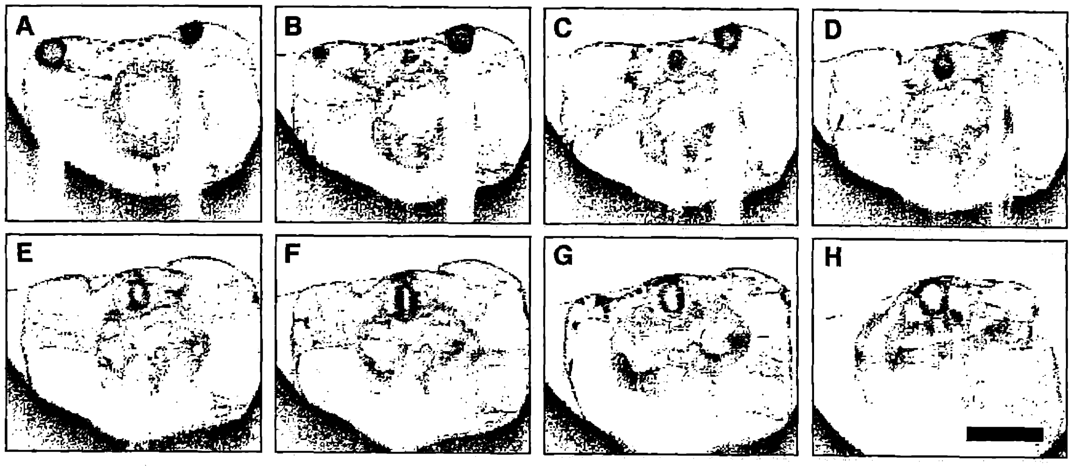

FIGURE 4-10: Abnormal neural tube development. Image sequence also demonstrates general morphological abnormalities and shadowing artifact from ocular structures in A-D. Bar represents 1 mm.

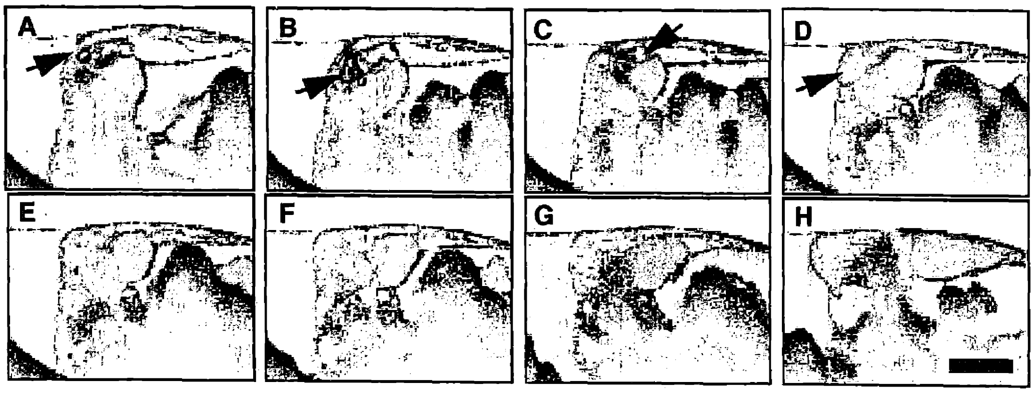

FIGURE 4-11: Abnormal cardiovascular development. Arrows in A,B indicate abnormal vasculature while arrows in C,D indicate poorly formed cardiac chambers. Bar represents 500 μm.

The ability of OCT to sample abnormal developing neural structure is shown in Figure 4-10. Cross-sections of an abnormal specimen were acquired every 200 μm along the anteroposterior axis as the specimen rested in a clay-lined dish. Representative images (3x3.5 mm, 300x350 pixels, 35 s acquisition) show a poorly developing nervous system as well as a greatly distorted body pattern. The developing optic cups are oriented dorsally rather than more lateral. Images in Figure 4-10A & B show portions of the left optic nerve and ocular muscles. The neural tube can be readily identified in each image in this sequence. To highlight particular neural abnormalities, imaging can be limited to just the brain or neural tube as was done for the normal specimen in Figure 4-5. These images are also intended to illustrate the potential for OCT to image many other systems within the developing specimen as imaging is possible through the entire specimen and into the clay. The highly backscattering ocular tissue in Figure 4-10C produces a shadowing effect on the underlying tissue below. As incident light travels through the specimen, photons are either scattered or absorbed. At regions deep within the specimen or in areas below scattering structures, less light is available to be backscattered and, hence, the signal-to-noise is lowered and the region appears faint. The shadowing that is observed below the ocular tissue is an extreme example of this effect. It is difficult to predict when this effect will be significant. For example, the neural tube and brain in these images are scattering structures yet little shadowing is observed. In fact, high contrast is still present in the tissue structures below.

The molecular pathways involved in heart development are complex, requiring the interaction of multiple genes at precise time-points during development[153]. Because of this, cardiovascular malformations are common. Abnormal developing cardiovascular structures are shown in Figure 4-11. These *in vitro* images of a *Xenopus* heart illustrate abnormal vasculature (arrows in Figure 4-11A and B) and poorly formed cardiac chambers (arrows in Figure 4-11C and D). Prior to OCT imaging, the Stage 43 (3 day) specimen was active, but future development is likely to be retarded due to the poorly functioning circulatory system. In Section 4.4, OCT is applied to imaging and measuring functional heart parameters from the developing cardiovascular system.

4.3.2 Tracking development

The non-contact nature of OCT and the use of low-power near-IR radiation for imaging causes few harmful effects on living cells. However, focused beams of 800 nm light from lasers used in optical tweezers, optical traps, and two-photon microscopes have been shown to induce irreversible damage within the cellular DNA[154,155]. This is highly significant if such techniques are to be used to assist *in vitro* fertilization procedures in humans. OCT imaging does not require the addition of fluorophores, dyes, or stains in order to improve contrast in images. OCT relies on the inherent optical contrast generated from variations in optical scattering and index of refraction. All of these advantages contribute to the use of OCT for extended imaging of development over the course of hours, days, or weeks.

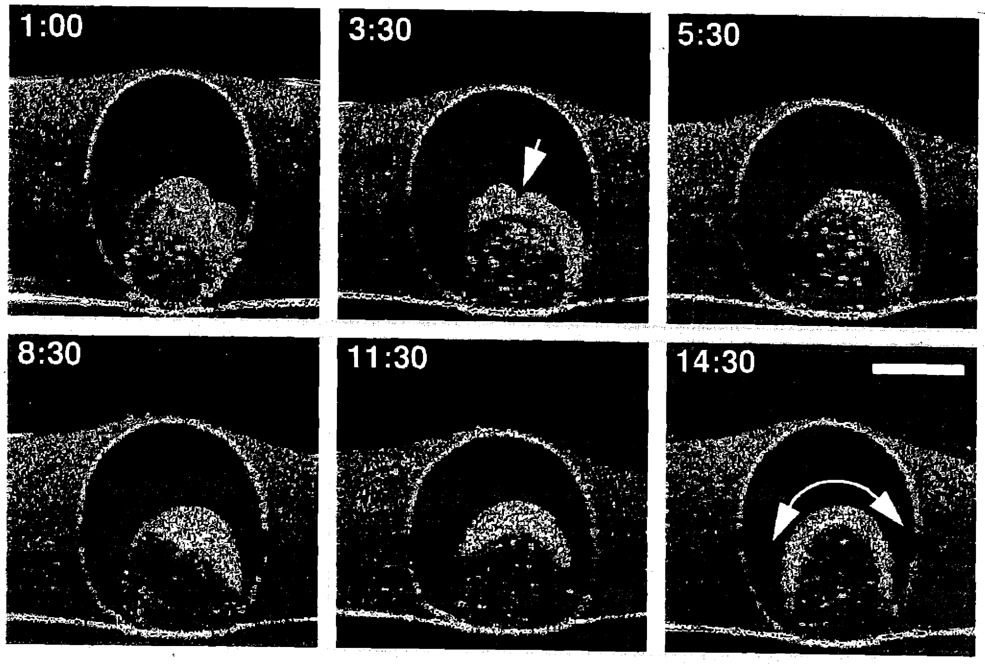

FIGURE 4-12: Early embryonic zebrafish development. Times are indicated in hours post-fertilization. At 3:30 hrs., cells have migrated to the dorsal pole (arrow). At 14:30 hrs., the anteroposterior axis has been established (arrow). Bar represents 500 μm.

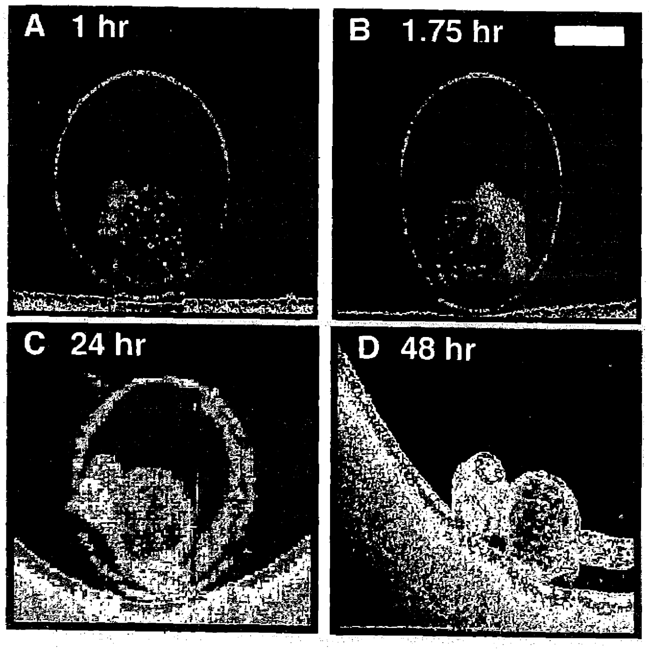

FIGURE 4-13: Early and late zebrafish development. A,B) 2- and 4-cell stages 1 and 1.75 hr after fertilization, respectively. C,D) Embryo before (24 hr) and after (48 hr) hatching. Bar represents 500 μm.

Figure 4-12 demonstrates the application of OCT for sequential imaging of development *in vivo*. Images (3x3 mm, 300x300 pixels) of a developing zebrafish embryo within its egg were acquired every 15 min beginning at one hour post-fertilization and continuing for 24 hrs. Images were acquired from the same cross-sectional plane within the specimen. The egg was suspended in low-temperature gelling agar to prevent egg movement and to maintain a uniform state of hydration. Developmental changes illustrate early cleavage beginning at the 8-cell stage, 1 h post-fertilization. Because of the high mitotic rate of the embryo, results of cellular division and migration are observed as well as the establishment of the antero-posterior axis. In this example, the zebrafish egg and embryo were semi-transparent and the use of OCT significantly complemented observations made using light microscopy. By imaging subtle differences in backscattering intensity, interfacial structural layers millimeters deep within specimens can be clearly delineated. In Figure 4-13A & B, images of a second zebrafish embryo are shown at the 2- and 4-cell stage, just minutes after fertilization. Images of a zebrafish embryo prior to and immediately after hatching are shown in Figure 4-13C & D.

A fundamental question in developmental biology is the establishment of patterns within the developing embryo and the interaction of genes which control this process. The *hox* gene is a member of the homeobox domain which governs antero-postero segmentation and limb development[156]. The development of *Xenopus* limb buds was followed using OCT and shown in Figure 4-14. Early images reveal a small limb bud which extends and develops into individual digits. A larger developing hindlimb is shown in Figure 4-15 which reveals internal vascular and skeletal development. A cross-section of the lower leg reveals the internal formation of the tibia and fibula. Genes responsible for limb development are a common site for genetic manipulation. OCT can be used to track the morphological expression of these genes without sacrificing the specimen for histological processing.

4.4 Functional Imaging

Previous OCT images have characterized morphological features within biological specimens. These structures are static even though they may have been acquired from *in vivo* specimens. *In vivo* imaging in living specimens, particularly in larger organisms and humans, must incorporate fast acquisition techniques to eliminate motion artifacts within the images. *In vivo* imaging is necessary but not sufficient to perform functional imaging. Functional imaging is the quantification of *in vivo* images which yield information characterizing the functional properties of the organ system or organism. Prime examples include the use of functional MRI (fMRI) to characterize brain activity during various states of consciousness, thought, or motor control, and determining cardiac performance using ultrasound, CT, or MRI. Functional imaging is currently utilized with neurosurgical procedures to determine proximity to sensitive brain areas. The intraoperative functional assessment of the patient status is critical information which can be used to determine if the surgical procedure should continue or be concluded. I predict morphological and functional imaging will be fully integrated in many surgical procedures in the near future. Developmental biology animal models represent a nearly ideal functioning system to demonstrate both high-speed and functional OCT imaging.

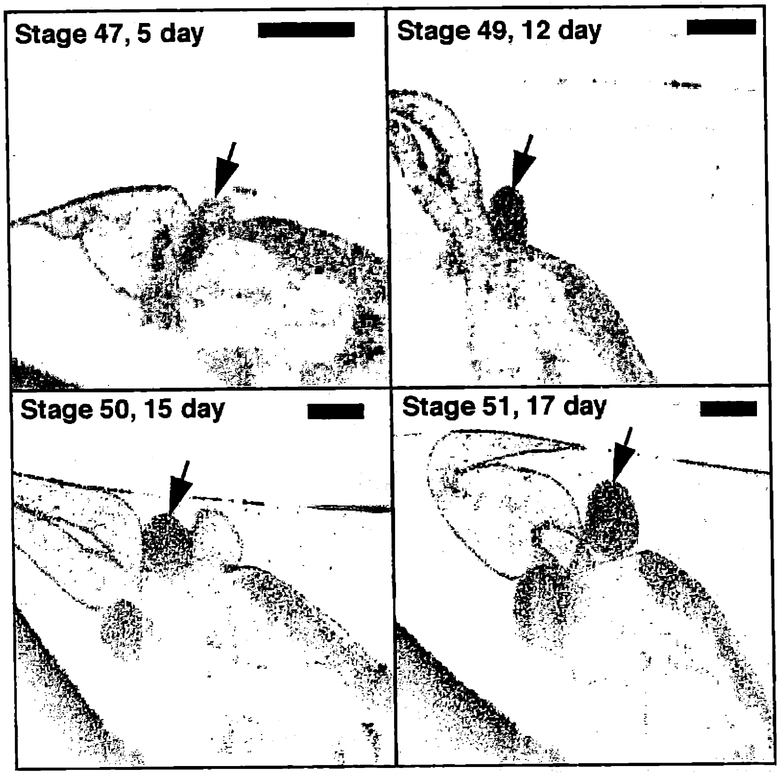

FIGURE 4-14: Early *Xenopus* hindlimb bud development. Arrow in each image indicates right hindlimb bud. Bar represents 500 μm.

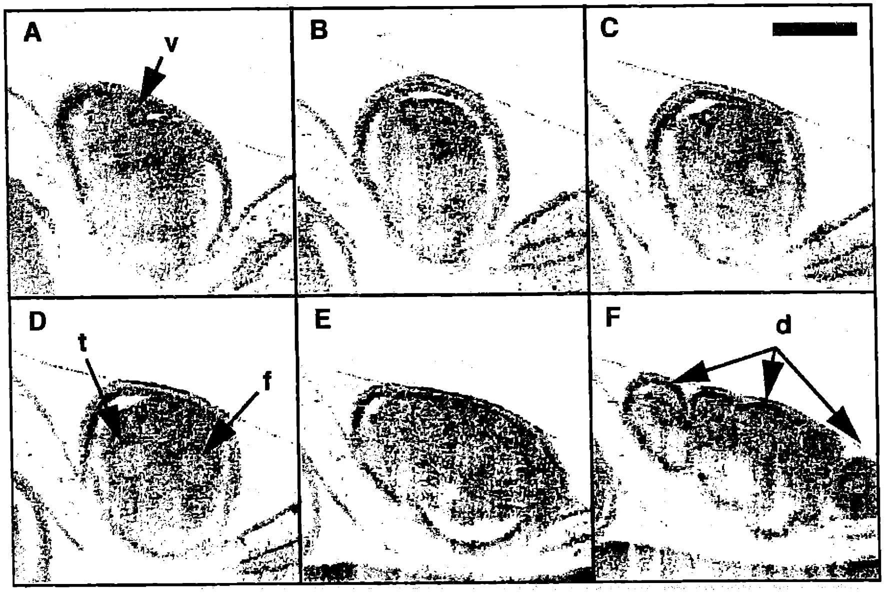

FIGURE 4-15: Cross-sections of internal hindlimb structures. Images were acquired proximal-to-distal along the length of one hindlimb. Abbreviations: d, digits; f, fibula; t, tibia; v, vasculature. Bar represents 500 μm.

4.4.1 Cardiovascular system

Studies investigating normal and abnormal cardiac development are frequently limited by an inability to access cardiovascular function within the intact organism. OCT has been used for the high-resolution assessment of structure and function in the developing *Xenopus laevis* cardiovascular system[157]. OCT, unlike technologies such as computed tomography and magnetic resonance imaging which require gated-image acquisition, provides real-time, high-speed *in vivo* imaging. This allows quantitative dynamic activity, such as ventricular ejection fraction, to be assessed. OCT imaging is analogous to both ultrasound M-mode and 2-D echocardiography.

Abnormal cardiac function remains a leading cause of morbidity and mortality worldwide. Developmental animal models have been used to assess molecular and physiologic mechanisms of not only congenital cardiac abnormalities, but also the genetic predisposition to acquired abnormalities. However, although imaging technologies exist which allow the progression of human adult cardiac function to be followed with time, comparable imaging does not exist for following cardiac function in the developing animal embryo. Video light microscopy has been used to acquire real-time images of the developing beating heart. However, it is limited to axial, *en face*, views and only surface morphology is visible. Therefore, investigators are either confined to using embryos that are transparent during early stages of development, exposing the heart via surgical intervention, or sacrificing the animal at a predetermined stage.

The Cr^{4+}:forsterite laser was used as a light source to enable high-speed OCT imaging. The laser provided additional power (2 mW) incident on the specimen in order to maintain a signal-to-noise ratio of 110 dB during high-speed imaging. Other modifications to the OCT system include the incorporation of a piezoelectric fiber stretcher as a replacement for the mechanical galvanometer reference arm scanner. This enabled faster axial scanning and an image acquisition rate of 4 images (300x300 pixels) per second. Faraday rotators compensated for the birefringence induced during stretching of the fiber. Both the axial and transverse resolutions were comparable to those for the super-luminescent diode source.

Though the relatively slow data acquisition rate of the diode-based system (30 s per image) is adequate for *in vitro* imaging of microstructure, two-dimensional *in vivo* imaging of the rapidly beating heart requires considerably faster imaging speeds. To illustrate the presence of motion artifacts, an *in vivo* image of a beating heart acquired with the diode-based system is shown in Figure 4-16A. The periodic bands within the image correspond to the movement of the cardiac chamber walls during the cardiac cycle. In contrast, in Figure 4-16B, an image of the same heart was generated at 4 frames/s. The morphology of the *in vivo* cardiac chambers is clearly delineated at this faster imaging speed. Image acquisition is fast enough to capture the cardiac chambers in mid-cycle. With this capability, images were acquired over many beats at various times during the cardiac cycle. A sequence of six frames is shown in Figure 4-17 which comprise a complete beat. These frames were assembled to produce a movie illustrating the dynamic, functional behavior of the developing heart.

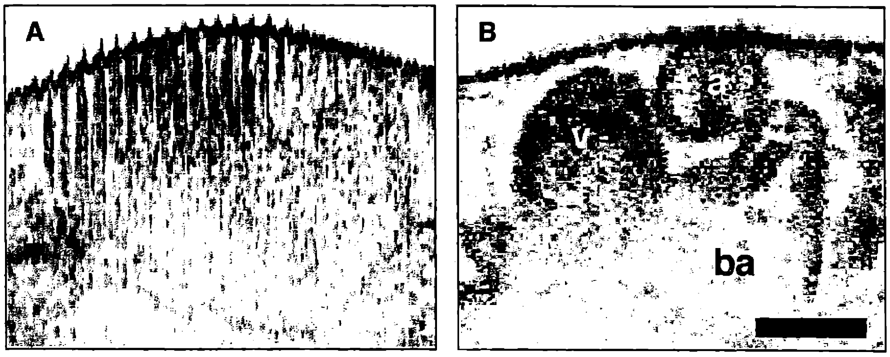

FIGURE 4-16: Comparison of slow and fast OCT imaging. Images of beating *Xenopus* heart were acquired in A) 30 s and B) 250 ms. Abbreviations: a, atrium; ba, bulbous arteriosis; v, ventricle. Bar represents 500 μm.

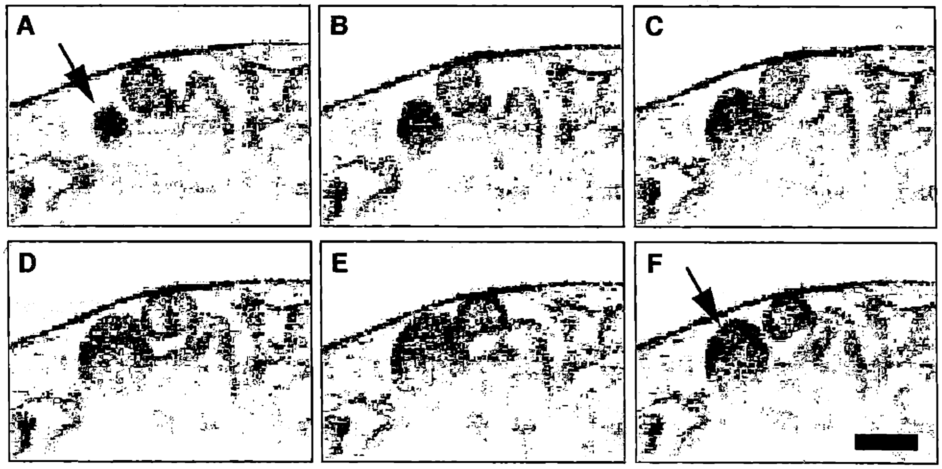

FIGURE 4-17: Single *Xenopus* heart beat sequence. Each image was acquired in 250 ms but from different cycles. Sequence from A) beginning of diastole with emptied ventricle (arrow) to F) beginning of systole with filled ventricle (arrow). Bar represents 500 μm.

Unlike the source used with the diode system, the high speed system utilized a laser which is not commercially available. Though commercial sources with bandwidth characteristics similar to the laser are anticipated in the near future, I investigated whether any dynamic information, other than two-dimensional imaging, can be obtained with the slower diode system. In particular, since a single axial scan can be acquired in approximately 100 ms with the diode-based system, an OCT optical cardiogram, analogous to a M-mode echocardiogram, can be obtained with this slower system. Characteristic oscillations corresponding to movement of the embryonic cardiovascular structure are observed. Both the ventral and dorsal walls of the ventricle, in addition to the ventricular lumen, can be identified as well as the oscillatory nature inherent during the cardiac cycle. To capture OCT optical cardiograms, the beam was positioned in one location over the ventricle (which corresponded to the center of the OCT image) and held stationary as data from this single location was acquired over time. In Figure 4-18A, the OCT beam was positioned over the ventricle at the site corresponding to the center of the image (arrow). Axial (depth) scans from this location were acquired over time and are shown in Figure 4-18B. Figure 4-18B is an OCT optical cardiogram of a normal functioning anesthetized heart.

OCT optical cardiograms permitted quantitative measurements of chamber function and allowed assessment of changes over time. Measurements included heart rate, chamber dimensions, filling and emptying time, and ejection fraction as shown in Figure 4-18B. For each beat within these cardiograms, four points were recorded by a blinded observer (using IP Lab 3.0, Spectrum Analytics) which corresponded to the locations of the dorsal and ventral ventricular wall. The end of systole was defined as the maximum ventricular dimension while the end of diastole was defined as the minimum ventricular dimension. No micropipet electrode was used to obtain an electrocardiogram for the specimens as this would have interfered with cardiac performance and optical imaging. Measurements were obtained for the heart rate (HR), end diastolic and systolic dimensions (EDD, ESD), and ejection and fill times (ET, FT). The ventral wall velocity (VWV) was calculated by

$$VWV = \frac{EDD - ESD}{2ET} \tag{4-1}$$

and the fractional shortening (FS) was calculated from

$$FS = \left(\frac{EDD - ESD}{EDD}\right) \times 100. \tag{4-2}$$

To determine the volume of the developing amphibian heart, an ellipsoid model was used assuming the two minor axes (a) were equal and the major axis was twice the length of a minor axis (2a)[158]. Therefore, the volume of the ventricle is

$$Volume = \frac{8}{3}\pi a^3. \tag{4-3}$$

The ejection fraction (EF) was then determined from

$$EF = \left(\frac{V_D - V_S}{V_D}\right) \times 100 \tag{4-4}$$

where V_D is the diastolic volume and V_S is the systolic volume.

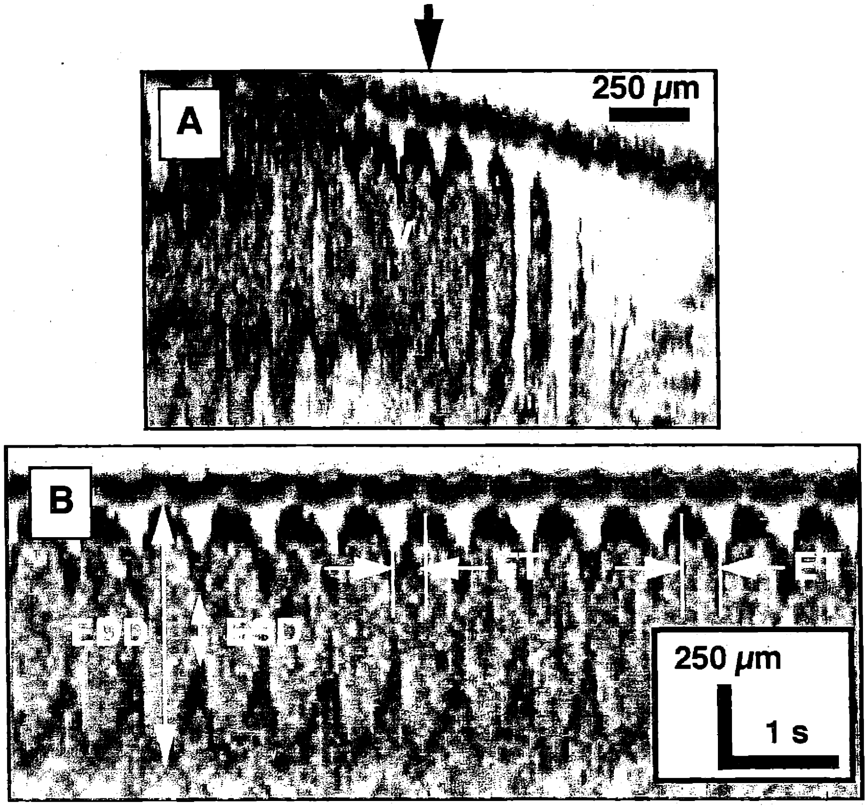

FIGURE 4-18: OCT optical cardiograms. A) OCT image of beating ventricle with arrow indicating acquisition site for B) Optical cardiogram of *in vivo* ventricle (v). Measured parameters: EDD, end-diastolic dimension; ESD end-systolic dimension; ET, ejection time; FT, filling time.

Measurement averages and standard deviations were obtained from 16 beats present in each optical cardiogram. Paired t-tests were performed on all the measured data (heart rate, end diastolic/systolic dimension, ejection/filling time) to determine if there were statistically significant changes between successive recording times. The results of these statistics are described in the next section and listed in Table 4-1 and Table 4-2 which compare the response following a dose of verapamil, a calcium channel blocker.

4.4.2 Response to pharmacological agents

Following acquisition of normal OCT optical cardiograms, verapamil, an inotropic drug, was administered to vary the functional behavior of the embryonic heart as well as to determine the sensitivity of OCT optical cardiograms for assessing functional changes. A 25 ng dose was administered to a specimen by placing drops on the ventral side of the tadpole as the specimen rested in the optical imaging setup. This permitted data acquisition prior to and immediately following administration and the observation of the transient effects of the drug as it diffused from the external membrane to the heart.

An image of the beating heart prior to the verapamil does is shown in Figure 4-19A with a normal optical cardiogram in Figure 4-19C. In Figure 4-19D and E, optical cardiograms illustrate the effects of verapamil on the functional properties of the heart. These optical cardiograms were acquired at 1 and 4 min, respectively, following administration of verapamil. Figure 4-19B is an image of the ventricle 10 min following the verapamil dose. Here, cardiac motion is minimal and dilation of the ventricular chamber is evident.

Cardiac measurements and heart parameters were obtained as described for the initial optical cardiograms. From each OCT optical cardiogram, dynamic indices (heart rate, end diastolic/systolic dimension, ejection/filling time) were measured (Table 4-1). Although many algorithms exist, such as the Pappus' rule, summated ellipsoid method and biplane Simpson's rule for modeling human ventricle volumes[158-160], few studies have modeled the developing amphibian heart. Based on OCT image data of these embryonic hearts, the ellipsoid model most closely approximates the *in vivo* ventricle. The calculated results are summarized in Table 4-2. For all the measured parameters, only 3 out of 20 paired t-tests failed to have a p-value below 0.05. In addition, 13 out of 20 had p-values less than 0.005. No significant change in heart rate occurred after 2 min and no significant change in filling time was noted between the initial measurement and 1 min after the verapamil dose. All other changes were statistically significant ($p < 0.05$).

As shown in Table 4-1 and Table 4-2, OCT demonstrated a decrease in heart rate after verapamil administration, in addition to reductions in fractional shortening and ejection fraction. The EF reached a minimum of 56±8% at 2 min before beginning to recover. The administration of an inotropic drug via diffusion from the external ventral membrane to the heart was chosen to minimize side-effects that would result from micropipet injections. Although diffusion does not result in a bolus of drug delivery, my emphasis in this research was to demonstrate the use of the OCT technology for noninvasively assessing changes in cardiac function, not to determine the specific effects of precise doses on the amphibian heart.

Incorporating high-speed OCT to assess the functional behavioral response to pharmacological drugs provides rapid feedback on the organism's state of health. The high-speed image sequences of the beating *Xenopus* heart shown in Figure 4-17 was assembled from several beats. Although each image was acquired in 250 ms (4 frames per second), the images were not sequential in time. This was a limitation of the data acquisition system and computer memory. The development of the optical delay line (Section 2.5.3) and direct data storage on super-VHS video tape enabled the acquisition of sequential images at 8 frame per second (256 x 248 pixels). The surgical microscope described in Section 3.3 was used for high-speed transverse scanning. The Cr^{4+}:Forsterite laser was used to provide high incident opti-

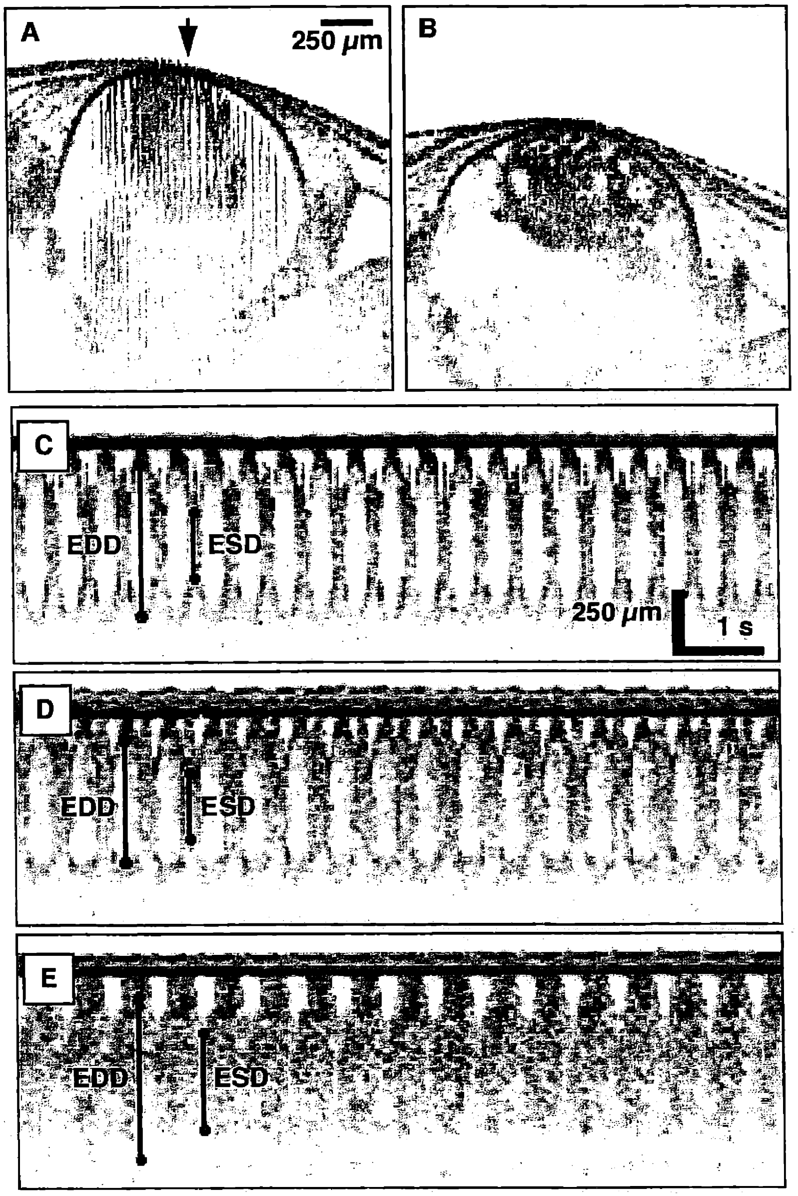

FIGURE 4-19: OCT optical cardiogram variations following verapamil dose. A) OCT image of beating *Xenopus* heart. C,D,E) Optical cardiograms acquired at 0, 1, and 4 min, respectively, following verapamil dose. Lines indicate measurements of end-diastolic (EDD) and end-systolic dimension (ESD) used to evaluate functional parameters. Image in B was acquired 10 min after dose when heart had stopped.

cal power to maintain an image SNR at 105 dB. The high-speed acquisition enabled immediate feedback of scan location within the tadpole. Arbitrary image angles were explored to rapidly optimize image quality. The images in Figure 4-20 show transverse, oblique, and sagittal orientations of the *in vivo* cardiovascular system. Valves were identified in Figure 4-20A and Figure 4-20B shows a longitudinal section of a branch of the aorta.

TABLE 4-1: Measured parameters of verapamil effects on *Xenopus* cardiovascular function.

Time (min)	Heart Rate (bpm)	End-Diastolic Dimension (μm)	End-Systolic Dimension (μm)	Ejection Time (ms)	Filling Time (ms)
Initial	128 ± 4	666 ± 18	398 ± 35	217 ± 22	251 ± 27
1	$124 \pm 5^{*}$	$616 \pm 13^{\ddagger}$	$371 \pm 27^{\ddagger}$	$236 \pm 20^{*}$	251 ± 20
2	$119 \pm 4^{*}$	$537 \pm 13^{\ddagger}$	$413 \pm 30^{\ddagger}$	$268 \pm 11^{\ddagger}$	$236 \pm 19^{\dagger}$
3	117 ± 5	$710 \pm 19^{\ddagger}$	$507 \pm 22^{\ddagger}$	$223 \pm 41^{\ddagger}$	$288 \pm 34^{\ddagger}$
4	115 ± 7	$741 \pm 17^{\ddagger}$	$478 \pm 20^{\ddagger}$	$279 \pm 31^{\ddagger}$	$240 \pm 17^{\ddagger}$
Significant Differences:	**$^{*}P < 0.05$**	**$^{\dagger}P < 0.01$**	**$^{\ddagger}P < 0.005$**		

TABLE 4-2: Calculated parameters of verapamil effects on *Xenopus* cardiovascular function.

Time (min)	Ventral Wall Velocity (μm/s)	Fractional Shortening (%)	Ejection Fraction (%)
Initial	630 ± 86	40 ± 6	77 ± 6
1	572 ± 109	40 ± 5	77 ± 6
2	366 ± 69	23 ± 5	56 ± 8
3	504 ± 104	29 ± 4	63 ± 7
4	585 ± 66	35 ± 3	73 ± 4

The administration of verapamil produced dramatic changes in the functional performance of the heart. Changes in heart rhythm from a 1:1 atrial-to-ventricle conduction to a 2:1 heart block was observed. A toxic dose of verapamil converted a normal ventricular rhythm heart into ventricular fibrillation. A series of this is shown in Figure 4-21. The initial image shows the ventricle and an atrium. Over time, the ventricle dilates and begins fibrillating.

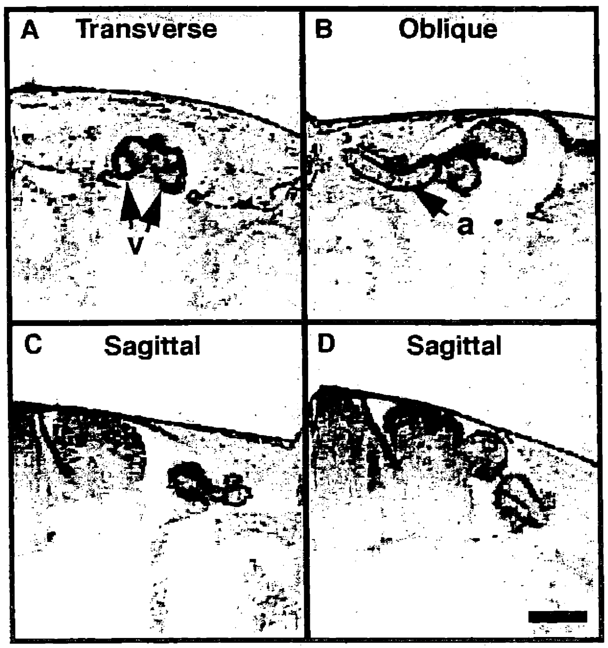

FIGURE 4-20: Orientations of *Xenopus* heart acquired at 8 fps. A,B) Transverse and oblique images illustrating valves (v) and artery (a). C,D) Sagittal sections of heart ventricle, atrium, and vasculature. Bar represents 500 μm.

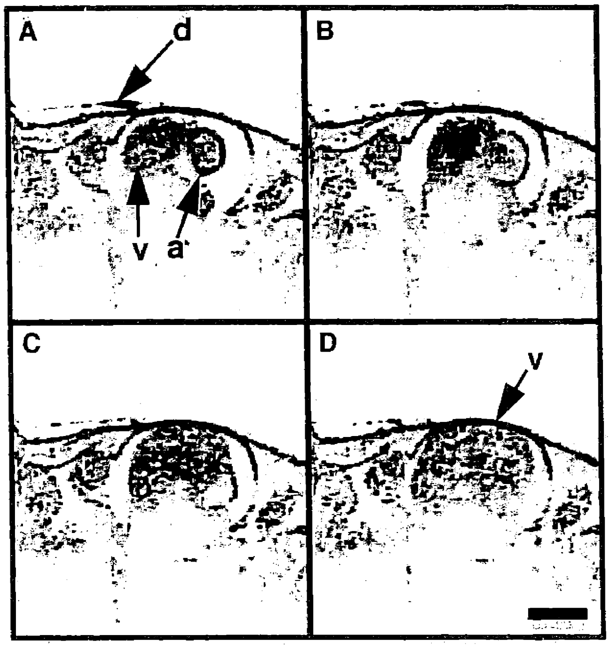

FIGURE 4-21: Verapamil-induced ventricular fibrillation. Drug (d) was applied on outer membrane. Atrium (a) was displaced from imaging plane by dilating ventricle (v). Bar represents 500 μm.

Optical measurements with OCT can be applied to the assessment of other variables such as cardiac output and flow velocity. To achieve this, OCT can be configured to measure the velocity of moving tissue and flowing blood using laser Doppler velocimetry[161-165]. Rather than having a fixed specimen in the sample arm and a moving reference arm mirror, the reference arm mirror may remain fixed and the moving sample produces Doppler-shifted backscatter. Other variations including a moving reference arm mirror are also possible. The frequency of this Doppler-shifted light can be used to calculate the velocity of the moving tissue or blood. This is analogous to Doppler ultrasonography and will be explored in greater detail in Section 5.4.

The investigation of cardiovascular development in animals models, utilizing the powerful technologies of molecular and cellular biology, has been aggressively pursued to understand the mechanisms underlying cardiac dysfunction. However, severe limitations exist with current methods for assessing cardiac structure and dynamics in these animal models, frequently forcing investigators to analyze phenotypes with postmortem histopathology. The disadvantages of this approach include an inability to assess dynamic information and the sacrificing of mutants which typically are in limited supply. I have demonstrated the feasibility of OCT for overcoming the limitations associated with both histopathology and current methods of imaging through its assessment of structural and dynamic information at micron-scale resolutions.

Though organisms were anesthetized prior to imaging, real-time acquisition (30 frames/s) may offer the potential for images to be obtained without the need to anesthetize specimens. Improved data acquisition rates will also enable 3-D images to be rapidly acquired and processed; permitting the 4-D (x, y, z, time) analysis of the dynamic functioning of the heart as well as morphological changes that occur during development. The high-resolution, high-speed imaging provided by OCT should represent a powerful tool for assessing and understanding the molecular basis of abnormal cardiovascular development.

4.5 Cellular and Subcellular Imaging

Optical coherence tomography is capable of cellular resolution imaging which may ultimately have a role in the early diagnosis of human malignancies[166]. Neoplasias are most responsive to medical intervention at early stages, prior to undergoing metastasis. When these disorders arise from known premalignant states, and if a detection method exists, the high risk population can be screened to reduce patient morbidity and mortality. Organs where these premalignant conditions occur at relatively high frequency include the esophagus, uterus, bladder, colon, and stomach. The ability to image these organs in real-time at cellular and subcellular resolutions could represent a powerful tool for the early identification of neoplasms.

4.5.1 Technical considerations

Imaging at cellular and subcellular resolutions with OCT is a major technical challenge. This is particularly difficult for human cells which vary in size from 5-20 µm. For example, the stratified squamous epithelium of the cervix has 10-20 µm diameter cells with 5-15 µm diameter nuclei. Larger cells include megakaryocytes at 30 µm and tumor giant cells as large as 100 µm in size. There are significant structural changes in tissue which begin immediately after the tissue is separated from its *in vivo* blood supply. Cells rapidly lose the oxygen and nutrients necessary to maintain ionic gradients and cell death begins within minutes to hours. The hydrated state of *in vivo* tissue improves OCT image contrast enabling smaller microstructure to be resolved. This will be illustrated in Section 6.6 with *in vivo* images of rabbit tissue.

Contrast in optical imaging can generally be defined as

$$\frac{\Delta I}{\bar{I}} = \frac{\text{Intensity Difference}}{\text{Average Image Brightness}}. \tag{4-5}$$

Intensity differences can arise from changes in absorption, fluorescence, refraction, reflection, phase-shifts, scattering, and polarization changes. A study by Dunn, *et. al.*[167] found that for confocal reflectance imaging, changes in index of refraction contributed most to image contrast followed by absorption then scattering. Assessment of indices of refraction for cellular components can be used to determine which structures are likely to provide contrast in OCT images[168]. A listing of cell structures and their index of refraction is shown in Table 4-3.

TABLE 4-3: Indices of refraction for cellular constituents[168-172].

Extracellular fluid	1.35
Cytoplasm	1.37
Nucleus	1.39
Mitochondria	1.42
Melanin	1.70
Structural fibers	1.43

High contrast should particularly be present with melanin granules, mitochondria, and structural fibers because of their relatively high index of refraction.

The macroscopic scattering coefficient can be defined as

$$\mu_s = \frac{\phi(1-\phi)}{V} \times C \tag{4-6}$$

where ϕ is the volume fraction of cells relative to tissue, V is the volume of a single cell, and C is the scattering cross-section[173]. The scattering coefficient represents an average of local tissue variation dependent on the size of the imaging volume. Larger focal spot sizes with correspondingly larger confocal parameters average out small scattering variations making individual cells difficult to resolve. In order to have sufficient contrast within single cells, the imaging focal volume must be smaller than the dimensions of the cell. Equation (4-6) also demonstrates why loss of tissue hydration or volume decreases the amount of contrast. For *in vivo* epithelial tissue, $\phi = 0.7$ with a μ_s of 60-105 cm^{-1}. If water is removed from tissue, the volume of a single cell decreases thereby increasing the scattering from the tissue. Regions of relatively low scattering are absent from the dehydrated tissue. Backscatter from a particular location within tissue is characterized on the macroscopic scale by the scattering coefficient and the anisotropy factor. Changes in backscatter depend on the size, shape, and index difference of the scatterers within the focal volume.

Contrast and resolution in OCT images degrade with increasing depth. Coherent multiple-scattering processes or speckle results in a reduction of lateral coherence at the detector aperture and produces a speckled appearance in OCT images. Additionally, interfacial reflections and absorption from overlying tissue reduce the power available at greater depths. One means of reducing speckle and improving contrast is by using higher NA objective lenses. Schmitt, *et. al.*[129] determined that broader bandwidth sources, with correspondingly shorter coherence lengths, improve image contrast. However, due to speckle noise, improvements in resolution are less obvious. A reduction in the coherence time from 50 to 16 fs does not change the nature of the speckle because during the detection time window, several cycles of the center optical frequency are still detected.

A study performed using high-frequency ultrasound compared various high-frequency transducers with achievable resolution[21]. At each resolution, the smallest resolvable tissue structure or cell was identified. The results are found in Table 4-4. Although acoustical properties of cells at these frequencies may permit individual cells to be resolved, this does not necessarily imply the same would hold true for optical resolutions. However, this study provides approximate resolutions needed for cellular imaging. This study therefore suggests that OCT resolutions of 5 μm may be sufficient to image cells 20-30 μm in diameter.

TABLE 4-4: High-frequency ultrasound imaging of human cell structure[21].

Frequency	Resolution	Observations
100 MHz	10 μm	macro cell structure
200	5	myocytes (20-30 μm)
400	2.5	lymphocytes (10-12 μm)
600	1.7	myofibrils (1.2 μm)

The *Xenopus* developmental animal model was selected because it is relatively easy to care for and handle. This model also provides a variety of cell-types with high mitotic indices. Many of the cells observed were as large as 100 μm in diameter, but ranged in size down to dimensions below the resolution of this OCT system. Images of various mesenchymal cells sizes are shown in Figure 4-22. The Cr^{4+}:forsterite laser was used for imaging. Axial and transverse resolutions were 5 and 9 μm respectively. These images provide an evaluation of cell size limits for future human investigations. Cells as small as 15 μm in diameter could be imaged with this OCT system. The size of most malignant cells in humans varies dramatically, showing an approximate correlation with the degree of differentiation. As a general rule, cell dimensions found in human neoplasias are typically in the range of 10-40 μm and therefore, similar in size to the cells imaged in this animal model. With low-grade dysplasias, cell size tends to be smaller and will be more difficult to resolve with OCT at 5 μm resolution.

The use of broader bandwidth laser sources at other wavelengths in the near-IR can be used to increase image resolution. Shorter coherence length laser sources have been used to achieve higher axial resolutions[88,89,174] on the order of 2 to 4 μm. OCT can be performed using a high numerical aperture lens to achieve high transverse resolutions, as in confocal microscopy, at the expense of reducing the depth of field[117]. With these higher resolutions, *in vivo* imaging of individual human cells may be possible.

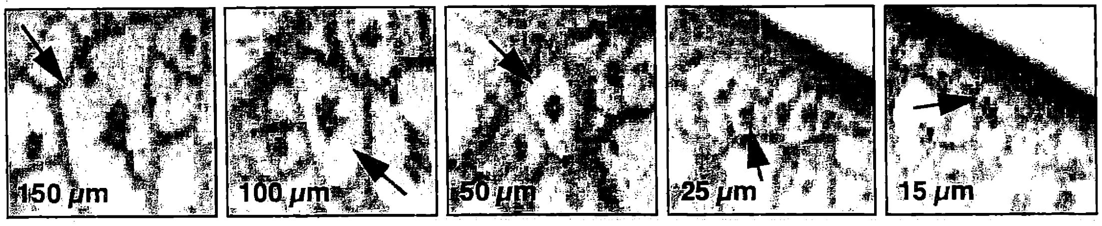

FIGURE 4-22: *In vivo* cell sizes imaged with OCT. Dimensions refer to diameter of cell indicated by the arrow.

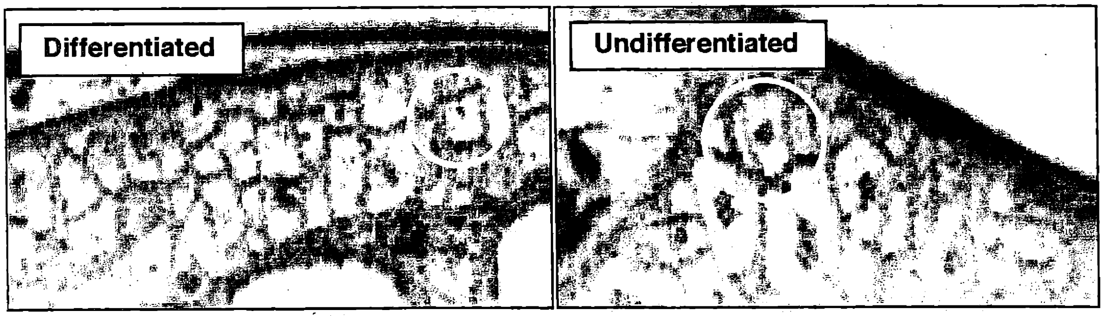

FIGURE 4-23: Differentiated and undifferentiated cells. Encircled cells represent two states of cellular differentiation. Differentiated cells have small nuclear-to-cytoplasmic (N/C) ratios whereas undifferentiated cells have larger N/C ratios.

Cellular imaging in *in vivo* human tissue may not be absolutely necessary to extract useful information regarding the state of differentiation of the cells within the tissue. The nuclear-to-cytoplasmic (N/C) ratio of a cell is a histopathological indicator of the state of differentiation. Cells with high N/C ratios are less differentiated often indicating a high degree of cellular division or rapid tumor growth. In addition, the degree of pleomorphism, the variation of differentiated and undifferentiated cells within a tissue, can indicate possible early neoplastic changes. Examples of these two types of cells are shown in Figure 4-23. The images shown were acquired from regions that, at this developmental stage, are considered differentiated and undifferentiated[151]. However, no molecular techniques were performed to validate the precise state of cell differentiation. Area measurements of the nucleus and cytoplasm were taken from each image using Image 1.60 (NIH). The comparison is shown in Table 4-5. The left image in Figure 4-23 was acquired from a more differentiated region of the *Xenopus* ventral membrane. The N/C ratio and the degree of pleomorphism is low compared to the undifferentiated image on the right, which was acquired from a rapidly developing region near the dorsal neural tube. In human cells, the N/C ratio approaches 1:1 for undifferentiated cells. The larger N/C ratio subsequently implies less cytoplasm which result in higher scattering coefficients. Studies by Liu, *et. al.*[171] have shown that a 100 nm decrease in the radius of a cell will affect the reduced scattering coefficient by as much as 37%. This indicates that changes in cell size or N/C ratios may be detectable using OCT.

TABLE 4-5: Comparison of differentiated and undifferentiated cell area measurements obtained from images in Figure 4-23.

	Differentiated cells	**Undifferentiated cells**
Nuclear area	small - 216 μm^2	large - 832 μm^2
Cytoplasmic area	large - 7488 μm^2	small - 12012 μm^2
Nuclear:cytoplasm ratio	low - 1:35	high - 1:14
Pleomorphism	low	high

Current subcellular imaging of developing *Xenopus* mesenchymal cells has helped establish necessary protocols for future *in vivo* cellular imaging in humans. The dynamic nature of living cells requires a means of tracking cells in tissue. For these experiments, three-dimensional OCT imaging was performed over time to enable subtle cell movements to be recorded within the acquired volume. A series of 2-D OCT cross-sectional images were acquired at spacings that ensured oversampling in the third dimension. Hence, the nuclei of the cells were imaged in at least one of the 2-D images contained within the 3-D volume. Such 3-D imaging may be necessary in humans. However, high-speed imaging at cellular resolutions may permit real-time tracking of a cell by positioning the OCT imaging plane at arbitrary angles. The ability to position the OCT imaging plane at arbitrary angles is advantageous especially when cell division is to be observed. The division of a parent cell into two daughter cells may not always occur in the same OCT imaging plane.

Precise image registration with histology is more problematic at the cellular level. The comparison of *Xenopus* cardiac structures in Figure 4-7 and mesenchymal cells in Figure 4-24 represents excellent correlation at the cellular level. Such correlations are difficult considering that cells may divide, enlarge, and migrate between the time the cells are imaged and the time the specimen is euthanized and fixed for processing.

4.5.2 *In Vivo* Imaging

Although previous studies have demonstrated *in vivo* OCT imaging of tissue morphology, most have imaged tissue at ~10-15 μm resolution which does not allow differentiation of cellular structure. The *Xenopus laevis* (African frog) tadpole was used to demonstrate the feasibility of OCT for *in vivo* cellular and subcellular imaging. The ability of OCT to identify the mitotic activity, the nuclear-to-cytoplasmic ratio, and the migration of cells was evaluated. OCT images were compared to corresponding histology to verify identified structures. These results have implications for OCT imaging of *in vivo* cellular morphology which, on extension to humans, could represent a powerful tool for the early evaluation of neoplastic changes.

Specimens ranged in age from 14-28 days (Stage 25-30). Drops of housing-tank medium were placed over the specimen at 5 minute intervals to prevent dehydration during imaging. Multiple two-dimensional cross-sections (900 x 600 μm, 300 x 300 pixels) were acquired perpendicular to the antero-posterior axis. Fifteen two-dimensional cross-sections acquired at 5 μm intervals were assembled to produce a 3-D data set. Three-dimensional volumes were acquired every 10 min from the region posterior to the eyes and lateral to the neural tube of the specimen.

Immediately following image acquisition, the location of the image planes was marked with India ink for registration between OCT images and histology. Specimens were euthanized by immersion in 0.05% Benzocaine for 1 hr. and then placed in a 10% buffered solution of formaldehyde for standard histological preparation. Histological sections, 5 μm thick, were sectioned and stained with hematoxylin and eosin for comparison with acquired OCT images. Correspondence was determined by the best match between OCT images and light microscopy observations of the histology. Images were processed using IP Lab 3.0 (Signal Analytics) on a Power Macintosh 9500/200. The 3-D volumes were analyzed to identify individual cells and track these cells within the acquired volumes over time. Cell position was determined by measuring distances from two internal reference points, the neural tube and the outer membrane.

A comparison between OCT images and corresponding histology is shown in Figure 4-24. The comparison between Figure 4-24A and B confirms the presence of multiple nuclei and cell membranes. The seemingly wide cell membranes in the OCT images are actually composed of membranes and extracellular matrix. The variation in correspondence between the OCT image and histology in Figure 4-24A and B is likely due to small angular deviations in the histological sectioning plane or cell movement prior to fixation. The OCT image in Figure 4-24A illustrates cells with varying size and nuclear-to-cytoplasmic ratios. Based on image measurements, cells as small as 15 μm in diameter can be imaged. An enlarged OCT image of a dividing cell is shown in Figure 4-24C with corresponding histology in Figure 4-24D. Two distinct nuclei are clearly shown. To the right of the nuclei, the membrane has begun to pinch in. The OCT image in Figure 4-24E demonstrates the high backscatter observed from melanin contained within neural crest melanocytes and tissue structures. Two melanocytes located within the superficial membrane are indicated by black arrows while a melanin layer from the pigmentation pattern is indicated by the white arrow. The corresponding histology in Figure 4-24F verifies these observations.

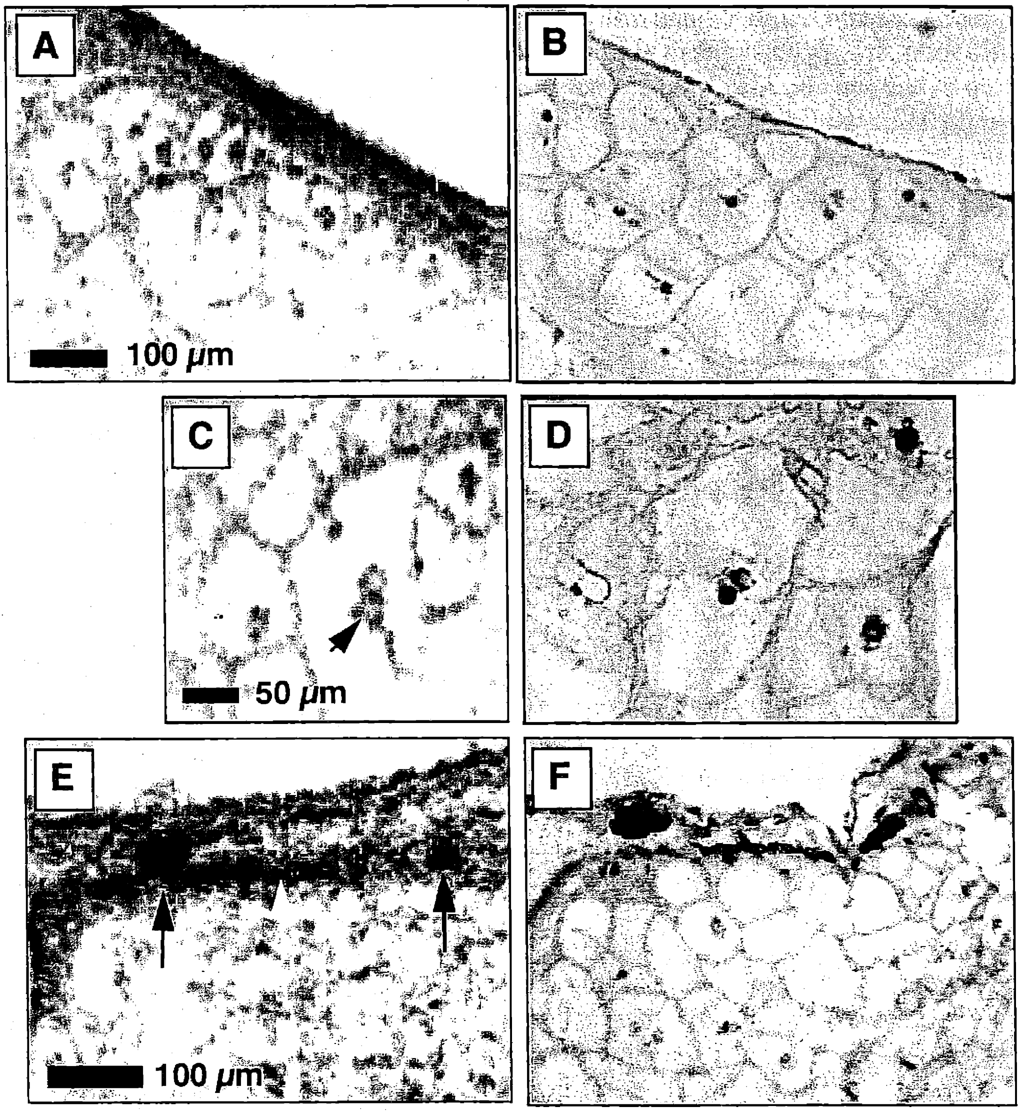

Figure 4-24: Cellular histological correlation. A-D) *Xenopus* mesenchymal cells, E,F) *Xenopus* melanocytes (black arrows) and pigmentation pattern (white arrows).

4.5.3 Cell Mitosis

Mitosis is the process by which a parent cell replicates DNA and physically divides into two daughter cells. This process contributes to the growth of an organism and the differentiation of progenitor cells into specific tissue types. Abnormal mitotic activity can result in unregulated growth, poor differentiation, and the growth of neoplasms. The ability to assess the mitotic stage of cells, *in vivo*, and to determine their state of differentiation will provide key diagnostic potential for the early detection of neoplasms in humans. The cell cycle is diagrammed in Figure 4-25.

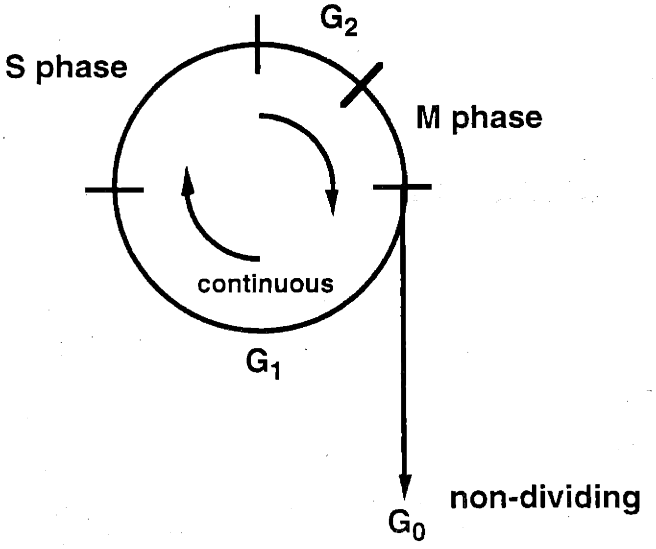

FIGURE 4-25: Cell cycle diagram.

The cycle is divided into four segments. During the S phase, synthesis of nuclear DNA occurs. The M phase represents actual cell division or mitosis. The synthesis and mitosis phases are separated by gap phases (G_1 and G_2) which provide additional time for cell growth. The G_1 phase can be very long depending on the age of the specimen and the local cellular environment. The G_2 phase serves as a safety gap ensuring DNA replication is complete before beginning to divide. The complete cell cycle, or mitotic index, can occur as rapidly as 8 min in developing embryos or as slowly as days to weeks in developed tissue. Cells may enter into a G_0 phase which is a resting state that can last for years. The mitosis portion of the cell cycle is when actual cell division occurs and is further broken into phases as shown in Figure 4-26.

Mitosis begins in interphase when chromosomes are decondensed. This is followed by prophase when chromosomes condense and separate chromatids may become visible. In metaphase, the spindle is formed which will function to separate the chromosome pairs. Centromeres divide in anaphase and in telophase, the nuclear membranes reform, microfilaments contract, and the two daughter cells pinch apart.

In order to confirm the ability of OCT to identify cell division, a sequence of OCT images following the mitotic activity of a single cell is shown in Figure 4-27. A number of mesenchymal cells are observed within each image. These undifferentiated cells range in size from 100 μm down to sizes below the current resolution of OCT. Cell nuclei and cell membranes are readily apparent as regions of high backscatter

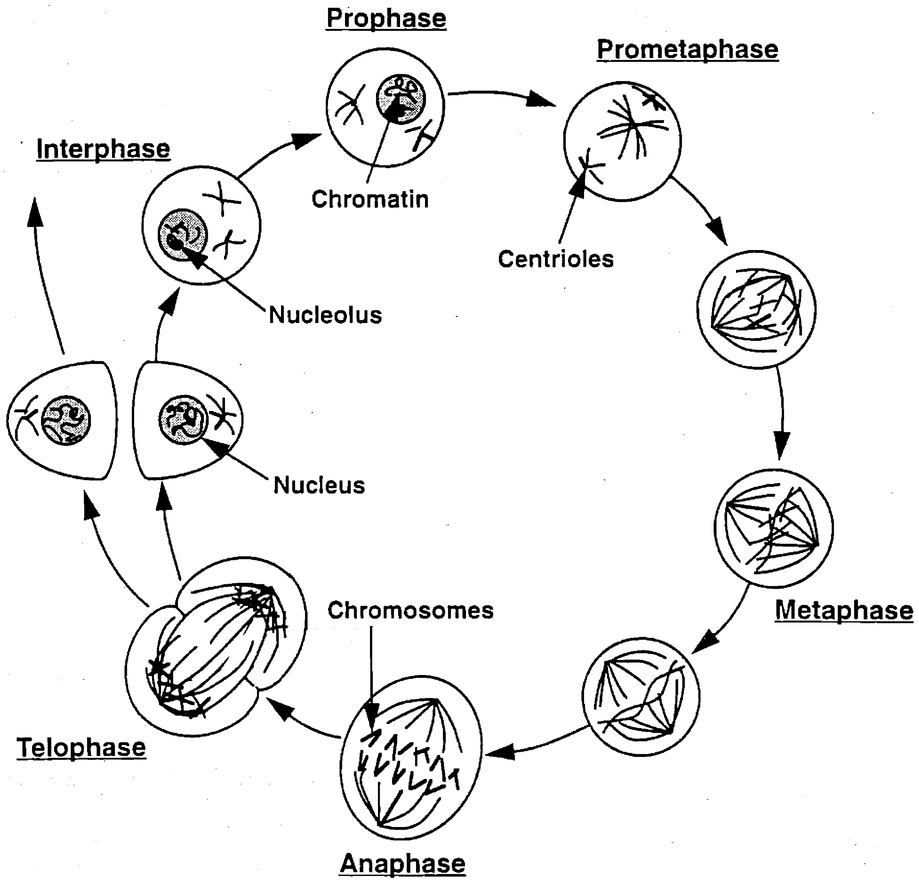

FIGURE 4-26: Cell mitosis phases[175].

compared with the low backscattering cytoplasm. A number of cells show sub-nuclear morphology such as the regions of increased optical backscatter within the nucleus in Figure 4-27A. One possibility is that these are regions of varying chromatin concentration, indicative of high mitotic activity.

Within each image, cells can be found in various stages of mitosis and exhibit a high degree of pleomorphism. Mitotic activity of one parent mesenchymal cell and the migration of the two daughter cells is shown in the sequence. The parent cell (arrow) in Figure 4-27A is in telophase and the chromosomes appear to have reached the mitotic poles. The membrane in the upper left of this cell has begun to pinch in. Ten minutes later, in Figure 4-27B, there is more distinct separation and the appearance to two adjacent nuclei. After an additional 10 minutes, the two daughter cells in Figure 4-27C have a distinct membrane separating them. The remaining figures (D-F) show the increasing separation of the nuclei and the growth in cell size.

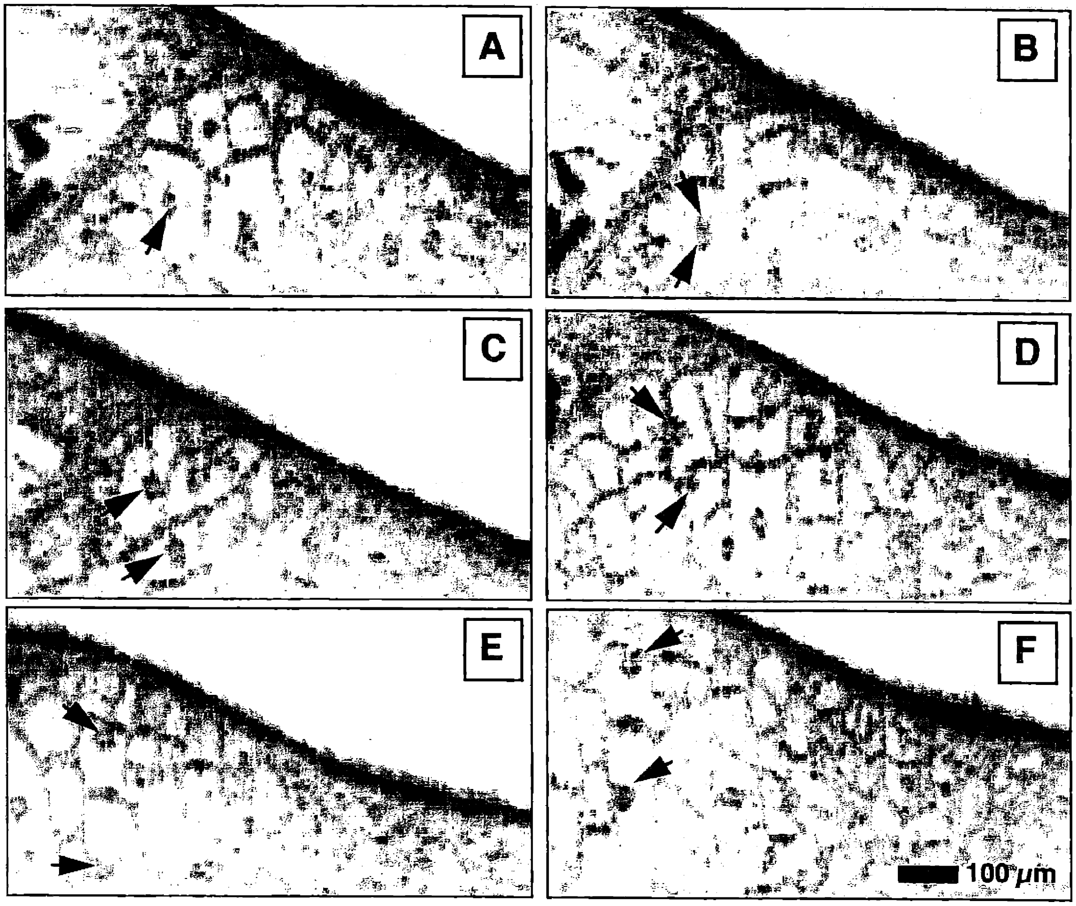

FIGURE 4-27: OCT imaging of *Xenopus* mesenchymal cell mitosis. Parent cell indicated by the arrow in A undergoes mitosis and divides into two daughter cells indicated by the two arrows in B-F. Following cell division, daughter cells migrate apart and increase in size, preparing for subsequent cell division. Images were from 3-D data sets acquired at 10 min intervals.

4.5.4 Cell Migration

Cell migration, like mitosis, has a positive role in development as well as a negative role in the spread of neoplasms. The capability of monitoring cell migration through an organism would be a powerful tool in a variety of developmental and molecular models and may have clinical applications in oncology. In developing embryos, neural crest cells originate from the newly formed neural tube and migrate to differentiate into cardiovascular and epidermal tissue. In neoplasms, tumor cells will migrate and penetrate tissue contributing to the growth and spread of the tumor. When a tumor metastasizes, the spread of tumor cells is over greater distances usually through the circulation. Tumor cell migration still occurs while the cell enters and exits the blood stream.

The neural crest cells of the developing embryo migrate along two distinct pathways as shown in Figure 4-28. Progenitor cells which migrate to the dermal layers follow Path 1 while cardiac progenitor cells follow Path 2. The neural crest cells of Path 1 are also called melanocytes due to their high concentration of melanin. These cells are also responsible for establishing the pigmentation patterns of the organism. Melanin has a high index of refraction compared to surrounding tissue structures and therefore results in higher optical backscattering in OCT images. This facilitates tracking melanocytes deep within scattering specimens.

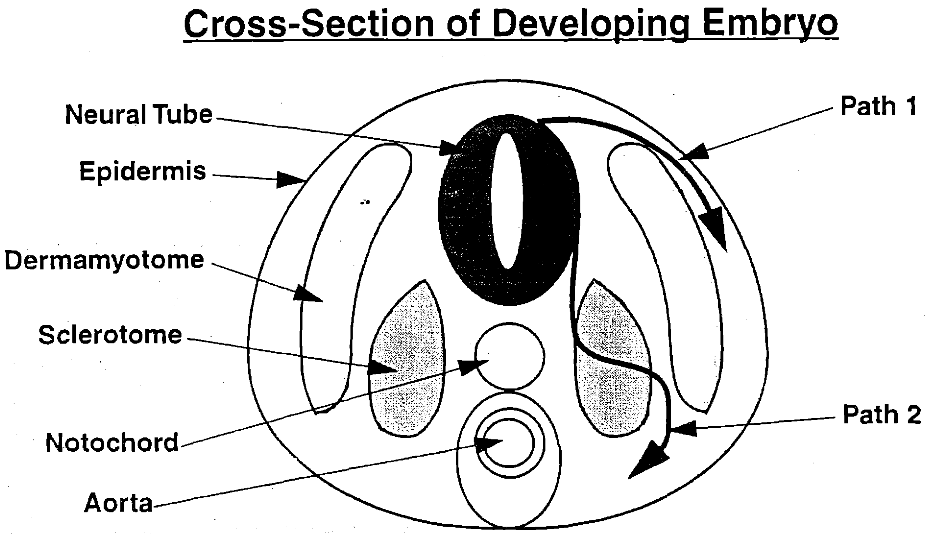

FIGURE 4-28: Pathways of neural crest cell migration[175]. Cells (melanocytes) migrating along Path 1 travel near dermal skin layers to establish the pigmentation pattern in the skin. Cells migrating along Path 2 travel from the dorsal neural tube to differentiate into cardiac and vascular tissues.

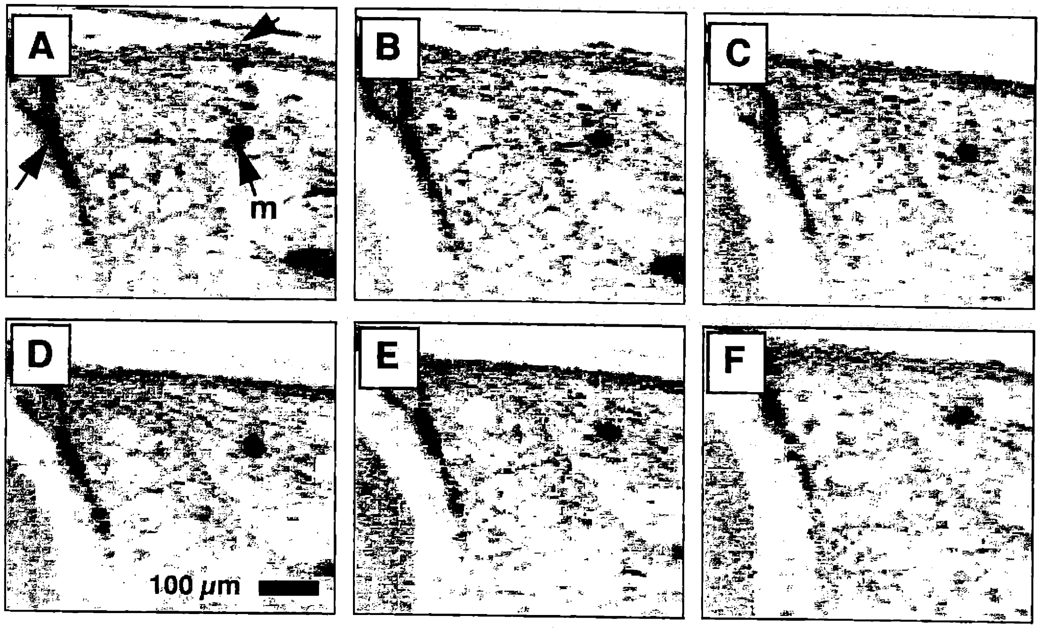

FIGURE 4-29: OCT tracking of neural crest cell (melanocyte) migration. A single migrating melanocyte (m) was tracked by acquiring 3-D data sets at 10 min intervals. Unlabeled arrows in A indicate internal points from which migration measurements were referenced.

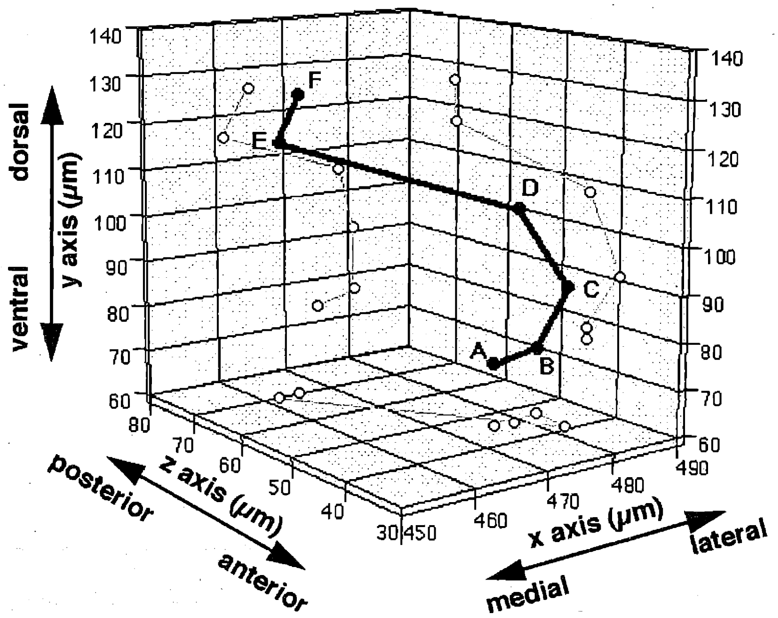

FIGURE 4-30: Three-dimensional plot of neural crest cell (melanocyte) migration. Labelled data points refer to images in Figure 4-29 from which X,Y measurements were obtained. Z measurements were obtained from position of OCT image plane within 3-D data set.

The ability of OCT to track individual cell movement is illustrated in Figure 4-29. A neural crest melanocyte (m) in Figure 4-29A, was imaged at 10 minute intervals by acquiring three-dimensional volumes containing the cell. From each volume, the 2-D cross-section acquired through the center of the cell is shown in Figure 4-29. Because of slight changes in specimen movement over time, internal morphological features and markers within the image were used as reference points. The top arrow in Figure 4-29A indicates the outer membrane of the specimen while the left arrow indicates a melanin layer covering the dorsal neural tube. Each was used as an internal reference point.

A three-dimensional plot of cell position within the specimen is shown in Figure 4-30. The X and Y Cartesian coordinates were determined from the image measurements obtained in Figure 4-29A-F. The Z coordinate was determined from the cell movement between planes of the three-dimensional volume. The points labelled A-F correspond to the images shown in Figure 4-29. The cell migration between each labelled point corresponds to 10 minute intervals. This plot indicates the cell migrated along a curved path progressing first dorsolaterally and then dorsomedially. Projections of the migration are also shown in Figure 4-30 in the transverse, coronal, and sagittal planes. The likelihood of specimen motion artifact within this data is high. Measured cell migrations of 20-60 µm were not significantly larger than the resolutions of the system. Although the specimen was repeatedly hydrated, drying and motion artifacts are possible. The movement in Figure 4-30 from point D to E is large and inconsistent compared to the movements during other intervals, suggesting a possible artifact. However, these results demonstrate a general protocol for tracking cell migration. More definitive results are possible with higher image resolutions and longer tracking times.

4.6 Significance for Developmental Biology

This research represents the fundamental demonstration of OCT in the field of developmental biology and microscopy. These results are significant because they illustrate OCT as a research microscopy technique for observing the *in vivo* morphological expression of the genetic program. With rapidly advancing molecular biology techniques, scientists can site-specifically modify the genomes of developmental biology animal models. OCT is useful to observe not only normal development, but also abnormal development and can characterize the morphological changes that result from mutations. OCT fills a niche between high-resolution light and confocal microscopy and the larger, more clinical modalities such as ultrasound, CT, and MRI. The 5-15 µm image resolutions are ideal for developing specimens a few millimeters in size. The size of these specimens is often too large for confocal and too small for MRI microscopy.

The cross-sectional imaging in non-transparent embryos at near-histological resolutions enables repeatable *in vivo* imaging without having to sacrifice the specimen. This is particularly useful in established mutant specimens which are often difficult to produce and limited in number. The non-contact, noninvasive imaging of OCT can be used to track the development of single specimens over time. The use of high-speed OCT imaging of cardiac structures enabled functional imaging to be performed in these specimens where previously this had been unattainable. OCT imaging will enable developmental research on genes which are expressed not only morphologically, but also functionally as in the cardiovascular system.

4.7 Implications for Human Tissue

Subcellular imaging was demonstrated in a living, nontransparent, organism with OCT. This suggests a feasibility for assessing neoplastic changes in humans. The observations of greatest clinical relevance were the ability to identify active cell division and assess nuclear-to-cytoplasmic ratios, two important markers of malignant transformation. Both observations were correlated with histopathology. In addition, to further confirm the ability of identifying cell division, a single cell was followed through a single division cycle and changes in morphology were noted. A change in the backscattering intensity from nuclei was also noted as a function of time. This is postulated to represent a change in the concentration or packing of chromatin, which may be of diagnostic relevance.

The ability to track single cells as they migrate through tissue has future clinical relevance. Following malignant cells *in vivo* in animal models may help researchers understand the mechanisms of cancer. In many cases, the resection of tumors and tumor cells must be complete, as even single cells may continue to divide and produce a second tumor. OCT imaging at the cellular level may have the potential to identify tumor cells which have migrated away from the central tumor. The first stage of tumor metastasis is the penetration of tumor cells through the basement membrane of epithelial tissue. This process may be monitored *in vivo* to further understand mechanisms and characterize treatment effectiveness.

The investigation of developmental biology animal models using OCT serves as a clear demonstration for imaging tissue microstructure. Imaging at high cellular resolutions in these models identifies the future challenges for imaging at the cellular level in human tissue. With this fundamental information, OCT images can be characterized and OCT imaging techniques can be applied toward surgical diagnostics.

Chapter 5

Image Characterization for Surgical Diagnostics

5.1 Introduction

The OCT images of biological tissue can be used to obtain diagnostic information relevant to surgical applications. Understanding the propagation, absorption, and scattering of near-infrared light in biological tissue will permit further insight into how OCT images represent tissue microstructure. The use of contrast-enhancing agents, either endogenous or exogenous, may improve discrimination of tagged structures. OCT can be configured to perform Doppler velocimetry for imaging moving backscatterers such as red blood cells. This diagnostic technique would enable assessment of tissue perfusion or detection of subsurface vessels during surgery. This chapter will also examine three-dimensional OCT imaging and the representation of 3-D data sets. Viewing OCT data in 3-D provides improved spatial orientation that can assist surgeons in localizing structures. Finally, signal processing techniques are demonstrated which may improve the quality of OCT images and segment selected morphological features for future computer-assisted diagnostics.

5.2 Optical Properties of Tissue

The use of longer wavelengths (1300 nm) for OCT imaging was found to improve imaging penetration in highly-scattering tissue compared to the 800 nm wavelength used for initial studies in ophthalmology[70]. This strong dependence on wavelength can be noted if one assumes that scattering is tissue is due to particles much smaller than the wavelength, called Rayleigh scattering[176]. The total scattered power is proportional to the fourth power of the wavenumber or inversely proportional to the fourth power of the wavelength[106]. Hence, longer wavelengths are scattered less than shorter wavelengths. The scattered power is also proportional to the sixth power of the radius of the scatterers within the Rayleigh limit. In human tissue, Rayleigh scattering occurs for small particles or molecules. However, Mie scattering, scattering from particles on the order of the wavelength[173,177], is dominant in human tissue[178]. Detailed descriptions of both Rayleigh and Mie scattering are beyond the scope of this thesis.

For propagation through biological tissue, the near-infrared wavelengths lie within the "biological window" in tissue[179] as illustrated in Figure 5-1. At shorter wavelengths, absorption is due to the protein and DNA within cells. Hemoglobin and melanin dominate absorption in the visible and near-IR wavelengths while at longer wavelengths, water absorption is prominent. Biological tissue is modeled as having

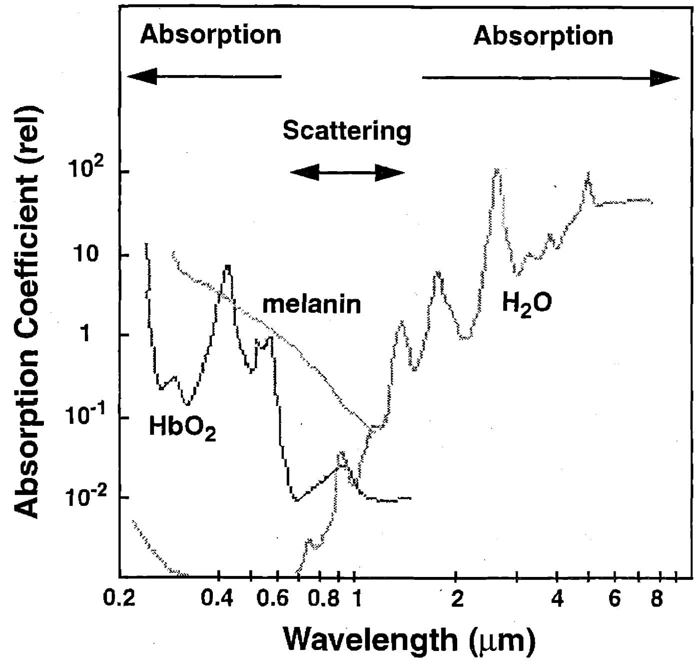

FIGURE 5-1: Wavelength dependence of absorption and scattering in biological tissue[180].

a 75% water content making water absorption at longer wavelengths a significant limiting factor. The near-IR wavelengths (800-1500 nm) lie within a region of minimum absorption where within this biological window, scattering processes dominate.

The absorption and scattering properties of tissue are defined by the absorption and scattering coefficients, μ_a (cm^{-1}) and μ_s (cm^{-1}), respectively. These coefficients are based on the transmission of light through a pathlength z in tissue

$$P_a = e^{-\mu_a z} \qquad P_s = e^{-\mu_s z} \tag{5-1}$$

where $\mu_a z$ and $\mu_s z$ are << 1 and $P_a P_s$ represents the probability that a photon will travel through a pathlength z and not interact with the tissue. The total attenuation coefficient μ_t is expressed as the sum of the absorption and scattering coefficients

$$\mu_t = \mu_a + \mu_s. \tag{5-2}$$

Alternatively, these coefficients may be used to express the mean free path (MFP) a photon travels before interaction with the tissue occurs. These are given by the reciprocal of the coefficients with units of centimeters

$$l_a = \frac{1}{\mu_a} \qquad l_s = \frac{1}{\mu_s} \qquad l_t = \frac{1}{\mu_t}. \tag{5-3}$$

In biological tissue, and particularly at near-IR wavelengths, scattering dominates over absorption ($\mu_s >> \mu_a$)[181]. Multiple scattering events will likely occur before absorption. When a scattering event occurs, the function which describes the probability of photon deflection is dependent on the deflection angle θ and the azimuthal angle ϕ. If one assumes a symmetry in the azimuthal plane, then only a θ dependence exists. An average dimensionless parameter g is used to characterize the scattering event. The parameter g is defined as

$$g = \langle \cos\theta \rangle = \int_{-1}^{1} P(\cos\theta)\cos\theta d[\cos\theta] \qquad (5\text{-}4)$$

where $P(\cos\theta)$ is the probability of a photon scattering at an angle θ and

$$\int_{-1}^{1} P(\cos\theta) d[\cos\theta] = 1. \qquad (5\text{-}5)$$

In tissue, scattering heterogeneities range from macromolecules (< 10 nm) to cellular organelles (≈ 100 nm) to cells (> 10,000 nm). Structures on the order of the wavelength (1000-1500 nm) are the strongest scatterers responsible for forward-directed Mie scattering. Structures much smaller than the wavelength are responsible for isotropic ($g = 0$) Rayleigh scattering. For the human dermis, the g in Mie scattering is ≈ 0.92 at 632 nm and about 10% of the scattering is Rayleigh[182,183].

The g parameter is incorporated with μ_s to define the reduced scattering coefficient

$$\mu'_s = \mu_s(1-g) \qquad (5\text{-}6)$$

which weights scattering with the anisotropy of the tissue. For high g values ($g = 0.92$), the reduced scattering coefficient is only 8% of μ_s.

The absorption and scattering coefficients are related to both the density ρ and cross-sectional area σ of the absorbers and scatterers within the tissue. These are related by

$$\mu_a = \rho_a \sigma_a = \rho_a \zeta_a A_a \qquad (5\text{-}7)$$

and

$$\mu_s = \rho_s \sigma_s = \rho_s \zeta_s A_s \qquad (5\text{-}8)$$

where A is the effective cross-sectional area and ζ is an efficiency factor. These equations illustrate that scattering or absorption will increase if the density or cross-sectional area increases. Light propagating through tissue is attenuated by absorption and scattering according to Beer's Law

$$E(z) = E_0(1 - r_{spec})e^{-(\mu_a + \mu_s)z} \qquad (5\text{-}9)$$

where E(z) is the fluence rate (W/m^2) of light at position z in the tissue, E_0 is the initial fluence, and r_{spec} is the Fresnel specular reflection at the surface. This exponential attenuation is observed in OCT images as the progressive loss of signal with increasing depths of penetration. The rate of attenuation observed is a factor of 2 times faster than given in Equation (5-9) because of round-trip propagation into and out of the tissue.

The OCT beam propagating through tissue will interact with refractive-index inhomogeneities which can be treated as individual particles with isotropic backscattering cross-sections. The focused illumination from the OCT light source is re-radiated as an approximately spherical wave and passes back through the imaging system where it interferes with the reference arm wave. Single backscatter theory assumes that the incident beam interacts with only one particle within the tissue. In this case, the signal at the detector would be a sum of currents produces by the individual particles. Despite the highly scattering tissue medium, a small probability exists that a single backscattering event will occur. This was given by P_s in Equation (5-1). A theoretical model for OCT of heterogeneous tissue has been developed by Schmitt and Knuttel[129]. Three reference planes are established. A lens plane at $L = 0$ contains the microscope objective which focuses the OCT beam onto the specimen. A tissue surface plane is located at $L = d$, and a backscatter plane at $L = d + nz$ contains the backscattering particle. If one lets R equal the radius of a collimated Gaussian beam and $|g(\tau)|$ equal the Gaussian function defined by

$$|g(\tau)| = \exp\left(\frac{-\tau^2}{\tau_c^2}\right) \qquad with \qquad \tau_c \approx \frac{0.44\lambda^2}{c\Delta\lambda} \tag{5-10}$$

then according to Schmitt and Knuttel[129], the amplitude of the forward-propagating unscattered optical field in the backscatter plane of the particle is given by

$$U_s(\vec{r}, L) = \frac{\sqrt{P_{samp}}}{\pi}\sqrt{\frac{k}{2LR}}|g(\tau)|\exp\left(\frac{-\mu_s z}{2}\right)\exp\left[i\frac{k}{2L}(\vec{r}-\vec{p})^2 - i\frac{k}{2nf}\vec{p}^2 - \left(\frac{\vec{p}}{2R}\right)^2\right]. \tag{5-11}$$

The vectors **p** and **r** are the field vectors in the lens and backscatter planes, respectively. The variable P_{samp} is the total power in the sample arm, $L = d + nz$ is the distance from the lens to the particle, and f is the focal length of the lens. If the small probability, P_s, of a single backscatter event is considered, then the sample-arm field propagated back to the lens is given by

$$U_s(\vec{p}, 0) = \frac{U_s(\vec{r}, L)\sqrt{\sigma_b}}{L}\exp(-\mu_s z)\exp\left[i\frac{k}{2L}(\vec{r}-\vec{p})^2 - i\frac{k}{2nf}\vec{p} - ikL\right] \tag{5-12}$$

where σ_b is the backscattering cross-section of the particle. The back-propagated field in the reference arm with a power P_{ref} is

$$U_r(\vec{p}, 0) = \sqrt{\frac{P_{ref}}{\pi R}}\exp\left(\frac{-\vec{p}^2}{2R^2} - i\frac{k}{2f}\right) \tag{5-13}$$

which can be interfered with the field from the sample arm in Equation (5-12). For a single backscatter event, phase information in the cosine term of the autocorrelation function is preserved. Previous work has established imaging depth limits for which single backscattering will occur in highly scattering tissue. A transillumination OCT system using a femtosecond laser demonstrated that for unscattered light, the maximum sample thickness was

$$t_s = \frac{1}{\mu_t}\ln\left(\frac{E}{2h\nu}\right) \tag{5-14}$$

where E/hv is the number of incident photons[184,185]. Using single backscattering theory in heterodyne detection as outlined above, an imaging depth limit with a SNR = 1 was determined as

$$t_s = \frac{1}{2\mu_t}\left(\frac{\pi^2}{4n_t^2}M^2\right) \tag{5-15}$$

where n_t is the index of the tissue and M is the magnification of the imaging lens[117]. For both of these limits, single-backscattering would occur up to 15-20 MFPs. These limits, however, neglect any contribution multiple scattering might have on the detected signal.

As the OCT sample arm beam propagates deeper into tissue, the likelihood of multiple scattering increases. Because scattering particles in tissue are roughly equal to or larger than the wavelength, multiple scattering will be in the forward direction. The loss of light, however, is minor because most of the light is forward scattered through a narrow angle. The overall divergence of the beam due to multiple scattering, in both the forward- and back-scattered directions, will induce a loss of transverse coherence at the detector aperture.

This loss of coherence can be investigated with the mutual coherence function which describes the spatial and temporal fluctuations of two functions at positions $\mathbf{r}_1$ and $\mathbf{r}_2$:

$$\Gamma(\vec{r}_1, \vec{r}_2, \tau) = \langle U^*(\vec{r}_1, t)U(\vec{r}_2, t+\tau)\rangle . \tag{5-16}$$

Normalized to the intensities at each point, the complex degree of coherence is obtained

$$\gamma(\vec{r}_1, \vec{r}_2, \tau) = \frac{\Gamma(\vec{r}_1, \vec{r}_2, \tau)}{\sqrt{I(\vec{r}_1)I(\vec{r}_2)}} . \tag{5-17}$$

The above function will vary between 0 when the two points are independent with randomly fluctuating phases to 1 when the two are completely correlated. Instead of being expressed in terms of time delays, the mutual coherence function can also be written in terms of position z in space

$$\Gamma(\vec{r}_1, \vec{r}_2, z) = \langle U^*(\vec{r}_1)U(\vec{r}_2)\rangle . \tag{5-18}$$

The squared detector current in terms of the mutual coherence functions from both the reference and sample arms can be written as

$$I_D^2 = 2\eta^2 q^2 |g(\tau)|^2 \int\int \Gamma_r(\vec{r}_1, \vec{r}_2, z)\Gamma_s(\vec{r}_1, \vec{r}_2, z)d\vec{r}_1 d\vec{r}_2 \tag{5-19}$$

where η is the quantum efficiency of the detector, q is the electronic charge, and $|g(\tau)|$ is the Gaussian function defined in Equation (5-10). The photocurrent generated from the multiply scattered light will retain the cosine phase term as for the case of single-backscattered light. However, the phase term represents a collection of scattering from many particles within the focal volume.

The total signal current at the detector is represented by the sum of the single-backscatter and multiple-backscatter components. Schmitt and Knuttel[129] express this as

$$|I_D(r, z)| = |I_{T, sb}| + \langle I_{T, ms}^2 \rangle^{1/2}. \qquad (5\text{-}20)$$

The first term in the sum is a coherent summation of single-backscattered components from a collection of independent particles within the tissue. The second term is obtained by summing the signal powers of multiple-scattering events from each particle. Because the phases are random, coherent summation is not possible.

Schmitt and Knuttel modeled the contributions from small and large particles using computer simulations[129]. These simulations offer practical insight into the OCT imaging characteristics of tissue. The size distribution of scatterers determines the relationship between attenuation and backscatter of the imaging beam[129]. Therefore, because tissue is composed of a wide size distribution of scatterers, the detected OCT signal is a combination of these two effects. Two different mechanisms are responsible for producing these effects. Small scattering centers are primarily responsible for the backscattered signal with little effect on coherence properties while the larger scatterers are responsible for attenuating the signal. When the contribution of multiple-scattered light exceeds that of the single-backscattered light, contrast in an OCT image is lost. Hence, contrast is best in tissue containing the lowest concentration of large spheres. The loss of image contrast also determines the maximum probing depth. Based on the optical properties of a typical soft tissue with a backscattering coefficient $\mu_b = 0.042$ mm^{-1}/sr, a scattering coefficient $\mu_s = 6.0$ mm^{-1}, and a mean scattering angle $\theta_{rms} = 8°$, a maximum probing depth of 1-1.5 mm was estimated[129]. This corresponds well with imaging depths observed in soft human tissues shown in Chapter 6.

By detecting the envelope of the signal current in Equation (5-20), phase information is lost. However, effects due to speckle are still present. Speckle is the result of multiple-scattering foci that are separated by less than one coherence length. Scattered fields can interfere constructively and destructively with one another at the detector. Within the image, speckle reduces resolution and contrast. Speckle can be reduced by decreasing the coherence time of the source, by low-pass filtering the signal current (which also blurs the OCT image), and by averaging of image data as will be shown in Section 5.6.1.

This model of OCT in heterogeneous tissue offers new insight into the dependency of OCT image characteristics on scatterer size and distribution. However, the model only uses two sphere sizes and is an extreme simplification. This model also does not account for non-random arrangements of scatterers, for light loss due to wide-angle scattering from large tissue structures, or for the effects due to polarization. In spite of these limitations, it provides a fundamental understanding of OCT image characteristics.

5.2.1 Tissue structure

The primary advantage of OCT is the accuracy to which an OCT image correlates with the *in vivo* tissue microstructure. Histological preparations of the imaged tissue are used for comparison. It must be re-emphasized that a thorough understanding of how each technique provides contrast within images is necessary. OCT images are composed of variations in optical backscatter intensity from a light source that has been directed from above the tissue. Contrast is highly dependent on the local absorption and scattering properties of the tissue and within the focal volume. Histological sections, in contrast, are differentially stained to highlight particular features and then viewed with transilluminated white light under a microscope.

The representation of tissue microstructure in OCT images depends largely on the resolution of the system. Because human cell sizes are close to the current resolution of OCT, distinguishing cells is complicated by speckle. To investigate whether small, highly backscattering foci in OCT images could possibly represent cell nuclei stained dark with hematoxylin and eosin (H & E), image processing was performed on a digitized histology image and compared with the corresponding OCT image. The results are shown in Figure 5-2. The initial histology image was from an H & E stained section of human uterus which was digitized with 1 μm resolution. The image is progressively blurred to 20 μm resolution using a 2-D Gaussian noise function. The OCT image of the same tissue and site is shown in the last figure. This was acquired with 6 μm axial and 18 μm transverse resolution. The three-times poorer resolution in the transverse direction is evident from the elongation of regions of high backscatter. The OCT image appears very different from the histology at 20 μm resolution. The dark regions in the histological image represent the dark cell nuclei and are large compared to the backscattering regions in the OCT image. The surface contour of the histological section is relatively smooth compared to the OCT image. The OCT image shows surface collections of fluid, giving the false impression of a smooth surface. This emphasizes the role that tissue fixation may play in tissue. Finally, this example illustrates why OCT images may not directly correlate with histology at the cellular level. The H & E staining of nuclei are responsible for the high contrast in the histology images. This contrast may not be equal to the contrast due to changes in index of refraction in OCT images.

The polarization state of light returning to the interferometer affects the amplitude of the detected signal. This was first characterized using a polarization-sensitive low-coherence reflectometer[186] and later used to image birefringence properties of *in vitro* tissue[187]. A number of biological tissues have regular, repeating structures that are birefringent and can affect the amplitude of the signal. The aligned collagen fibers of the cornea, the retinal nerve fiber layers, and striations of muscle have all have birefringent properties. The birefringence properties can be used to selectively image these regions of tissue.

Twisting the fiber in the reference arm varies the polarization state in this arm which will maximally interfere with the same polarization state returning from the sample. For layers of muscle fibers, this results in increased signal from various birefringent layers of muscle depending on the orientation of the muscle fibers. A demonstration of the effects this has on OCT images is shown in Figure 5-3. The vertical black bar identifies a region of low backscatter which is shifted through the tissue as the polarization state in the reference arm is varied. In addition to varying the polarization state to diagnostically assess tissue structure, loss of birefringent structural properties may be an early indication of tissue damage during thermal laser ablation[187,188].

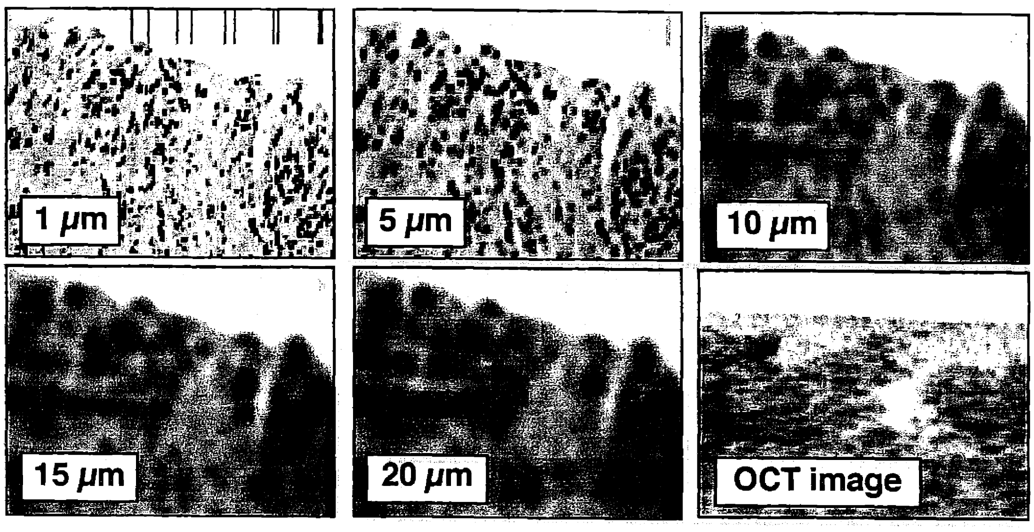

FIGURE 5-2: Progressive blurring of histology image for comparison with corresponding OCT image. Tissue specimen is human uterus. Upper left image is an H&E stain histological section digitized with 1 μm resolution. Image is blurred to 20 μm resolution and compared to the corresponding OCT image. The 18 μm transverse resolution is noticeably worse than the 6 μm axial resolution as evident by the elliptical regions of high backscatter.

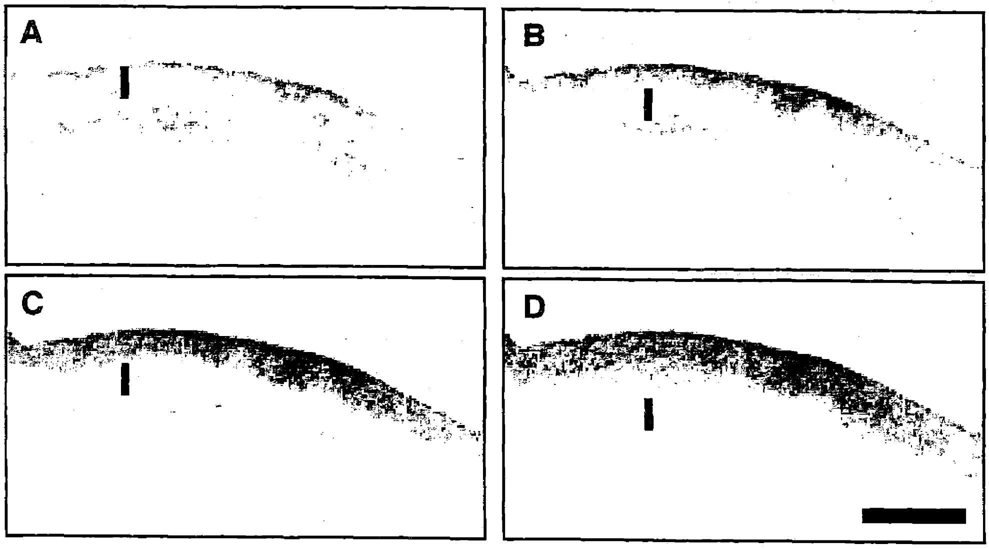

FIGURE 5-3: Birefringent properties of bovine muscle. Vertical bars illustrate region of low-backscatter which was shifted in depth by varying the polarization state of the reference arm. Horizontal bar represents 1 mm.

5.2.2 Image artifacts

In addition to inherent tissue properties which affect the representation of tissue in OCT images, image artifacts can falsely represent tissue morphology. Curved surfaces either at the tissue surface or embedded within the tissue are locations where refraction will occur. In an image, the represented tissue will be angularly displaced from its actual position. This will be clearly demonstrated in Section 5.3.1 where an air-filled microsphere does not appear spherical in the OCT image.

Shadowing by highly backscattering tissue represents loss of signal to positions below. These artifacts are clearly identified as vertical streaks within the image as seen in Figure 4-10 where the highly backscattering pigments of the *Xenopus* retina prevent signal from penetrating deeper into the tissue. The same effect is observed when blood is present during imaging. The highly scattering red blood cells will prevent underlying tissue from being imaged.

All of the tissue imaged for this thesis was either living or maintained fresh in a saline solution. This was an effort to maintain near *in vivo* tissue quality. Fixation of tissue begins by immersion in formalin which is buffered formaldehyde. This solution causes coagulation or precipitation of protoplasmic substances such as proteins, lipids, carbohydrates, and inorganic salts without loss of structural cellular definition. Because this fixation process is well characterized, fresh and fixed tissue were imaged to investigate what affects this process of protoplasmic coagulation has on OCT imaging. Single axial scans were acquired from fresh normal human brain and fresh brain tumor. The tumor was a melanoma which had metastasized to the brain. These axial scans were then compared with scans from the same locations after the tissue had been placed in formalin for 24 h. The comparison of axial scans is shown in Figure 5-4. The fixation of the normal brain tissue resulted in an increase in optical backscatter from the superficial layers of the tissue. Coagulation and dehydration of protoplasmic substances may reduce the density of small scatterers within the tissue thereby increasing the scattering coefficient. The backscatter from the brain tumor, however, showed little change between fresh and fixed tissue. This may be due to the already high optical backscatter contributions from melanin present within the tumor cells or may be due to the high degree of cellularity within the tumor. These factors may be relatively unaffected by the fixation process.

5.3 Image-Enhancing (Contrast) Agents

Inherent contrast within OCT images is sufficient to resolve variations in tissue morphology. However, when a specific tissue structure is to be imaged and that structure is optically similar to surrounding tissue, discrimination will be difficult. This situation has been encountered across all imaging technologies. The use of contrast agents such as iodine in CT, gadolinium in MRI[14], fluorophores in confocal microscopy[32,189,190], and air-filled microspheres in ultrasound[15-17] all improve contrast within images and target specific tissues or sites. The same technique would be beneficial in OCT to specifically label individual cells, such as those within a tumor, or particular tissues such as early dysplastic lesions of the gastrointestinal tract.

The use of fluorophores in confocal microscopy is an extremely sensitive technique. Emitted fluorescence is at a known wavelength permitting complete rejection of background light and a high SNR. This is in contrast to other imaging modalities which must use agents to increase or decreases contrast against a background of noise and image information. OCT is in the latter group. Effective agents must either increase or decrease the local contrast sufficiently to differentiate this region from baseline. This can be done either by affecting the local absorption or scattering properties of the tissue.

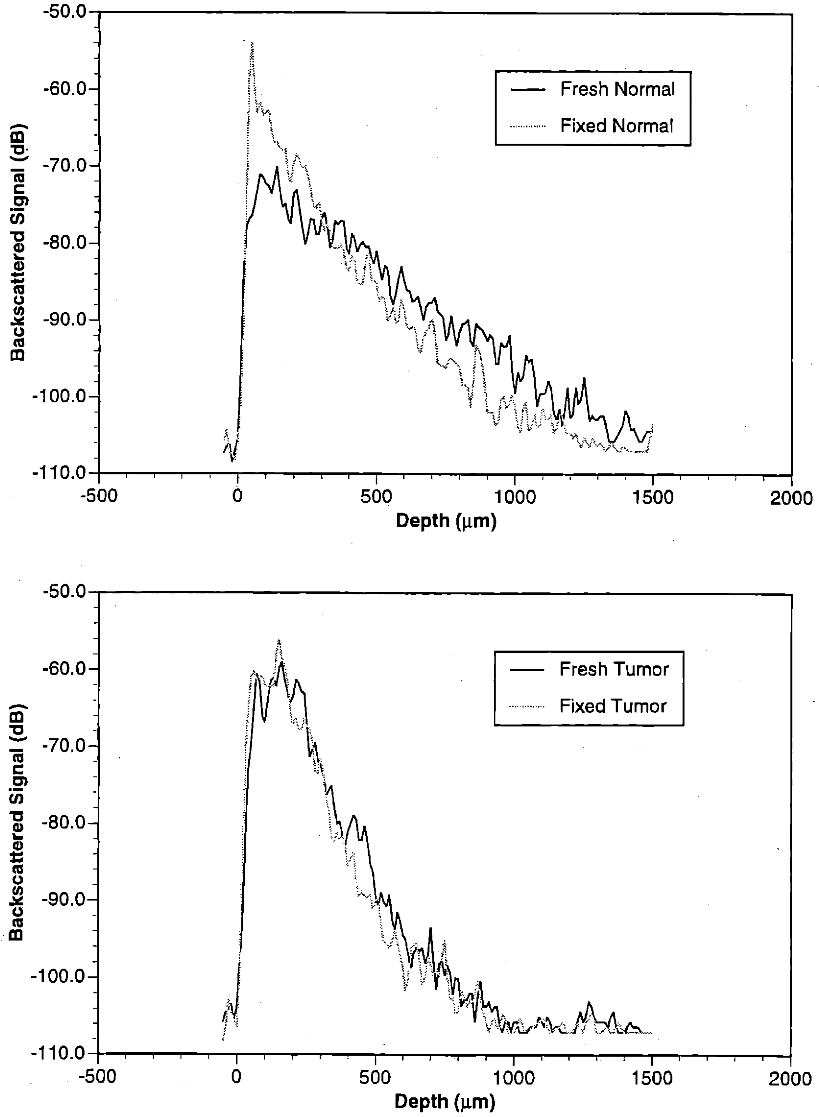

FIGURE 5-4: Comparison of fresh and fixed brain tissue specimens. Axial scans were obtained from the same location on normal brain and brain tumor both for fresh and fixed states.

In theory, there is the potential for developing an OCT molecular probe that would allow cellular movements to be followed on a macro-cellular level. It may be possible to utilize melanin granules or air-filled albumin microspheres to vary the absorption or reflectance properties in labelled cells or tissues. With increasingly more complex molecular biology techniques, genes which produce melanin may be transfected into cell lines to generate melanin-labelled cells. In developmental biology, cell fate and lineage analysis could be performed millimeters deep within *in vivo* or *in vitro* tissue.

5.3.1 Exogenous agents

Exogenous contrast agents are considered foreign to biological tissue. Dyes or stains which selectively adhere to sites can provide contrast against background tissue. Toluidine blue has been used as a means of detecting oral cancers by attaching to rapidly dividing DNA[191]. Discrimination is based on visual appearance following a mouthwash of the dye. The array of fluorescent molecular probes used for confocal microscopy has grown considerably. However, there are currently no probes available which absorb wavelengths above 1100 nm[192]. Current probes would be ineffective for use with the 1300 nm wavelength commonly used for OCT imaging in highly scattering tissue. Several probes, however, are available around 800 nm, the center wavelength for $Ti:Al_2O_3$ KLM lasers and SLDs. Cells labelled with these probes would absorb the incident OCT radiation and reduce the amount backscattered and detected. The extent at which this would provide sufficient contrast remains to be determined.

By varying the local index of refraction within tissue, contrast may be enhanced. This has been demonstrated acoustically in cardiac ultrasonography by the addition of albumin-coated, air-filled microspheres[15]. The air within microspheres provides acoustic impedance variations which are manifested in increased backscatter of ultrasonic waves. Similar principles apply to optical wavelengths and for enhancing contrast in OCT images.

To model this behavior for OCT, air-filled bubbles were created in low-temperature gelling agar. The agar medium permitted the bubbles to remain suspended for extended periods of time during OCT imaging. Bubbles ranging in size from 500 nm to 1 mm were formed by rapidly forcing liquid agar through a syringe and inducing cavitation within the agar. Representative images are shown in Figure 5-5. The bubbles are of varying size. Contrast effects include refraction of the incident OCT imaging beam as well as shadowing below the bubble. If the bubble was imaged in the plane containing the normal surface, then a markedly increased backscatter is observed at both surfaces of the bubble. This is shown by the arrow in Figure 5-5A. The representation of the microbubble on the OCT image is not spherical (Figure 5-5B and C). This is the result of refraction at the gel-air interfaces and the differences in optical pathlengths between the air and agar. The low-backscattering vertical streaks on each side of the microbubble occur when the OCT imaging beam is incident on the sphere at an angle greater than the critical angle. Total internal reflection within the agar directs the beam out of the collection angle of the focusing lens.

Bubbles as small as 10 μm were imaged (arrow, Figure 5-5C) and provided increased contrast. Contrast was diminished, but bubble boundaries were still resolved, when 500 μm of a lipid solution ($\mu_s = 45$ cm^{-1}, $\mu_a = 0.42$ cm^{-1}, g = 0.8) was placed over the suspension. Normal incidence reflections are still prominent (Figure 5-5D). The use of air-filled microspheres may be useful following injection into tissue for a non-hazardous means of identifying tissue planes or for improving contrast within the vasculature. Enhanced contrast and backscatter could improve the SNR of OCT Doppler velocimetry.

5.3.2 Endogenous agents

Melanin is an endogenous molecule that has been shown to provide strong contrast in *in vivo* confocal scanning laser microscopy of human skin[193]. Similarly, melanin will increase the contrast within OCT images. Tracking the migration of melanin-laden neural crest cells as described in Section 4.5.4 was possible due to the enhanced contrast of these cells within the surrounding scattering tissue. Melanin has an index of refraction of 1.7, significantly higher than surrounding cell and tissue constituents[172].

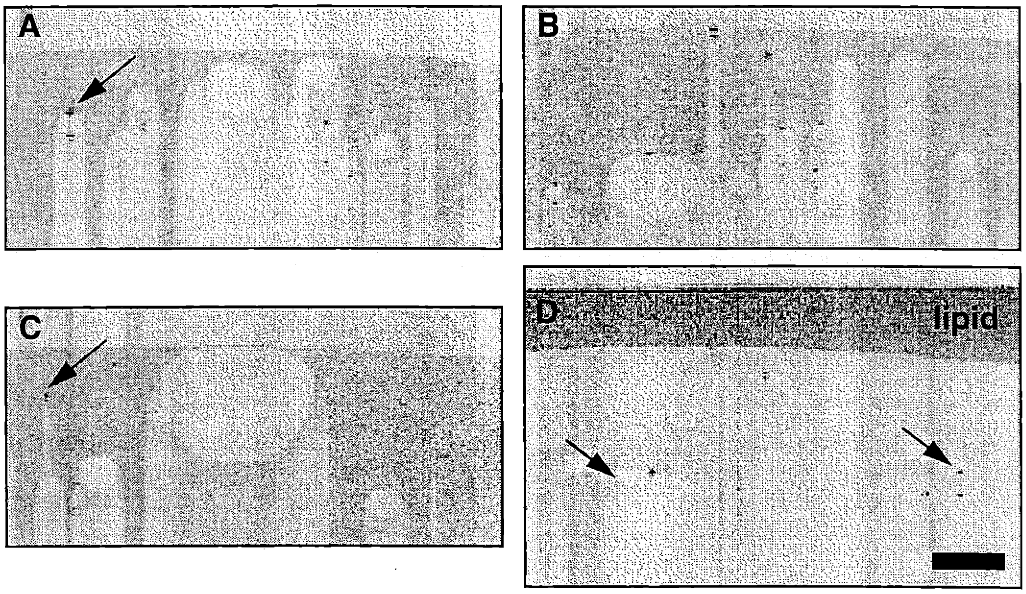

FIGURE 5-5: Air-filled microbubbles suspended in agar. Index differences between air and agar contribute to image contrast. Normal beam incidence increases contrast as shown by the arrows. In D, contrast was evident after addition of scattering lipid over agar surface. Bar represents 500 μm.

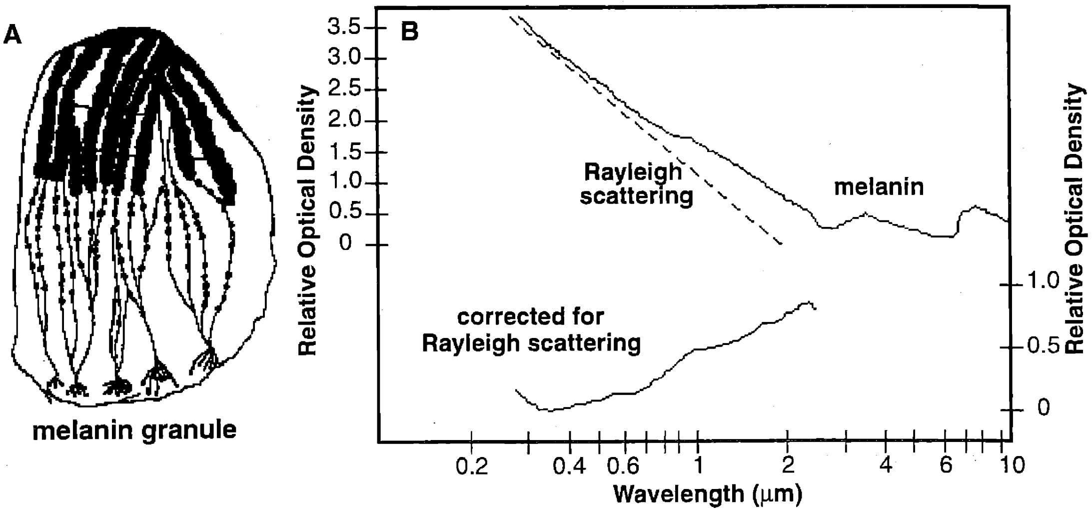

FIGURE 5-6: Optical properties of melanin[195]. A) Illustration of melanin granule structure. B) Wavelength-dependent optical density of melanin before and after correction for Rayleigh scattering.

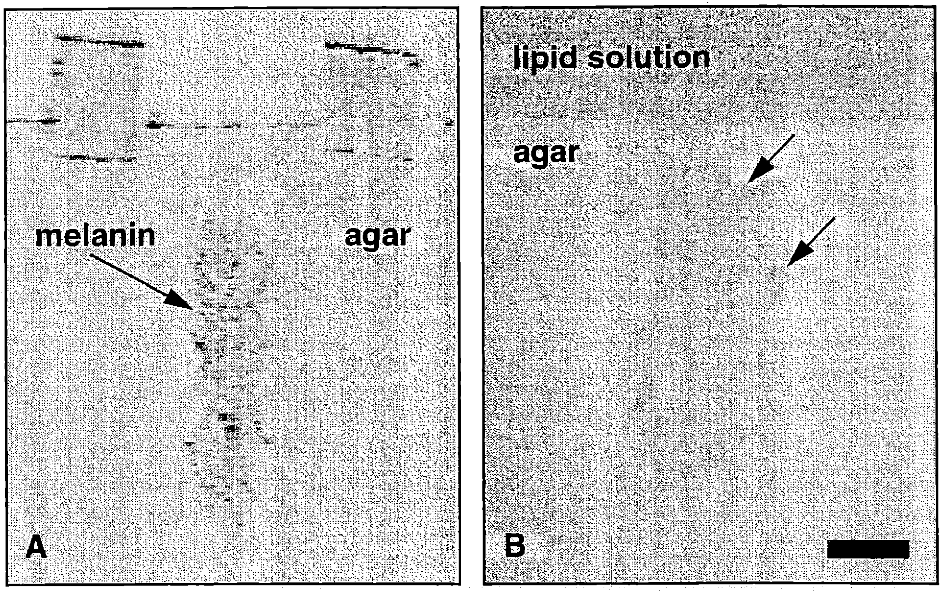

FIGURE 5-7: Melanin as an OCT contrast agent. A) Injection of melanin granules in gelled agar. B) Contrast (arrows) through a scattering lipid solution. Bar represents 500 μm.

Melanin is formed naturally within particular cells, notably within the skin and eye, and has been characterized spectroscopically *in vivo*[194]. Melanin appears as ≈ 1 μm granule structures that have an absorption curve described in Figure 5-6B. Within the melanin granules, there is a randomly spaced array of scattering macromolecules. The conjugation of these macromolecules are responsible for the deep black color. Although melanin is broadly absorbing in the UV, visible, and near IR wavelengths, this absorption is weak with Rayleigh scattering being the first-order effect. The lower curve in Figure 5-6B is the absorption of melanin after Rayleigh scattering has been taken into account. To demonstrate the contrast afforded by melanin, natural melanin particles from *Sepia officinalis* (cuttlefish) were injected into a bed of gelled agar (Figure 5-7A). A 1.5 mm thick lipid solution ($\mu_s = 45\ \text{cm}^{-1}$, $\mu_a = 0.42\ \text{cm}^{-1}$, $g = 0.8$) was placed over the agar. Through this scattering solution, contrast was clearly evident as shown in Figure 5-7B. Interestingly, the regions of highest contrast appear to arise from air spaces within the agar, not from the melanin pigment, suggesting the index difference between agar and air is greater than between agar and melanin. The presence of melanin within melanomas of the skin and other tissues provides a benefit of increased contrast for OCT guided resection. The melanin region would be relatively more backscattering than adjacent normal tissue. A demonstration of this in human tissue is described in Section 6.2.1.

5.4 Doppler Imaging

The heterodyne detection of OCT permits frequency-selection of the backscattered signal. The linear translating reference arm mirror described in Section 2.5.1 not only varies the pathlength between the two arms but also induces a Doppler-shift in the frequency of the reflected light. For a moving source and a stationary observer, the observed Doppler-shifted frequency is defined by

$$f_{obs} = \frac{f_0}{1 \mp v_M / v_L} \tag{5-21}$$

where v_L is the velocity of the center wavelength of light, v_M is the velocity of the mirror and f_0 is the original frequency of the source. The minus and plus signs are used when the source is approaching and leaving the stationary observer, respectively. Applied to moving particles in a fluid, such as red blood cells, the local Doppler frequency f_D generated from moving scatterers is related to the mean velocity of the scatterers v_S by

$$v_s = \frac{\lambda_0 f_D}{2 n_t \cos\theta} \tag{5-22}$$

where θ is the angle between the incident beam and the direction of motion of the scatterers and n_t is the average index of the surrounding tissue. OCT can be used to detect a moving tissue sample or moving scatterers within tissue, such as red blood cells. This technique using low-coherence reflectometry was first described by Wang, *et. al.*[161] in a flowing cell model. Later studies in highly scattering media and in living animal models demonstrated a possible application in humans[162-165]. OCT Doppler imaging may provide assessment of tissue perfusion, identification of subsurface blood flow for avoiding vasculature, and to assess successful arterial anastomosis. Because near-IR light transmittance through blood varies for oxygen saturation, erythrocyte concentration, and depth[196-199], it may be possible to simultaneously characterize these parameters. Two techniques for performing OCT Doppler imaging will be described.

5.4.1 Fast Fourier transform method

The autocorrelation function for each axial OCT scan contains frequency components corresponding to the Doppler shift induced in the returned light. As described in Section 2.3, the amplitude of the interferogram envelope is used to determine the backscattered intensity from within the focal volume. The information contained within the interference fringes is used in spectral radar (Section 2.8) to obtain frequency-encoded depth information. In OCT, the Fourier transform of the interferogram produces a frequency spectrum of the Doppler-shifted frequency components between the arms of the interferometer.

For a mirror placed in the sample arm of the OCT setup, the time-dependent autocorrelation function from Equation (2-4) in terms of the Doppler-shifted frequency f_D is

$$I_D(t) = \frac{1}{4}I_r + \frac{1}{4}I_s + \frac{1}{2}\sqrt{I_r I_s} Re[\Im\{S(\omega)\}]\cos(2\pi f_D t). \tag{5-23}$$

The Fourier transform of this function is a single peak centered at the Doppler frequency f_D induced by the moving reference arm mirror. If multiple moving objects are present in the reference or sample arm, then these contribute to an autocorrelation with multiple frequency components

$$I_D(t) = \frac{1}{4}I_r + \frac{1}{4}I_s + \frac{1}{2}\sqrt{I_r I_s} Re[\Im\{S(\omega)\}]\sum_{i=1}^{j}\cos(2\pi f_{Di} t). \tag{5-24}$$

The Fourier transform then has multiple peaks (at f_{D1}, f_{D2}, f_{D3}, ...), each corresponding to the contribution at that frequency. Therefore, one method for obtaining the velocity of a moving tissue or scatterer is by digitizing the interference fringes and taking the fast Fourier transform (FFT). The spatial resolutions of OCT imaging, and similarly for Doppler OCT imaging, have been defined in Section 2.7.1. The velocity measurement resolution is defined as the minimum resolvable velocity v_{min} and is proportional to the minimum detectable Doppler shift. This is defined as

$$v_{min} = \frac{\lambda_0 f_D}{2n_t \cos\theta} \cdot \frac{v_m \cdot p_x}{NL} \tag{5-25}$$

where p_x is the number of pixels within the axial scan length L and N is the window size used to compute the FFT[165]. This method was used to obtain the fluid flow velocity profiles in an experimental vessel model.

Flexible silicone tubing was used as a vessel model to demonstrate OCT Doppler imaging. The tube had dimensions and parameters as shown in Figure 5-8. Blood was passed through the vessel model using a linear syringe pump calibrated for flow velocities. Fluid flow within a cylindrical tube will follow a laminar flow profile if the Reynolds number is less than or equal to 3000, the threshold for turbulence. This is calculated by

$$N_R = \frac{\rho v D}{\eta_{dv}} \tag{5-26}$$

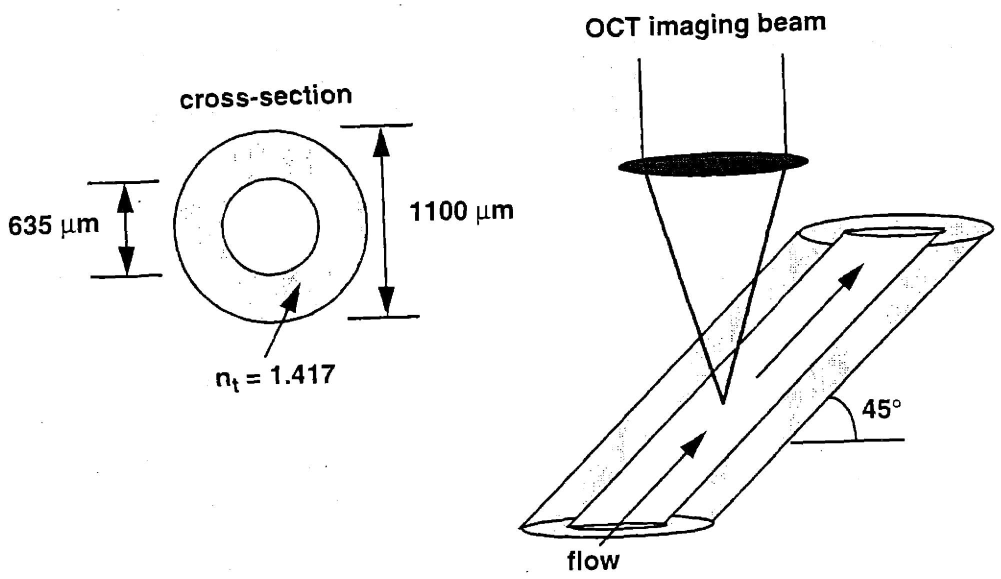

FIGURE 5-8: Vessel model parameters. Silicone medical tubing provided scattering conduit for OCT Doppler imaging studies.

where ρ is the fluid density, v is the flow velocity, D is the inner diameter of the cylinder and η_{dv} is the dynamic viscosity of the solvent. For these studies, $v < 5$ cm/s, $D < 0.1$ cm, $\rho < 10$ g/cm^3, and $\eta_{dv} \approx 0.010$ g/cm-s, giving $N_R < 500$. The entrance length l_E of a cylindrical conduit is defined as the length over which the flow profile evolves from a constant cross-sectional profile to a parabolic profile. This is determined by

$$l_E = 0.03 D N_R. \tag{5-27}$$

The entrance length using the experimental parameters stated above is ≈ 1.5 cm. Since the vessel model tubing was 1 m in length, a parabolic flow profile was expected.

For laminar flow through a cylindrical enclosure, the velocity distribution across the cylinder at radial position r is given by

$$V(r) = \frac{D^2 \Delta p}{16 \eta_{dv} \Delta L}\left[1 - \left(\frac{2r}{D}\right)^2\right] \tag{5-28}$$

where Δp is the pressure difference along the length ΔL. For this experiment, Δp/ΔL was used as a fitting parameter. OCT Doppler imaging was used to measure the fluid flow profile within the vessel model. The tube was placed on the translational stages and oriented at a 45° angle with respect to the OCT imaging beam. Refraction through the tube wall resulted in a 30° incident angle of the beam into the blood ($n = 1.42$) contained within the tube. The focus of the OCT beam was then placed at one wall of the tube and stepped across the lumen diameter in 20 μm increments. At each step, the reference arm mirror was held stationary while the interference fringes were digitized and Fourier transformed using the FFT. A Doppler frequency was obtained at each position. The Doppler frequency was related to the velocity by Equation (5-22). The velocity resolution in Equation (5-25) was calculated using $p_x = 300$, $v_M = 30$ mm/s, L = 3 mm, and N = 512 to be 3 μm/s. The measured Doppler frequency and fluid flow velocity of the blood were plotted versus radial position and compared with the theoretical parabolic profile for laminar flow. This comparison is shown in Figure 5-9. There is excellent agreement demonstrating that this method can accurately predict fluid flow velocity. The fluid flow velocities generated in this model are consistent with *in vivo* blood flow rates. Arteries 4 mm in diameter have flow rates as high as 45 cm/s while smaller 50 μm diameter arterioles have rates of 5 cm/s.

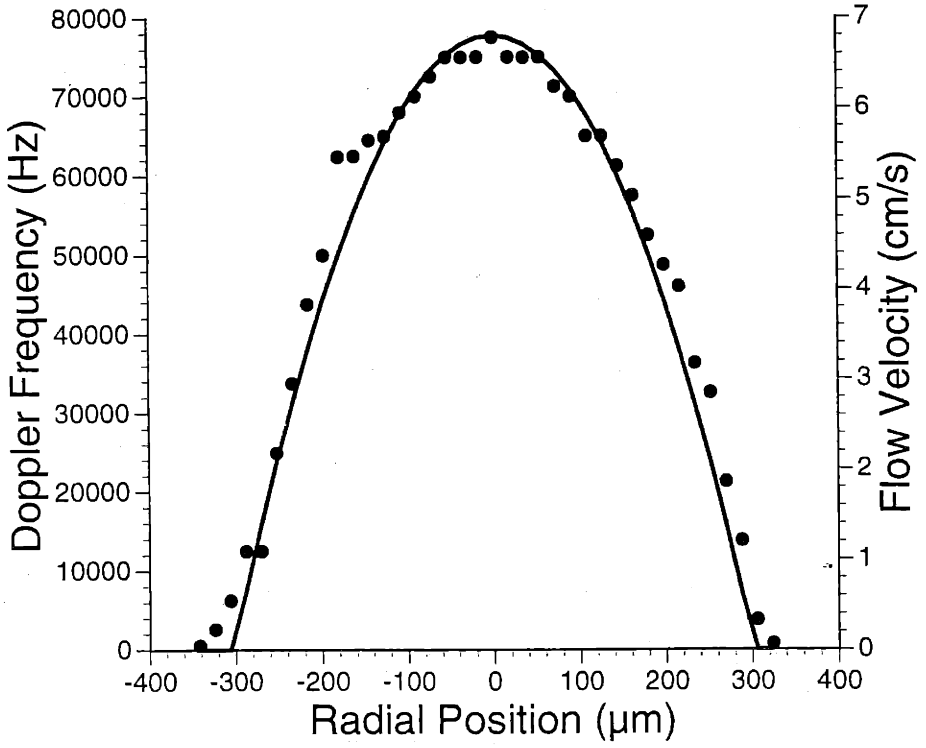

FIGURE 5-9: Laminar blood flow within vessel model. OCT Doppler measurements (data points) of blood flow compared well with theoretical blood flow velocity distribution (solid line).

This technique was then used to measure fluid flow within an *in vivo* animal model. Blood flow in the *Xenopus* tadpole was used. A specimen was anesthetized using the protocol described in Section 4.3 and placed ventral side up on the translational stage. The OCT imaging beam was focused on the center of a ventral aorta shown in the inset in Figure 5-10. The aorta is shown to be periodically displaced with the beating heart. A frequency spectrum obtained from this measurement is shown in Figure 5-10. A number of frequency components are present due to the complex fluid flow dynamics of the blood exiting the beating heart. The largest component at 83 kHz corresponds to a velocity of 39.5 mm/s and is a reasonable estimate of the flow velocities in these specimens. Mapping the flow profile throughout the heart, however, is complicated by the highly turbulent blood flow and dynamic tissue movements within the embryo. Two-dimensional mapping has been accomplished in this model using an iterative technique and flow profiles have been overlaid with acquired images[165].

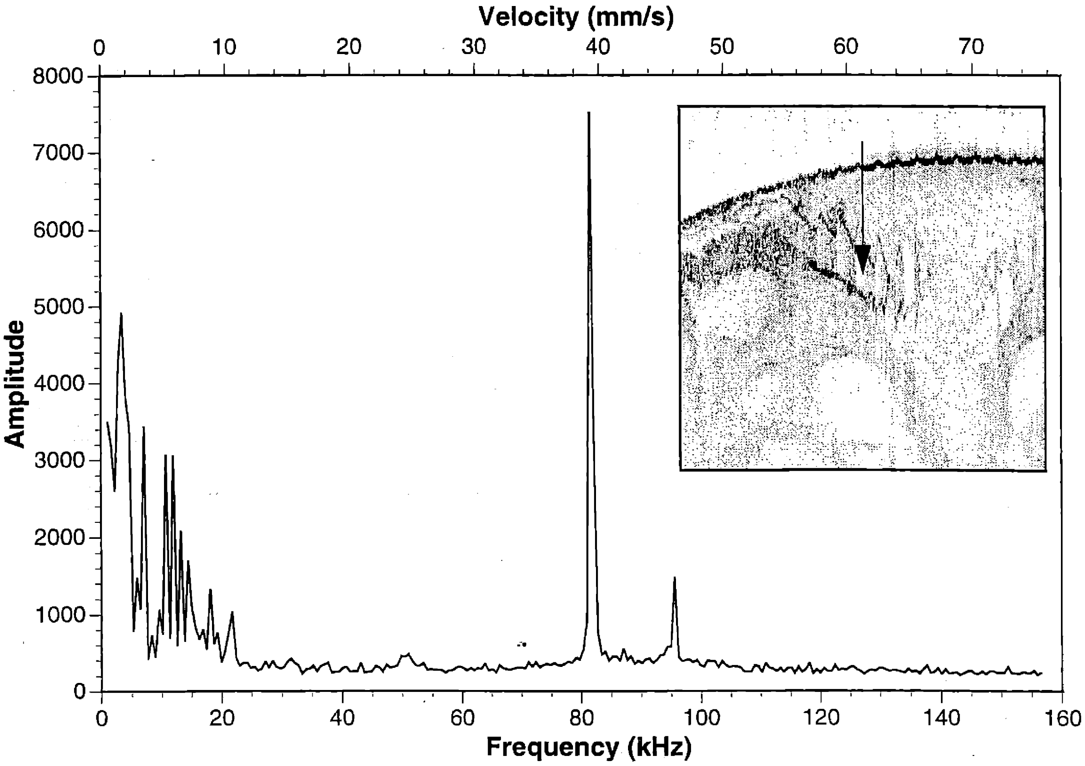

FIGURE 5-10: *In vivo* OCT Doppler data. Frequency spectrum acquired from ventral aorta of a *Xenopus* tadpole. Inset shows image and location where Doppler data was acquired.

Assessing fluid flow in vessels can be accomplished qualitatively from OCT images or quantitatively using velocity profiles. A qualitative assessment using the vessel model is shown in Figure 5-11. For Figure 5-11A-C, the tube was positioned at a 45° angle with respect to the OCT beam. When no blood is present, the tube has an elliptical shape due to the angle of inclination and the index of the tube material (Figure 5-11A). When blood is flowing through the model (Figure 5-9B), distortion of the lower wall results from the presence of blood within the lumen. The flowing blood Doppler-shifts the signal from the lumen out of the detector bandwidth. When the blood flow stops (Figure 5-9C), signal from the blood in the lumen is apparent. When imaging is performed at 90° with respect to the flowing blood as shown in Figure 5-9D-F, this Doppler shift is not observed. The last image shows the formation of a clot, as indicated by the arrow, within the stagnant blood.

These techniques can be applied intraoperatively following the surgical anastomosis of blood vessels (Section 6.3.1) to determine the presence of distal blood flow and the flow profile through the anastomosis site. In addition, the ability to determine blood flow profiles from the external surface of an artery may have a significant impact on the assessment of coronary atherosclerosis. The presence of plaques within the lumen of the artery will disrupt the laminar flow profiles measured in Figure 5-9. This data could be used as a diagnostic for the precise localization of plaques.

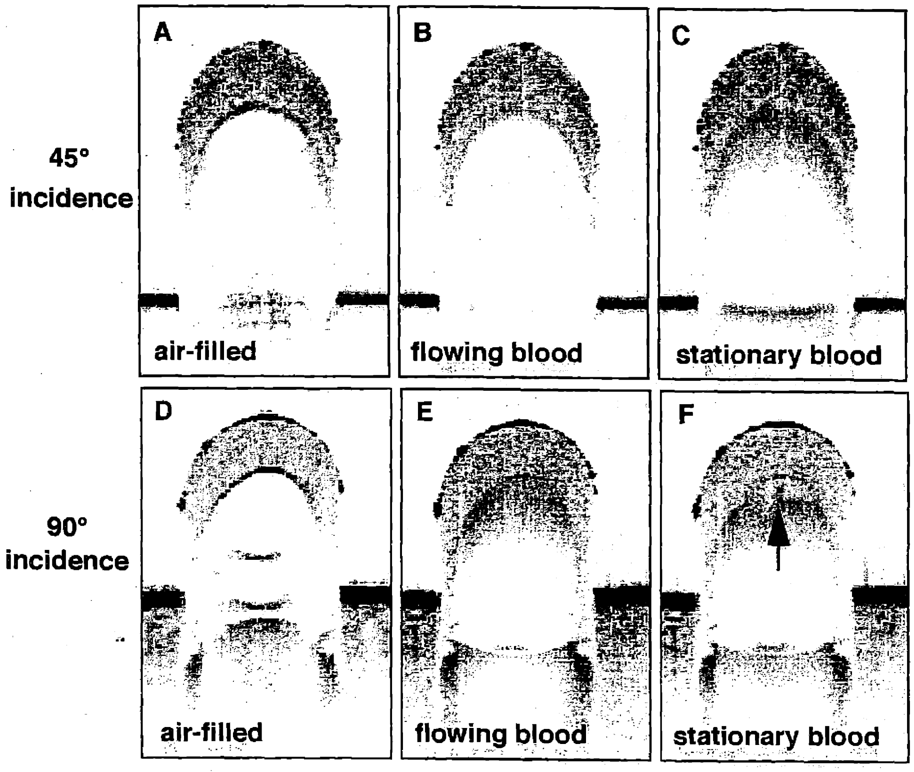

FIGURE 5-11: Qualitative assessment of fluid flow in vessel model. A-C) Images acquired with OCT beam incident at a 45° angle. Loss of backscatter from the lumen in B is the result of flowing blood Doppler-shifting the detected signal out of the detection filter bandwidth. This effect is not observed in D-F for a 90° incident beam. In F, a clot (arrow) has begun to form in the stationary blood.

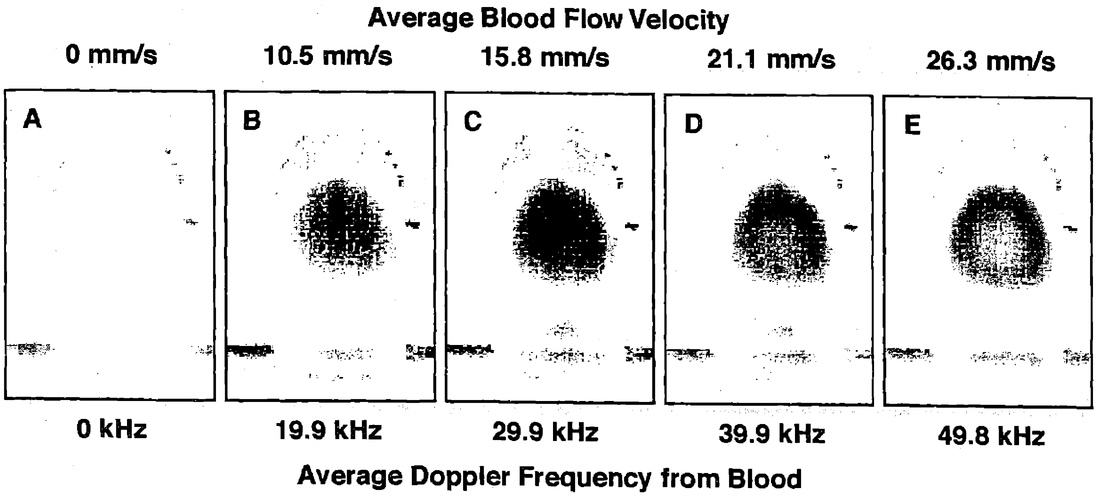

FIGURE 5-12: Detection bandwidth selective Doppler OCT imaging. The finite bandwidth of the detector bandpass filter provides a frequency window for imaging specific velocities present in the laminar flow profile.

5.4.2 Detection bandwidth selectivity

Digitizing the autocorrelation function and obtaining the FFT to produce the frequency spectrum is computationally intensive. To obtain a 2-D image of fluid flow velocity would require a significant amount of time and would only be useful for flows that remain constant over the acquisition period. Simple parameter modifications to the existing galvanometer-based OCT setup can be made to rapidly acquire 2-D flow profiles. This method uses the fixed detection bandwidth of the electronics and varies the Doppler-shift contribution from the moving scatterers in the sample arm. The total Doppler-shift at the detector is the sum of the contributions from the reference and sample arms of the interferometer

$$f_D(total) = f_D(mirror) + f_D(fluid) \tag{5-29}$$

assuming that both the mirror and the backscatterers in the fluid are moving toward a stationary detector. This equation can also be represented in terms of the velocities

$$v_{M+S} = \frac{\lambda_0 f_{DM}}{2} + \frac{\lambda_0 f_{DS}}{2n_t \cos\theta}. \tag{5-30}$$

The contribution from the reference arm is the moving mirror which simultaneously varies the pathlength between the two arms. The contribution from the sample arm is the moving backscattering particles within the fluid. The finite bandwidth of the bandpass filter will enable a window of frequency components to be detected. When varying the fluid flow velocity, only the frequency (velocity) components within the filter bandwidth will appear in the OCT image. An example of this technique using the vessel model is shown in Figure 5-12. The image in Figure 5-12A is of the tube without any blood flow and with the reference arm Doppler shift at 20 kHz (v_M = 12.8 mm/s). The bandpass filter has a center frequency at 50 kHz and a bandwidth of 16.6 kHz. In Figure 5-12B-D, the reference arm Doppler-shift is held constant at 20 kHz while the total Doppler-shift is increased by increasing the blood flow velocity. The images reveal the 2-D profile of the laminar flow within the tube. At first, only the peak of the parabolic laminar flow profile is detected in the center of the lumen. With increasing blood flow velocity, more of the peak is observed and finally in Figure 5-12D and E, the center has passed out of the detection filter bandwidth and the shoulders of the parabolic profile near the lumen wall are prominent. These images provide qualitative assessment of fluid flow without the computational overhead of digitizing the interferogram and performing the FFT.

There are alternative methods for utilizing the detection filter bandwidth for Doppler OCT imaging. When imaging blood flow *in vivo*, the reference arm velocity could be varied to position Doppler frequencies within the fixed detection filter bandwidth. However, this will vary the image acquisition rate. Each image in Figure 5-12 was acquired in 15 s. This acquisition time could be decreased substantially using the fast-scanning OCT system (Section 2.5.3). A complete series of Doppler images could be obtained rapidly by sweeping the center frequency of the detection filter bandwidth while collecting OCT images. These could be assembled to produce the 3-D fluid flow profile in several seconds as opposed to the minutes to hours required to computationally reconstruct the profile.

5.5 Three-Dimensional Imaging

Three-dimensional OCT imaging provides a surgical diagnostic tool for improved visualization of tissue structure. Improved visualization is critical for assessing proper approaches for surgical resection of tumors, particularly when vessels and nerves are in close proximity or intertwined. Understanding the network of vessels and nerves is extremely difficult from a series of 2-D images because of the unpredictable 3-D spatial orientations that these structures may have. The importance of binocular viewing and 3-D imaging is most appreciated when it is absent, as in current MIS endoscopes and laparoscopes. The 2-D image of distant tissue makes surgical manipulation extremely difficult. Years of residency training are required to accommodate for the lack of 3-D spatial cues.

Currently, the majority of OCT systems acquires data with depth-priority. The 2-D images acquired represent cross-sections of the tissue. Transverse-priority scanning may be more applicable for high-resolution, focus-tracking systems. This mode is similar to optical sectioning performed in confocal microscopes. There will be more consideration for 3-D OCT imaging when transverse-priority scanning systems are implemented. The 3-D data set will allow re-sectioning at arbitrary planes, particularly at cross-sectional planes that can be correlated with histological findings. Acquisition of a 3-D volume of OCT data permits repeatable resectioning post-acquisition. The user is not confined to the imaging plane established at the time of data collection. This is an advantage over histology where a single sectioning plane is identified and maintained. Resectioning 3-D data sets permits more precise OCT-histology correlation.

Several algorithms exist for representing data in three dimensions. The reconstruction can be performed on the volume as a whole using voxels or only on the surface using sheets of polygons. Three-dimensional projections project the 3-D data volume onto a 2-D screen positioned at arbitrary angles.

5.5.1 3-D reconstructions

When sectioning 3-D OCT data sets, only the selected planes are seen and much of the information in the data set is not used. The volumetric display of 3-D reconstructions incorporates all of the 3-D voxel information. The imaged tissue represents an object that has both surface and volume features. Generating an image of an object's surface that approximates the appearance of a real, physical surface is a process called surface rendering. The physical rules which are used to represent the appearance of real surfaces are diagrammed in Figure 5-13. The critical variables are the location of the light source, the viewer, and the intensity of the light from the object. The intensity from the object is defined by

$$I_{obj} = k_{diff} I_{amb} + \frac{I_{source}}{d}[k_{diff}(\vec{N} \bullet \vec{L}) + k_{spec}(\vec{V} \bullet \vec{R})^{\gamma}] \tag{5-31}$$

where the k values are the diffuse and specular reflection coefficients, the I values are the intensities of the ambient and source lighting, d is the distance from the object, and γ is a constant describing the breath of the specular reflection from the object[200]. This γ factor will vary depending on the fine-scale surface features of the object. The vectors are defined in Figure 5-13. Smooth surface rendering of 3-D objects requires the use of triangles or polygons to connect adjacent discrete-height pixels[201,202]. Creating realistic-looking objects is computationally difficult because of the number of polygons that must be calculated and drawn. Surface rendering can be combined with transparency factors to permit visualization of structures within the 3-D volume. In this case, volume rendering must be performed, increasing the level of computation.

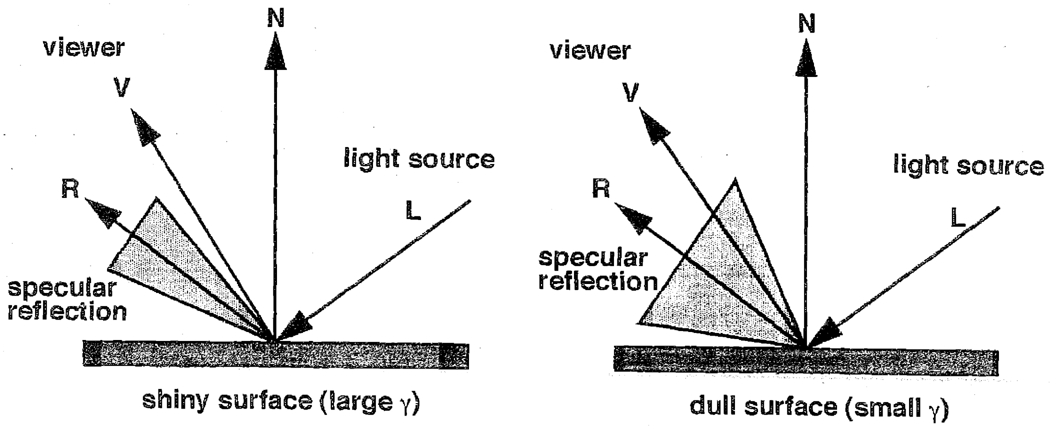

FIGURE 5-13: Rules for surface rendering representation. A dull surface exhibits specular reflections over a larger angle. Defined variables are used in Equation (5-31).

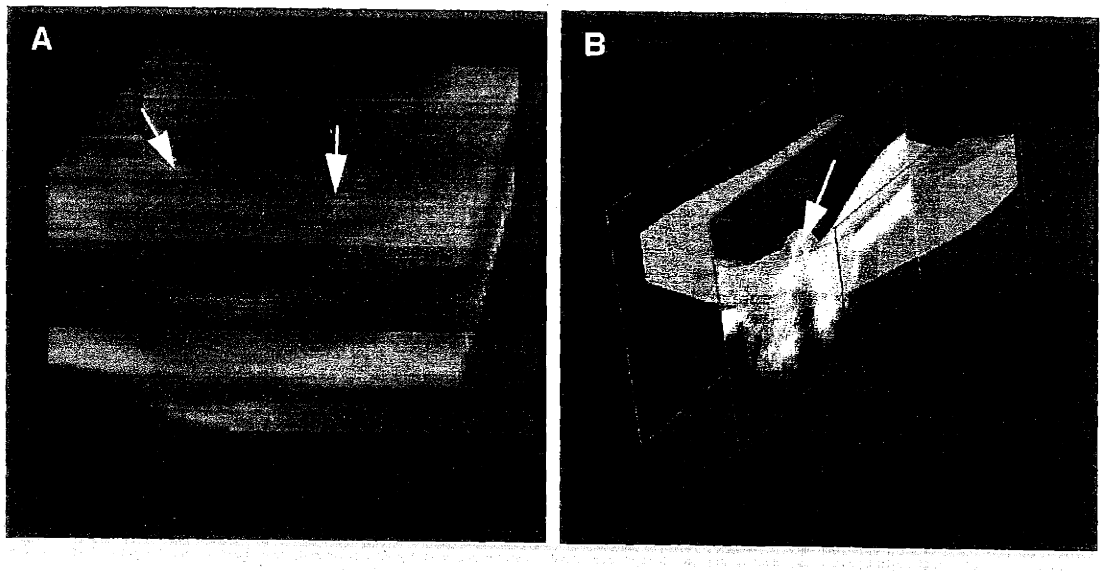

FIGURE 5-14: 3-D surface and volume rendering of *in vivo* optic disk. A) Arrows indicate retinal vessels exiting optic disk. B) Cross-section through volume-rendered data set illustrates retinal vessel lumen (arrow).

Three-dimensional OCT reconstructions using surface and volume rendering were obtained from a series of 60 cross-sectional OCT images of the *in vivo* rhesus optic disk. OCT images were imported and processed on a Silicon Graphics workstation using Segment View software[203]. The surface rendering of the 3-D data set is shown in Figure 5-14A. From this 3-D surface image, the spatial orientation of the retinal vessels can be observed as they exit the disk (arrows). Volume rendering was performed on the same data set and shown in Figure 5-14B. A highlighted slice through the volume-rendered data shows a retinal artery lumen (arrow). Three-dimensional images of the optic disk may be useful for the assessment of early stages of glaucoma when changes in cup-to-disk ratio occur.

5.5.2 3-D projections

Three-dimensional projections are obtained from less computationally taxing algorithms. A series of 2-D images represent a stack or 3-D volume. Projections of this 3-D volume are made onto a 2-D screen located at arbitrary positions as shown in Figure 5-15. The projection onto the 2-D screen can be the maximum value, mean value, or sum of values through the 3-D volume. Variations in surface and interior depth cueing as well as surface and depth opacity permit the highlighting of particular features.

An example of a 3-D OCT projection is shown for the developing *Xenopus* heart. Data was processed on a Macintosh 9500/200 using Image 1.60 (National Institutes of Health). Computer-controlled stages with micron step size were used to position the specimen under the imaging beam. The sequence of *in vitro* images shown in Figure 4-8 demonstrates precise registration between spatially acquired images. A series of 45 images were acquired every 25 μm from a stage 49 (12 day) tadpole and used to produce the 3-D projections shown in Figure 5-16. Four projections of this 3-D data set are used to illustrate the 3-D morphological arrangement of developing cardiac structure which is often difficult to envision from a series of 2-D images. Two major branches of the ventral aorta, one atrium, and the ventricle are distinguishable. The second atrium is difficult to visualize near the ventricle. A cut-away section of the ventricle allows the internal trabeculae carneae network and papillary muscles to be visualized.

The ability of OCT to assess cardiovascular anatomy and function in three dimensions could also represent a powerful tool for the developmental and molecular biologist. Morphologic abnormalities may not clearly be identified or appreciated in two dimensions, particularly those involving misorientation of cardiovascular structures. Three dimensional reconstruction may extend the sensitivity of analysis. As shown in Figure 5-16, an advantage of reconstruction is that rotation of the volume around any axis is possible, preventing the limitations associated with interpretation based on a single viewing plane.

Additional examples of 3-D OCT projections will be illustrated in later sections. Three-dimensional OCT imaging can be extended to four dimensions by acquiring volumes over time. This was performed to observe mitotic activity and to follow migrating cells as described in Section 4.5.3 and Section 4.5.4. Current limitations for 3-D and 4-D imaging are the increased acquisition times, maintenance of image registration, and the computational processing needed to display, update, and manipulate the volumes. At the current acquisition rate of 8 fps, the 3-D volume shown in Figure 5-16 could be acquired in 5.6 s. Improvements in acquisition time and computational power will make 4-D OCT imaging possible in the near future.

5.6 Image Processing

Signal and image processing techniques can be applied to improve the quality of OCT images and to extract quantitative surgical diagnostic information from the image data[204]. In the field of ophthalmology, cross-correlation routines examined adjacent axial scans to remove axial movement artifacts[59]. More

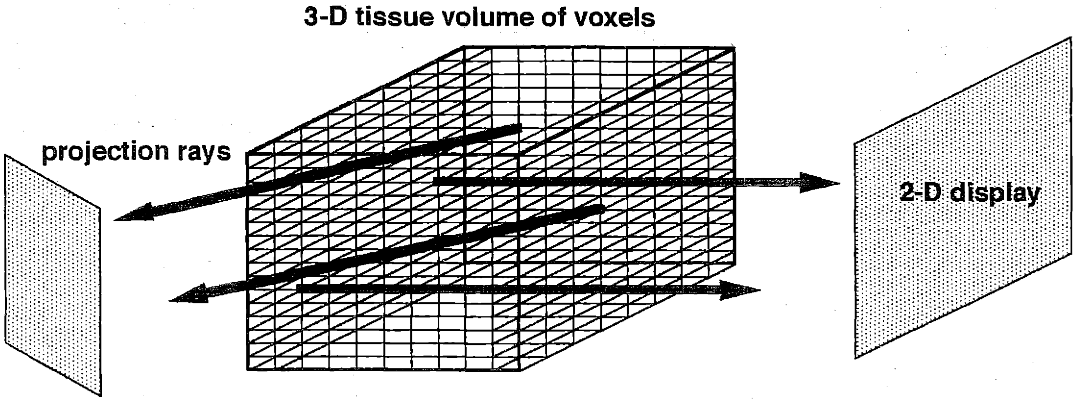

FIGURE 5-15: 3-D projection diagram. Projections are 2-D representations of 3-D data sets obtained by propagating rays through the volume on to a 2-D plane. The 2-D plane can be located at arbitrary positions around the volume.

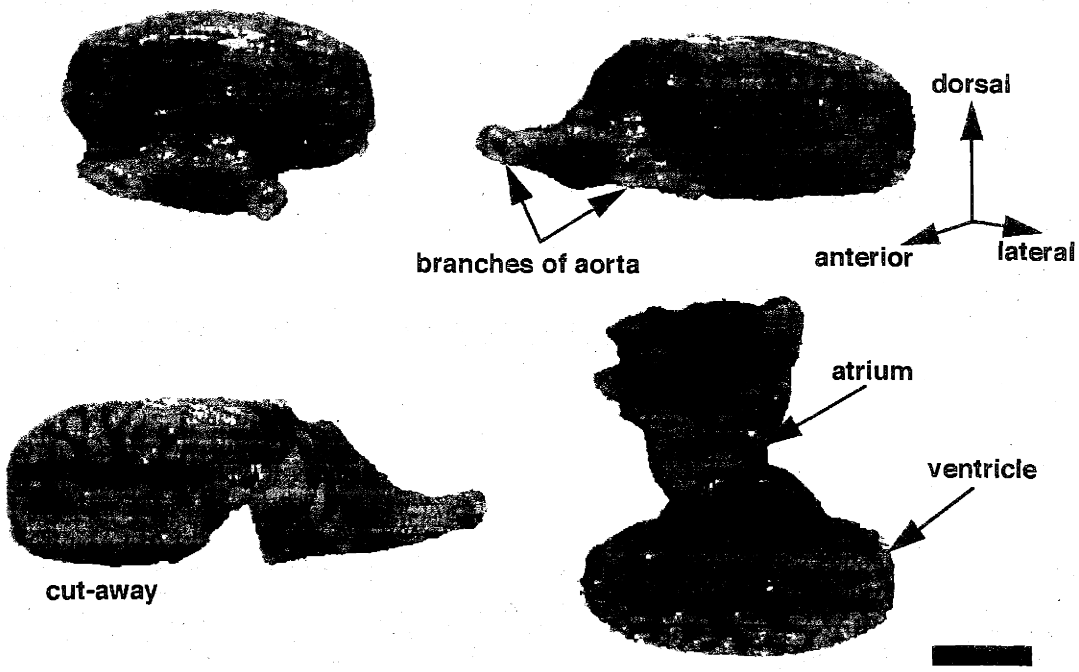

FIGURE 5-16: 3-D projections of a *Xenopus* heart. Four projections are shown to illustrate the 3-D spatial orientation of an atrium, the ventricle, and the branches of the aorta. A cut-away of the ventricle reveals the internal trabeculae carneae network. Bar represents 500 μm.

advanced algorithms identified the thickness of retinal layers to produce topographic maps of retinal thickness for diagnostic information on macular edema and to predict early thinning of the retinal nerve fiber layer in glaucoma[64,68,69]. In relatively homogeneous scattering tissue, the OCT signal will have a depth-dependent attenuation characterized by Beer's Law given in Equation (5-9). Therefore, an exponential correction can be applied to compensate for this attenuation[205]. Homogeneous tissue, however, is relatively uninformative and this correction induces additional artifacts if the tissue is composed of large variations in tissue index of refraction. For this thesis, fundamental image processing techniques were explored to determine the effect on image quality.

5.6.1 Averaging

Image averaging techniques were applied to reduce the degree of speckle and noise present in OCT images. Because speckle is the result of random coherent scattering processes from adjacent scatterers within the focal volume, averaging images will reduce the speckle and noise contribution while improving the signal from actual microstructure. Averaging reduces noise in proportion to the square root of the number of frames averaged. The signal represents the mean backscatter value from each pixel. The noise is measured by the standard deviation from this mean given by

$$\sigma = \sqrt{\frac{\sum B_k^2 - (i \cdot B_{mean}^2)}{(i-1)}} \tag{5-32}$$

where i is the number of scans averaged and B is the backscatter from each pixel. In addition to image averaging, array detection schemes have been used to reduce speckle in optical coherence microscopy[206]. Removal of speckle may be necessary to image cellular structure in human tissue. Currently, the resolutions of OCT are not sufficient to definitively identify human cells. The presence of speckle produces artifacts which resemble cell membranes and cell nuclei, making accurate cell identification difficult. An example of questionable human cellular structure is shown in Figure 5-17. Within this image, it is impossible to determine if the features indicated by the arrows are cell nuclei surrounded by cell membranes or the result of speckle from multiple scatterers within the focal volume.

Averaging was performed by two methods. The first, named frame-averaging, acquired i images (frames) in a sequential manner. The resultant averaged image was computed by summing the intensity at each pixel and dividing by the number of images (frames), i. The second method was step-and-repeat averaging. For the resultant averaged image, the OCT beam was placed at one location on the tissue and i axial scans were acquired. The intensity at each position in this axial scan was summed and averaged by dividing by i. Once averaging was performed for one axial position, the OCT beam was stepped transversely to the next position. The results of these averaging methods are shown in Figure 5-18.

The tissue sample was *in vitro* human endometrium that is glandular in structure. The left image was a single image acquired with no averaging. The center image in Figure 5-18 was the result of frame-averaging three images. Slight blurring has occurred as a result of either translation stage misalignment or tissue movement. Each image was acquired in 20 s. At these slow rates, sub-micron to micron positioning error in both the stages and the tissue are to be expected. Although the degree of speckle has been reduced by empirically visualizing the circled region, other artifacts are induced during the acquisition and averaging process. Step-and-repeat averaging eliminates some of the blurring because averaging is performed at each axial scan over much shorter time intervals. Some reduction in blurring is observed in the right image in Figure 5-18 where averaging of 3 axial scans was performed at each transverse position. The images shown in Figure 5-18 are displayed on a logarithmic scale. Thus, the effect of averaging is less apparent than if the images were displayed on a linear scale. Pixel variations between frames or axial scans require the acquisition of larger numbers of frames or axial scans before the effects of averaging will be obvious in these logarithmic-scaled images.

Averaging techniques do not appear beneficial for these slow acquisition rates. Implementing these techniques during high-speed acquisition will prove advantageous when larger numbers of images can be averaged and tissue movement during each image acquisition can be minimized. Additionally, by observing the rapidly updated screen during acquisition, the retinal response will average out speckle, giving the appearance of a higher contrast image.

5.6.2 Segmentation

Segmentation of OCT images permits the extraction of useful data while rejecting erroneous information. Complex algorithms can be developed which automate the segmentation process for the real-time improvement of image quality. Established segmentation algorithms for CT and MRI data cannot be directly applied to OCT images due to the presence of speckle and the reduced contrast between tissue types. Manual segmentation was performed on the embryo heart images used to generate the 3-D projections in Figure 5-16. This enabled all surrounding tissue structure to be excluded from the projection.

Threshold segmentation can be performed by establishing two intensity levels, either manually or automatically. Image pixels with intensity values between these two thresholds are considered part of the region of interest and all others are considered part of the background. Threshold segmentation was applied to extracting a highly backscattering tumor region from an OCT image of human brain. The threshold level was chosen to include all of the backscattering tumor while rejecting the surrounding normal brain tissue from the image. Because the normal brain tissue was considered part of the background, the threshold-segmented image was superimposed over the original image to display both regions. The resulting images are shown in Section 6.2.1.

Other segmentation techniques employ training algorithms which can recognize and remove patterns, textures, or noise from images[207,208]. If the speckle and noise within OCT images can be adequately modeled, then these contributions can be removed, leaving only cell and tissue image data.

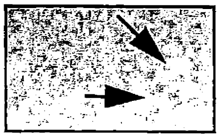

FIGURE 5-17: Speckle artifact or human cell? Arrows indicate image features which may potentially be human cells, but evidence is complicated by the presence of speckle.

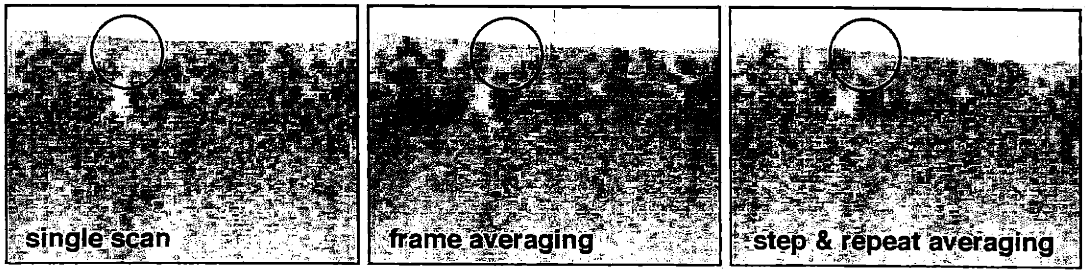

FIGURE 5-18: Comparison of averaging methods. Images of frame- and step-and-repeat averaging represent averages of 3. The encircled areas illustrate a reduction in speckle for frame averaging compared to a single scan. Step-and-repeat averaging appears similar. For longer acquisition times, however, other movement artifacts are introduced into the averaged images.

Chapter 6

Surgical Guidance

6.1 Introduction

The use of imaging modalities for surgical guidance has resulted in improved patient outcome and a reduction in patient morbidity. If the surgeon is provided with the ability to view or image tissue intraoperatively, then collateral damage to normal tissue can be minimized. Integrating imaging modalities with surgical techniques requires solutions to a number of technical problems. Fast image acquisition is necessary to eliminate motion artifacts from either the patient's physiological processes or the surgeon's repositioning of instruments. There must also be an accurate system of registration between acquired images and the tissue to enable guidance of the surgical procedure.

Precedences for image-guided surgery have been established[209]. Open-magnet MRI permits the surgeon to obtain 3-D MRI volumes of the surgical field intraoperatively[9,210]. These instruments, roughly only ten in operation, are extremely expensive and complex systems. Studies have yet to show a positive patient outcome compared to standard surgical procedures partly due to the relatively small numbers of patients undergoing these procedures. Ultrasound has been used to guide placement of needles for biopsies with good success due to imaging penetrations of 10-30 cm. However, 100 μm resolutions limit ultrasound to imaging larger tissue morphology. The high resolutions of OCT may enable image-guided surgery to approach another level of investigation. OCT has already been demonstrated for imaging surgically relevant tissue[211]. Image guidance may be performed at near-cellular resolutions. The localization of small vessels and nerves will be possible as may the discrimination of abnormal neoplastic tissue. Surgical procedures are likely to become a more precise art. In this chapter, I demonstrate OCT imaging in an array of surgically-relevant human tissues. Incidence statistics are presented to illustrate the relevancy of improving techniques for the surgical treatment of pathologies. Differences between OCT images of normal and diseased tissues are examined. Significant differences potentially enable OCT imaging to identify pathologies and guide surgical treatment. These organ and tissue systems represent the environment in which surgical guidance is performed.

6.2 Nervous System

The human nervous system is divided into the central and peripheral nervous systems. Both contain relevant surgical tissue which can be imaged during surgical procedures. Tumors of the brain and nervous system have several unique characteristics that are not common to neoplastic processes in other parts of the body. The distinction between benign and malignant lesions is less evident. By nature of the location of benign lesions, they can have equally lethal consequences. In addition, the ability to surgically remove neoplasms is restricted by functional anatomic considerations. The tissue of the nervous system is highly sensitive to damage often resulting in loss of memory, motor, or sensory function. The incidence of intracranial tumors ranges from 10 to 17 per 100,000 and account for as many as 20% of all cancers in childhood[212]. Although the five-year survival rate has shown a statistically significant improvement ($p < 0.05$) since 1974, it still remains around 29%[213]. The sensitivity of these tissues limits the amount that can be physically biopsied for histopathological examination. The use of OCT to optically biopsy or guide resection of tissue may offer a potential reduction in patient morbidity.

6.2.1 Central nervous system

The central nervous system is composed of the brain and spinal cord. During the resection of central nervous system neoplasias, precise intraoperative identification of the tumor margin is vital both for the complete resection of the neoplasm and the prevention of iatrogenic injury. Because of this, various imaging modalities including ultrasound, CT, and MRI have been utilized in an attempt to improve patient morbidity[26,214-218]. Unfortunately, the resolutions of such modalities are often hundreds of microns; thereby poorly resolving small tumors and reducing the sharp definition of the tumor margin. Furthermore, the registration of images with tissue at the sub-millimeter level is problematic and extensive research and development have explored means of stereotactically aligning the two[210]. Optical techniques including fluorescence and Raman spectroscopy have enabled quantitative identification of brain tumor cells and tumor margins based on detected spectra[219-221]. Image representation of tumors based on these techniques is limited to surface features without cross-sectional imaging or optical ranging into the tissue. High-resolution video imaging for discrimination of brain tissues has been effective, but requires the administration of topical or systemic fluorescent dyes[26,222].

Frozen-section biopsy of tissue acquired intraoperatively is another means of identifying tumors and their margins. Light microscopy observations of histologically prepared specimens offer exceptional resolution and have been the gold-standard for pathology identification. However, obtaining a frozen-section biopsy lengthens the time of the surgical procedure, often halting progress until results are obtained, and is only representative of the small region in direct proximity to the site. Additionally, in particular regions of the brain, tissue biopsy is not feasible due to the risk of injury and loss of vital sensory or motor function. The optical properties of brain and nervous system tissues have been characterized[223,224]. Therefore, a technology capable of performing intraoperative optical biopsy, the imaging of tissue at near-histological resolutions, may provide high-resolution discrimination between normal and pathologic tissue. If this optical biopsy could be performed in real-time, it could be a powerful tool for the surgeon resecting central nervous system neoplasms, allowing tumor margins to be rapidly defined as the intervention progresses.

In addition to its high resolution, several features of OCT suggest it will be useful for the guidance of surgical procedures. First, unlike MRI, the OCT instrument is compact and portable, approximately the size of a personal computer. Second, unlike ultrasound, OCT is noncontact with no requirement for a transducing medium. Third, the fiber-based design allows straightforward integration with scalpels, microscopes, or pencil-sized hand-held probes, which are well suited for the tight confines of the operative suite[132].

OCT is demonstrated for the detection of brain tumors and their interfaces with normal brain parenchyma, suggesting a role for guiding surgical resection[225]. The hand-held surgical imaging probe described in Section 3.4 has been constructed for this application. The compact and portable probe enables OCT imaging within the surgical field while the OCT instrument can be remotely located in the surgical suite. The probe is used to acquire 2-D cross-sectional images of *in vitro* human cortex and metastatic melanoma lesions. OCT images are correlated with corresponding histology. Variations in optical properties between normal cortex and tumor are used for tumor discrimination. Three-dimensional OCT imaging is performed on a melanoma lesion to determine the extent of tumor penetration into normal cortex. A cerebral artery is imaged and correlated with histology; demonstrating the potential use of OCT for identifying and avoiding vascular structures during tumor resection.

A 1 cm^3 specimen of outer human cerebral cortex with metastatic melanoma was obtained within 24 hrs. postmortem and stored in 0.9% saline. Two-dimensional imaging was performed across multiple metastatic lesions using the hand-held surgical probe. The cortical surface was scanned for cerebral arteries and veins. The position of the imaging beam was visualized via a coincident visible aiming beam. Images (3 x 3 mm, 300 x 400 pixels) were each acquired in 30 s and were used for comparison with corresponding histology. The hand-held probe was then replaced with the research microscope and the tissue specimen was place on the translational stages for three-dimensional imaging. The research microscope focused the imaging beam to a 23 μm diameter spot (625 μm confocal parameter). The axial resolution was 16 μm. Twenty-four cross-sectional images were acquired at 50 μm intervals to produce the 3-D data set. Following image acquisition, the tissue was fixed in buffered formalin and underwent standard histological processing. Five-micron sections were stained with hematoxylin and eosin and digital images were acquired using light microscopy.

Acquired OCT images and 3-D projections were processed using NIH Image 1.60 on a Power Macintosh 9500/200. The logarithm of the optical backscatter intensity data was displayed in 2-D and 3-D gray-scale or false-color images and projections. Images were threshold segmented to reveal tumor regions of increased optical backscatter. Original images were overlaid with segmented regions to visualize regions of tumor against surrounding cortex. Single axial reflectance profiles through normal cortex and tumor were analyzed for changes in optical properties. Linear curve fitting using the method of least squares was performed on the reflectance profiles using DeltaGraph Pro 3.5. Tumor margins were determined from relative changes in optical backscatter.

Cross-sectional OCT imaging of malignant melanoma in the human cortex is demonstrated in Figure 6-1. The OCT images in Figure 6-1A and B were acquired through the tumor as indicated by the lines on the digital *en face* view of the cortex (Figure 6-1G). These original images were threshold segmented to identify regions of high backscatter within the tumor. The original images were then overlaid with the segmented data and are shown in Figure 6-1C and D. The OCT images show increased optical backscattering in the region of the larger tumor (white arrows). Smaller tumor lesions also appear within the image (black arrows). A shadowing effect is observed below each tumor site due to the increased optical backscatter and the subsequent loss of optical power penetrating beneath the tumor. In Figure 6-1A and C, the boundary of the tumor can be identified. In Figure 6-1B and D, the tumor is identified below the surface of normal cortex. The histology in Figure 6-1E and F confirms the presence and relative size of the tumor. The digital image shown in Figure 6-1G illustrates the characteristics of this particular metastatic melanoma. Multiple small (< 500 μm) metastases are shown surrounding the larger lesion. It is likely that the primary tumor had seeded a large number of tumor cells which were widely distributed across the gray matter of the cortex.

The location of the lower tumor margin and a quantitative assessment of the optical backscattering changes between tumor and normal cortex were obtained from single axial reflectance profiles. These are plotted in Figure 6-2. The air-tissue interfaces for the normal and tumor regions were aligned for comparison of reflectance changes with increasing depth. The plot of the normal cortex shows a uniformly attenuated reflectance with increasing depth. A line with a slope of -0.30 dB/μm (R^2=0.97) was fitted to the plot of the logarithm of the optical backscatter intensity versus depth. At these wavelengths, attenuation is largely due to scattering. Hence, the slope indicates the degree of scattering from the tissue. Using the same laser power, detection sensitivity, and beam focusing optics, an axial reflectance profile was acquired

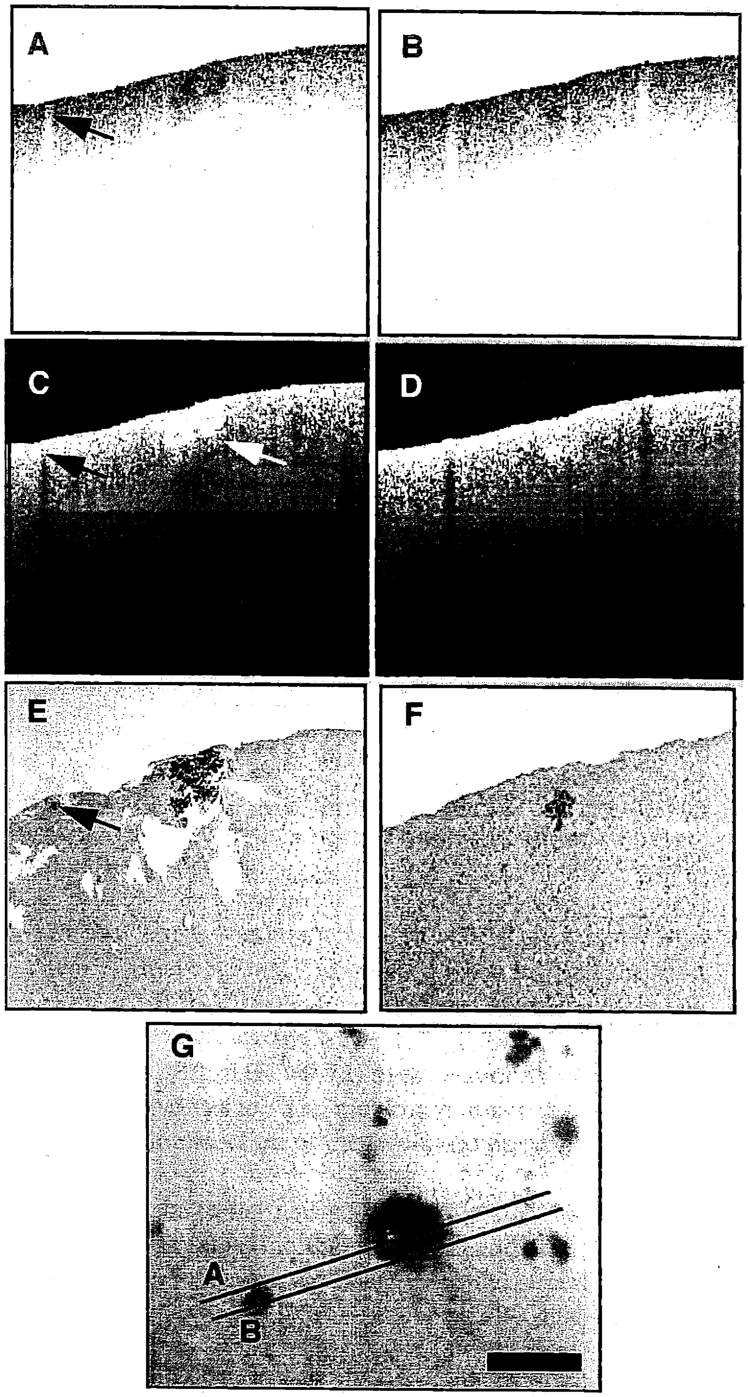

FIGURE 6-1: Malignant melanoma in human cortical brain tissue. Original images (A,B) were threshold segmented (C,D) to highlight backscattering tumor. Comparison with histology (E,F) is strong. Scan locations are shown in the digitized image of the cortex surface (G). Bar represents 1 mm.

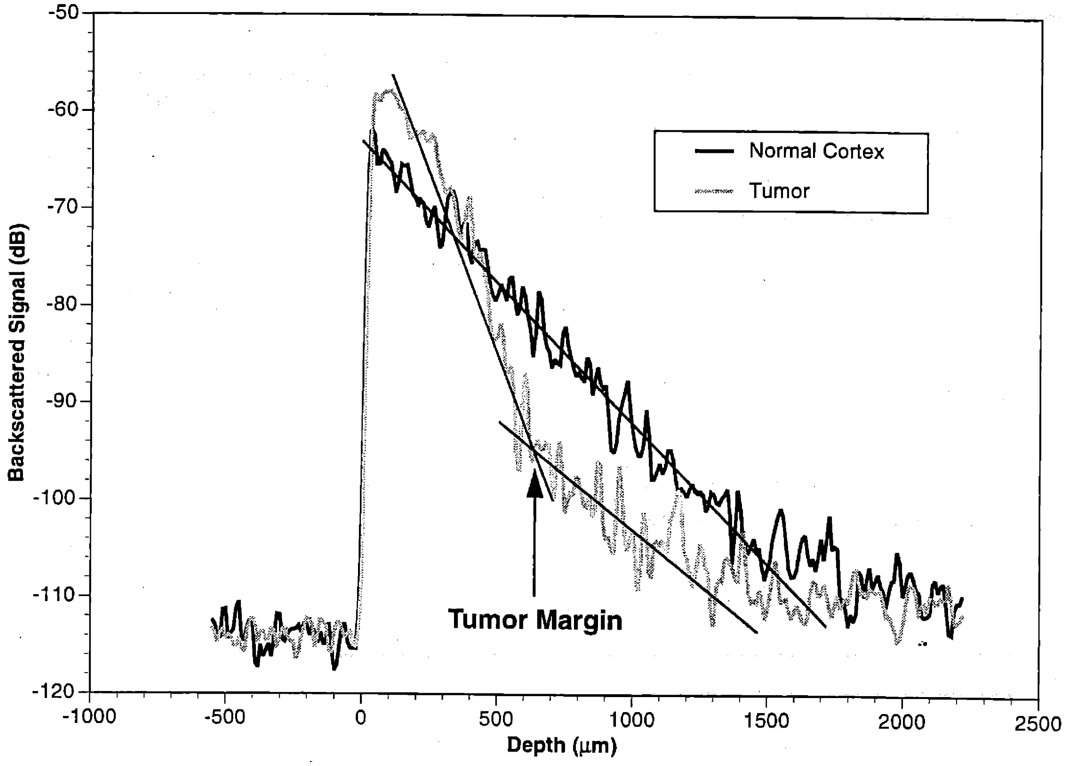

FIGURE 6-2: Axial profiles of normal brain and tumor. Differences in slope represents different scattering properties between normal brain and tumor. Intersection of fitted lines indicates position of tumor margin.

through the center of the tumor. There was an increase in optical backscatter from the surface. This reflectance profile consists of two distinct regions. Lines were fitted for each of these regions and slopes were determined. The initial slope of -0.52 dB/μm (R^2=0.90) was approximately 1.7 times as steep as that for normal cortical tissue. Hence, there was nearly a two-fold relative increase in optical scattering within the tumor. The second slope of -0.28 dB/μm (R^2=0.72) in the tumor axial profile is within 7% of the slope for normal cortex and represents normal tissue. The maximum tumor depth of 650 μm, which correlated with histology, was determined by the intersection of the two fitted lines.

Subsurface visualization of the tumor and its margins is demonstrated by the 3-D projections shown in Figure 6-3. The 3-D data set was rotated in the horizontal and vertical planes to view the tumor at arbitrary angles. Rotation direction is indicated with respect to the superior-inferior and medial-lateral axes. Four viewing angles are shown in Figure 6-3. The two vertically rotated projections (Figure 6-3C and D) show the lower boundary of the tumor with regions that penetrate deeper into normal cortex (arrows in Figure 6-3D). These regions of tumor can be further visualized by sectioning the three-dimensional data set at planes parallel to the cortical surface as shown in Figure 6-4. The top image in Figure 6-4 illustrates the section plane orientation through the tumor. Sections 100-1200 μm below the cortical surface are shown in Figure 6-4. The tumor distribution, which appears white, is shown at varying depths. The section at 1100 μm depth indicates a small region of tumor (arrow) which has penetrated beyond the central lesion. The color-scale transition of normal cortex from light yellow (at 100 μm) to dark red (at 1200 μm) is a result of signal attenuation with increasing depth. The darkest region (arrow) shown most prominently at 1200 μm depth is the result of shadowing from the tumor above.

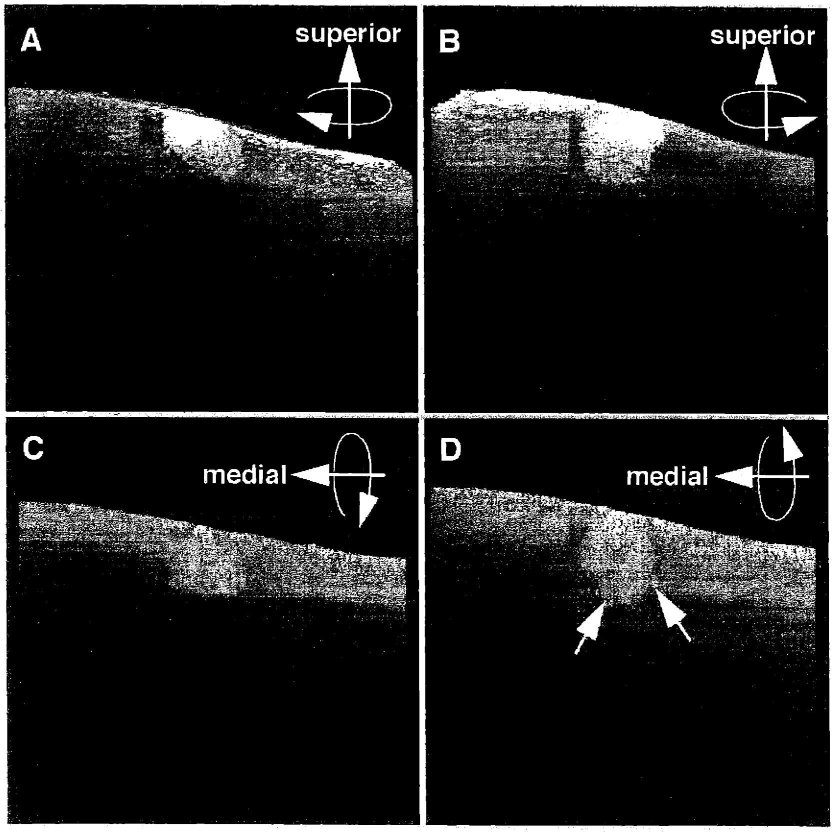

FIGURE 6-3: Three-dimensional projections of malignant intracortical melanoma. Arrows indicate direction of horizontal (A,B) and vertical (C,D) rotation with respect to superior and medial axes. The two additional arrows in D show regions of tumor penetrating away from the bulk tumor into normal cortex.

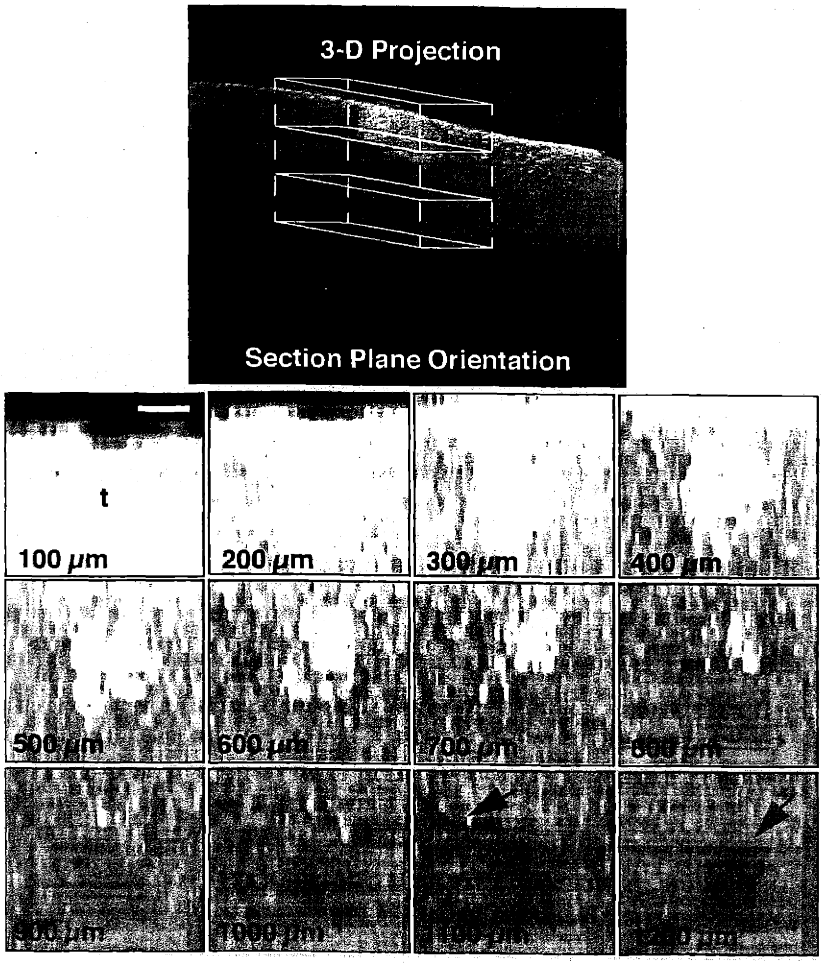

FIGURE 6-4: Resectioning of 3-D brain tumor data set. Resectioning produces planar sections from data sets acquired in cross-section. Arrow at 1100 μm indicates deepest tumor (t) extent. Arrow at 1200 μm indicates shadowing from tumor above. Bar represents 500 μm.

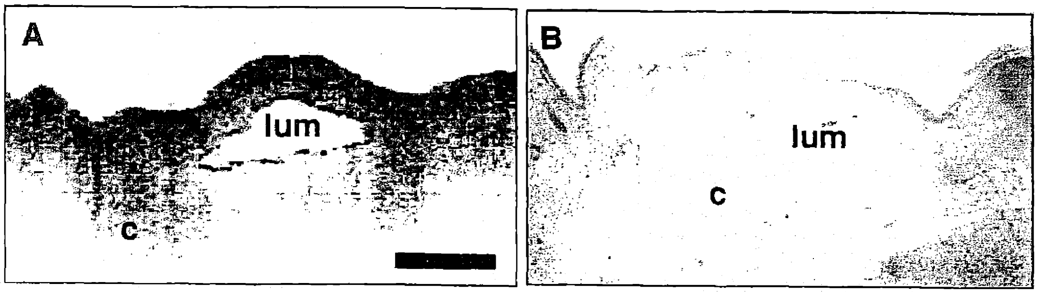

FIGURE 6-5: Cerebral vasculature. A) OCT image and B) corresponding histology of a subsurface cerebral artery. Artery is clearly distinguished in the OCT image by variations in optical backscatter between the intima, media, and adventitia. Abbreviations: c, cortex; lum, cerebral artery lumen. Bar represents 500 μm.

During tumor resection, cerebral vascular structures must be avoided. OCT has the potential to identify subsurface vascular structures as shown in Figure 6-5. The lumen of the cerebral artery is patent and clearly shown in the OCT image. Individual arterial layers corresponding to the intimal and media can also be identified. The intima appears as a thin, highly backscattering region surrounding the lumen of the artery. The less-backscattering media is noticeably thicker. The cerebral artery is surrounded by normal, relatively homogeneous cortex. The morphology observed in the OCT image correlates well with the corresponding histology. Light microscopy of this histological specimen confirms the arterial morphology.

These results demonstrate micron-scale optical coherence tomographic imaging of *in vitro* metastatic melanoma in the human brain. The OCT images acquired with the probe in Figure 6-1 show excellent correlation with the corresponding histology despite the histological sectioning artifact in Figure 6-1E. This artifact is likely due to the different mechanical tissue properties between normal cortex and tumor, which resulted in different tensions across the microtome blade. The tumor shows increased optical backscatter compared to normal cortex. The difference likely results from the higher concentration of subcellular organelles (i.e. nuclei and mitochondria) in the tumor compared with the high concentration of loose supportive tissue in the gray matter[226]. However, melanin within this particular tumor may also contribute. OCT relies on the inherent contrast within tissue rather than the addition of exogenous dyes. Contrast within images is therefore determined by variations in the index of refraction as would occur between tumor and normal cortex. Future studies will have to examine other tumor morphologies which do not contain melanin, such as astrocytomas and glioblastomas, to determine their imaging properties.

The depth of penetration for OCT imaging in cortical brain tissue is somewhat limiting. However, once a tumor is identified and resection begins, OCT can continually image ahead of the resection plane to search for the tumor margin or subsurface vessels. The use of OCT for optical biopsy may permit the non-excisional imaging of the walls of the brain cavity to ensure all tumor has been removed.

The fiber-optic based OCT instrument and probe rely on the well-established technology of the communications industry and are therefore reliable and robust. The use of optical fibers permit compact and portable instrument designs as with the hand-held surgical probe. Because of the small design, implementation in the surgical field is less obtrusive particularly since the remainder of the OCT instrument can be located elsewhere in the room. The fiber-optic based OCT may also be integrated with scalpels and forceps rather than introducing another instrument into the field. The noncontact nature of light would permit forward-directed imaging prior to tissue incisions. High-power laser radiation may be coupled into the probe to allow simultaneous OCT imaging with focused laser therapy and ablation. The surgical probe design uses a single piezoelectric cantilever for scanning and is therefore limited to 2-D scanning.

Three-dimensional OCT imaging permits multi-angle visualization of the tumor and its extent as shown in Figure 6-3. Although axes orientation and direction of rotation are provided, 3-D information is best obtained by observing rotation in real-time. Planning for surgical resection may be improved by the acquisition of 3-D data sets intraoperatively. The rapid acquisition of 3-D volumes permits computer-based sectioning of the data sets at arbitrary planes as was demonstrated in Figure 6-4. In this example, planes sectioned parallel to the cortical surface provided visualization of tumor distribution as would be encountered at increasing depths during tumor resection.

The resolutions achieved in this study were as high as 16 μm, higher than any current ultrasound, CT, or MRI intraoperative imaging technique. This allowed the tumor-cortex interface and the extent of tumor below the surface to be defined with high resolution. Resolutions as high as 2-3 μm have been achieved using solid-state ultrafast laser sources[88,89]. At these resolutions, it may be possible to image individual tumor cells which have migrated away from the central tumor. Resection must include these cells to prevent regrowth. High-speed OCT imaging will be required for *in vivo* imaging to eliminate motion artifacts within images. Although studies are required to determine which acquisition rates are necessary for *in vivo* imaging, early experimental observations suggest that rates of 8-16 frames per second are sufficient. OCT represents a new high-resolution optical imaging technology that has the potential for identifying brain tumors and tumor margins on the micron scale and in real-time. OCT offers imaging performance not achievable with current imaging modalities and may contribute significantly toward the surgical resection of brain tumors.

6.2.2 Peripheral nervous system

The peripheral nervous system encompasses distal nerves that relay sensory and motor signals to and from the central nervous system. Peripheral nerves are frequently injured during complex surgical procedures and trauma, often requiring the microsurgical anastomosis or reconnection of the two severed ends[25]. The incidence of neurosensory changes in the oral cavity and lip ranges from 0.4% to 11.5% following mandibular third molar removal because of the proximity to the lingual and inferior alveolar nerves[227]. Trauma seen at military medical units during troop engagements are predominantly of the limbs[133]. Of all injuries, 75% are the result of explosive ammunition while 25% are from bullets from small arms[228]. Therefore, multiple site involvement is common. A peripheral nerve is actually a bundle of fascicles contained within an outer sheath called the epineurium. Microsurgical anastomosis can be performed either epineurally or perineurally[229]. Epineural anastomosis involves suturing only the outer neural sheath. Greater neural function is restored if the corresponding fascicles can be aligned during perineural attachment. This, however, requires the identification of fascicles based on the longitudinal orientation and the relative diameter. Currently, no technique exists for obtaining this information without physically dissection of the nerve *ex vivo*.

OCT has been used to image *in vitro* peripheral nerves and identify individual fascicles[230]. Longitudinal tracking of the spatial orientation of rabbit peripheral nerve fascicles is demonstrated in Figure 6-6 using OCT. Representative cross-sectional images (3 x 2.2 mm, 300 x 600 pixels) of the peripheral nerve are shown in Figure 6-6A-D. For each slice, one fascicle was manually segmented, colored white, and tracked through the acquired volume of data. Forty images at 100 μm spacing were assembled for the 3-D projections shown in Figure 6-6E and F. The horizontally- and vertically-rotated projections of the peripheral nerve dramatically reveal the twisted path of the segmented fascicle along the longitudinal axis of the nerve. In addition, a branch in another, unsegmented fascicle is observed in Figure 6-6F. Previously, this feature had not been recognized from examining the 2-D images.

OCT image data of a human retroperitoneal nerve was correlated with corresponding histology in Figure 6-7. The human retroperitoneal nerve illustrates the imaging of individual fascicles and correlates well with histology. Because of the large diameter of this nerve, the OCT optical beam is attenuated and deeper fascicles (f_3 and f_4) are somewhat difficult to resolve, except for the sheath surrounding each fascicle.

Precision realignment of individual nerve fascicles increases the likelihood that end-organ function will be restored after peripheral nerve reconstruction[231]. These results show that OCT can image peripheral nerves in cross-section and that individual fascicles can be identified and segmented. The use of OCT to acquire multiple cross-sectional images and three-dimensionally reconstruct the peripheral nerve offers the opportunity to determine the relative diameters of individual fascicles and to longitudinally track their spatial orientation. The 3-D projection of the segmented peripheral nerve in Figure 6-6F not only revealed the twisted course of one fascicle, but also revealed a bifurcation of a second fascicle, a feature not previously appreciated from the 2-D images. Three-dimensional imaging increased the information content of the acquired data.

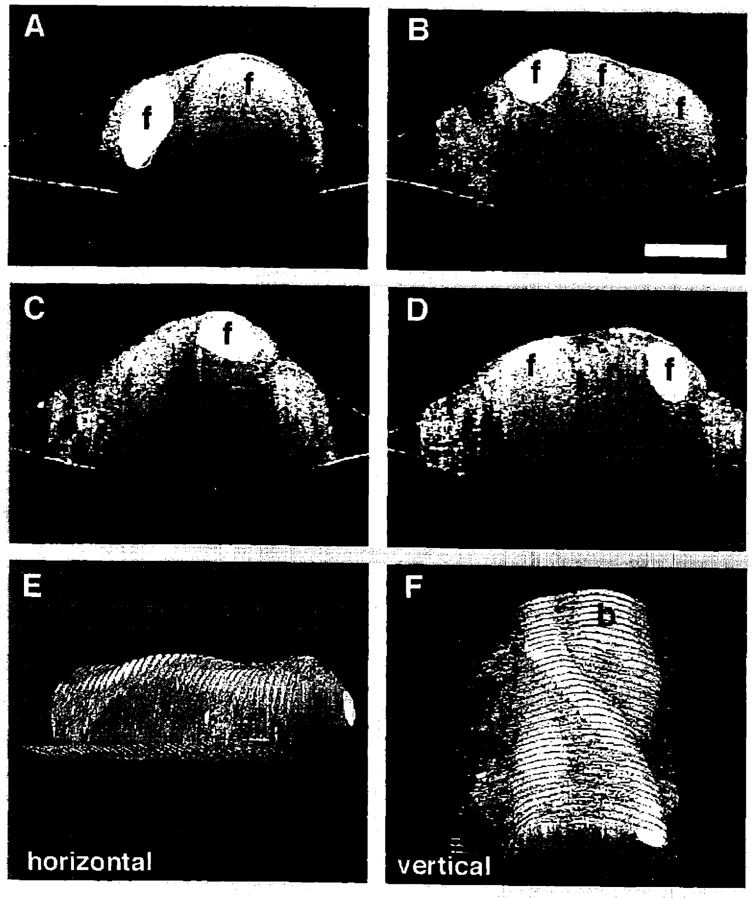

FIGURE 6-6: Longitudinal tracking of rabbit peripheral nerve fascicles (A-D). A single fascicle was segmented and followed longitudinally along the length of the nerve. E,F) 3-D projections rotated in the horizontal and vertical directions. Abbreviations: b, bifurcation; f, fascicle. Bar represents 1 mm.

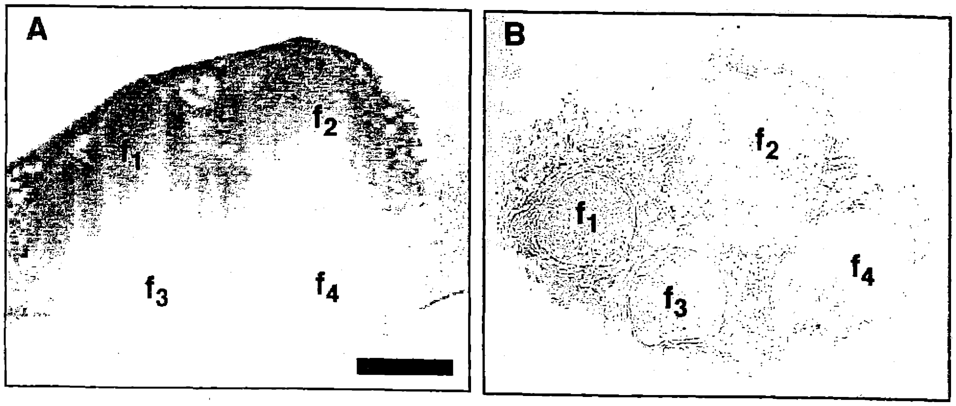

FIGURE 6-7: Correlation of OCT image of peripheral nerve with corresponding histology. Individual fascicles (f) are numbered. Bar represents 1 mm.

6.3 Cardiovascular System

Heart and cerebrovascular diseases represent the first and third leading causes of death in the United States[213]. Because of these statistics, tissues of the human cardiovascular system have been extensively investigated with OCT. *In vitro* coronary arteries have been imaged to identify thin- and thick-walled plaques[70]. Radial catheter-based OCT imaging has been compared with current intravascular ultrasound (IVUS)[232,233]. *In vivo* OCT catheter-based imaging has been performed in the rabbit aorta[234]. The cardiovascular system represents tissue that cannot readily be excised for histopathologic examination. Because of this, a non-excisional approach for diagnostics and surgical guidance would have a significant impact on the quality of patient care. The use of OCT to guide and assess the surgical anastomosis or re-attachment of severed vessels is investigated in this section.

6.3.1 Microsurgery of vessels

The repair of injured vessels and nerves is necessary to restore function following traumatic injury[235]. Although the repair of sensitive structures are performed with the aid of surgical microscopes and loupes to magnify the surgical field[24], surgeons are limited to the *en face* view that they provide. A technique capable of subsurface, three-dimensional, micron-scale imaging in real-time would permit the intraoperative monitoring of microsurgical procedures, offering immediate feedback to the surgeon and a likely improvement in patient outcome. The capabilities of OCT for the intraoperative assessment of microsurgical procedures are demonstrated[230]. High-speed OCT imaging is integrated with the surgical microscope described in Section 3.3 to performed micron-scale three-dimensional imaging on microsurgical specimens.

To demonstrate the use of OCT imaging for diagnostically assessing microsurgical procedures, *in vitro* microsurgical specimens were first acquired from animal and human tissue. Segments of inguinal-area arteries were resected from a 3.5 kg New Zealand White rabbit immediately after the rabbit was euthanized with a 5 ml injection of sodium pentobarbital (65 mg/ml). The specimens were immediately placed in 0.9% normal saline and stored at 0 °C. An artery segment was bisected cross-sectionally with a scalpel and then re-anastomosed. A No. 10-0 nylon suture with a 50 µm diameter needle was used to place a continuous suture and perform an end-to-end anastomosis. For precise registration of 3-D images, the anastomosed segment was positioned on micron-step, computer-controlled, motorized translational stages in the sample arm. A series of 40 cross-sectional images were acquired perpendicular to the long axis at 100 µm interval spacing. Imaging was performed through the anastomosis site and several millimeters on either side. Following imaging, the specimen was digitally imaged with a CCD camera.

As a demonstration of the ability of OCT to locate vessels embedded in highly scattering tissue in real-time, a 1 cm^3 block of human tissue was removed from the left lateral ankle of an amputated foot, immediately placed in 0.9% normal saline, and stored at 0 °C. The foot had been amputated as a result of complications associated with vascular insufficiency secondary to diabetes. The block of tissue was manually manipulated under the surgical microscope while OCT imaging was being performed at 8 frames per second in a single cross-sectional plane. Images were acquired and stored directly to S-VHS video tape while being viewed on a monitor. The magnified scan location was directly viewed through the surgical scope as various locations were imaged in search of subsurface morphology. Specimens to be processed for histological comparison were placed in 5% buffered formaldehyde immediately after imaging and later embedded in paraffin, sectioned, and stained with hematoxylin and eosin.

Cross-sectional OCT images and 3-D data set projections were processed and displayed using rendering software (NIH Image 1.60). A color-scale table was assigned to the logarithm of the data in each image in a manner analogous to ultrasound. Multiple slices were assembled into a stack and used to generate projections of the 3-D data set. The projections were rotated in the x, y, and z planes to view particular features and determine planes at which arbitrary sections could be displayed.

The ability of OCT to assess internal structure and luminal patency within an arterial anastomosis was demonstrated by acquiring cross-sectional OCT images (2.2 x 2.2 mm, 250 x 600 pixel) and 3-D projections of a 1 mm diameter rabbit inguinal artery shown in Figure 6-8A. Two-dimensional cross-sectional images in Figure 6-8B-E were acquired from the locations labelled in Figure 6-8A. Figure 6-8B and E were acquired from each end of the anastomosis. These images clearly show arterial morphology corresponding to the intimal, medial, and adventitial layers of the elastic artery. The muscular media appears less backscattering than the adventitia which merges with the surrounding collagenous tissue. The patent lumen is readily apparent. This is in contrast to what is observed in Figure 6-8D where at the site of anastomosis, the lumen had been obstructed by a tissue flap. The image in Figure 6-8C reveals a tissue flap in cross-section. Note that the presence of additional tissue has attenuated the signal from the lower wall and hence, reduces the ability to resolve individual layers. By assembling a series of cross-sectional 2-D images, a 3-D data set was produced. From this data set, arbitrary planes can be selected and corresponding sections displayed. For an arterial anastomosis, often it is more informative to image longitudinally along the axis of the artery and through the anastomosis site. Figure 6-8H is a longitudinal section from the 3-D data set which confirms the occlusion within the anastomosis site.

Three-dimensional projections of the arterial anastomosis are shown in Figure 6-8F and G. These horizontally- and vertically-rotated projections are comprised of 80 slices at 50 μm spacing. At this high slice density, the internal structure shown in Figure 6-8B-E is difficult to visualize. However, high slice densities are necessary if the 3-D data set is to be sectioned at arbitrary planes as shown in Figure 6-8H. Additionally, micron-scale surface features which were not readily apparent from the 2-D slices are more prominent.

OCT image data was correlated with corresponding histology in Figure 6-9. Cross-sectional images were acquired from a rabbit arterial bifurcation. The arterial segment was imaged distal to the bifurcation and two independent lumens are shown. The OCT image clearly resolves individual layers within the arterial wall and demonstrates patent lumens. Above the arteries is a region of adipose tissue which appears less backscattering in the OCT image except for the nuclei and cell walls.

The OCT instrument was integrated with a surgical microscope to obtain the images shown in Figure 6-10. Because the OCT imaging beam and visible aiming beam were co-aligned with the optical axis of the microscope, the scan location on the specimen could be directly viewed through the microscope. A block of tissue was manually manipulated under the microscope while images (3 x 2.75 mm, 256 x 256 pixels) were acquired at 8 frames per second. Subsurface microsurgical structures were immediately identified including numerous small arteries, veins, nerves, and even a vascular clip from previous surgical repair. All structures were embedded in adipose and connective tissue. Figure 6-10A illustrates a cross-section of an artery located 500 μm below the surface and surrounded by adipose tissue. This artery could not be visualized with the microscope alone. The image clearly shows the characteristically thick wall and multiple layers of the artery. To the right of the artery is a portion of dense connective tissue which does not have the clear, low-backscattering regions present in adipose tissue. Figure 6-10B is a longitudinal section of the same artery after the tissue block had been rotated by 90°. The thick arterial wall is readily identified. The right edge of Figure 6-10B shows an oblique cross-section of a vein with its characteristic thin wall.

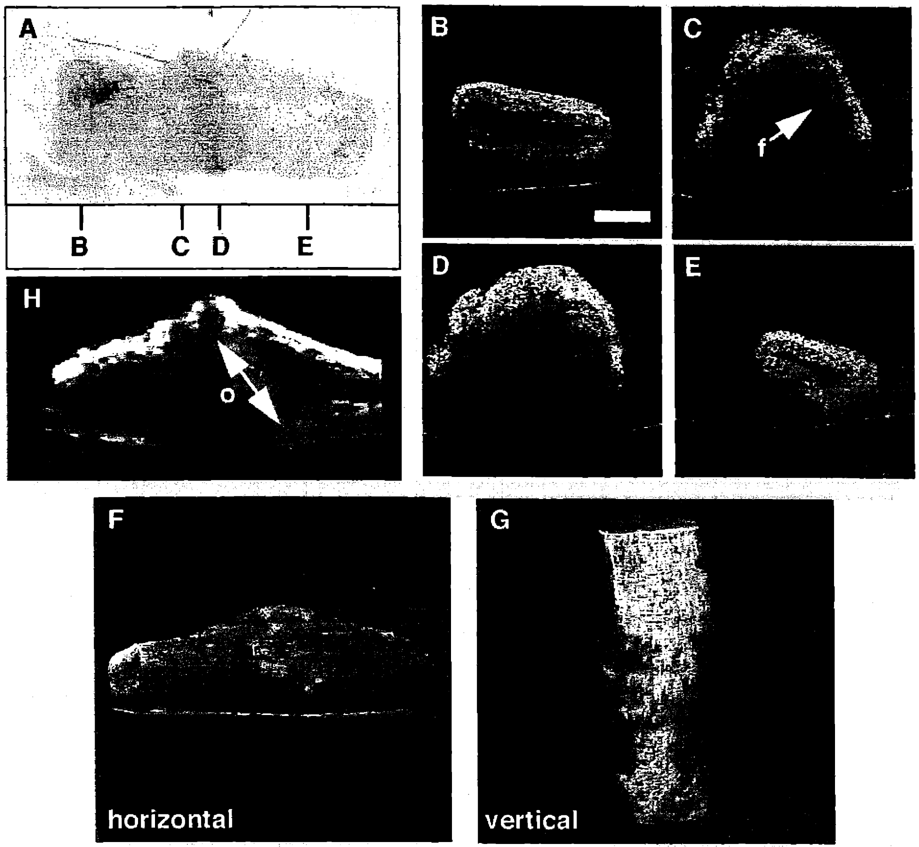

FIGURE 6-8: Arterial anastomosis. Labelled vertical lines in A refer to cross-sectional imaging locations (B-E) from an anastomosis of an *in vitro* rabbit artery. An obstructive flap is identified in C. By resectioning the 3-D data set, a complete obstruction is observed in H. Horizontally- and vertically-rotated 3-D projections are shown in F and G, respectively. Abbreviations: f, flap; o, occlusion. Bar represents 1 mm.

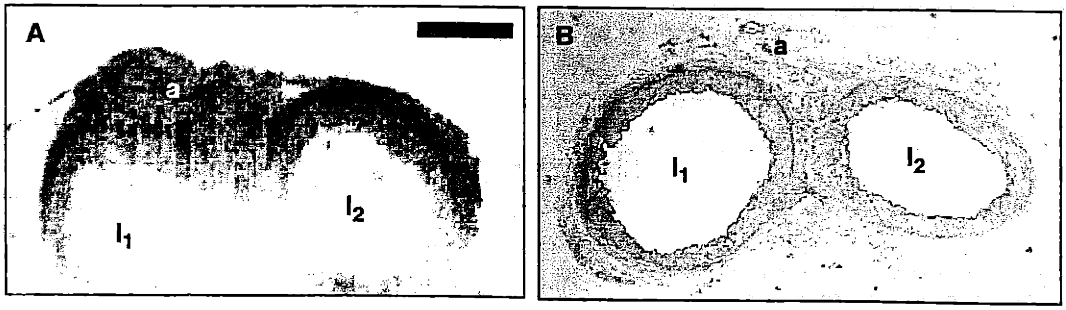

FIGURE 6-9: Arterial bifurcation correlated with histology. The OCT image of a rabbit arterial bifurcation shows multiple layers within the arterial wall. Abbreviations: a, adipose tissue; l_1, l_2, arterial lumens. Bar represents 1 mm.

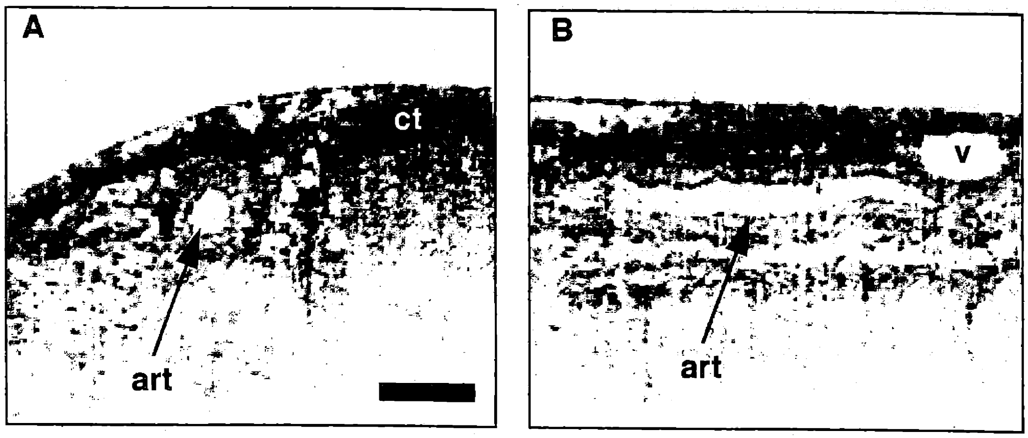

FIGURE 6-10: High-speed (8 fps) imaging of embedded *in vitro* human vessels. A) Cross-sectional image of artery adjacent to connective tissue. B) The same artery was rotated and viewed in longitudinal cross-section. An oblique cross-section of a vein is also observed. Abbreviations: art, artery; ct, connective tissue; v, vein. Bar represents 500 μm.

During microsurgical procedures, patient outcome can be substantially influenced by the ability of the surgeon to assess tissue microstructure[236]. The use of a surgical microscope serves to magnify the tissue, but only provides a surface, or *en face*, view. OCT should improve intraoperative diagnostics by providing high-resolution, subsurface, cross-sectional imaging of vessels in real-time.

The *in vitro* arterial anastomosis imaged in Figure 6-8 demonstrated the ability to assess internal structure within an anastomosis site and evaluate patency. Intraoperative assessment of luminal obstructions is critical if a successful procedure is to be performed. OCT can be used to identify the location of the obstruction and the longitudinal extent. This would include the presence of a thrombogenic adventitial flap or intimal inversion which predisposes the site to post-operative subacute occlusion.

The capabilities of an integrated surgical microscope have been demonstrated by acquiring *in vitro* images of subsurface human vessels at 8 frames per second. Integrating high-speed OCT imaging with a surgical microscope was a challenge. An aberration-free beam had to be tightly focused at a long working distance and maintained throughout the entire scan range. Integration with the surgical microscope permitted not only *en face* visualization, but also cross-sectional OCT imaging, simultaneously. The microscope-based OCT system was used to demonstrate the potential of OCT for preventing iatrogenic injury during surgical procedures. Vessels, which could not be identified from *en face* imaging, were clearly identified in OCT images. Performance of many fine surgical procedures in vulnerable tissue would likely benefit from high-resolution subsurface imaging. In an analogous manner to Doppler ultrasound, OCT may be configured to perform laser-Doppler velocimetry as described in Section 5.4. This technique has been used to measure blood flow velocities through *in vivo* animal model vessels[165] and may be useful for assessing perfusion following vascular anastomosis.

Potential limitations of OCT imaging are the maximal penetration and the effect of blood on imaging. Utilizing longer wavelengths in the near-IR, imaging depths have been increased from 1 mm up to 2-3 mm due to decreased optical absorption and scattering in tissue. These depths may still appear somewhat limiting. However, the majority of microsurgical complications occur in vessels and nerves less than two millimeters in diameter and are suitable for OCT imaging. The presence of blood in the surgical field may influence the quality of OCT images.

These results have shown the 3-D imaging capabilities of OCT and how acquired images can provide diagnostic feedback to assess microsurgical anastomoses. This previously unavailable diagnostic ability offers the potential to directly impact and improve patient outcome by incorporating high-speed, high-resolution intraoperative image-guidance during microsurgical procedures.

6.4 Reproductive System

The use of MIS and diagnostic optical techniques are frequently applied to imaging the organs of the female reproductive tract. Laparoscopic imaging is becoming the gold-standard for diagnostic and surgical gynecological procedures such as tubal ligation, management of benign ovarian cysts, and oophrectomy. Laparoscopy is used as a second-look procedure when ultrasound resolutions fail to diagnose ovarian pathology and has been suggested as a surgical screening tool for the early detection of ovarian cancer[237]. Although laparoscopy provides a closer look at tissue structure, only surface features are visible and subsurface microstructural abnormalities are undetectable. A non-excisional means of imaging tissue at near-histological resolutions has the potential to improve diagnostic capability without the need to physically resect suspect samples of sensitive tissue. Improvements in imaging and diagnosing early neoplasms will likely have a subsequent reduction in patient morbidity and mortality.

OCT was used to image over eighty sites on laparoscopically-accessible gynecological pathology to demonstrate a feasibility for imaging and assessing normal and abnormal microstructure[238]. Images are correlated with histology. High-speed non-excisional OCT imaging through laparoscopes has the potential to increase and improve sampling without the need for physical resection. Intraoperative OCT imaging has the potential for *in situ* diagnoses of early-stage gynecologic neoplasms.

6.4.1 Uterus

The laparoscopic approach to the uterus is transabdominally. The peritoneal surface of the uterus is often the site of endometrial foci. Endometriosis is the transplantation of endometrial cells from the interior uterine wall to sites on the peritoneal abdominal wall, peritoneal surface of the uterus, ovaries, or fallopian tubes. Theory suggests that this occurs as a result of cells passing through the fallopian tubes following endometrial wall shedding[239]. The growth of endometrial sites results in extreme abdominal pain. In a recent US Health Interview Survey, 50% of those reporting having endometriosis had stayed in bed all day because of their condition at some time during the past year, with the average of 17.8 bed-days[240]. Thus, this disease is costly in terms of a woman's quality of life, medical expenses, and impact in the workplace. Because endometriosis can only be definitively diagnosed during a course of pelvic surgery or laparoscopic exam, prevalence estimates are based on surgical populations. Endometriosis was diagnosed in approximately 25% of women (range is 4.5% to 82% across all studies) who had laparoscopy because of pelvic pain[241]. Surgical treatment is by laparoscopic-guided ablation of foci with either electrosurgery, radio-frequency electrodes, or a laser. Visual determination of endometrial sites is difficult, relying solely on color cues. Foci can also be located below the peritoneal surface making *en face* visualization and diagnosis uncertain. OCT was used to image subsurface endometrial foci to demonstrate a feasibility for improved discrimination.

The amplified superluminescent source described in Section 2.4.1 was used for imaging. Human uterus samples were obtained postmortem, stored in saline, and imaged within 24 hrs. Cross-sectional OCT images (6 x 3 mm, 600 x 400 pixels) were obtained from the peritoneal surface of each specimen with the orientation consistent with that encountered during a laparoscopic examination. Immediately following image acquisition, the location of the image plane was marked with India ink for registration between OCT images and histology. Specimens were placed in a 10% buffered solution of formaldehyde for standard histological preparation. Histological sections, 5 μm thick, were sectioned and stained with hematoxylin and eosin for comparison with acquired OCT images. Correspondence was determined by the best match between OCT images and light microscopy observations of the histology.

Figure 6-11 compares and contrasts normal uterus with a site of endometriosis. Both images were acquired from the peritoneal surface as would be imaged laparoscopically. The normal peritoneal uterine surface in Figure 6-11A and B shows a relatively smooth peritoneal surface with occasional invaginations. Small regions of adipose cells surrounded by normal myometrium are observed in both the OCT image and histology. This is in contrast to the endometriosis observed in Figure 6-11C and D. The elevated peritoneal surface with irregular boundaries and glandular spaces is indicative of secretory endometrium. It is this tissue morphology that is believed to result in extreme abdominal pain.

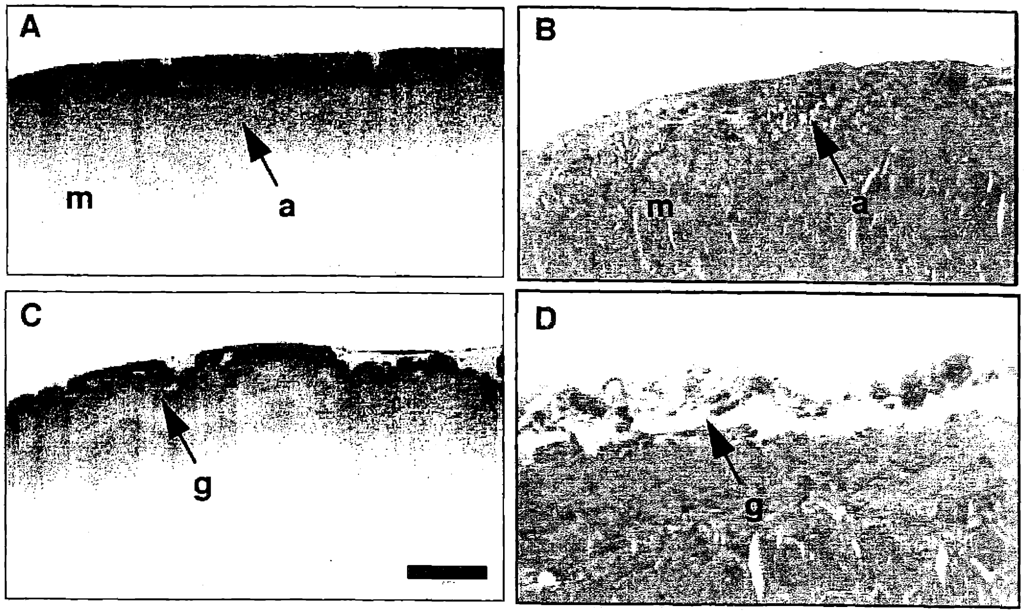

FIGURE 6-11: Endometriosis. A,B) Normal peritoneal surface of *in vitro* human uterus and C,D) endometriosis with corresponding histology. Abbreviations: a, adipose cells; g, glandular tissue; m, myometrium. Bar represents 1 mm.

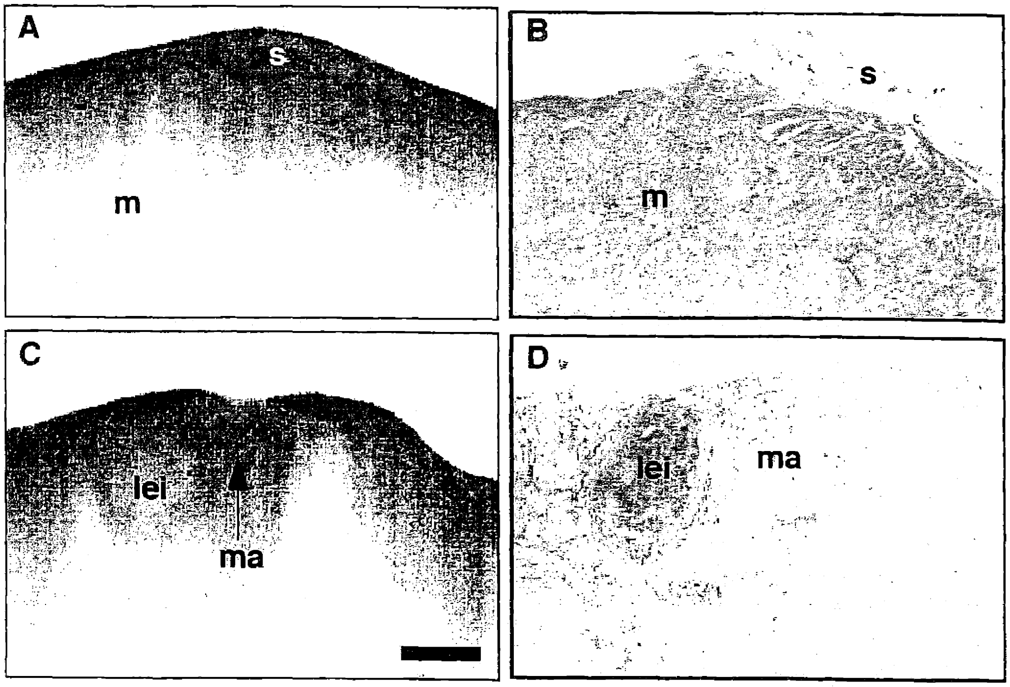

FIGURE 6-12: Ovarian adenoma on human uterus. A,B) Normal *in vitro* uterine peritoneum compared and contrasted with C,D) ovarian adenoma spread to uterus. Abbreviations: lei, subserosal leiomyoma; m, myometrium; ma, metastatic adenoma; s, serosa. Bar represents 1 mm.

The peritoneal surface of the uterus can also exhibit other abnormal tissue morphology. The OCT images and histology in Figure 6-12 compare and contrast the normal peritoneal surface of the uterus with that of an ovarian adenoma that had spread to the peritoneal surface of the uterus. This likely resulted from contact between the two organs. The normal uterus in Figure 6-12A and B is relatively homogeneous. Serosal tissue is shown adjacent to the uterus myometrium. The ovarian adenoma in Figure 6-12C and D show characteristic glandular morphology which is difficult to resolve in the OCT image at these resolutions. A sub-serosal leiomyoma is also observed adjacent to the glandular morphology of the adenoma. The use of OCT to identify subtle morphological changes, as seen here, is a powerful application for diagnostics. In addition, the use of OCT laparoscopy can guide the surgical ablation of suspect tissue sites or the placement of biopsy forceps when tissue specimens are physically resected for histopathological examination.

6.4.2 Ovary

Ovarian cancer has a high mortality rate largely due to poor techniques for early detection. In 1997, 54% of the deaths from cancers of the female reproductive system were due to ovarian cancer[242]. High-resolution OCT imaging from the external surface of the ovary can identify atypical morphology as is shown in Figure 6-13. Normal ovary is relatively homogeneous compared to the cystic and papillary structures observed in the ovarian tumor.

The ability to image and diagnose early precursors of ovarian cancer[243,244] would enable more effective treatment options and improved patient outcomes. Laparoscopy is one minimally invasive technique which enables diagnostics and surgery to be performed with decreased morbidity. Although laparoscopy offers exceptional visualization of remote, internal tissue, imaging is limited to surface features. OCT enables cross-sectional, subsurface imaging of biological structure. The combination of these two techniques has the potential for significantly improving the ability to non-excisionally sample suspect gynecological tissue at high resolutions.

Subsurface OCT imaging of laparoscopically-accessible gynecological tissue has been demonstrated. Correlations with corresponding histology are strong, suggesting that OCT can accurately represent the morphological tissue structure. Two engineering advancements are necessary before *in vivo* laparoscopic imaging is feasible: the construction of a steralizable OCT laparoscope and improvements in image resolution. Current laparoscopes are designed to image at visible wavelengths. Special optics and optical coatings are required to permit simultaneous visualization at visible wavelengths and OCT imaging at near-IR wavelengths. The OCT imaging beam is invisible to the human eye, however, a visible aiming beam can be co-linearly aligned to permit the OCT scan location to be visualized through the laparoscope. Although the image resolutions in this study permitted the definition of microscopic morphology, resolutions were not high enough to definitively image individual cells. Higher resolutions will improve the intraoperative diagnostic ability of OCT. If an accurate diagnosis could be made in real-time, OCT could guide surgical resection without requiring the patient to return to the surgical suite for a second surgical procedure.

OCT imaging of laparoscopically-accessible gynecological tissue suggests a feasibility for integrating this technology into a clinically useful device. Demonstrated performance of current laparoscopic imaging may be improved by OCT imaging of subsurface morphology in real-time at near-histological resolutions. The use of OCT for the early detection of neoplasms without having to physically resect sensitive tissue has the potential for improvement in treatment protocols and a reduction in patient morbidity and mortality.

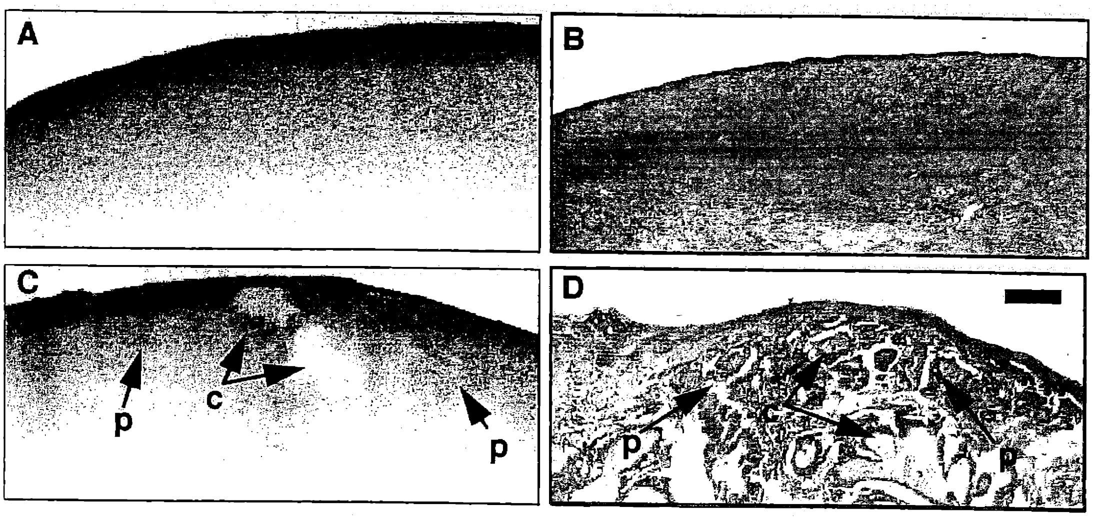

FIGURE 6-13: Ovarian cancer. Normal *in vitro* human ovary (A,B) and ovarian cancer (C,D) with corresponding histology. Abbreviations: c, cystic cavities; p, papillary structures. Bar represents 500 μm.

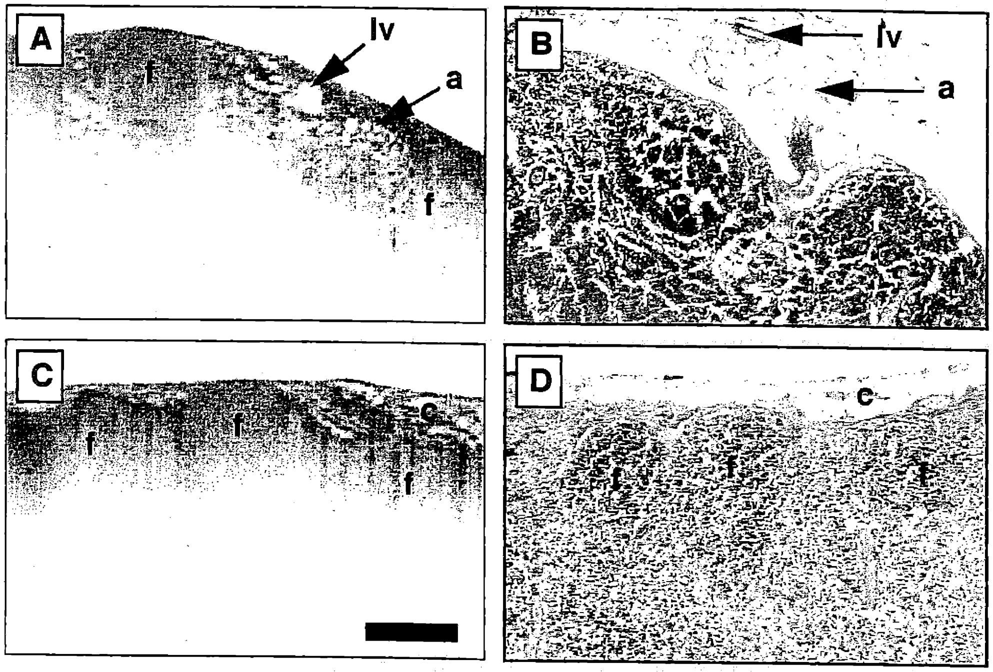

FIGURE 6-14: Pediatric lymph nodes. *In vitro* pediatric lymph nodes show characteristic follicular structures. Abbreviations: a, adipose tissue; c, capsule; lv, lymphatic vessel; f, fascicle. Bar represents 1 mm.

6.5 Immune System

Recent advances in minimally invasive laparoscopic surgery have been applied to the pediatric oncology patient for tumor staging, assessment of resectability, and evaluation of recurrent and metastatic disease[245]. Hodgkin's Disease, non-Hodgkin's lymphoma, and the leukemias are malignant tumors of the immune and lymph system. For male children and young adults between the ages of 15 and 34, leukemia and non-Hodgkin's lymphoma represent the two leading causes of death due to cancer[213]. Staging of the tumor can be performed laparoscopically[246] with subsequent lymph node biopsy. Staging requires sampling of numerous lymph nodes, only a few of which can be physically resected for histopathologic examination. Ultrasonography has been used to image relative sizes of normal and abnormal lymph nodes *in vitro*, but resolutions were not sufficient to resolve internal architecture[247]. A means of optically imaging the architectural morphology of lymph nodes in real-time with high-resolution and without having to physically resect and histologically prepare specimens would permit the rapid intraoperative staging of tumor extent.

The feasibility of using OCT to image subsurface architectural morphology in pediatric lymphoid tissue is demonstrated[248]. The ability to image subsurface lymph node microstructure offers the potential for reducing the number of biopsies necessary to stage tumors not only in the pediatric population, but also in adult malignancies as well. Integration with current laparoscope designs will permit simultaneous subsurface OCT imaging with existing *en face* visualization. By sampling greater numbers of lymph nodes, a potential exists for more accurate tumor staging, more precise treatment protocols, and a reduction in patient morbidity.

The Kerr-lens modelocked solid-state Cr^{4+}:forsterite laser described in Section 2.4.2 was used for imaging. Pediatric thymus and cervical lymph nodes were obtained postmortem, stored in saline, and imaged within 24 hrs. Thirty-five cross-sectional OCT images (2 x 1 mm, 500 x 500 pixels) were obtained from the outer surface of each specimen with the orientation consistent with that encountered during a laparoscopic examination.

Two cross-sectional OCT images of two cervical pediatric lymph nodes are shown with corresponding histology in Figure 6-14. The OCT images shows characteristic follicular morphology. A cross-section of a lymphatic vessel is identified in Figure 6-14A, surrounded by adipose tissue. The vessel and adipose tissue have been displaced in the histological section (Figure 6-14B) due to processing artifact. An outer capsule is noted in Figure 6-14C and D. Correspondence between OCT images and histology is strong. Much of the internal cortex is relatively homogeneous at these image resolutions.

An OCT image and corresponding histology of the thymus is shown in Figure 6-15. The outer collagenous capsule is clearly evident in Figure 6-15A, however, it has been lost during histological processing. Subsurface imaging was possible through the outer capsule and into the cortex of the thymus. Two deep invaginating septa are observed. The correspondence with histology is also strong although at this imaging resolution, individual cells are not observed.

The ability to accurately assess tumor stage and evaluate recurrent or metastatic disease allows more effective treatment options and improved patient outcomes. Laparoscopy is one minimally invasive technique which enables more sensitive tumor staging by lymph node involvement with deceased surgical morbidity. Although laparoscopy offers exceptional visualization of remote, internal tissue, imaging is limited to surface features. OCT enables cross-sectional, subsurface imaging of biological structure. The combi-

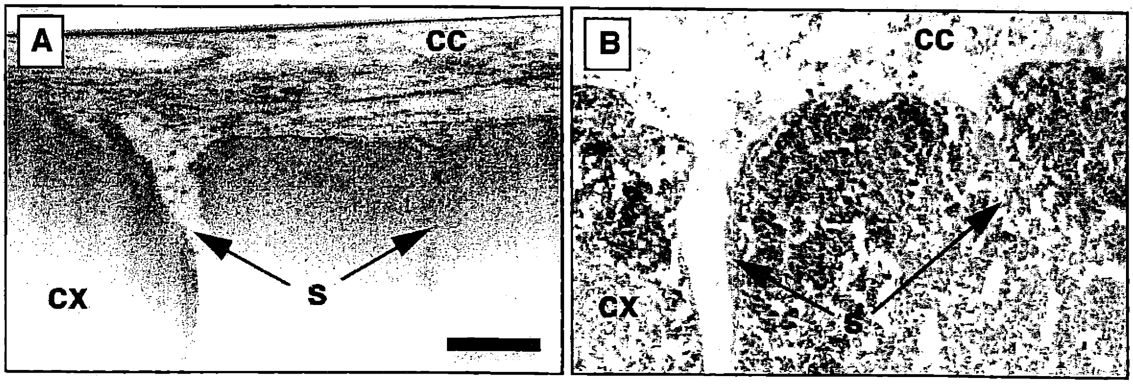

FIGURE 6-15: Pediatric thymus. *In vitro* pediatric thymus with characteristic septa. Abbreviations: cc, collagenous capsule; cx, cortex; s, septa. Bar represents 1 mm.

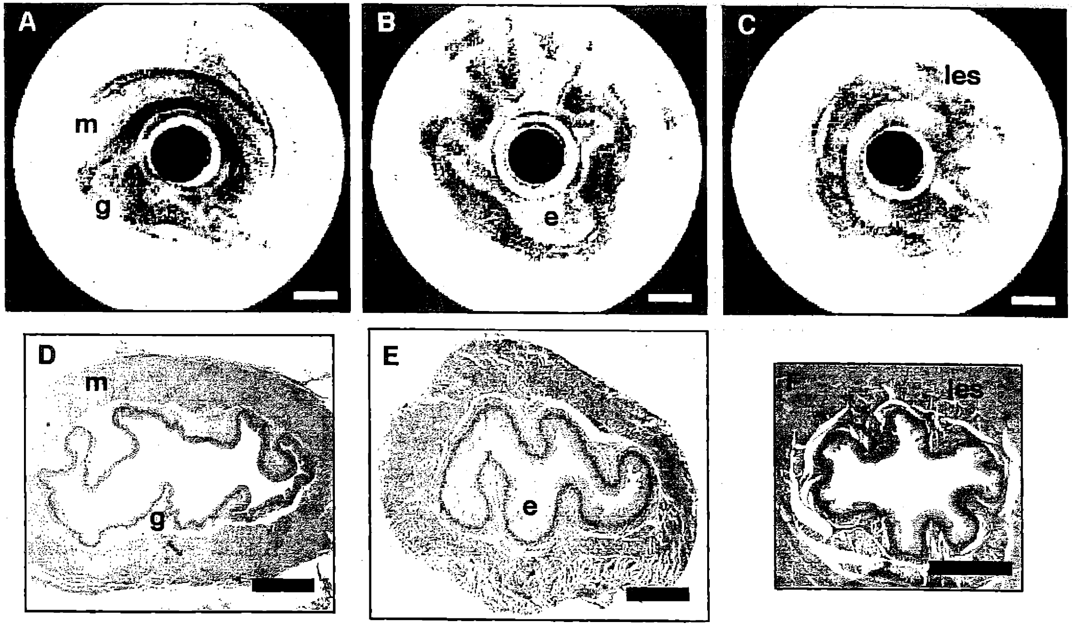

FIGURE 6-16: *In vivo* rabbit esophagus at three longitudinal positions. A,D) Proximal, B,E) Middle, and C,F) Distal. Abbreviations: e, stratified squamous epithelium; g, secretory glands; les, lower esophageal sphincter; m, muscular layers. Bar represents 1 mm.

nation of these two techniques has the potential for improving the ability guide surgical resection of lymph nodes for histopathological examination or to rapidly sample greater numbers of suspect lymph nodes and more accurately stage tumor involvement.

High-resolution subsurface OCT imaging of pediatric lymphoid tissue has been demonstrated. Correlations with corresponding histology are strong, suggesting that OCT can accurately represent the morphological tissue structure. Individual follicles were clearly identified along the outer margins of these normal lymph nodes. Future studies will compare follicular structure, patterns, and optical scattering properties of normal lymph nodes with those from patients with Hodgkin's disease and metastatic tumors.

OCT represents an optical imaging modality for high-resolution subsurface imaging in pediatric lymphoid tissue. Integrated with laparoscopic instruments, OCT may permit surgical guidance for lymph node biopsy or possibly the non-excisional optical sampling of lymph nodes for tumor staging.

6.6 Gastrointestinal System

The upper and lower gastrointestinal tracts are readily accessed with catheters and flexible endoscopes[249]. Diagnostic procedures provide *en face* visualization of the epithelial lining to evaluate colonic polyps or esophageal disorders. Surgical procedures include, among many, endoluminal resection of polyps and small tumors of the colon[37,250] and more recently, administering photodynamic therapy (PDT)[180,251] as a treatment for Barrett's esophagus. Barrett's esophagus is a condition where the stratified squamous epithelial lining of the lower esophagus is replaced by columnar epithelium of the stomach[252]. This dysplastic change is likely a result of acid reflux from the stomach and is found in up to 20% of patients who undergo endoscopic examination for evaluation of gastroesophageal reflux disease[253]. Patients with Barrett's esophagus are 30-40 times more likely to develop adenocarcinoma compared to the general population[212]. Therefore, these patients must be routinely examined endoscopically and biopsied. High-resolution imaging with OCT may be useful to sample large areas of the esophagus and to guide surgical biopsy for diagnosis. Imaging in *in vitro* human gastrointestinal tract has been performed with OCT[205,254]. Depths of penetration are sufficient to image through the esophagus mucosa and submucosa. Resolutions are sufficient to identify morphological changes of colonic inflammation and pseudomembranes.

To demonstrate high-speed catheter-based OCT imaging of *in vivo* esophageal mucosa, a rabbit animal model was used. A 5 kg New Zealand White rabbit was anesthetized with ketamine (35 mg/kg) and xylazine (5 mg/kg) given intramuscularly. Maintenance anesthesia was achieved with intravenous ketamine (8 mg/kg) and xylazine (1 mg/kg) administered via a marginal ear vein. Bite blocks were placed bilaterally to prevent damage to the catheter. The chin of the rabbit was placed forward and anterior with the tongue maximally extended to reduce the likelihood of entering the trachea. The OCT catheter was introduced into the upper gastrointestinal tract through the oral pharynx. The *in vivo* rabbit esophagus was imaged from the pharynx to the lower esophageal sphincter and into the stomach. Following imaging of the gastrointestinal and urinary tracts (described in Section 6.7), the rabbit was euthanized with an intra-arterial injection of 5 ml sodium pentobarbital (65 mg/ml). The esophagus was dissected out and sections from the proximal, middle, lower esophagus and lower esophageal sphincter were placed in formalin for standard histological processing. The established protocols for the care and handling of the animals used in this research were approved by the Committee on Animal Care, Massachusetts Institute of Technology.

Representative catheter-acquired images are shown in Figure 6-16. The upper esophagus, shown in Figure 6-16A and D reveal a large lumen with fewer folds. The OCT image in Figure 6-16A demonstrates full-thickness imaging through the esophageal wall. The OCT image in Figure 6-16B shows increasing numbers of folds. The lower esophageal sphincter is shown in Figure 6-16C and F. The esophageal wall is surrounded by smooth muscle. OCT imaging penetration falls off rapidly in this circumferential muscle layer.

The *in vivo* images of the rabbit esophagus epithelium suggest a feasibility for staging and following conditions such as Barrett's esophagus. Because early dysplastic changes result in the increase in numbers and size of epithelial nuclei, changes in optical backscatter may be able to identify suspect regions. Larger scale structural epithelial changes occurring in later stages of Barrett's esophagus will be even more evident. The depth of imaging in the esophagus suggests that deeper structures such as esophageal varices can be evaluated *in vivo* to guide surgical treatment of those which are prone to rupture.

6.7 Urinary System

The urinary tract represents a system that is readily accessed with catheters and endoscopic instruments[255]. Hence, a great deal of MIS procedures are performed to diagnose and treat diseases of the urinary system. OCT imaging has been performed on *in vitro* human tissue suggesting that *in vivo* imaging could resolve microstructure relevant to surgical procedures of the urinary tract[256]. The OCT radial imaging catheter is of suitable diameter to pass through the human urethra and into the bladder. In this section, OCT imaging is performed *in vivo* in a rabbit and on *in vitro* human specimens.

6.7.1 Bladder/Ureter

Bladder cancer was responsible for 11,700 deaths in 1997 affecting males twice as often as females[242]. Because of accessibility to the bladder, diagnostic procedures using catheters are common when suspect regions are found on CT, MRI, or ultrasound. The use of OCT for high-resolution imaging of the bladder wall may enable early detection or staging of tumor growth. Using the OCT catheter in a rabbit animal model, *in vivo* images were acquired, compared with histology, and shown in Figure 6-17. The small size of the rabbit urethra prevented catheter access via this route. Instead, the bladder was exposed following an abdominal incision and the catheter was inserted through a slit in the bladder wall. Urine in the bladder increased scattering and degraded image quality. For this reason, the bladder was emptied and then filled with saline prior to imaging. The OCT image in Figure 6-17A reveals multiple folds or rugae of the bladder wall. Full thickness penetration into the surrounding adipose tissue is possible.

Within the same animal, the ureters were investigated. The ureters are distendable allowing the catheter to pass a few millimeters into the lumen. An OCT image and corresponding histology are shown in Figure 6-18. Passage of a catheter through the human ureter enables minimally invasive access to the kidney for evaluation.

6.7.2 Prostate

In the U.S., prostate cancer is the most commonly diagnosed male cancer accounting for 317,000 new cases in 1996 alone[257]. The incidence of prostate cancer increases faster with age than any other major cancer[258] with probabilities of < 1:10000 before age 39, 1:78 for age 40-59, and 1:6 for age 60-79. Recognizing prostate cancer from benign prostatic hypertrophy (BPH), an enlargement of the prostate gland which affects greater than 90% of men by the eighth decade[259], is a major research endeavor. BPH results in enlargement of the prostate with urethral obstruction, delayed urination, and an increased incidence of urinary tract infections[260]. Surgical procedures to reduce the obstruction or remove the prostate

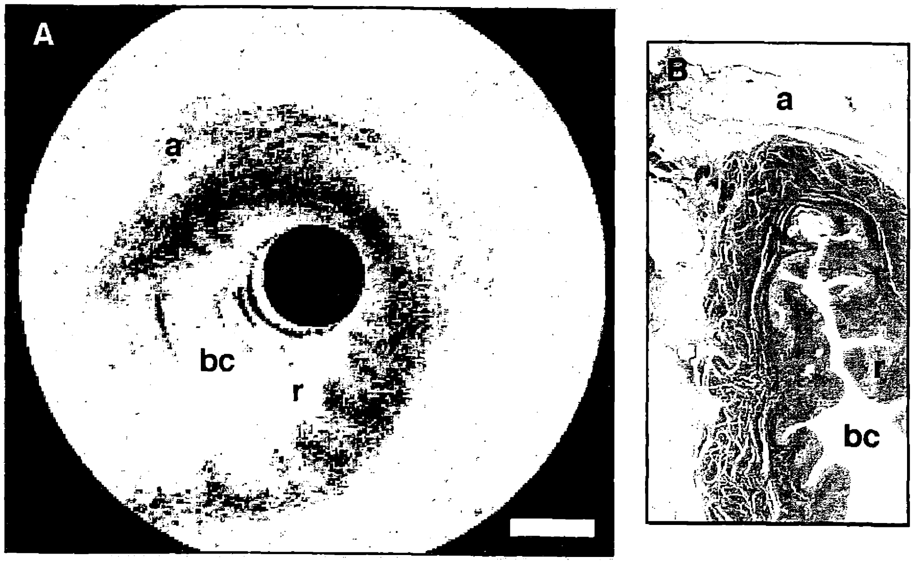

FIGURE 6-17: *In vivo* rabbit bladder. Full-thickness OCT imaging is possible, identifying surrounding adipose tissue. Abbreviations: a, adipose tissue; bc, bladder cavity; r, rugae. Bar represents 1 mm.

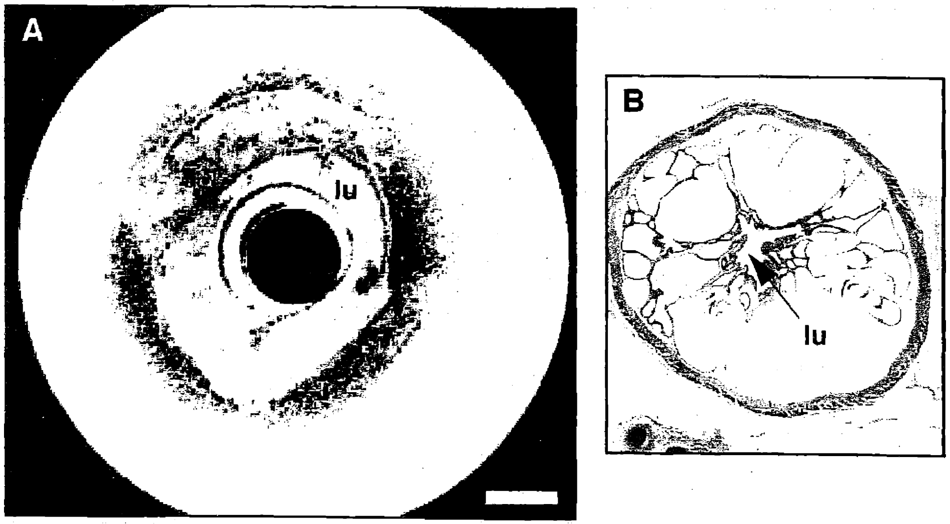

FIGURE 6-18: Rabbit ureter. A distendable lumen (lu) permits catheter entry. Histological image shows relaxed ureter wall. Bar represents 1 mm.

are methods to relieve the symptoms of BPH. A major morbidity factor of radical prostatectomy is impotence which results from injury to neurovascular bundles which lie adjacent to the prostate[261]. The use of OCT to locate these bundles and guide surgical resection of the prostate could significantly reduce morbidity. Imaging of the *in vitro* human prostate was performed using the Cr^{4+}:forsterite laser at high resolutions (9 μm transverse, 6 μm axial). The prostate was bisected through the urethra and imaging was performed transversely across the urethra. An image and corresponding histology are shown in Figure 6-19. The prostate appears relatively homogeneous in the OCT images. Larger submucosal glands and the urethral sinus, however, can be identified.

The radial imaging catheter was passed into the dilated urethra of an *in vitro* human prostate to image in an orientation that would be encountered *in vivo*. This image is shown in Figure 6-20. The imaging depth of OCT is insufficient to locate the prostate-adipose border, a site where neurovascular bundles are located. However, the use of OCT during prostatectomy may be feasible. By continually imaging ahead of the resection plane, OCT may be able to identify when the prostate-adipose border is approached.

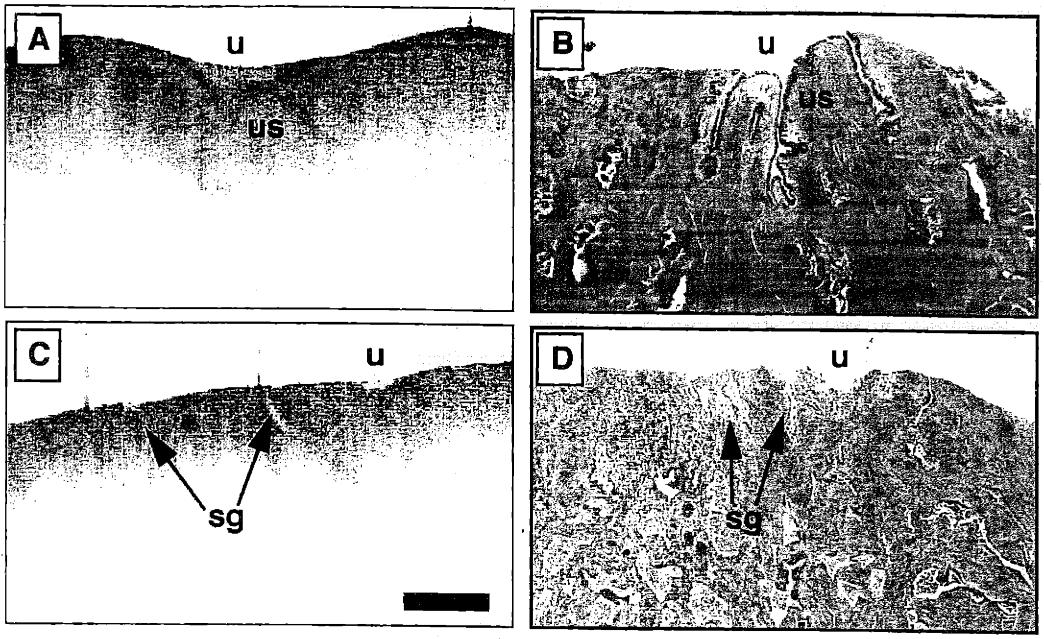

FIGURE 6-19: Human prostate. *In vitro* human prostate images acquired by hemi-secting the prostate through the urethra and imaging perpendicular to the longitudinal axis of the exposed urethra. Abbreviations: sg, submucosal glands; u, urethra; us, urethral sinus. Bar represents 500 μm.

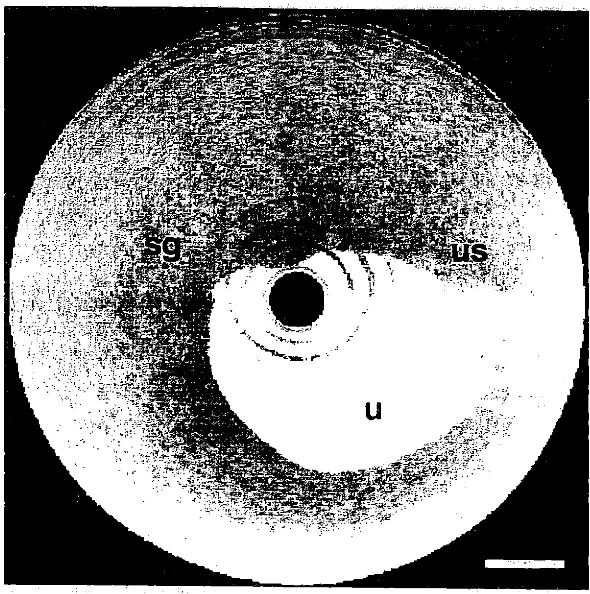

FIGURE 6-20: Radial catheter imaging of intact *in vitro* human prostate. Abbreviations: sg, submucosal glands; u, urethra; us, urethral sinus. Bar represents 1 mm.

Chapter 7

Surgical Intervention

7.1 Introduction

Surgical intervention is the process of interfering with disease pathogenesis by surgically modifying its course. Scalpels, catheters, radio-frequency (RF) ablation electrodes, and lasers are examples of instruments used to intervene. Lasers have been used extensively in interventional procedures to thermally coagulate tissue, control bleeding, and remove unwanted or diseased tissue through ablation. The feasibility of OCT to perform image-guided surgical intervention is investigated in this chapter. The imaging capabilities of OCT will be used to guide and assess the progress of the surgical intervention. High-power argon laser ablation will be used as the representative interventional technique and will be compared with more traditional RF ablation in both heart myocardium and human prostate. Emphasis should be given to the fact that thermal argon laser and RF ablation are representative of a wide array of interventional devices and techniques that OCT can potentially guide. The tissue response to thermal injury has been well-characterized over the last several decades and this thesis research does not attempt to verify previous results. Instead, this research using high-speed OCT demonstrates dynamic changes that occur in a variety of clinically-relevant tissues. These results will demonstrate the concept and limitations of OCT image-guidance during representative surgical interventions.

The use of OCT in an interventional procedure was first demonstrated by the OCT image-guided placement and assessment of retinal laser lesions in the *in vivo* primate eye[262-264]. This study examined the dynamic evolution of retinal lesions from continuous wave, and nanosecond, picosecond, and femtosecond pulses at visible wavelengths (514-580 nm). Although images were acquired every 5 seconds, the time evolution of lesion morphology enabled a better understanding of the mechanisms of damage. With an increasing use of lasers in ophthalmology for the repair of detached retinas, the disruption of posterior capsules following cataract surgery, and as a treatment for glaucoma, a thorough understanding of damage mechanisms is necessary for optimal therapy and a reduction in iatrogenic injury.

Faster image acquisition rates (4-8 fps) now enable rapid microstructural changes to be observed sequentially over time. This research demonstrates, for the first time, the use of high-speed OCT to characterize the morphological changes that occur in highly scattering tissue following thermal tissue injury.

7.1.1 Laser Safety Standards

The American National Standards Institute (ANSI) has established safety standards for the safe use of lasers[265]. These standards are used to protect individuals from ocular and skin injury as the result of exposure to high-power laser irradiation. As shown in Equation (2-65), the SNR of OCT is directly proportional to the laser power returning from the sample. Therefore, by maximizing the safe laser exposure to tissue, a maximum SNR can be achieved. Identifying safety limits also allows one to predict what powers are necessary to intentionally coagulate or ablate tissue during a surgical intervention. For laser-based interventions, laser powers must be optimized to effectively ablate tissue while minimizing the effects of collateral damage.

The two representative wavelengths investigated are the visible 514 nm from the argon laser used to thermally injure and ablate tissue and the 1300 nm near-IR wavelength used for OCT imaging. ANSI characterizes the safety limit as the maximum permissible exposure (MPE) to either the skin or the eye. Plots for these wavelengths and tissue are shown in Figure 7-1. Because of the significant absorption of visible wavelengths, the MPE is predominantly lower for visible wavelengths than for the near-IR wavelengths. The MPE for the eye is significantly lower than for the skin because of the increased sensitivity to light. Shorter exposure durations also permit the use of higher incident powers.

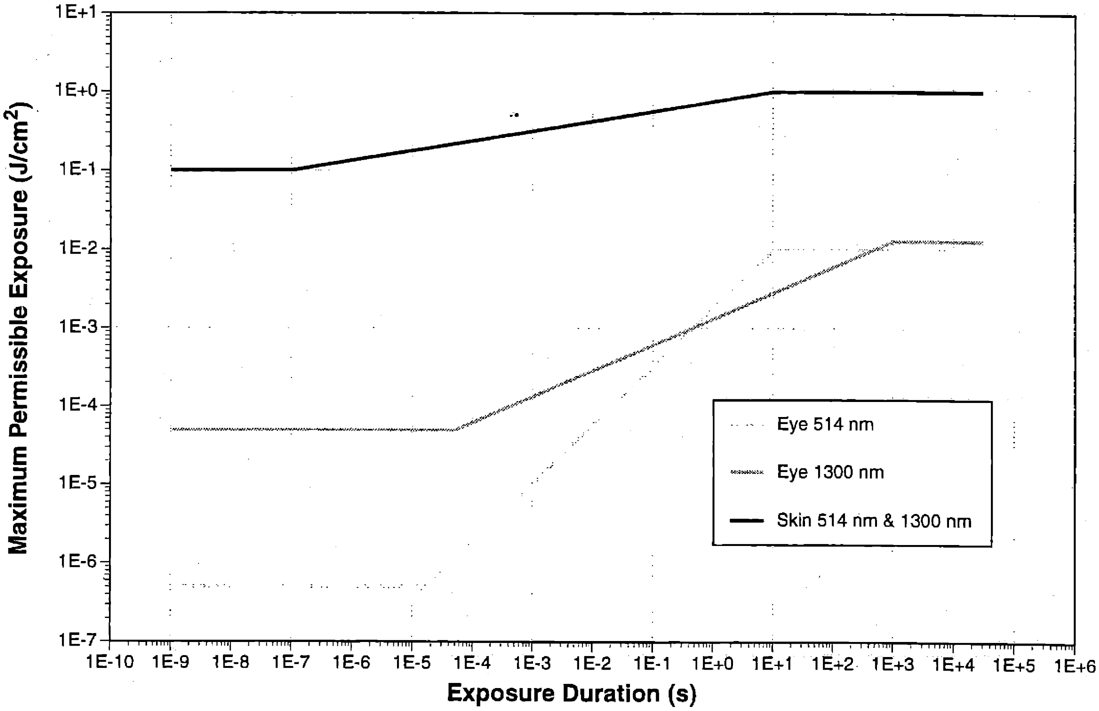

FIGURE 7-1: ANSI laser safety standard for maximum permissible skin and eye exposure. Standard is plotted for visible argon (514 nm) and OCT imaging (1300 nm) wavelengths.

The maximum incident power that can be used for OCT imaging at 1300 nm wavelength is calculated based on the exposure duration E_d for a single spot size given by

$$E_d = \frac{t_a d}{L_s} \tag{7-1}$$

where t_a is the image acquisition time, d is the diameter of the focused beam, and L_s is the total scan length. For catheter-based OCT imaging at 4 fps with 1300 nm output from the Cr^{4+}:forsterite, a circumferential scan length of 12.6 mm, and a 30 μm diameter spot size, the MPE is 10 mW. All *in vivo* imaging was performed within this limit. Imaging of the skin and other highly scattering tissue with the hand-held probe for a $L_s = 3$ mm, d = 30 μm, and for various image acquisition times, gives the following MPE values shown in Table 7-1. Typical sample-arm powers when using either the amplified SLD or the Cr^{4+}:forsterite laser are 1-5 mW. These results indicate that for imaging with the hand-held probe at less than 4 fps, the MPE is exceeded. No tissue damage from the 1300 nm imaging beam has been observed in histological samples although tissue drying is accelerated during exposure. These ANSI limits must be considered when *in vivo* human studies are performed.

TABLE 7-1: Representative MPE values for imaging skin with the hand-held probe. Values were calculated for a scan length of 3 mm and a beam spot size diameter of 30 μm.

Image Acquisition Time	MPE
30 s	95 μW
10 s	217 μW
1 s	1.2 mW
250 ms	3.4 mW
125 ms	5.6 mW
33 ms	15.7 mW

Typical 1300 nm optical powers exiting beam delivery instruments represent a potentially hazardous condition for retinal injury. Assuming the 5 mW output power from the probe is focused to a 30 μm diameter spot 5 mm from the tip of the device, and the operator or patient is exposed for 250 ms, the MPE is 6.4 mW/cm^2. The MPE is exceeded if the beam is viewed within 71.5 mm from the tip of the probe. The increasing availability of high-power sources will require operators and users to wear protective eyewear to prevent accidental retinal injury.

This thesis research demonstrates thermal ablation in highly-scattering non-ocular tissue. The skin MPE for the 514 nm argon wavelength was calculated for the experimental conditions. The argon output was focused to a 800 μm diameter spot for 1-5 s. MPE for 1 and 5 s exposures were 27.5 mW and 8.2 mW, respectively. The 1 W incident on the tissue exceeded the MPE for skin by approximately 1-2 orders of magnitude, sufficient to induce thermal damage.

7.1.2 Laser damage mechanisms

Laser irradiation damages tissue by three mechanisms: chemical, thermal, and mechanical. Chemical effects result from low-level irradiation ending in either nonlethal or lethal changes within cells. Damage results from the breaking of molecular bonds, cross-linking of DNA, the production of free radicals, and the disruption of enzymatic and biochemical pathways. Nonlethal changes are difficult to detect, frequently requiring molecular biology techniques to assess DNA and RNA stability or variations in cell metabolism. Few morphological changes occur which can be observed with standard histopathology. Transmission electron microscopy, however, is one technique which can be used to assess ruptured cellular membranes and distorted organelles.

The developing embryo is a model organism with increased susceptibility to mutagenic agents, including optical radiation[266]. Studies have shown that high power near-IR irradiation can lethally damage cells trapped within optical tweezers[154,155]. Powers of 1-10 mW focused to micron spot sizes are typical in these devices. The optical powers from KLM lasers used in OCT imaging represent a possible source for photochemical cell damage, however, no studies have been performed to assess this. Although *in vivo* imaging was successfully performed on the developing amphibian animal model, occasionally, specimens did not return to normal feeding and swimming behavior following imaging. Whether this was the result of handling, the anesthetic, or the laser irradiation remains to be determined.

Thermal damage mechanisms range from delayed effects of edema and hyperemia to significant thermal coagulation of tissue and explosive vaporization of water[267]. Intracellular edema is the result of dysfunctional cell metabolism and the accumulation of fluid. As temperatures increase due to increased optical fluence, coagulation of cellular and extracellular structural proteins occurs. Cells and organelles will shrink due to denaturization of proteins and water loss through ruptured membranes[268] while collagen will form an amorphous mass in response to heat[269]. Thermal coagulation results in disruption of birefringence in muscle tissues and of fibrillar collagens in tendons[188]. As temperatures in tissue approach 100 °C, the effects of water vaporization become dominant. At the tissue surface, water vaporization results in accelerated drying of the tissue. This same process within tissue results in rapid formation of water vapor trapped within vacuoles. The vacuoles expand and rupture, causing an explosive ablation of tissue, ejection of tissue from the site, and crater formation. Continued heating produces a carbonization of the tissue which may accelerate absorption of incident light as well as prevent OCT imaging of deeper tissue.

For thermal damage to occur, the incident radiation must first be absorbed by the tissue. Therefore, tissue with higher absorption coefficients will require lower levels of optical power before damage occurs. Coagulation, loss of birefringence, vacuolization, and explosive ablation will be demonstrated using high-speed OCT imaging. Thermal damage can be modeled as a rate process similar to chemical reaction kinetics and was first described in a series of papers by Henriques and Moritz[270] in 1947. Under this model, tissue constituents transition from a native state to a damaged state. An energy barrier ΔH^* separates the two states as shown in Figure 7-2. The enthalpy ΔH^* is the difference in internal thermal energy between the native M state of a molecule and the activated state M*. The factors k_a, k_b, and k_d are the rate constants. Typically ΔH^* is much less than ΔH, making the reaction likely given a small amount of energy input. For energy inputs less than ΔH^*, the activated tissue will relax back into its native state and reversible cell damage will be repaired. The rate equations can be described by

$$M + M \underset{k_b}{\overset{k_a}{\rightleftharpoons}} M + M^* \qquad\qquad M^* \xrightarrow{k_d} M^d \tag{7-2}$$

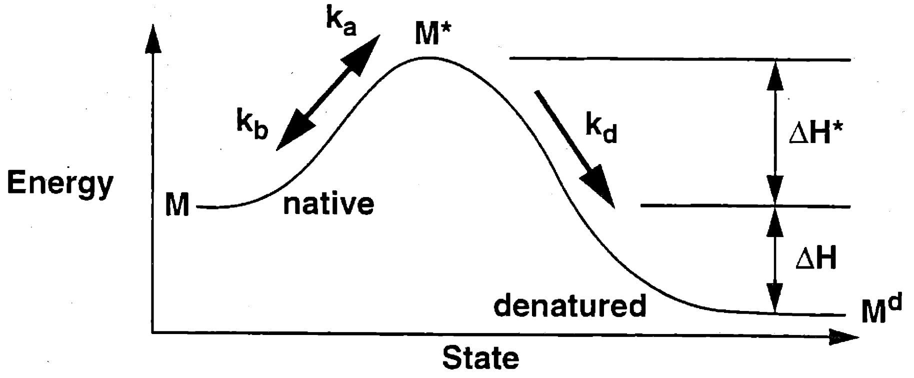

FIGURE 7-2: Tissue damage state diagram. Tissue damage model based on rate processes similar to chemical reaction kinetics. Overcoming an energy barrier ΔH^* changes tissue from a native state (M) to an activated state (M^*) and finally to an irreversible damaged state (M^d).

where the irreversible damage to the molecule M^d occurs at a rate k_d. The rate of thermal damage is largely determined by the forward rate k_a which can be expressed by

$$k_a = A\exp\left(-\frac{\Delta H^*}{RT}\right) \cong A\exp\left(-\frac{E_a}{RT}\right) \tag{7-3}$$

where T is the temperature, R is the gas constant of 1.987 cal/mol-K, A is a scaling constant, and E_a is the activation energy needed to produce irreversible damage. The rate k_a can be recast into an Arrhenius integral to describe a measure of damage $\Psi(\tau)$ given by

$$\Psi(\tau) = \ln\left[\frac{M(0)}{M^d(\tau)}\right] = \int_0^{\tau} A\exp\left(-\frac{E_a}{RT}\right)dt. \tag{7-4}$$

The logarithm of the ratio of the original concentration of native tissue M(0) to the damaged tissue $M^d(\tau)$ is given by an integral summation of temperature-induced damage. The characteristics of this kinetic damage model describe a process of little damage accumulation below a temperature threshold, with a sharp exponential increase in damage once this threshold has been reached. Examples of this behavior will be given in the next section.

Mechanical damage is the result of rapid thermoelastic expansion of tissue and the ejection of ablated material. Stress waves which travel at the speed of sound in tissue emanate from the lesion site. Shock waves at speeds greater than the speed of sound may be generated if the pulse length is shorter than the time required for the wave to propagate out of the lesion site. Mechanical damage can also occur acoustically with ultrashort ($< 10^{-9}$ s) pulses of high energy. Pulse durations are exceptionally short, preventing extensive temperature rise and thermal injury in tissue[271,272].

Acquisition rates of 4-8 fps are sufficient to capture effects of thermal damage mechanisms that occur with time constants of 1 s or more. Extended heating of regions of tissue permits the observation of mechanical effects as well. Chemical damage at the cellular level is beyond the resolution and sensitivity of OCT, however, tissue stains which indicate biochemical activity are used to provide insight into cell viability surrounding the lesion site. Acoustic damage from ultrashort pulses occurs with time-scales comparable to the length of the pulse, too rapid for OCT imaging. Although acoustic and mechanical effects may occur on time-scales faster than can be imaged with OCT, OCT can still image the integrated tissue effects and injury, providing useful information to guide surgical interventions.

7.2 Thermal Laser Ablation

The pathologic effects described in Table 7-2 are the result of increasing temperature within biological tissue[267]. The thermal and mechanical effects of laser tissue ablation have been previously analyzed[137].

TABLE 7-2: Pathologic Thermal Effects in Biological Tissue[267].

Thermal Damage Mechanism	Temperature (°C)	Heating Duration	Histopathologic Effect
Low-temperature accumulation processes	40-45	Hours	Reversible cell injury Inactivation of enzymes Accelerated metabolism
	45+	Hours	Cell shrinkage and death Denaturization of structural proteins
	Unknown	Unknown	Cell membrane rupture
	55-95	Minutes	Birefringence changes in collagen
Water-dominated processes	100-200	Seconds to milliseconds	Vacuole formation, rupture Explosive fragmentation
High-temperature ablation processes	200+	Seconds to picoseconds	Tissue ablation

The majority of studies have used static histological preparations to document the tissue changes that occur. Dynamic changes in tissue optical properties have been characterized[273,274], but no studies have been performed using high-speed OCT to image changes in optical backscatter in highly scattering tissues. To image the dynamic effects of thermal injury, an OCT setup using a modified surgical microscope from Section 3.3.2 was constructed. An argon beam was incorporated and aligned within the OCT imaging plane, centered within the transverse OCT scan length. A schematic of this modified setup is shown in Figure 7-3. The Cr^{4+}:forsterite KLM laser enabled image acquisition up to 8 fps. A mechanical shutter was used for timed argon laser (514 nm) exposures on the sample. The 1-3 W argon beam was focused by a 24.5 cm focal length lens to a 0.8 mm diameter spot on the tissue surface. This setup permitted image acquisition immediately prior to and after exposure to track the optical changes occurring within the tissue due to the thermal damage.

Before performing dynamic imaging studies, a single thermal lesion was thoroughly investigated to determine what optical changes were detectable with OCT. A 10 s, 3 W exposure on rat rectus abdominis muscle was used to form an ablation crater. The specimen was then placed on a multi-axis translational stage to perform 3-D imaging of the crater. Imaging was performed using the Cr^{4+}:forsterite with 7 μm axial and 28 μm transverse image resolution. Sixty cross-sectional images (400 x 600 pixel, 4 x 6 mm) were acquired at 100 μm intervals to produce a 3-D data set. Two projections of this data set are shown in Figure 7-4. The deep crater can be seen in the center of the projection. Surrounding the crater is an ele-

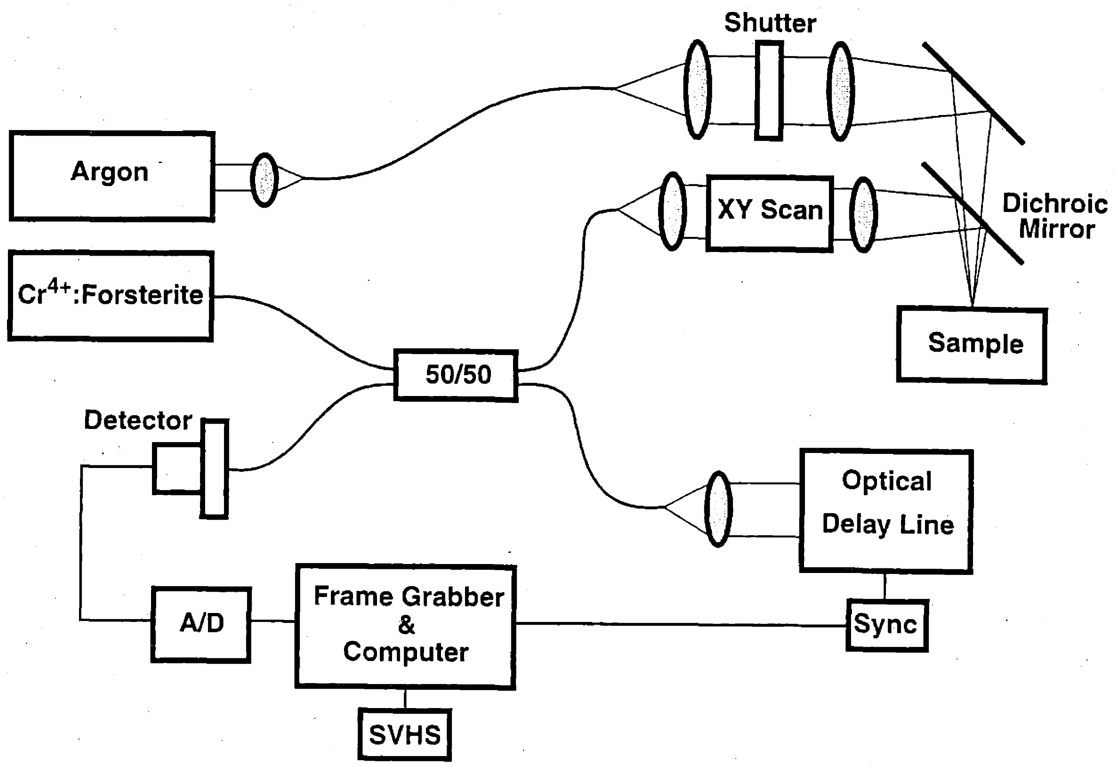

FIGURE 7-3: Interventional laser delivery setup. A mechanical shutter-controlled argon laser is aligned with the OCT imaging plane via a dichroic mirror. Dynamic changes in tissue optical backscatter due to thermal injury can be image at 8 fps using the high-speed OCT system.

vated region of damage which decreases radially outward from the center. The projection in Figure 7-4B shows the crater viewed from below the tissue surface illustrating the deep penetration of the lesion into the tissue.

A sequence of cross-sectional images from this data set is shown in Figure 7-5. These provide information on the depth-dependent distribution of the thermal energy. The number in each image refers to the distance from the center of the crater at which the cross-sectional image was acquired. At a distance of 3.75 mm from the center, small distortions in the muscle layers (arrow) are observed, although little change has occurred at the tissue surface. At 3.0 mm, thermal injury has elevated the tissue surface and distorted an internal low-backscattering layer. At 2.25 mm, a region of increased optical backscatter has appeared. This region appears deeper in the 1.5 mm section. At 0.75 mm from the center, carbonization of the tissue results in significant shadowing of underlying structures. A cross-section through the center of the crater is shown in the last image. The vertical bands of low backscatter adjacent to the crater are due to shadowing by the vertical crater walls which are lined with carbonized tissue. Carbonized tissue scatters and absorbs the incident light, decreasing imaging penetration.

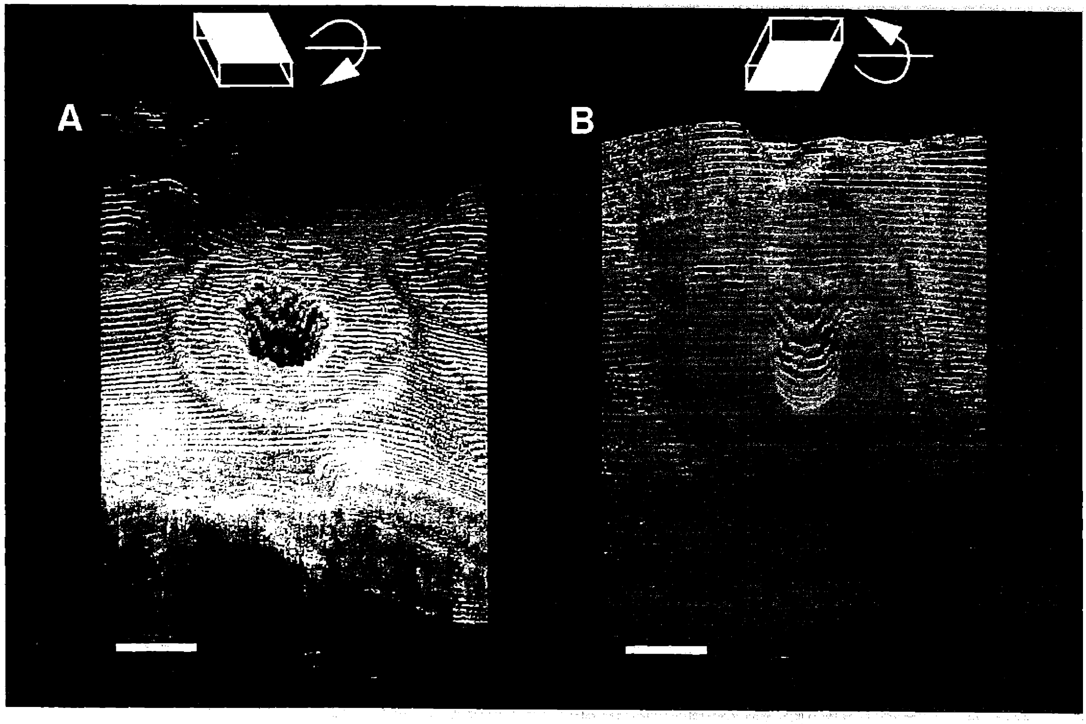

FIGURE 7-4: Three-dimensional projections of laser ablation crater in rat rectus abdominis muscle. Crater was formed by 3 W of argon power during a 10 s exposure. Argon beam was focused to a 0.8 mm diameter spot. Crater and concentric zone of thermal injury are viewed from A) above and B) below the tissue surface. Bar represents 1 mm.

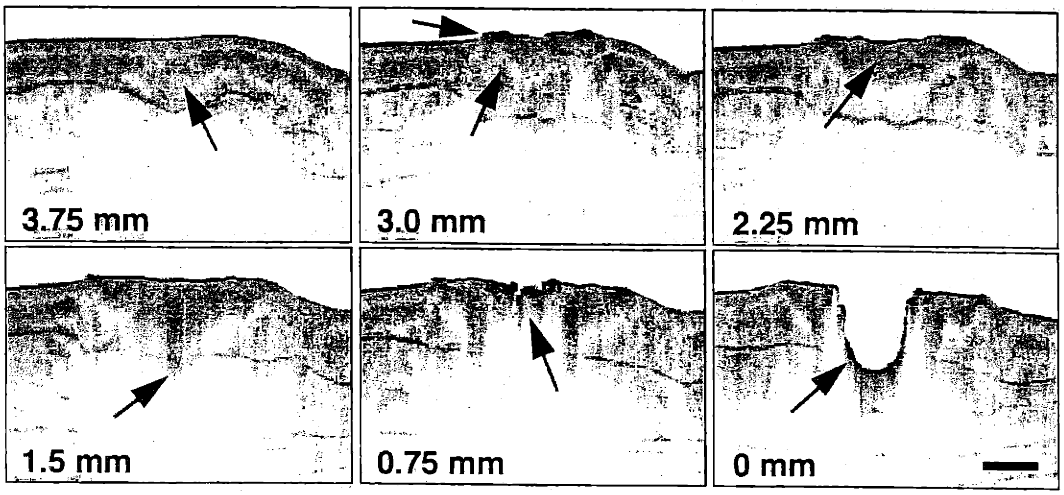

FIGURE 7-5: Cross-sectional images of laser ablation crater shown in Figure 7-4. Numbers refer to distance from crater center which the image was acquired. At 3.75 mm, arrow indicates early subsurface changes of layered structure. Arrows at 3.0 mm show elevated tissue surface and irregular subsurface layers. Arrow at 0 mm illustrates deep crater with carbonized wall. Bar represents 1 mm.

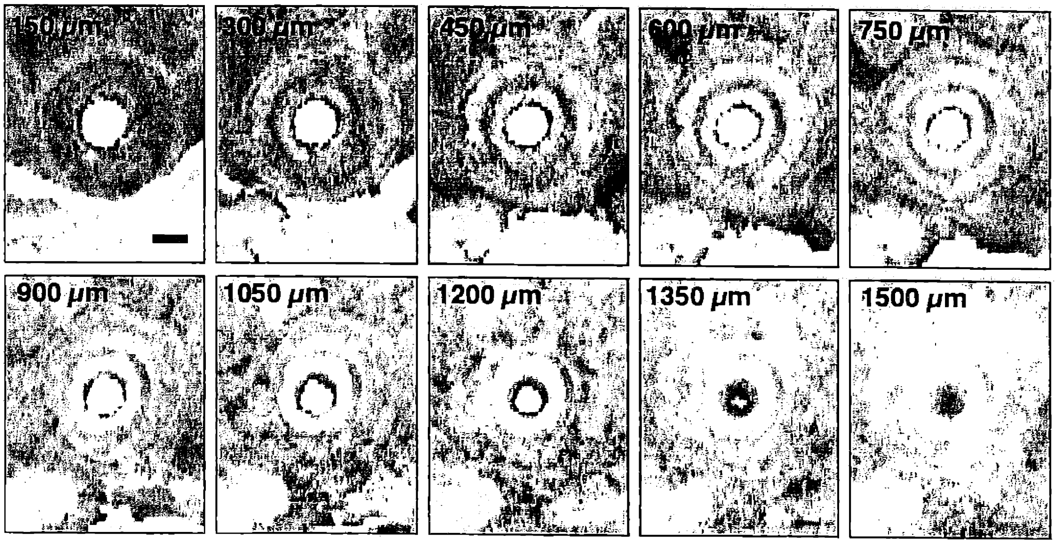

FIGURE 7-6: Re-sectioning of 3-D crater data set to illustrate *en face* plane. 3-D data set was shown in Figure 7-4. Numbers refer to depth below tissue surface. Concentric rings of thermal injury are observed at all depths. Bar represents 1 mm.

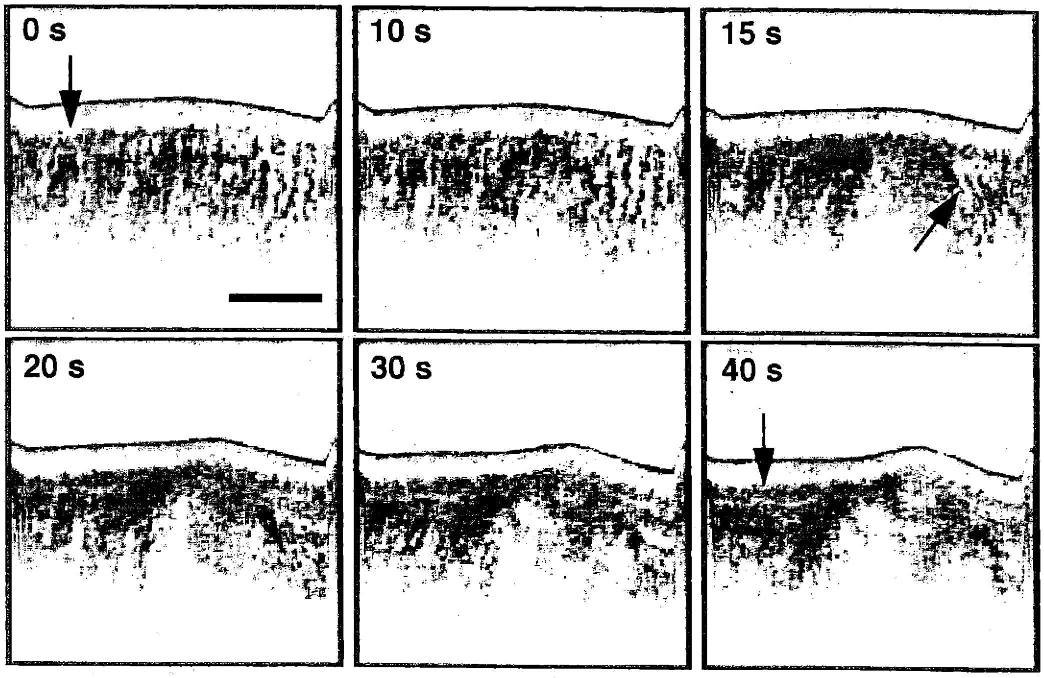

FIGURE 7-7: Possible birefringence changes from collagen disruption in chicken tendon. Collagen fiber bundles were oriented perpendicular to the OCT imaging plane. Arrow at 0 s shows normal collagen bundles. After 15 s of exposure from a 2 W argon beam, bundles have begun to contract toward the argon beam center. At 40 s, arrow indicates changes in tissue birefringence located 1 mm from the incident argon beam. Bar represents 1 mm.

Surrounding the deep crater in Figure 7-4A lie concentric rings of tissue damage. These are the result of a radial thermal distribution outward from the site of the incident beam. The differences between each ring are likely the result of different thermal damage mechanisms, if one assumes the tissue is homogeneous. To optimally assess these radial distributions, the 3-D data set is re-sectioned in the *en face* plane, as would be viewed from the surface and with increasing depth into the tissue. Re-sectioned slices are shown in Figure 7-6. The number in each figure refers to the depth from the surface at which the plane was sectioned. The shallow planes (150-600 μm) lack regions of tissue (lower white regions) because the axes of the tissue block were not precisely aligned with the translation stage axes. The image at 150 μm shows a relatively uniform ring consistent with the elevated region appearing in the 3-D projection of Figure 7-4A. At greater depths (450-900 μm), however, a multiple-ring pattern is evident, possibly indicating different zones of tissue damage. An alternative explanation may be a concentric elevation of birefringent tissue layers presenting as regions of low and high optical backscatter. At a depth of 1350 μm, the crater bottom is approached and the concentric rings have diminished. At 1500 μm, the region of high backscatter in the center represents tissue immediately below the crater bottom and the white ring of reduced optical backscatter is due to the attenuation of the incident beam by the carbonized tissue lining the nearly vertical crater walls.

According to Table 7-2, at temperatures exceeding 45 °C, the birefringence of collagen is disrupted. Subtle changes in optical backscattering properties were observed surrounding the lesion in the rat rectus abdominis muscle in Figure 7-5. More dramatic changes were observed in the highly ordered collagen fibers from a chicken tendon. The tendon in Figure 7-7 was imaged in cross-section and oriented with the collagen fiber bundles running perpendicular to the OCT imaging plane. Shown in the initial image, the bundles appear as discrete regions of high backscatter. During exposure from a 2 W argon beam, the bundles move inward as thermal coagulation proceeds (arrow at 15 s). After 40 s, the central lesion is thermally coagulated. Regions outside of this lesion (shown by the arrow at 40 s) exhibit a possible change in birefringence when compared to the initial image (0 s).

The extent of thermal damage can be characterized by both OCT imaging and histopathology techniques. Changes in images of tissue during ablation have been used to validate models of thermal propagation through tissue. This is one method which will be used in this thesis. However, changes which appear in images do not always correlate with the extent of tissue damage and comparisons must be made with histology to determine the limitations of the imaging methods. Still, observations from histological slides are limited to the physical findings from cells and extracellular components with no indication of metabolic or enzymatic changes which may reflect the viability of the cells surrounding the lesion. Therefore, in an effort to more accurately correlate OCT image findings with thermal damage, a cell viability study was performed.

7.2.1 Cell viability

Disruption of cellular biochemical processes resulting from elevated tissue temperatures is the first mechanism of thermal injury that occurs, as described in Section 7.1.2. Although histological findings of thermally-induced structural damage have been used to validate damage models, ultimately it is the extent of non-viable cells that must be determined. The extent of non-viable cell injury must be correlated with OCT images if OCT is to be used for controlled intervention. The zones of non-viable cells which extend beyond the lesion site contribute to the limiting distance that a surgical intervention must not breach if the integrity of sensitive tissue structures is to be preserved. To our benefit, normal healing responses in biological tissues can repair limited zones of non-viable cells.

Cell viability following thermal laser injury was assessed using two tissue stains: trypan blue and a nitrophenyl-substituted ditetrazolium salt (Nitro-BT or NBT). Trypan blue has a greater affinity for serum proteins than for cellular proteins. Therefore, intact viable cells will not be stained and non-viable damaged cells will be stained blue. In contrast, NBT stains cellular metabolism enzymes dark. Any disruption in the normal metabolic pathways of a cell will prevent the enzymes from retaining the stain. Preliminary studies with these stains indicated that NBT-stained specimens exhibited more contrast than the trypan blue-stained specimens. The trypan blue tended to stain all exposed surfaces of the tissue that contained non-viable cell layers. This prevented identification of India ink registration marks and poor localization of the laser lesions for histological processing. Both the trypan blue and NBT stains failed to penetrate far into the tissue. Penetration of NBT was greater than trypan blue, but limited to $< 250\ \mu m$. The limited penetration meant only surface changes could be used to document the extent of injury surrounding the lesion.

Fresh rectus abdominis muscle and myocardial tissue were obtained from 4 Sprague-Dawley rats immediately after being euthanized by intraperitoneal injection with 42 mg/kg phenobarbital (Nembutal). The rectus abdominis muscle was chosen because of the large, uniform area of tissue for the placement of a grid-pattern of lesions. The myocardium was chosen for its increased vascularity and an absorption coefficient approximately 10-times higher than that of rectus abdominis muscle. The increased absorption of the argon wavelength in myocardium resulted in rapid tissue ablation and crater formation. Crater formation could only be achieved in the rectus abdominis for powers of 3 W and exposures > 10 s. The tissue was placed in the sample arm of the OCT setup shown in Figure 7-3 and lesions were placed with an argon beam according to the diagram in Figure 7-8. OCT imaging was simultaneously performed at 8 fps for each lesion. OCT imaging was also performed at two control sites without argon lesions to assess if the OCT imaging beam affected cell viability. Immediately following exposure, the tissue specimens were divided into two groups, the first group was placed in NBT stain for 45 min and the second group was temporarily stored in 0.9% saline. After 45 minutes, the lesions from each group were viewed under a light microscope and digitized with a CCD camera. The specimens were then fixed in 10% buffered formalin. Both groups underwent standard histological processing and were stained with hematoxylin and eosin to provide a background stain for assessment of physical tissue damage. Much of the NBT stain present on the surface of the specimens was lost during histological processing.

Digitized images of tissue specimens from one rat are shown in Figure 7-9. A comparison between the NBT and H&E specimens shows NBT-stained tissues exhibit improved contrast of the concentric ring pattern. The concentric rings of tissue damage were first shown in the OCT images in Figure 7-6. The multiple-ring pattern observed previously also appears on the NBT-stained specimens. Likewise, improved contrast is evident for the specimens of myocardium. The control regions did not show any biochemical or structural injury from the OCT imaging beam.

Comparisons were made between initial OCT images of the lesion site, OCT images following exposure, the histology of the lesion, and characteristics of the NBT-stained regions. Representative lesions are shown in Figure 7-10. The first lesion, shown in Figure 7-10A-D and H was from a 2 W, 5 s argon exposure. A large region of increased optical backscatter appears in the OCT image (Figure 7-10B). This corresponds to a region of coagulated tissue as confirmed with histology. Cross-sectional and surface images of the NBT-stained lesion sites demonstrate regions of non-viable cells. A second lesion is shown in Figure 7-10E-H. This 2 W, 3 s exposure is characteristically similar to the first lesion, but injury is confined to a smaller region. A crater was formed in rat myocardium and shown in Figure 7-10I-M. The carbonized crater lining reduces both imaging and argon laser penetration. As observed in Figure 7-10K, the thermal damage does not extend greater than 400 μm beyond the crater wall, compared to 1-1.5 mm depths of injury in the rectus abdominis where no crater was formed.

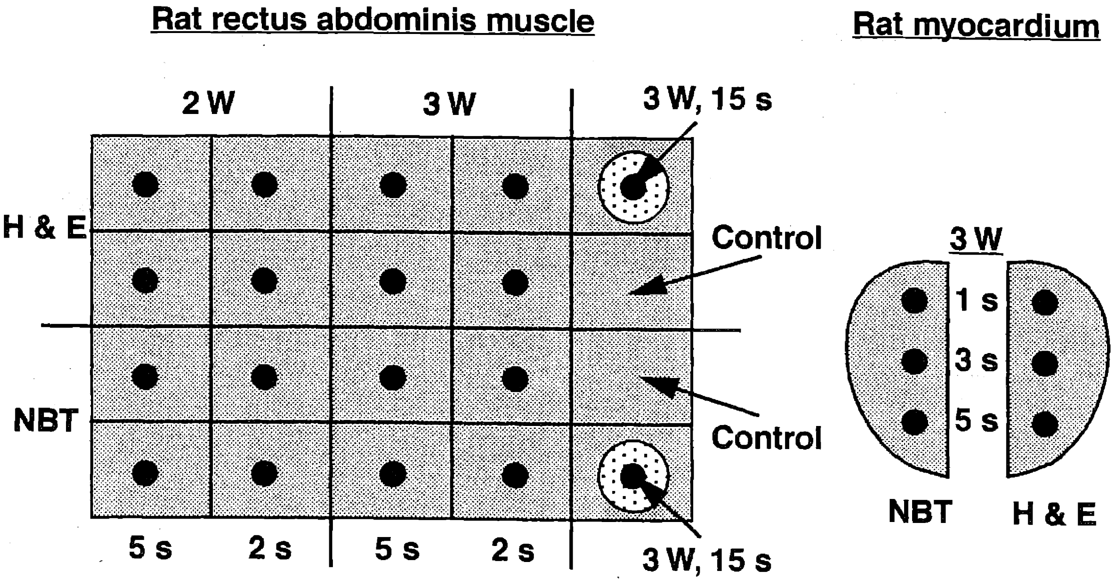

FIGURE 7-8: Lesion diagram for cell viability study. Fresh tissue specimens from rat rectus abdominis muscle and myocardium were exposed to varying argon powers and durations. High-speed (8 fps) OCT imaging was performed simultaneously. Control regions were imaged with OCT without placing argon lesions to assess if OCT imaging beam powers were sufficient to cause cell damage.

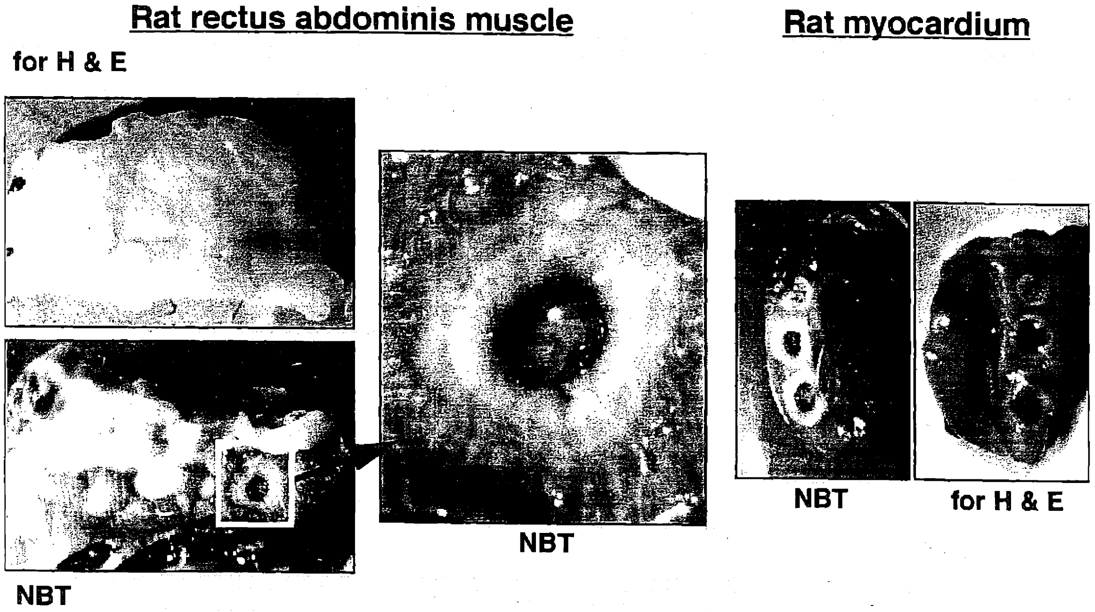

FIGURE 7-9: Tissue specimens for cell viability study. Increased contrast of lesions and concentric rings of injury are apparent for NBT-stained specimens. Lesion diameters were measured and compared with corresponding OCT images and histological preparations.

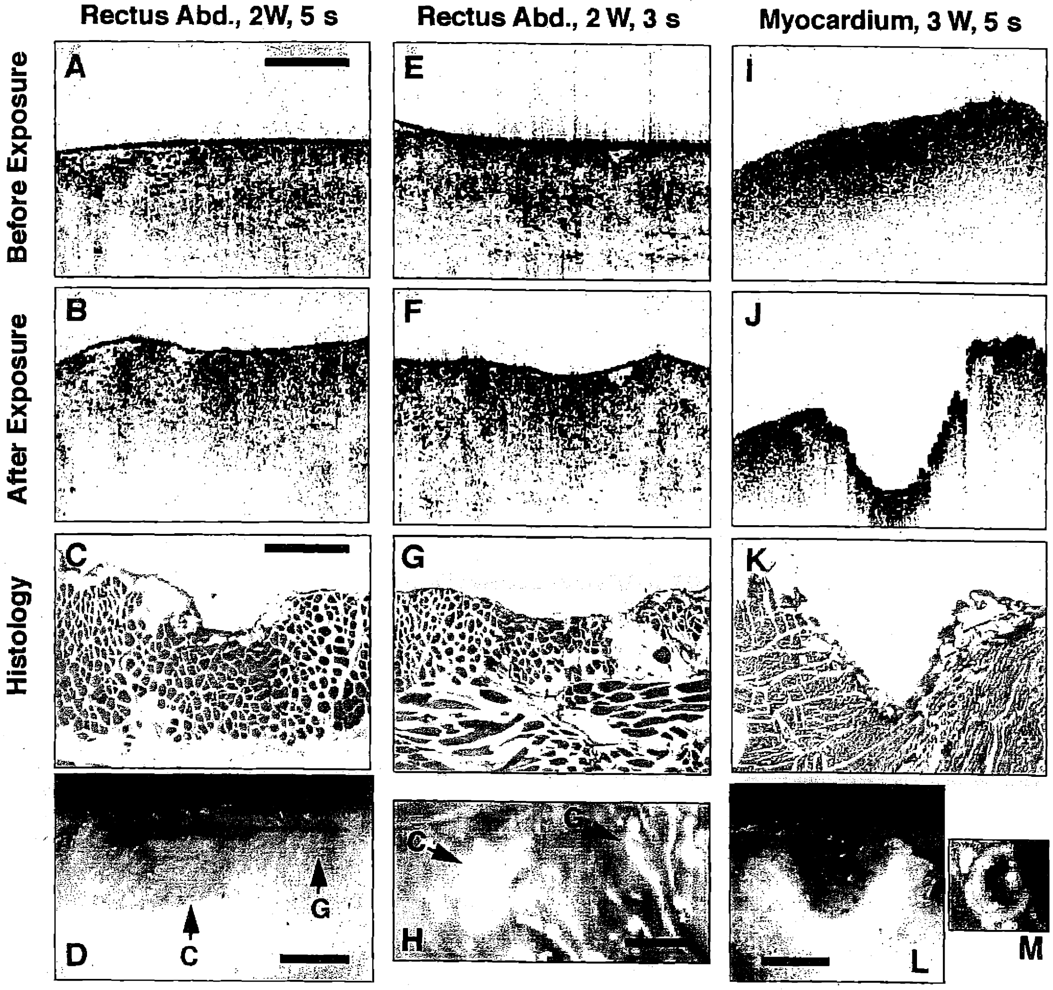

FIGURE 7-10: Comparison of OCT images, histology, and cell viability markers. A-C) 2 W, 5 s argon exposure of rectus abdominis, E-G) 2 W, 3 s argon exposure of rectus abdominis. D,H) Cross-sectional and surface images of NBT-stained lesions (C & G). I-M) 3 W, 5 s argon exposure of myocardium. Bars represent 1 mm.

Measurements of the zones of damage observed in the OCT images, NBT-stained specimens, and histology, were made. On average, OCT images underestimated the depth of structural damage by 13% compared to histology. This percentage, however, did not account for the dehydration of the histological specimen nor the possibility of histological processing artifacts. In addition, a reduction in OCT imaging penetration could account for the low estimation. OCT images underestimated the width of structural damage by 5% compared to histology. This difference may be due to histological processing artifact or the difficulty in determining lesion width due to low contrast in the OCT image. Compared with the NBT-stained specimens, biochemical cellular injury extends approximately 7% beyond the lesion width imaged with OCT. This is likely due to regions of non-viable cells which have not been thermally coagulated. Changes in optical backscatter detected with OCT are predominantly due to coagulation of tissue. Within the limits of detecting backscatter changes in OCT images and cellular injury in histology, there were no lesions where OCT detected cellular injury that was not evident on histopathology. Surgical interventions using thermal damage mechanisms to remove or injure tissue must consider the full range to which this damage extends, and also note that normal healing mechanisms can repair a limited extent of cell injury. This information can be used to monitor and guide the placement of the laser intervention near sensitive tissue structures.

7.2.2 Ablation of clinically-relevant tissue

The response of tissue to thermal injury is highly dependent on the absorption and scattering properties. To demonstrate the variability encountered between tissue types, sequences of thermal injury and ablation are first shown for two strikingly different tissue types, bovine muscle and chicken breast. Then, more clinically-relevant tissue will be investigated. Laser therapy is used clinically to ablate regions of neoplastic tissue in the brain, liver, lung, and kidney, among others. The use of OCT to monitor this ablative therapy in real-time may enable more precise control of laser delivery.

An ablation sequence in bovine muscle ($\mu_a = 1.5\ \text{cm}^{-1}$) with 2 W incident argon power is shown in Figure 7-11. Within 0.5 s of exposure, an outward propagating front of increased optical backscatter is observed (arrow). This front appears to reverse, or is followed by an inward propagating front of decreased optical backscatter (arrow at 1.5 s). The inward propagating front erupts and expels tissue from the surface as seen at 2.25 s. A crater is formed at 2.5 s which is lined with carbonized tissue that limits imaging penetration. Further ablation during the 5.0 s exposure results in a deepening of the ablation crater.

These ablation dynamics can be compared and contrasted with the thermal damage to chicken breast. Chicken breast has a lower absorption coefficient $\mu_a = 0.12\ \text{cm}^{-1}$ and hence, requires longer exposure durations for even minimal optical changes in the OCT image. The sequence for 2 W of incident power is shown in Figure 7-12. Subtle increases in optical backscatter become evident at 2 s directly under the incident beam. This region slowly increases in size and backscatter intensity. For the bovine muscle in Figure 7-11, crater formation began at 2 s while for the chicken breast, no similar event had occurred. No ablation crater could be induced in chicken breast at 2 W of power even after a 30 s exposure.

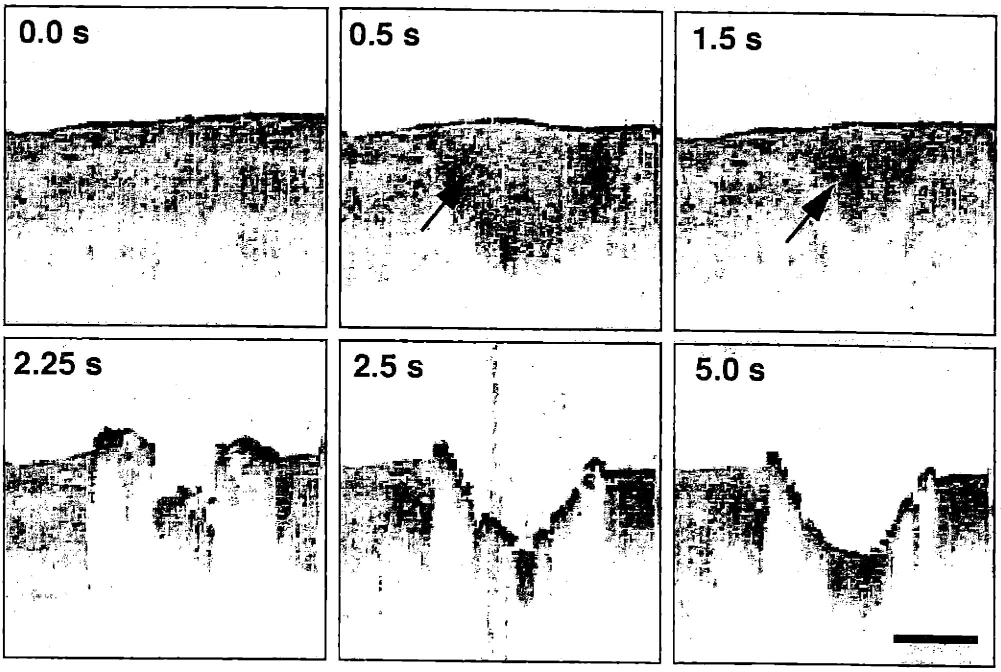

FIGURE 7-11: Bovine muscle ablation. Times indicate seconds during exposure from 2 W argon beam. At 0.5 and 1.5 s, arrows indicate outward and inward propagating fronts of high and low optical backscatter, respectively. Bar represents 1 mm.

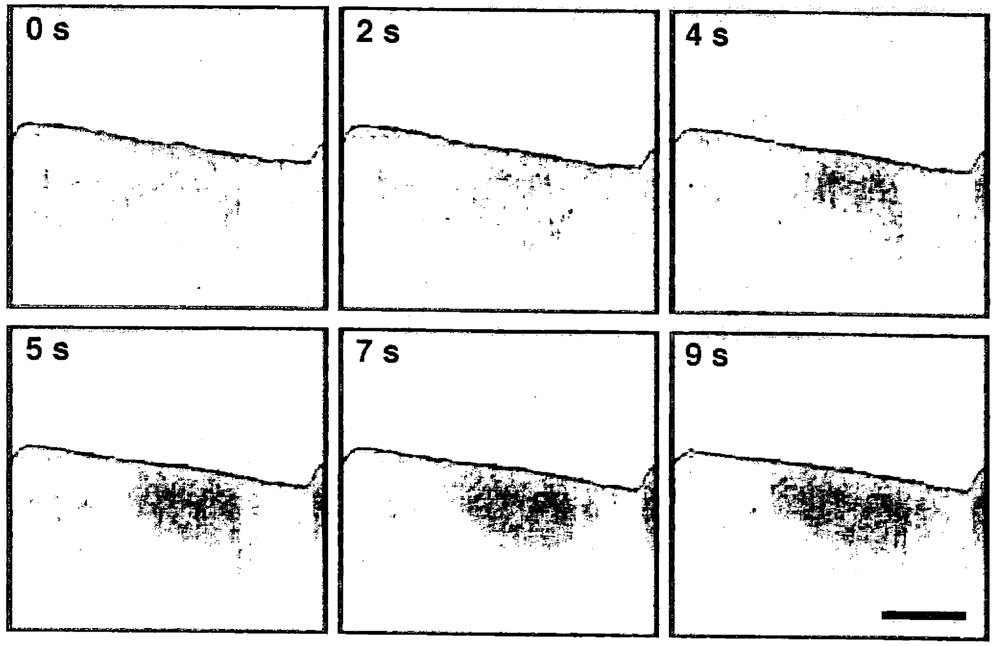

FIGURE 7-12: Chicken breast thermal damage. No ablation crater could be formed at 2 W incident power as was observed for the bovine muscle in Figure 7-11 due to the lower absorption coefficient. Bar represents 1 mm.

A similar comparison can be made between two clinically-relevant tissue types harvested from a rat. A kidney thermal injury sequence is shown in Figure 7-13. The OCT images illustrate the homogeneous nature of the outer cortex of the kidney ($\mu_a = 1.21$ cm^{-1}). Imaging penetration in this tissue is limited to ≈ 1 mm. This 1 W, 3 s exposure was below the threshold for surface membrane rupture, tissue ablation, and crater formation. An outward front of increased backscatter is observed (0.6 s) followed by a region of low backscatter at the center of the lesion (1.6 s). Backscatter from this region increases over time (2.0-3.0 s). Membrane rupture would have occurred within the following second if the exposure had continued. The corresponding histology is also shown, indicating a region of coagulated tissue (arrows) with no tissue fragmentation. Contrasted with this tissue is the ablation of rat brain tissue ($\mu_a = 0.19$ cm^{-1}) in Figure 7-14. The lower absorption coefficient implies that longer exposure durations are required for the same incident power to produce similar effects. This was observed for 1 W incident on brain tissue for 20 s. In this sequence, significant vacuolization and tissue heating occur (5.5-13 s) before the surface membrane is ruptured at 14 s. Membrane rupture is followed by ejection of tissue from the lesion, evolution of a smoke plume (16-17 s), and crater formation (20 s).

Observations from high-speed OCT imaging of thermal laser injury suggest that in order for tissue ablation and crater formation to occur, the outer membrane of the tissue must first be ruptured. Membrane rupture represents an ablation threshold with subsequent ejection of tissue from the lesion site. This threshold, however, must not be confused with the activation energy described in Section 7.1.2 for irreversible cell damage. Considerable thermally-induced cell injury and death occurs before membrane rupture and ablation. Characterizing the threshold for ablation is highly variable and dependent on both optical and tissue properties. In these studies, the threshold is identified empirically based on acquired OCT images.

The ablation threshold is documented by a comparison of thermal injury in rat liver ($\mu_a = 12$ cm^{-1}) for thermal energy doses below and above the ablation threshold. Two sequences with corresponding histology are shown in Figure 7-15. The first exposure at 1 W is halted after 1 s, prior to the ablation threshold. The second exposure is allowed to continue for 7 s, past the ablation threshold, resulting in ejection of tissue and crater formation. The corresponding histology for the sub-threshold lesion indicates a region of coagulated tissue (arrows). The disrupted membrane shown in this histology image is likely a processing artifact since this was not observed in the imaging sequence. In contrast, the above-threshold lesion histology shows marked tissue ablation and fragmentation within the lesion crater. Below the crater extends a zone of coagulated tissue (arrows) which is not observed in the OCT image due to the poor penetration through the carbonized crater wall.

Finally, the architectural structure of biological tissues contributes to the response of thermal laser intervention. Ablation of rat lung ($\mu_a = 2$ cm^{-1}) is shown in Figure 7-16. Inflated air-filled alveolar spaces represent a large portion of the tissue space making this tissue more inhomogeneous compared to previous specimens. A 1 s exposure of 1 W argon collapses most of the alveoli (0.5-1.0 s) resulting in the rapid deflation of the lung followed by the formation of a shallow crater.

Observing thermally-induced optical changes in highly absorbing (high μ_a for visible wavelengths) homogeneous tissues such as kidney and liver is difficult with the current resolutions of OCT. Improvements in resolution will subsequently improve the ability to detect thermal damage in these tissues. At current resolutions, however, OCT image-guided placement of interventional laser lesions is optimal in tissues with larger morphological variations such as muscle and lung.

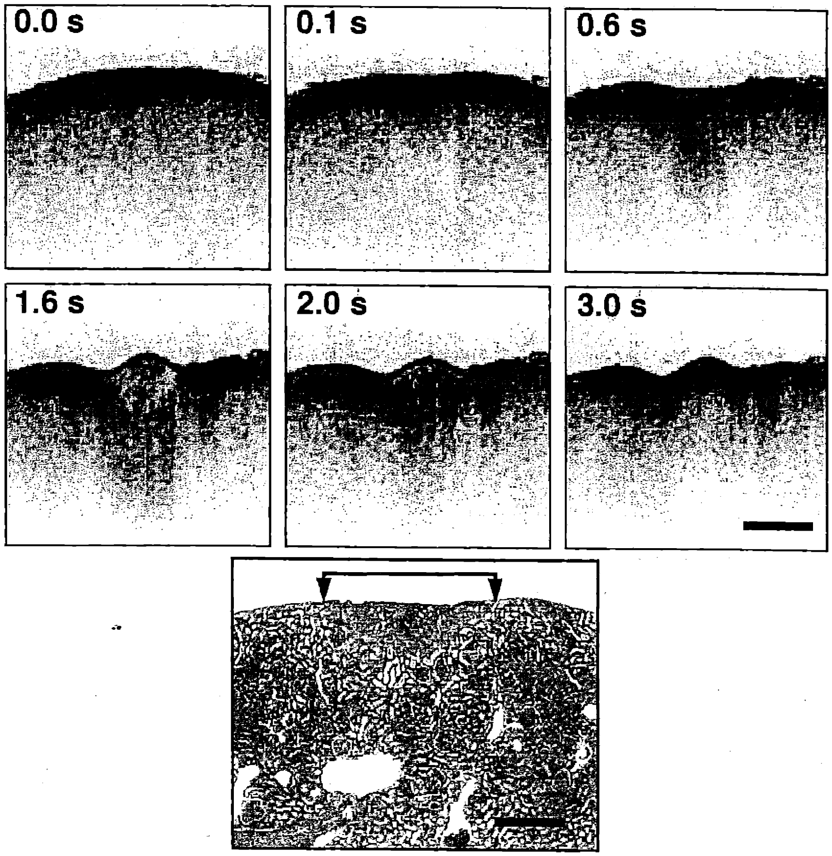

FIGURE 7-13: Kidney laser thermal damage. Rat kidney was exposed to 1 W of argon power for 3.0 s. Exposure was stopped prior to membrane rupture of rat kidney. Arrows in the corresponding histology indicate zone of thermal damage. Bar represents 1 mm.

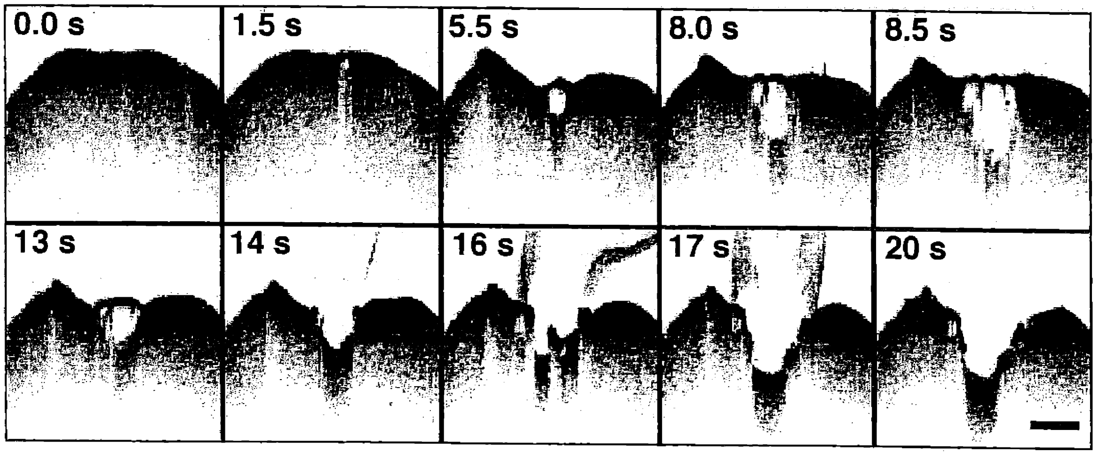

FIGURE 7-14: Brain laser ablation. Rat brain was exposed to 1 W of argon power for 20 s. Bar represents 1 mm.

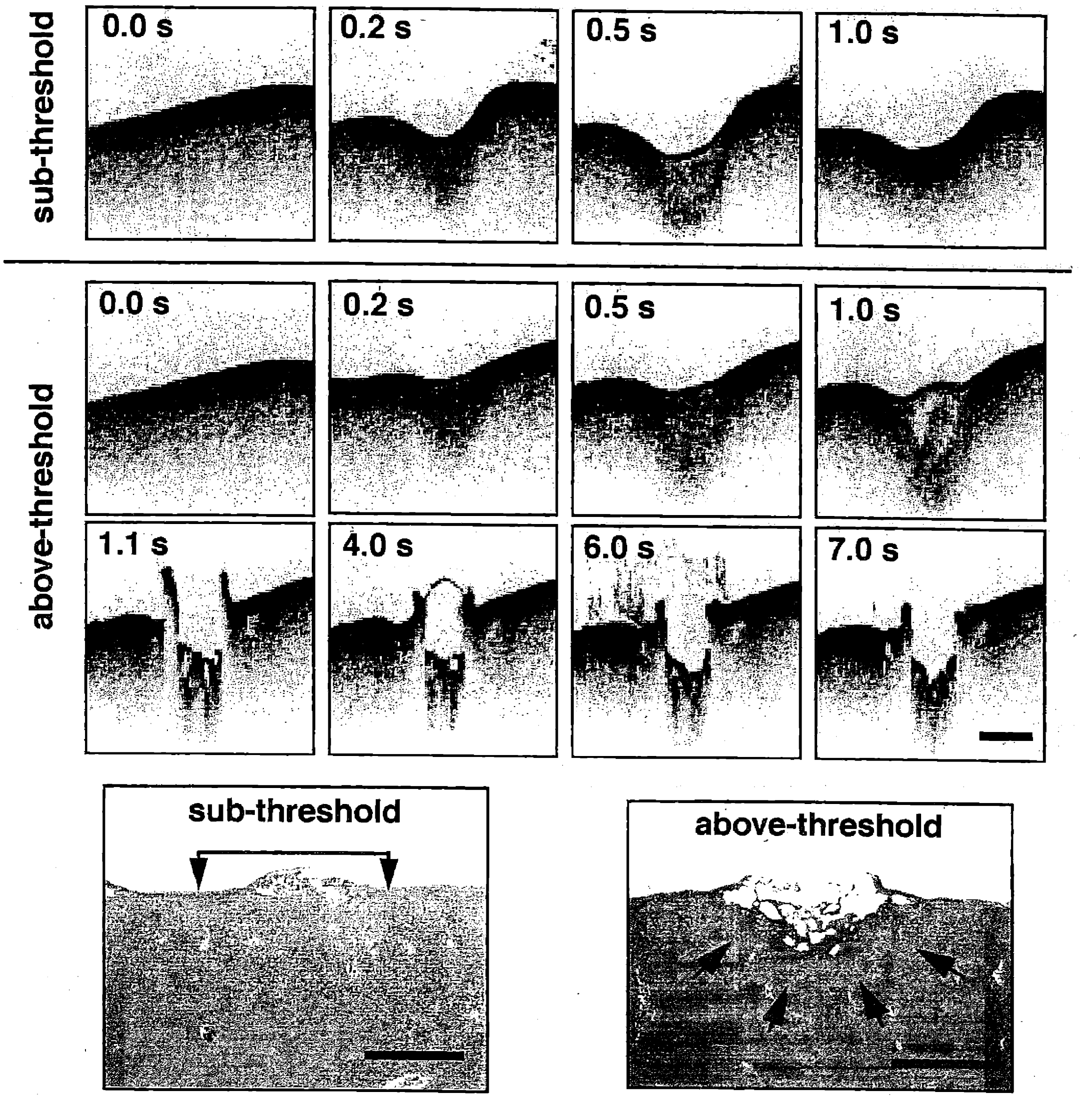

FIGURE 7-15: Sub- and above-threshold ablation of liver. Rat liver was exposed to 1 W argon power for 1 and 7 s. Arrows in histology images illustrate regions of thermal damage. The disrupted tissue observed in the sub-threshold histology is due to histological processing artifact. This is in contrast to the significant tissue disruption observed in the above-threshold histology. Bar represents 1 mm.

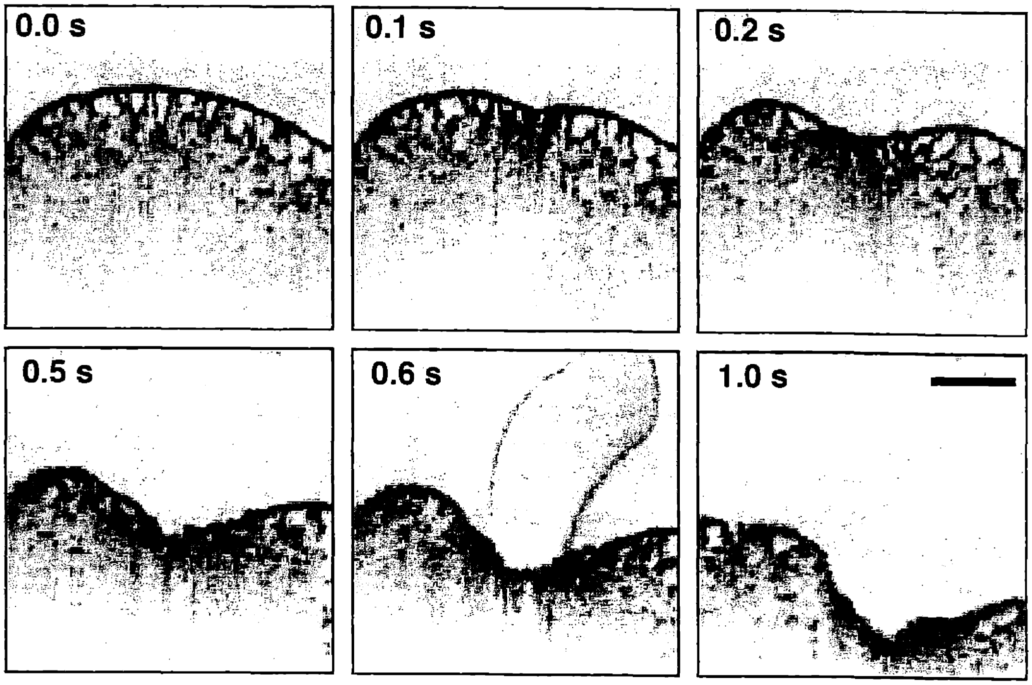

FIGURE 7-16: Lung laser ablation. Thermal damage from the 1 W argon beam results in rapid deflation of rat lung alveoli. Bar represents 1 mm.

7.2.3 Selective vessel ablation

The highly absorbing properties of hemoglobin in blood ($\mu_a = 116\ cm^{-1}$) can be used to selectively ablate vessels within surrounding less-absorbing tissue[275]. A primary clinical application for selective vessel ablation is the removal of nevus flammeus (port-wine stains) from the skin. Port-wine stains are regions of increased vascularity within the upper dermal layers and are usually present at birth[276]. Although benign, when present on the face, they can often be unsightly and cause a great deal of psychosocial difficulties for the individual. Treatment is with the use of dye or argon lasers. The 514 nm wavelength is readily absorbed by the blood and induces a subsequent temperature rise and heating of the vessel by conduction. Coagulation of red blood cells and the vessel wall results in thrombosis and vessel occlusion with minimal damage to the surrounding tissue. Laser treatment has been effective, yet requires a frequent number of procedures because of the small incident spot size and the risk of collateral tissue damage[277]. The superficial location of vessels within the dermis (≈ 0.1 - 1.5 mm) would permit OCT imaging during treatment to assess the ablation of vessels. More importantly, since excessive heating results in scar formation, OCT image-guidance may be used to control the amount of injury to the surrounding tissue.

To demonstrate OCT imaging of selective vessel ablation, a 2 mm thick specimen of rat rectus abdominis muscle with a pair of vessels located 1.5 mm below the surface was harvested and immediately placed in the setup shown in Figure 7-3. The incident argon beam was positioned 250 µm off of the center of the vessels. The vessels contained fresh blood as visualized with the eye from the underside of the specimen. Cross-sectional imaging at 8 fps was performed while 1 W of argon power was delivered for 1 s. The acquired image sequence is shown in Figure 7-17. The initial image (0.0 s) of the vessel pair (arrows) reveals lumens with low-backscatter. At 0.1 s, the lumen of the larger vessel (black arrow) becomes highly backscattering. This is immediately followed at 0.2 s by the same change in the second vessel (white arrow). At 0.5 s and later, the vessels become obscured by a shadowing artifact from overlying optical changes in the tissue. The central lesion becomes evident at 0.6 s and more prominently at 1.0 s (arrows). The last image in the sequence was compared with the corresponding histology shown in Figure 7-18. The overlying tissue shows some evidence of thermal injury (arrow in Figure 7-18A) while the blood within the vessels has been thermally coagulated as seen in the magnified image in Figure 7-18B. These results suggest that OCT imaging can be used to assess changes in the vasculature during the treatment of port-wine stains. Because port-wine stain laser treatments require weeks to months before the full effect is appreciated, OCT may potentially be useful for following the extended healing response. In this preliminary imaging example, the increased absorption by the blood prompted thermal effects in the vessels earlier than in the surrounding tissue. This is important during surgical procedures where little damage may be apparent in low-absorbing tissue with increased damage to the nearby vasculature.

The *in vivo* vessel ablation and tissue response is likely to be different compared with this *in vitro* demonstration. In this study, the blood within the vessels was stationary. Flowing blood will dissipate heat downstream, requiring higher incident powers. In practice, the dye or argon laser is pulsed to limit the amount of thermal injury. In addition, the volume of blood which is rapidly heated represents an extremely small fraction of the total blood volume and will not significantly increase blood or tissue temperatures at other sites.

At a second location along the same vessel pair, a 5 s exposure of 1 W argon was performed, leading to rapid ablation and crater formation. This sequence is shown in Figure 7-19. The initial images in this sequence first illustrate the changes in the vessel followed by thermal injury at the beam location in the center of the image. This thermal injury expands outward to eventually shadow the coagulated vessel pair. Internal vacuolization occurs prior to surface membrane rupture and rapid formation of a deep crater. To

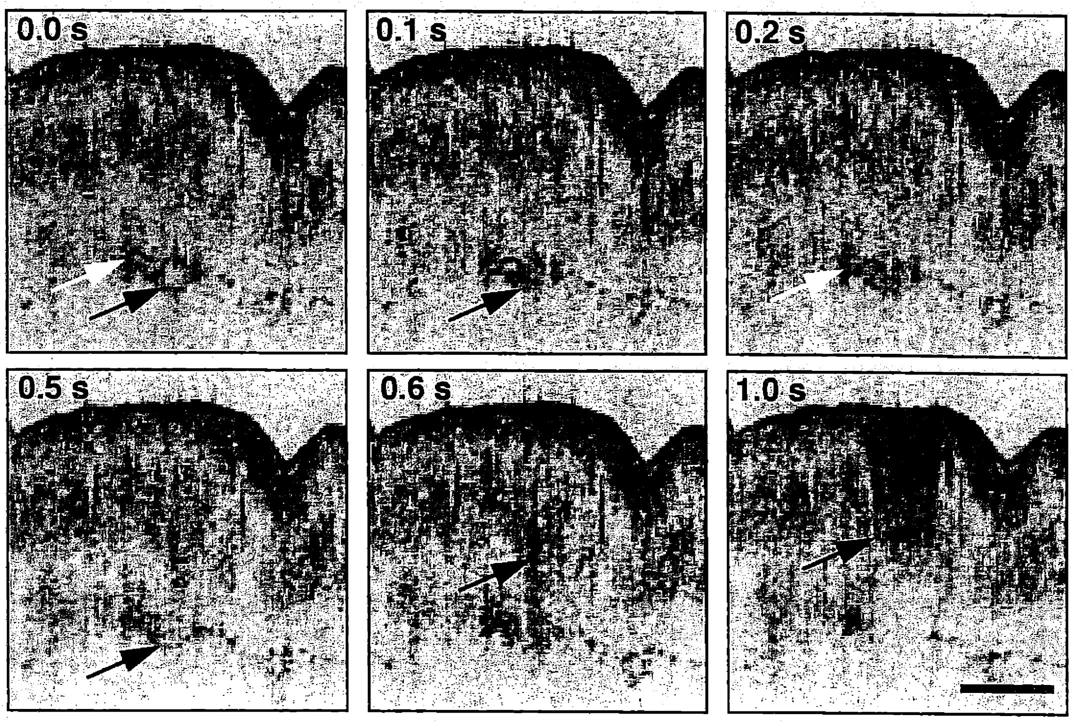

FIGURE 7-17: Selective vessel coagulation. White and black arrows indicate vessel pair in rat rectus abdominis muscle. During the 1.0 s exposure of 1 W argon power, blood within vessels coagulates prior to optical changes in the overlying tissue. Bar represents 1 mm.

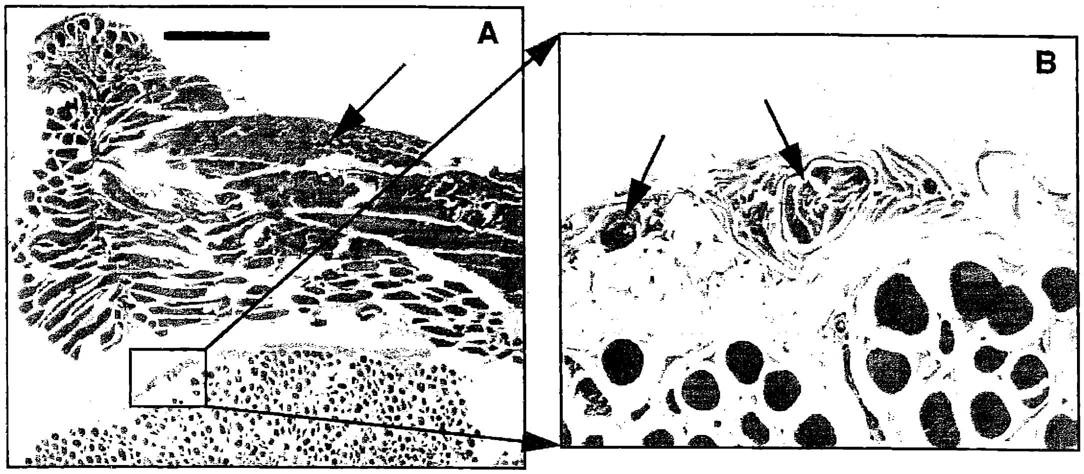

FIGURE 7-18: Vessel coagulation histology. Histology corresponds to image sequence in Figure 7-17. A) Rat rectus abdominis muscle exhibits slight thermal injury (arrow) overlying B) coagulation of blood in a pair of vessels (arrows). Bar represents 1 mm.

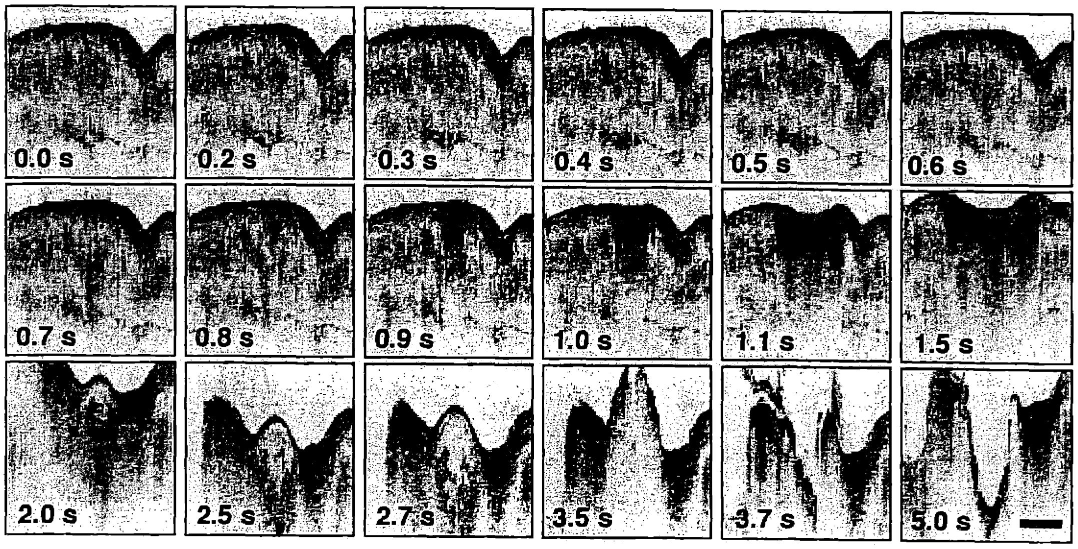

FIGURE 7-19: Coagulation of vessels and ablation of rat rectus abdominis muscle. During 5.0 s exposure of 1 W argon power, expanding lesion forms subsurface vacuolization prior to membrane rupture and deep crater formation. Bar represents 1 mm.

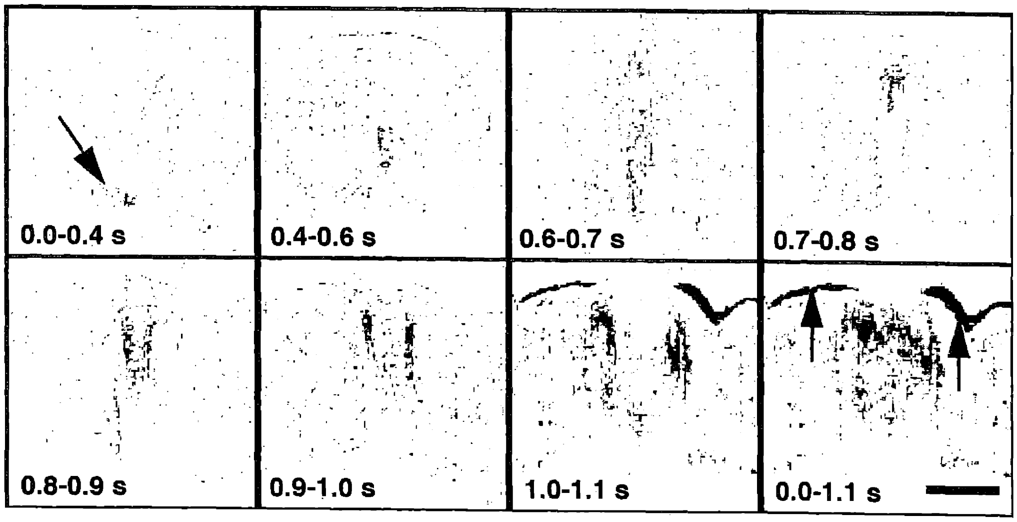

FIGURE 7-20: Difference images of selective vessel ablation. Original images shown in Figure 7-17. Times indicate the time interval during which the changes shown in the image occurred. The arrow in the first image shows early changes occurring within vessels. Arrows in the last image indicate changes in tissue surface elevation from thermal injury. Bar represents 1 mm.

illustrate more clearly the changes that occurred between successive imaging frames, images at early time-points were subtracted from those acquired at later time-points to produce difference images. A sequence of these difference images is shown in Figure 7-20. The signal in each difference image represents the change that occurred between the successive time-points. Between 0.0 and 0.4 s, changes are localized to the region of the vessel pair as indicated by the arrow. Later times reveal changes along the argon beam axis. For the last image, which represents the overall change between 0.0 and 1.1 s, the change along the surface of the tissue (arrows) is likely due to tissue expansion during heating.

The treatment of port-wine stains represents a surgical intervention that could readily be monitored using OCT. Selective vessel ablation can not only be beneficial as in the treatment of port-wine stains, but also detrimental if interventional laser radiation is preferentially absorbed in vessels prior to indications of injury in the bulk, lower-absorbing tissue.

7.3 Radio-Frequency Ablation

Radio-frequency (RF) ablation is a second, more established, interventional technique used in surgical procedures. Radio-frequency waves, ranging from 3 kHz to 300 GHz, are readily absorbed by biological tissues which are essentially water-dominated dielectrics with electrolytes and both polar and non-polar molecules. An adhesive grounding pad is applied to the patient's leg prior to the procedure. A second electrode, a hand-held probe or a catheter, is used to deliver electrical current to a localized tissue site. Depending on the frequency, power, and shape of the waveform, the current can be used to thermally coagulate or cut vessels. Higher currents delivered in a continuous sinusoidal wave can be used to cut tissue for dissection techniques[278].

The cutting and coagulation efficiency of both RF (electrosurgical) and laser ablation have been compared for a number of surgical procedures in the cardiovascular, gynecological, musculoskeletal, and urinary systems[279-282]. Zones of collateral damage have been measured histologically to determine how well each ablation technique can be controlled. No known study, however, has evaluated these two ablation techniques in real-time according to their dynamic effects. OCT was used to monitor and compare the cross-sectional effects of thermal damage from RF and argon laser ablation to assess the degree of collateral damage.

7.3.1 Cardiovascular applications

A catheter-based application for RF ablation is the removal of secondary aberrant conduction pathways through the heart. Alternate electrical conduction pathways can lead to irregular heart rhythms, possible atrial and ventricular fibrillation, and death. An RF catheter is inserted into the arterial or venous system and passed into the atrium or ventricle of the heart. In a monitoring mode, the catheter is used to locate the aberrant pathways prior to RF ablation. The technique may be guided using x-ray angiography to ensure proper placement of the catheter tip, but angiography has insufficient resolution to monitor the effectiveness and extent of the RF ablation.

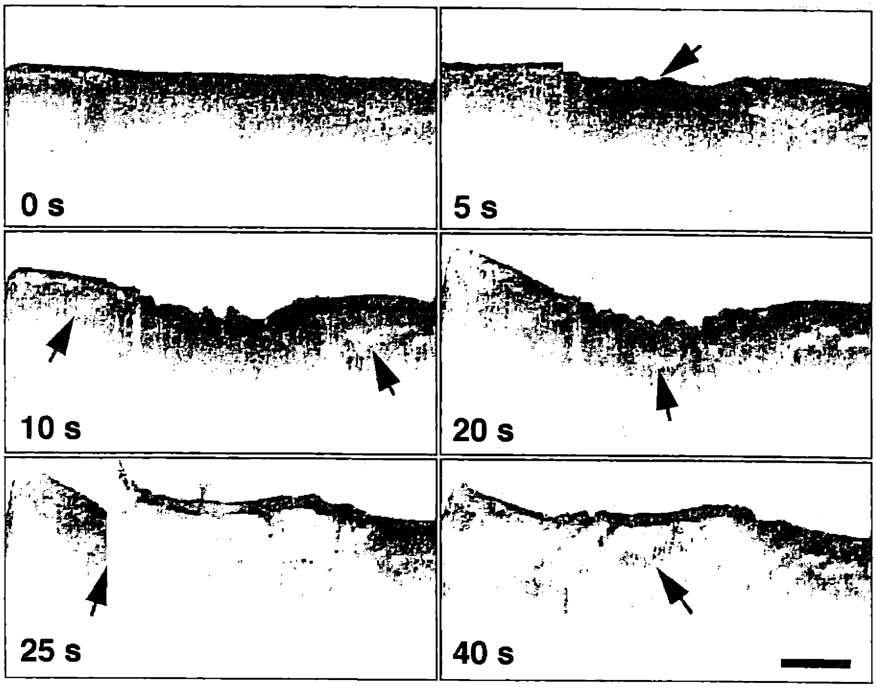

FIGURE 7-21: RF ablation of goat myocardium. Catheter electrode delivering 2 W RF power was located outside of the OCT image plane to prevent shadowing artifacts. At 5 s, arrow indicates early contraction of myocardium. At 10 s, vacuolization begins at the outer lesion margins. Tissue dissection begins at 20 s. Dynamic disruption of tissue and the formation of a dissection plane is imaged at 25 s. Finally at 40 s, heated tissue fluids (arrow) circulate within the dissection plane. Bar represents 1 mm.

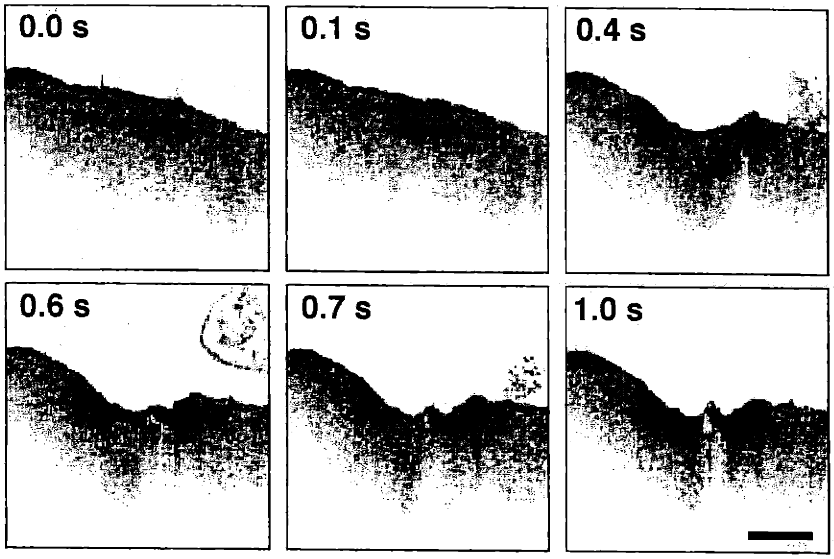

FIGURE 7-22: Argon laser ablation of rat myocardium. Exposure of 1 W argon power for 1.0 s results in localized tissue ablation and vacuolization. Bar represents 1 mm.

The interventional OCT setup shown in Figure 7-3 was used to monitor ablation dynamics. A 3 mm diameter RF ablation catheter with a distal-tip electrode was used to deliver RF energy to specimens while OCT imaging at 4 fps was simultaneously performed. The grounding electrode was placed in the saline bath containing the specimen. Specimens of goat and rat myocardium were used for RF and laser ablation, respectively. A sequence of OCT images acquired during RF ablation of goat myocardium using 2 W RF power is shown in Figure 7-21. Images were acquired at 4 fps rather than 8 fps to capture a larger horizontal scan length and accommodate the large 3 mm diameter of the RF catheter tip electrode. Because the metal tip interfered with OCT imaging, the tip was located at the center of the OCT scan, but immediately outside of the scan plane. At 5 s, the myocardium began to constrict (arrow). Surrounding the lesion, vacuoles were formed, as indicated by the arrows at 10 s. Tissue dissection began at 20 s (arrow) and at 25 s, abrupt dissection was imaged in progress (arrow). A large dissection plane filled with liquid (arrow) was created at 40 s when the RF power was shut off.

To compare RF with argon laser ablation, rat myocardium ($\mu_a = 10.1\ \text{cm}^{-1}$) was placed in the interventional OCT setup. A power of 1 W was delivered to the tissue for 1 s. Ablation was imaged at 8 fps and shown in Figure 7-22. The initial image shows relatively poor image penetration (≈ 1 mm) in this tissue. A region of increased backscatter is observed at 0.1 s followed by rapid tissue ejection and crater formation. After 1.0 s, some vacuolization is still occurring. The transverse extent of damage from laser ablation is significantly more confined than for RF ablation. Large dissection planes are not created because of the focused delivery of laser energy and possibly because laser ablation is more of a surface-interaction phenomena.

In practice, the influence of blood within the chambers of the heart represents a significant limitation for OCT image-guided intervention in the cardiovascular system. The high concentration of scattering red blood cells severely limits OCT imaging penetration at the 1300 nm wavelength. A study of *in vivo* arterial imaging in a rabbit using the catheter-based OCT system encountered a similar limitation[234]. For vascular access, however, saline injections can be used to temporarily clear blood from the imaging site. Within the heart chambers, the volume of blood is too great and saline flushes are likely to be impractical and ineffective. Potentially, catheter balloons might be used to clear blood from the site prior to OCT imaging. However, this increases the complexity of the procedure.

7.3.2 Urological applications

A second clinical application for both RF and laser ablation is the partial or complete removal of the prostate. As described in Section 6.7.2, BPH affects > 90% and prostate cancer affects > 17% of men by the eighth decade of life[258,259]. The number of prostatectomies that occur every year is increasing as is the numbers of newly reported cases. Thermal and mechanical techniques are used to improve urodynamics or to remove the prostate[283]. The thermal-mechanical technique of electrosurgery was first described in 1929 by Mclean[278] and is routinely used for transurethral resection of the prostate (TURP)[284]. Thermal ablation has been performed with focused ultrasound[285], microwaves[286], and lasers[287]. Guidance for these procedures is provided by cystoscopy, MRI, or ultrasound. A major morbidity factor of prostatectomies is impotence and incontinence resulting from damage to neurovascular bundles that lie within the adipose tissue surrounding the prostatic capsule. These bundles are often too small to be resolved with either MRI or ultrasound and are located below the surface, thus endoscopically invisible. A previous OCT imaging study of the urinary tract demonstrated that OCT resolutions are sufficient to image these neurovascular bundles[256]. The use of OCT to monitor prostatectomies and identify both the prostate-adipose border and neurovascular bundles could significantly reduce the morbidity from this procedure.

Cadaveric human prostate was hemi-sected through the urethra and placed in the interventional OCT setup. A 3 mm RF ablation catheter with a distal-tip electrode was positioned on the specimen just outside of the OCT imaging plane. A grounding electrode was placed in the surrounding tissue bath. An RF power of 2 W was delivered to the specimen for 15 s while OCT imaging at 4 fps was performed. The sequence of acquired images is shown in Figure 7-23. The initial image shows urethral sinuses of the hemi-sected urethra filled with collections of saline. At 4 s, the tissue has constricted and portions have moved out of the imaging plane. A larger collection of saline is shown. From 6-11 s, tissue is being coagulated at the lesion site. The large lesion site is shown at 15 s. The corresponding histology reveals excellent correspondence. The thermally-coagulated tissue is more evident along the right side of the crater. Much of the glandular structure observed in the histology, however, was not seen during OCT imaging due to limited resolutions.

Argon laser ablation using 2 W delivered for 8 s was performed at an adjacent site. OCT imaging was simultaneously performed at 8 fps. The sequence with corresponding histology is shown in Figure 7-24. A small localized lesion of coagulated tissue is rapidly formed at 1 s. This is enlarged with ejection of tissue occurring at 3 s (arrow). At 5 s, vacuolization is observed to the left of the crater and at 8 s, a deep carbonized crater has been formed. Comparison with histology confirms the presence of vacuoles adjacent to the crater (arrow). However, the vacuoles created below the crater were not observed with OCT because of the shadowing effect from the carbonized tissue lining the wall of the crater.

The laser ablation of prostate is more confined because of the focused beam. RF catheters with electrodes similar in size to the argon beam spot size (≈ 1 mm) would likely produce similar effects. The advantages of using optical energy for thermal ablation of tissue include non-contact delivery, wavelength-specific absorption rates, delivery via small optical fibers, and the potential for integrating a coincident imaging system to assess and control the progress of the ablation. However, there are two major limitations: 1) the ablation and imaging beams must propagate through body fluids, namely blood, resulting in significant attenuation, and 2) surgical operating time will be increased, compared to electrosurgery, because ablation occurs at a single focused spot on the tissue which must be raster-scanned over the surface for large-area ablation.

Both RF and argon laser ablation was performed from the urethral surface of the prostate as would be encountered during a transurethral prostatectomy. Two limiting factors prevented OCT image-guided ablation to the prostate-adipose border. The 3 mm RF catheter tip produced extensive lateral ablation which extended beyond the 6 mm OCT scan range. Ablation in depth was difficult to achieve in a controlled manner. Deep ablation could be achieved with the argon laser, but the argon laser was not scanned to ablate tissue across the transverse OCT scan range as would be necessary to ablate large surface areas of tissue. The axial scan length for OCT imaging was limited to 3 mm. Either the axial scan range or the tissue specimen would have to be translated to maintain the position of the tissue ablation site within the OCT image.

As was demonstrated by these examples of surgical intervention, the use of OCT for guidance during these procedures provides insight into the mechanisms of tissue damage and permits the high-speed subsurface imaging of the ablation process. Integration of OCT with an incisional or ablative device has the potential for reducing iatrogenic injury frequently caused during surgical interventions.

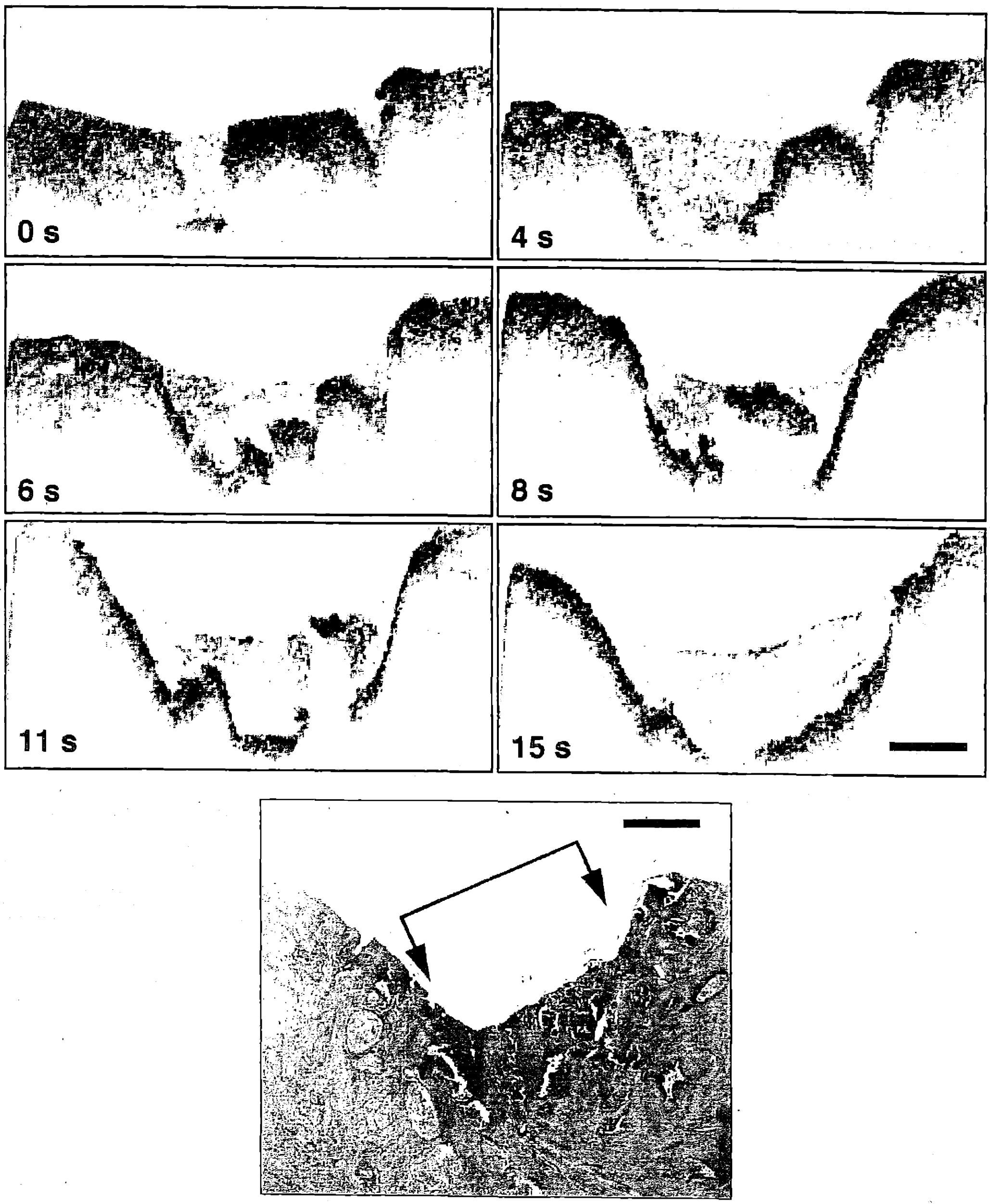

FIGURE 7-23: RF ablation of human prostate with corresponding histology. 2 W RF power was delivered via a catheter electrode. The catheter was located immediately outside of the OCT imaging plane to prevent shadowing artifact. Arrows in histology indicate region of coagulated tissue. Bar represents 1 mm.

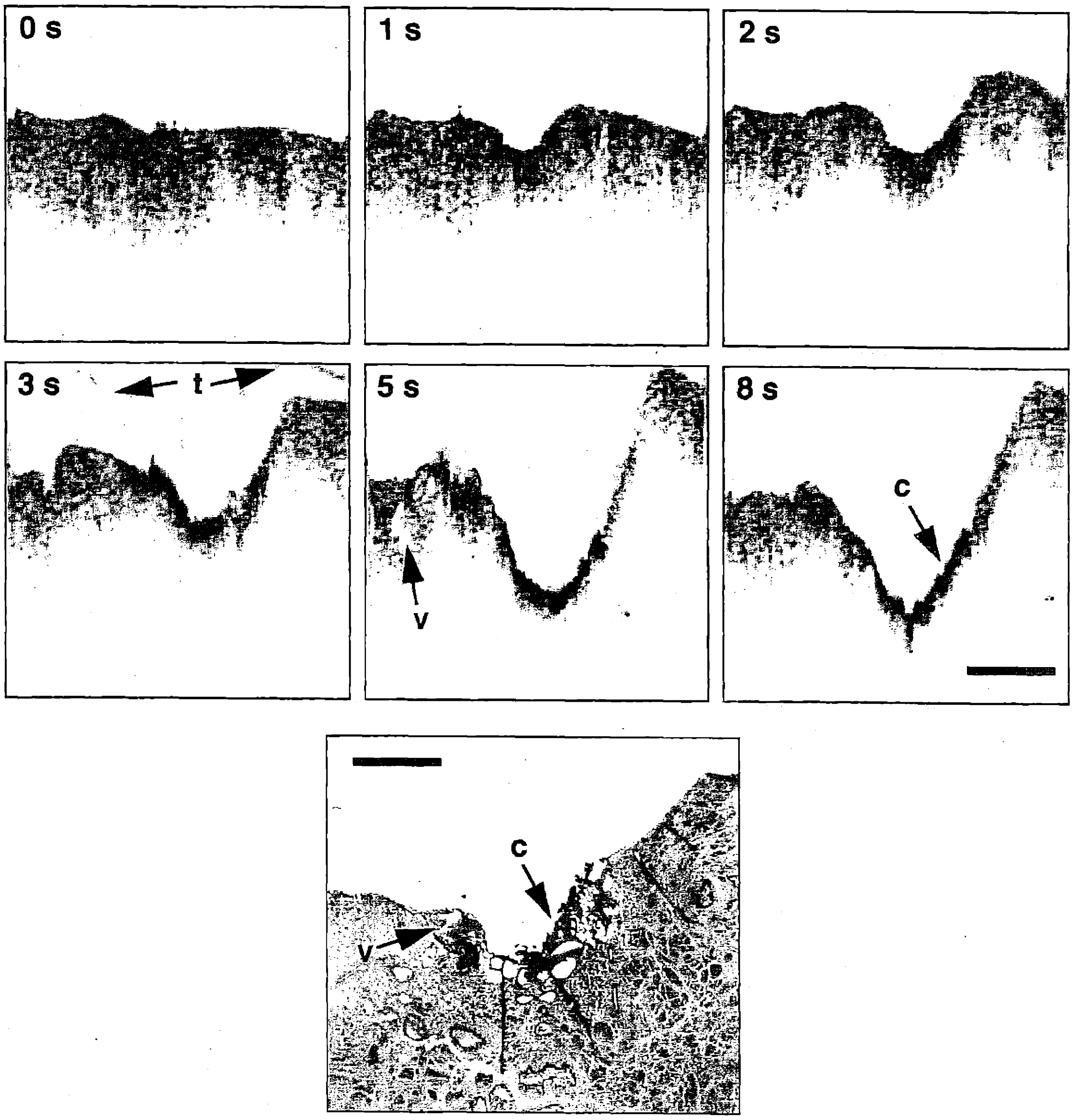

FIGURE 7-24: Argon laser ablation of human prostate. 2 W argon power was delivered for 8 s. Localized ablation resulted in tissue disruption shown at 3 s, vacuolization along the outer margins at 5 s, and crater wall carbonization at 8 s. The corresponding histology reveals the presence of vacuoles and carbonized tissue. Abbreviations: c, carbonization of crater wall; t, ejected tissue; v, vacuoles. Bar represents 1 mm.

Chapter 8

Summary and Conclusions

8.1 Summary

This thesis research has demonstrated the use of OCT for surgical diagnostics, guidance, and intervention. Equally significant, this thesis research has established the fundamental microscopy application of OCT in the field of developmental biology. In comparison with other imaging modalities, OCT offers micron-scale resolutions that are higher than any clinical imaging technique. As a research microscopy instrument, the use of near-IR wavelengths coupled with coherent optical heterodyne detection enables imaging penetrations of 2-3 mm in scattering tissues, a depth 5-10-times greater than is possible with standard confocal microscopy. The compact fiber-optic based design is readily integrated with existing surgical imaging techniques such as endoscopy and laparoscopy.

The OCT technology has advanced since its evolution from OTDR and OCDR measurement techniques in the early 1990's. Solid-state Kerr-lens modelocked laser sources such as the titanium:sapphire and the chromium:forsterite provide average output powers > 100 mW and spectral bandwidths > 100 nm, enabling high-speed OCT imaging and axial resolutions as high as 1.9 μm. As source technology improves, compact and portable diode and fiber-laser sources with equivalent power and bandwidth will replace these laboratory systems. The development of a rapid-scanning optical delay line based on femtosecond pulse-shaping techniques enabled high-speed OCT image acquisition of 256 x 248 pixel images at 8 fps. Higher frame rates are possible at the expense of image size. Spectral radar and frequency-scanning OCT are two new methodologies for performing coherent optical ranging. Obtaining frequency-encoded depth information of optical backscatter in spectral radar is an attractive method which does not rely on a moving reference arm or variations in optical pathlength. Frequency-scanning OCT may be advantageous if rapidly tunable sources become reliable and computing power continues to advance.

The design and engineering of beam delivery instruments has lead to integrated designs for coupling the scanning of a single-mode optical beam through existing optical surgical instruments. Functioning as a research microscope, the OCT beam can be focused by high numerical aperture objective lenses into a specimen placed on multi-axis translational stages similar to confocal microscopy. Maintaining overlap between the OCT detection envelope and the objective focus will require new techniques for focus tracking; necessary for performing imaging with high transverse resolutions (< 10 μm). The surgical microscope permitted rapid three-dimensional OCT imaging using a pair of orthogonal galvanometer scanners to direct the imaging beam on the specimen. Alignment of the OCT imaging beam with the optical axis of the microscope enabled simultaneous high-magnification viewing of the OCT scan location. This will be increasingly necessary as OCT resolutions increase, scan lengths on biological tissue decrease, and when precise registration is required between the scan location and the histological sectioning plane. The hand-held surgical imaging probe incorporated a compact piezoelectric cantilever for forward-directed imaging. Improvements in the probe design, from translating a GRIN focusing lens to the use of a telescope design, permitted linear high-speed scanning with 3-4 mm scan lengths and minimal artifacts. The simple pen-like design should be less intrusive in the surgical environment. The piezoelectric translation mechanism was extended for use in an OCT laparoscope. A single 19.5 cm GRIN rod lens was used to maintain and relay the single-mode beam profile to the distal end of the device. The established use of laparoscopy in minimally invasive surgery enables visualization of tissue at remote, internal sites within the body. OCT imaging was performed through a single GRIN rod optical element permitting simultaneous *en face* visualization of the tissue, visualization of the OCT scan location, and OCT imaging of subsurface tissue morphology. Modifications to the radial-scanning catheter design improved imaging performance. The use of a free-space optical coupling improved reliability by reducing the occurrence of backreflections at the coupling which tended to saturate the detector and obscure the image. New shorter-working-distance catheters were constructed to place the beam focus within 1 mm of the catheter sheath. This enabled intraarterial imaging and imaging of small lumens which previously would have been located outside of the confocal parameter, resulting in lower transverse image resolutions.

The ability of OCT to image tissue microstructure was demonstrated using developmental biology animal models. These frog and fish embryos provided a nearly ideal *in vivo* model because of the variety of organ systems, morphological variations, and cellular structures that developed over time. Morphological abnormalities during development were identified and compared with histology. The non-contact, non-invasive nature of OCT permitted repeatable imaging over extended periods of time at resolutions that approach the level of histology. No contrast agents, which would have limited the viability of cells, were necessary, as in laser-scanning confocal microscopy. OCT can be used to track the morphological and functional expression of genes without having to sacrifice specimens for histological observations. The first demonstration of functional OCT imaging was performed in the developing *Xenopus* cardiovascular system. Optical cardiograms and high-speed OCT imaging were used to assess functional parameters of the normal heart and one affected by doses of inotropic agents. The Cr^{4+}:forsterite laser was used as a high-resolution source ($\approx 5\ \mu m$ axial resolution) to image cell nuclei and membranes. Cell mitosis and migration were tracked in these animal models. Cellular imaging studies in these animal models provided insight into the relevant issues for cellular imaging in humans.

Surgical diagnostic techniques using OCT were explored. The optical properties of tissue were defined as were the contributions of single and multiple backscattered light in the detected OCT signal. The contributions of speckle significantly limit the observation of tissue structures which are close to the resolution limit of OCT, namely human cells. Important distinctions were made between histological observations and regions of optical backscatter within OCT images. Mechanisms of contrast between these techniques are different and must be fully understood for accurate interpretation of OCT data. Contrast in OCT images can be enhanced using exogenous air-filled microbubbles or endogenous melanin. Both increase the local index of refraction difference thereby increasing the amount of optical backscatter. Digitization of the interferometric signal permits Fourier analysis of the Doppler frequency (velocity) components present in the reference and sample arms of the interferometer. Doppler OCT was demonstrated by measuring a laminar fluid flow profile in a blood vessel model. This concept was extended to imaging the two-dimensional flow profile by using the detector filter bandwidth as a window for imaging a range of frequency (velocity) components within the image. The three-dimensional display of OCT images and techniques for improving the quality of image data were discussed and demonstrated as working concepts applied to the data presented in this thesis.

The environment in which OCT surgical guidance will perform was investigated by systematically imaging human organ systems which may benefit from improved visualization. Both the central and peripheral nervous systems contain sensitive tissue structures that require guidance to avoid loss of sensory and motor functions. The use of OCT to longitudinally track peripheral nerve fascicles and estimate fascicle diameters provides previously unavailable information to the microsurgeon to successfully anastomose corresponding ends of a severed peripheral nerve. In a second microsurgery demonstration, OCT was used to assess the quality of a microsurgical arterial anastomosis and was able to identify occlusions transmurally which would lead to post-operative complications. Imaging of gynecological pathology of the uterus and ovary was performed from the orientation consistent with laparoscopic examination, suggesting an advantage for subsurface imaging integrated with this device. Subsurface imaging of pediatric lymph nodes revealed follicular structure. Changes in follicular lymph node architecture occur during lymphoid malignancies or tumor metastasis. An OCT optical biopsy of *in vivo* lymph nodes may increase the sample size and ability to diagnose tumor stage. Accurate tumor staging subsequently would improve treatment and outcome. The urinary and gastrointestinal systems were imaged in an *in vivo* rabbit to demonstrate the integrated high-speed catheter-based OCT imaging system. Human prostate was imaged *in vitro* with the catheter to demonstrate diagnostic capabilities for evaluating BPH.

Representative surgical interventions were demonstrated using an argon laser and RF catheter to thermally ablate tissue. National safety standards (ANSI) were evaluated to determine maximum permissible exposure limits and to determine power levels sufficient to induce thermal damage in tissue. Damage to tissue can occur by photochemical, thermal, and mechanical mechanisms. Each mechanism occurred during laser and RF ablation. Biochemical tissue stains were used to determine the extent of photochemical damage and assess cell viability surrounding thermal lesions. OCT imaging at 4-8 fps guided the placement of thermal lesions and imaged the dynamic evolution of the tissue injury. Thermal and mechanical damage mechanisms were observed with OCT and confirmed with histology. Comparisons of thermal ablation and resulting lesions were made between clinically-relevant tissue types, including brain, kidney, liver, lung, and muscle. The increased absorption of blood permitted selective vessel ablation prior to damage to surrounding muscle tissue. This demonstrated an OCT application for monitoring the treatment of port-wine stains. RF ablation was directly compared with argon laser ablation in the heart and prostate using OCT. Ablation of aberrant conduction pathways in the heart is a treatment for arrythmias and ablation of the prostate is a surgical intervention for the treatment of BPH and prostate cancer. The use of OCT enables rapid feedback, visualization, and control of the surgical intervention.

8.2 Future Studies

Research and development of OCT and its applications to surgery and medicine represent a continuum. The results from this thesis research, like most research projects, invite more questions than they answer. This section describes some key areas for continued investigation.

8.2.1 Mutagenesis of developmental biology models

The rapidly advancing fields of developmental and molecular biology now have the ability to modify the genome of organisms with gene-specific accuracy[288,289]. Much of our current understanding of the function of genes is learned by the process of removing a gene from the genome and observing what effect this has on the developing specimen. This is referred to as a "knock-out" technique[290]. All of the developmental biology specimens used in this research started with a genome that was unaltered by human intervention. The abnormal specimens imaged in Section 4.3 were the result of random mutations or environmental toxins rather than specific mutagenic agents. One of the primary advantages of OCT is for screening large numbers of developing embryos for morphological variations *in vivo*, without having to sacrifice the specimen for histological preparation. In addition, if a mutation expresses itself differently at various stages in development, then many specimens are needed for serial studies because histological examination can only be performed at one time-point in development. Inter-specimen variations then come into question.

The developing cardiovascular system is an area of increasing research and clinical interest. Malformations of the heart and blood vessels account for the largest percentage of human birth defects, 1% of live births and nearly 10% of stillbirths[153]. The high incidence of malformations is due to the complex interactions and precise timing of cell migration and differentiation between multiple embryonic cells types[291]. OCT may be a key investigative instrument which would permit the identification of malformations in animal models. As was shown in Section 4.4, OCT can be used to determine functional parameters of cardiovascular dynamics. Whereas histology can only investigate morphological malformations, OCT can provide a means of identifying mutations that affect the functional state of the heart.

Retinoic acid (RA), a potential metabolite of retinol (vitamin A), is an established chemical mutagen that affects the development of normal pattern formation[292], the nervous system[293], and the cardiovascular system[294] in both amphibian and fish model systems. Retinoic acid belongs to a family of compounds, the retinoids, which have diverse effects on cell differentiation, metabolism, and growth. Administered to the bath medium containing developing embryos, mutagenic effects can be induced in a manner linearly dependent on RA concentrations. The use of RA to induce genetic malformations is a relatively simple and established technique which could provide specimens for investigating mutagenesis with OCT.

This thesis research represents the first application of OCT in the field of developmental biology. OCT can be used to observe the expression of the genetic program *in vivo*, and therefore represents a powerful tool for improving our understanding of the morphological and functional changes that occur when the normal genetic program fails. Similarly, OCT can provide insight into how site-specific genetic mutations are expressed in a living organism.

8.2.2 Pharmacologic and toxicologic effects on development

Understanding the safety issues associated with the use of pharmacologic agents is of primary concern for physicians and patients. The developing embryo is extremely sensitive to environmental toxins and pharmacological drugs. The field of teratology is devoted to determining the effects of drug and toxin exposure during pregnancy and the risk of harm to the developing fetus. Animal models have traditionally preceded human patients as the assay for determining the effectiveness and side-effects of new drugs[295,296]. Heightened awareness about the appropriate use of animals in testing, however, has prompted scientists to use more sensitive techniques in smaller animal models. Testing at the cellular level may offer useful information. Prior to the introduction for use in humans, the effects of drugs must be characterized by a dose-response relationship, periods of greatest sensitivity, a biological basis for metabolism, and genetic susceptibility[297].

The use of one pharmacologic agent, verapamil, was used to alter the functional state of the *Xenopus* heart in Section 4.4. Other inotropic agents which affect the cardiovascular system as well as classes of vasoconstrictors and vasodilators are possible pharmacological agents which produce dynamic effects measurable with OCT. Small animal models such as frogs and fish imaged with OCT may offer a viable assay for future pharmacological studies.

In addition to measuring the physiological effects of pharmaceuticals on developmental biology animal models, potentially hazardous effects from chemical and environmental toxins can be assessed with OCT. Interest in environmental hazards is best exemplified by world-wide public concern of the appearance of severely mutated frogs in remote Northwest regions of the United States[298]. These mutated frogs lived in areas which were once thought to be environmentally pure. Depletion of the ozone layer and increased amounts of ultraviolet (UV) radiation were suggested as possible causes[299,300] raising fear that these frogs may be early sensitive indicators of damage to our environment, and ultimately to ourselves. Ultraviolet damage to sensitive developing embryos is one environmental factor that can be assessed with OCT. Although extrapolation to humans is difficult and rather undefined, these studies would document hazardous UV effects on living organisms.

8.2.3 Neoplastic progression in tissue

A significant advance for OCT to gain broad and rapid integration into the surgical and medical communities would be the ability to detect pre-malignant and malignant cells within the human body. If discrimination between healthy and neoplastic tissue could be determined, this information could be used to diagnose neoplasms, stage malignancies, guide surgical resection, direct radiation, and deliver optimal chemotherapy. Characteristic cellular morphologies found in neoplastic tissue include a high degree of pleomorphism and high nuclear-to-cytoplasmic ratios as was discussed in Section 4.5 using the *Xenopus* amphibian animal model. Imaging at cellular resolutions in humans is likely to be achieved with improvements in imaging resolution and perhaps image processing techniques.

Resolutions of 0.5-1.0 μm in confocal microscopy permit the imaging of human cells and subcellular structures[149,301]. Achieving these resolutions in the transverse image direction implies high-NA optics with correspondingly short confocal parameters. Focus-tracking methods must be implemented to ensure overlap between the beam waist and the OCT detection envelope. Achieving these resolutions in the axial dimension is dependent on the center wavelength and bandwidth of the source. As shown in Figure 2-16, shorter center wavelengths and broader spectral bandwidths maximize axial resolution. For 1 μm axial resolution in tissue ($n = 1.35$) using a $Ti{:}Al_2O_3$ KLM laser at 800 nm center wavelength, a 210 nm bandwidth is required. Femtosecond pulse or spectral shaping techniques may enable spectra from one or more sources to be combined, shaped, and smoothed to attain these resolutions.

Image processing techniques may be used to remove the effects of non-Gaussian spectra which will likely occur when shaping broad bandwidths. Speckle is most deleterious when detecting structure with dimensions on the order of the image resolution, as is the case when imaging human cells at current OCT resolutions. Cross-correlation between adjacent axial scans may reduce the contribution from speckle. Advanced image processing algorithms may be able to model and remove the effects of speckle and enable definitive detection of human cells. Once cellular-level imaging is demonstrated in human tissues, identification of pre-malignant and malignant cells would follow based on well-established characteristics for each cell type.

8.2.4 *In vivo* human imaging

In vivo human OCT imaging has been performed in the fields of ophthalmology[62,66,67] and dermatology[73,118,120]. Early reports have demonstrated *in vivo* OCT imaging in human gastrointestinal, urinary, and reproductive systems as well[79]. Implementation of OCT in the clinical setting raises many logistical issues of safety, reliability, transportability, and unforeseen *in vivo* imaging conditions which remain to be investigated.

The limiting factor for *in vivo* human imaging in a surgical or clinical environment has been the availability of a suitable low-coherence source. The amplified SLD manufactured by AFC Technologies, Inc. and described in Section 2.4.1 has sufficient power and bandwidth to perform OCT imaging

(256 x 248 pixels) at 8 fps with ≈ 19 μm axial resolution and a SNR of 105 dB. This source is compact and reliable making it the primary choice for surgical or clinical implementation. Acquisition rates of 8 fps are sufficient, based on experimental observations, for preliminary *in vivo* human imaging experiments. Faster 16-30 fps acquisition rates will be necessary when imaging rapidly moving tissue in the respiratory and cardiovascular systems. Achieving video acquisition rates (30 fps) is limited by the speed and linearity of the galvanometer in the optical delay line. Although resonant-scanning galvanometers can achieve sufficiently high speeds, the non-linear (sinusoidal) rotation of the galvanometer would require real-time signal processing algorithms to correct for the non-linear axial scanning.

Of the beam delivery systems discussed in Chapter 3, the radial-imaging catheter is the most developed device for surgical or clinical implementation. The 1 mm outer diameter of the catheter can be passed down the 2-3 mm diameter working instrument channels in existing flexible endoscopes. Endoscopes have integrated flexure-positioning systems and distal micro-CCD chips for *en face* visualization which can be used to guide the OCT catheter and observe the scan location. Primary safety issues involve the sterilization of instrument components and the reliability of the distal optics. A sterile outer catheter sheath can be replaced with each use. Based on two *in vivo* experimental trials in rabbits, damaged distal optics which become separated from the optical fiber are contained within the sealed catheter sheath and would likely represent negligible risk to the patient. This system would permit *in vivo* human imaging of the upper and lower gastrointestinal tracts and potentially access to the respiratory and reproductive tracts. Used alone or with small endoscopes, the OCT catheter could be inserted into the human urinary tract.

Whereas the radial-imaging catheter is ideal for systems with tubular lumens, forward-directed imaging is more applicable for tissues with larger, exposed surface areas. The forward-imaging probe can be adapted for *in vivo* human imaging by ruggedizing the probe housing and ensuring that the device can be sterilized between uses. The cervix has been a target for probe-based fluorescent spectroscopic diagnostics and is relatively accessible with the forward-imaging probe[302,303]. Skeletal joint spaces which have been opened prior to replacement or amputation represent a second *in vivo* human tissue site that is accessible in a clinical and surgical setting with minimal risk to the patient. Imaging an opened joint capsule would serve as a feasibility study for future *in vivo* arthroscopic OCT investigations. Preliminary *in vitro* studies suggest that OCT may differentiate between various stages of cartilage degeneration[304].

Future surgical applications of OCT for *in vivo* human imaging will most likely be dictated by the safety, efficacy, and cost-benefit analysis for its use in surgical procedures. Close collaborations with surgeons and approval by the Federal Drug Administration (FDA) will be necessary for more complicated procedures.

8.2.5 OCT image-guided laser surgery

OCT is well-suited for performing image-guided laser surgery, as was demonstrated in Chapter 7. For this demonstration, the argon laser radiation was aligned with the OCT imaging plane using bulk optics in a large configuration. The optical beam delivery system in OCT can be modified to directly incorporate the delivery of high-power continuous wave radiation for thermal ablation or high-energy ultrashort pulses for mechanical ablation. An immediate implementation would involve independent optical fibers which may be integrated into a hand-held surgical probe. The fiber delivering the ablation radiation could remain fixed in the center of the OCT scan range or be translated to ablate larger regions of tissue in synchrony with OCT imaging. For the delivery of single high-energy pulses, delivery could be timed with OCT scanning to fire at the center of the scan range. Delivery of high-energy ultrashort optical pulses has been demonstrated in a probe designed for intraocular laser surgery[305]. However, 1064 nm wavelength pulse delivery from a Q-switched Nd:YAG laser was accomplished through a multi-mode optical fiber and focused by a GRIN lens. No optics for simultaneously imaging and no mechanism for lateral translation of the focal position were incorporated. Propagation of high-energy pulses or high-power cw beams through the single-mode fiber in OCT is problematic.

An initial demonstration of an integrated device would be to thermally incise tissue, using OCT to guide placement and monitor depth and extent of thermal injury. Thermal ablation could be performed adjacent to sensitive structures such as blood vessels and nerves. Histology could document the confined regions of damage and verify reduced collateral damage. OCT image-guided laser ablation of a tumor would demonstrate its use in guiding surgical resection. Results based on histology could be used to compare OCT image-guided surgical resection with resection using visual cues alone. An integrated device could be used to perform thermal laser welding of tissue or vessels under OCT image guidance[269]. Arterial anastomoses, such as the one performed and imaged in Section 6.3.1, could be done without the use of a nylon suture. Equally interesting would be the application of OCT for monitoring the healing response following a surgical intervention. The long time-period required for the healing response would permit controlled, high-resolution, OCT imaging studies to document the changes that occur within a wound. The concept of an interventional technique with an integrated imaging system would represent a significant advance in surgical methodology.

8.3 Conclusions

Optical coherence tomography is a high-resolution, high-speed optical imaging technology that can detect microstructural tissue morphology based on variations in optical backscatter. This thesis research has investigated the use of OCT for surgical diagnostics, guidance, and intervention. Optical beam delivery instruments used as vehicles to integrate the OCT technology into the surgical suite have been designed and engineered to minimize the change in protocol after the introduction of this new technique. Rapid advancements in compact optical sources will expand the use of OCT from the research laboratory to the research surgical suite, and possibly into routine surgical practice. The ability of OCT to image tissue microstructure has been investigated using developmental biology animal models. This investigation represents a fundamental demonstration of OCT in the field of developmental biology and has established OCT as an innovative microscopy technique. The capabilities of OCT for imaging surgical tissue during interventional procedures has also been demonstrated. These results suggest a feasibility for performing *in vivo* intraoperative OCT imaging with resolutions that are unprecedented in the surgical community. This technology has the potential to create an entirely new field of high-resolution microsurgery as the ability to visualize pathologic tissue moves from morphological structures at the organ and tissue level to microstructures at the cellular level. Although numerous logistical issues remain to be solved once *in vivo* OCT-guided surgery is performed, these should not inhibit the investigation of this new surgical methodology. The application of OCT for image-guided surgery is warranted if only for the possibility of improving patient care.

References

1. Roentgen WK. On a new kind of rays. Nature 53:274-276, 1896.
2. Feldman DR, Kulling DP, Hawes RH, Kay CL, Muckenfuss VR, Cotton PB, Bohning DE, Young JWR. MR endoscopy: Preliminary experience in human trials. Radiology 202:868-870, 1997.
3. Goldberg BB, Liu J-B, Merton DA, Feld RI, Miller LS, Cohn HE, Barbot D, Gillum DR, Vernick JJ, Winkel CA. Sonographically guided laparoscopy and mediastinoscopy using miniature catheter-based transducers. J. Ultrasound Med. 12:49-54, 1993.
4. Allemond R. Basic technical aspects and optimization problems in x-ray computed tomography. In *Physics and Engineering of Medical Imaging,* Guzzardi R, Editor. Martinus Nijhoff Publishers: Boston, MA. p. 207-217, 1987.
5. Brink JA. Technical aspects of helical (spiral) CT. Radiologic Clinics of N. Amer. 33:825-841, 1995.
6. *Medical Device Register-Official Directory of Medical Suppliers.* Vol. 1. Medical Economics Co.: Montvale, NJ, 1996.
7. Morton EJ, Webb S, Bateman JE, Clarke LJ, Shelton CG. Three-dimensional x-ray microtomography for medical and biological applications. Phys. Med. Biol. 35:805-820, 1990.
8. Rajyaguru JM, Kado M, Nekula K, Richardson MC, Muszynski MJ. High resolution x-ray micrography of live *Candida albicans* using laser plasma pulsed point x-ray sources. Microbiol. 143:733-738, 1997.
9. Black MP, Moriarty T, Alexander E, Stieg P, Woodard EJ, Gleason PL, Martin CH, Kikinis R, Schwartz RB, Jolesz FA. Development and implementation of intraoperative magnetic resonance imaging and its neurosurgical applications. Neurosurg. 41:831-845, 1997.
10. Markisz JA, Aquilia MG. *Technical Magnetic Resonance Imaging*. Appleton & Lange: Stamford, CT, 1996.
11. Bell RA. Economics of MRI Technology. J. Mag. Res. Imaging 1:10-25, 1996.
12. Jacobs RE, Fraser SE. Magnetic resonance microscopy of embryonic cell lineages and movements. Science 263:681-684, 1994.
13. Jacobs RE, Fraser SE. Imaging neuronal development with magnetic resonance imaging (NMR) microscopy. J. Neurosci. Meth. 54:189-196, 1994.
14. Smith BR, Johnson GA, Groman EV, Linney E. Magnetic resonance microscopy of mouse embryos. Proc. Natl. Acad. Sci. USA 91:3530-3533, 1994.
15. Winkelmann JW, Kenner MD, Dave R, Chandwaney RH, Feinstein SB. Contrast echocardiography. Ultrasound in Med. & Biol. 20:507-515, 1994.
16. Hoff L. Acoustic properties of ultrasonic contrast agents. Ultrasonics 34:591-593, 1996.
17. de Jong N, Hoff L, Skotland T, Bom N. Absorption and scatter of encapsulated gas filled microspheres: Theoretical considerations and some measurements. Ultrasonics 30:95-103, 1992.
18. Hibberd MG, Vuille C, Weyman AE. Intravascular ultrasound: Basic principles and role in assessing arterial morphology and function. Am. J. Card. Imag. 6:302-324, 1992.

19. Masotti L. Basic principles and advanced technical aspects of ultrasound imaging. In *Physics and Engineering of Medical Imaging,* Guzzardi R, Editor. Martinus Nijhoff Publishers: Boston, MA. pp. 263-317, 1987.

20. Foster FS, Pavlin CJ, Lockwood GR, Ryan LK, Harasiewicz KA, Berube LR, Rauth AM. Principles and applications of ultrasound backscatter microscopy. IEEE Trans. Ultrason. Ferroelec. Freq. Contr. 40:608-617, 1993.

21. Chandraratna PAN, Awaad MI, Chandrasoma P, Khan M. High-frequency ultrasound: Determination of the lowest frequency required for cellular imaging and detection of myocardial disease. Am. Heart J. 129:15-19, 1995.

22. Turnbull DH, Starkoski BG, Harasiewicz KA, Semple JL, From L, Gupta AK, Sauder DN, Foster FS. A 40-100 MHz B-scan ultrasound backscatter microscope for skin imaging. Ultrasound Med. & Biol. 21:79-88, 1995.

23. Turnbull DH, Ramsay JA, Shivji GS, Bloomfield TS, From L, Sauder DN, Foster FS. Ultrasound backscatter microscope analysis of mouse melanoma progression. Ultrasound Med. & Biol. 22:845-853, 1996.

24. Rooks MD, Slappey J, Zusmanis K. Precision of suture placement with microscope- and loupe-assisted anastomoses. Microsurgery 14:547-550, 1993.

25. Merle M, De Medinaceli L. Primary nerve repair in the upper limb. Our preferred methods: Theory and practical applications. Microsurgery 8:575-586, 1992.

26. Haglund MM, Berger MS, Hochman DW. Enhanced optical imaging of human gliomas and tumor margins. Neurosurgery 38:308-317, 1996.

27. Minsky M. Memoir on inventing the confocal scanning microscope. Scanning 10:128-138, 1988.

28. Spielmann C, Curley PF, Brabec T, Krausz F. Ultrabroadband femtosecond lasers. IEEE J. Quant. Elec. 30:1100-1114, 1994.

29. Piston DW, Kirby MS, Cheng H, Lederer WJ, Webb WW. Two-photon-excitation fluorescence imaging of three-dimensional calcium-ion activity. Appl. Opt. 33:662-669, 1994.

30. Svoboda K, Denk W, Know WH, Tsuda S. Two-photon-excitation scanning microscopy of living neurons with a saturable Bragg reflector mode-locked diode-pumped Cr:LiSrAlFl laser. Opt. Lett. 21:1411-1413, 1996.

31. Maiti S, Shear JB, Williams RM, Zipfel WR, Webb WW. Measuring serotonin distribution in live cells with three-photon excitation. Science 275:530-532, 1997.

32. Stricker SA, Centonze VE, Paddock SW, Schatten G. Confocal microscopy of fertilisation-induced calcium dynamics in sea urchin eggs. Dev. Biol. 149:370-380, 1992.

33. Girard S, Clapham D. Acceleration of intracellular calcium waves in *Xenopus* oocytes by calcium influx. Science 260:229-232, 1993.

34. Boppart SA, Deutsch TF, Rattner DW. Optical imaging technology in minimally invasive surgery. Surg. Endosc. Submitted, 1998.

35. Geis WP, Kim HC, McAfee PC, Kang JG, Brennan EJJ. Synergistic benefits of combined technology in complex minimally invasive surgical procedures: Clinical experience and educational processes. Surg. Endosc. 10:1025-1028, 1996.

36. Grimm H. Endoscopic ultrasonography with the ultrasonic esophagoprobe. Endosc. 26:818-821, 1994.

37. Walsh RM, Ackroyd FW, Shellito PC. Endoscopic resection of large sessile colorectal polyps. Gastrointest. Endosc. 38:303-309, 1992.

38. Asamura H, Nakayama H, Kondo H, Tsuchiya R, Naruke T. Thoracoscopic evaluation of histologically/cytologically proven or suspected lung cancer: A VATS exploration. Lung Cancer 16:183-190, 1997.

39. Miller A, Stonebridge PA, Tsoukas AI, Kwolek CJ, Brophy CM, Gibbons GW, Freeman DV, Pomposelli FB, Campbell DR, LoGerfo FW. Angioscopically directed valvulotomy: A new valvuotome and technique. J. Vasc. Surg. 13, 1991.

40. Easter DW, Cuschieri A, Nathanson LK, Jones ML. The utility of diagnostic laparoscopy for abdominal disorders. Diag. Laparoscopy 127:379-383, 1992.

41. Hemming AW, Nagy AG, Scudamore CH, Edelmann K. Laparoscopic staging of intraabdominal malignancy. Surg. Endosc. 9:325-328, 1995.

42. Watt I, Stewart I, Anderson D, Bell G, Anderson JR. Laparoscopy, ultrasound and computed tomography in cancer of the oesophagus and gastric cardia: A prospective comparison for detecting intra-abdominal metastases. Br. J. Surg. 76:1036-1039, 1989.

43. Tomkinson TH, Bentley JL, Crawford MK, Harkrider CJ, Moore DT, Rouke JL. Rigid endoscopic relay systems: A comparative study. Appl. Opt. 35:6674-6683, 1996.

44. Reddick EJ, Olsen DO. Laparoscopic laser cholecystectomy: A comparison with minilap cholecystectomy. Surg. Endosc. 3:131, 1989.

45. Escarce JJ, Bloom BS, Hillman AL, Shea JA, Schwartz JS. Diffusion of laparoscopic cholecystectomy among general surgeons in the United States. Med. Care 33:256-271, 1995.

46. Orlando R, Russell JC, Lynch J, Mattie A. Laparoscopic cholecystectomy: A statewide experience. Arch. Surg. 128:494-499, 1993.

47. Fujimoto JG, Brezinski ME, Tearney GJ, Boppart SA, Bouma BE, Hee MR, Southern JF, Swanson EA. Biomedical imaging and optical biopsy using optical coherence tomography. Nature Medicine 1:970-972, 1995.

48. Huang D, Swanson EA, Lin CP, Schuman JS, Stinson WG, Chang W, Hee MR, Flotte T, Gregory K, Puliafito CA, J.G. F. Optical Coherence Tomography. Science 254:1178-1181, 1991.

49. Barnoski MK, Rourke MD, Jensen SM, Melville RT. Optical time domain reflectometer. Appl. Opt. 16:2375, 1977.

50. Barnoski MK, Jensen SM. Fiber waveguides: A novel technique for investigating attenuation characteristics. Appl. Opt. 15:2112, 1976.

51. Fujimoto JG, DeSilvestri S, Ippen EP, Puliafito CA, Margolis R, Oseroff A. Femtosecond optical ranging in biological systems. Opt. Lett. 11:150-152, 1986.

52. Stern D, Lin WZ, Puliafito CA, Fujimoto JG. Femtosecond optical ranging of corneal incision depth. Invest. Ophthalmol. Vis. Sci. 30:99-104, 1989.

53. Takada K, Yokohama I, Chida K, Noda J. New measurement system for fault location in optical waveguide devices based on interferometric technique. Appl. Opt. 26:1603-1606, 1987.

54. Youngquist RC, Carr S, Davies DEN. Optical coherence-domain reflectometry: A new optical evaluation technique. Opt. Lett. 12:158-160, 1987.

55. Fercher AF, Mengedoht K, Werner W. Eye-length measurement by interferometry with partially coherent light. Opt. Lett. 13:186-190, 1988.

56. Hitzenberger CK. Optical measurement of the axial eye length by laser Doppler interferometry. Invest. Ophthalmol. Vis. Sci. 32:616-624, 1991.

57. Hitzenberger CK. Measurement of corneal thickness by laser Doppler interferometry. Invest. Ophthalmol. Vis. Sci. 33:98-103, 1992.

58. Huang D, Wang J, Lin CP, Puliafito CA, Fjimoto JG. Micron-resolution ranging of cornea anterior chamber by optical reflectometry. Lasers Surg. Med. 11:419-425, 1991.

59. Swanson EA, Izatt JA, Hee MR, Huang D, Lin CP, Schuman JS, Puliafito CA, Fujimoto JG. *In vivo* retinal imaging by optical coherence tomography. Opt. Lett. 18:1864-1866, 1993.

60. Swanson EA, Huang D, Hee MR, Fujimoto JG, Lin CP, Puliafito CA. High-speed optical coherence domain reflectometry. Opt. Lett. 17:151-153, 1992.

61. Izatt JA, Hee MR, Swanson EA, Lin CP, Huang D, Schuman JS, Puliafito CA, Fujimoto JG. Micrometer-scale resolution imaging of the anterior eye *in vivo* with optical coherence tomography. Arch. Ophthalmol. 112:1584, 1994.

62. Hee MR, Izatt JA, Swanson EA, Huang D, Lin CP, Schuman JS, Puliafito CA, Fujimoto JG. Optical coherence tomography of the human retina. Arch. Ophthalmol. 113:325-332, 1995.

63. Wilkins JR, Puliafito CA, Hee MR, Duker JS, Reichel E, Coker JG, Schuman JS, Swanson EA, Fujimoto JG. Characterization of epiretinal membranes using optical coherence tomography. Ophthalmol. 103:2142-2151, 1996.

64. Hee MR, Pulifito CA, Wong C, Duker JS, Reichel E, Rutledge B, Schuman JS, Swanson EA, Fujimoto JG. Quantitative assessment of macular edema with optical coherence tomography. Arch. Ophthalmol. 113:1019-1029, 1995.

65. Hee MR, Puliafito CA, Wong C, Duker JS, Reichel E, Schuman JS, Swanson EA, Fujimoto JG. Optical coherence tomography of macular holes. Ophthalmol. 102:748-756, 1995.

66. Hee MR, Baumal CR, Puliafito CA, Duker JS, Reichel E, Wilkins JR, Coker JG, Schuman JS, Swanson EA, Fujimoto JG. Optical coherence tomography of age-related macular degeneration and choroidal neovascularization. Ophthalmol. 103:1260-1270, 1996.

67. Hee MR, Puliafito CA, Wong C, Reichel E, Duker JS, Schuman JS, Swanson EA, Fujimoto JG. Optical coherence tomography of central serous chorioretinopathy. Am. J. Ophthalmol. 120:65-74, 1995.

68. Schuman JS, Hee MR, Puliafito CA, Wong C, Pedut-Kloizman T, Lin CP, Hertzmark E, Izatt JA, Swanson EA, Fujimoto JG. Quantification of nerve fiber layer thickness in normal and glaucomatous eyes using optical coherence tomography: a pilot study. Arch. Ophthalmol. 113:586-596, 1995.

69. Schuman JS, Pedut-Kloizman T, Hertzmark E, Hee MR, Wilkins JR, Coker JG, Puliafito CA, Fujimoto JG, Swanson EA. Reproducibility of nerve fiber layer thickness measurements using optical coherence tomography. Ophthalmol. 103:1889-1898, 1996.

70. Brezinski ME, Tearney GJ, Bouma BE, Izatt JA, Hee MR, Swanson EA, Southern JF, Fujimoto JG. Optical coherence tomography for optical biopsy: Properties and demonstration of vascular pathology. Circulation 93:1206-1213, 1996.

71. Bouma BE, Tearney GJ, Golubovic B, Fujimoto JG. Optical coherence tomographic imaging using a mode locked Cr^{4+}:forsterite laser source. Ultrafast Phenomena Conference, San Diego, CA, May 28-June 1, 1996.

72. Schmitt JM, Knuttel A, Yadlowsky M, Eckhaus MA. Optical coherence tomography of a dense tissue: Statistics of attenuation and backscattering. Phys. Med. Biol. 39:1705-1720, 1994.

73. Schmitt JM, Yadlowsky MJ, Bonner RF. Subsurface imaging of living skin with optical coherence microscopy. Dermatology 191:93-98, 1995.

74. Pan Y, Birngruber R, Rosperich J, Engelhardt R. Low-coherence optical tomography in turbid tissue: Theoretical analysis. Appl. Opt. 34:6564-6574, 1995.

75. Schmitt JM, Knuttel A, Bonner RF. Measurements of optical properties of biological tissues by low-coherence reflectometry. Appl. Opt. 32:6032-6042, 1993.

76. Tearney GJ. Optical Characterization of Human Tissues using Low Coherence Interferometry. MS Thesis, Department of Electrical Engineering and Computer Science, Massachusetts Institiue of Technology, Cambridge, MA, 1995.

77. Tearney GJ, Brezinski ME, Southern JF, Bouma BE, Hee MR, Fujimoto JG. Determination of the refractive index of highly scattering human tissue by optical coherence tomography. Opt. Lett. 20:2258-2260, 1995.

78. Tearney GJ, Brezinski ME, Bouma BE, Boppart SA, Pitris C, Southern JF, Fujimoto JG. *In vivo* endoscopic optical biopsy with optical coherence tomography. Science 276:2037-2039, 1997.

79. Sergeev AM, Gelikonov VM, Gelikonov GV, Feldchtein FI, Kuranov RV, Gladkova ND. *In vivo* endoscopic OCT imaging of precancer and cancer states of human mucosa. Opt. Express 1:432-440, 1997.

80. Swanson EA, Hee MR, Tearney GJ, Fujimoto JG. Application of optical coherence tomography in nondestructive evaluation of material microstructure. Conference on Lasers and Electro-Optics, CLEO'96, Anaheim, CA, June 2-7, 1996.

81. Bashkansky M, Duncan MD, Kahn M, Lewis III D, Reintjes J. Subsurface defect detection in ceramics by high-speed high-resolution optical coherent tomography. Opt. Lett. 22:61-63, 1997.

82. Chinn SR, Swanson EA. Multi-layer optical readout using direct or interferometric detection and broad-bandwidth light sources. Opt. Mem. and Neural Net. 5:197-218, 1996.

83. Chinn SR, Swanson EA. Multilayer optical storage by low-coherence reflectometry. Opt. Lett. 21:899-901, 1996.

84. Wiener N. Acta Math. 55:117, 1930.

85. Khintchine A. Math. Ann. 109:604, 1934.

86. Zhou JZ, Taft G, Huang CP, Murnane MM, Kapteyn HC. Pulse evolution in a broad-bandwidth ti:sapphire laser. Opt. Lett. 19:1149-1151, 1994.

87. Asaki MT, Huang CP, Garvey D, Zhou J, Kapteyn HC, Murnane MM. Generation of 11-fs pulses from a self-mode-locked ti:sapphire laser. Opt. Lett. 18:977-979, 1993.

88. Clivaz X, Marquis-Weible F, Salathe RP. Optical low coherence reflectometry with 1.9 μm spatial resolution. Elec. Lett. 28:1553-1555, 1992.

89. Bouma BE, Tearney GJ, Boppart SA, Hee MR, Brezinski ME, Fujimoto JG. High resolution optical coherence tomographic imaging using a modelocked Ti:Al_20_3 laser. Opt. Lett. 20:1486-1488, 1995.

90. Bouma BE, Tearney GJ, Bilinsky IP, Golubovic B, Fujimoto JG. A self-phase-modulated Kerr-lens-modelocked Cr:forsterite laser source for optical coherence tomography. Opt. Lett. 21:1839-1841, 1996.

91. Seas A, Petricevic V, Alfano RR. Generation of sub-100-fs pulses from a cw mode-locked chromium-doped forsterite laser. Opt. Lett. 17:937-939, 1992.

92. Yanovsky V, Pang Y, Wise F, Minkov BI. Generation of 25-fs pulses from a self-mode-locked Cr:forsterite laser with optimized group delay dispersion. Opt. Lett. 18:1541-1543, 1993.

93. Tomlinson WJ, Stolen RH, Shank CV. Compression of optical pulses chirped by self-phase modulation in fibres. J. Opt. Soc. Amer. B 1:139-149, 1984.

94. Gomes ASL, Gouveia-Neto AS, Taylor JR, Avramopoulos H, New GHC. Optical pulse narrowing by the spectral windowing of self-phase modulated picosecond pulses. Opt. Comm. 59:399-404, 1986.

95. Butcher PN, Cotter D. *The Elements of Nonlinear Optics*. Cambridge University Press: Cambridge, 1990.

96. Bouma BE, Ramaswamy-Paye M, Fujimoto JG. Compact resonator designs for mode-locked solid-state lasers. Appl. Phys. B 65:213-220, 1997.

97. Shi Y, Poulsen O. High-power broadband singlemode Pr^{3+}-doped fibre superfluorescence light source. Elect. Lett. 29:1945-1946, 1993.

98. Muendel M. Personal Communication, 1996.

99. Digonnet JF. *Rare Earth Doped Fiber Lasers and Amplfiers*. Marcel Dekker, Inc.: New York, 1993.

100. Bouma BE, Nelson LE, Tearney GJ, Jones DJ, Brezinski ME, Fujimoto JG. Optical coherence tomographic imaging of human tissue at 1.55 µm and 1.8 µm using Er- and Tm-doped fiber sources. J. Biomed. Opt. 3:76-79, 1998.

101. Tearney GJ. Optical Biopsy of *In Vivo* Tissue Using Optical Coherence Tomography. PhD Thesis, Department of Electrical Engineering and Computer Science, Massachusetts Institute of Technology, Cambridge, MA, 1996.

102. Basics of Piezoelectric Positioning. Physik Instrumente: Physik Instrumente, 1996.

103. Guide to modern piezoelectric ceramics. Morgan Matroc, Inc., Electro-Ceramics Division: Bedford, OH, 1993.

104. Sergeev A, Gelikonov V, Gelikonov A. High-spatial-resolution optical-coherence tomography of human skin and mucous membranes. Conference on Lasers and Electro Optics '95, Anaheim, CA, May 21-26, 1995.

105. Luke DG, McBride R, Jones JDC. Polarization mode dispersion minimization in fiber-wound piezoelectric cyliners. Opt. Lett. 20:2550-2552, 1995.

106. Kong JA. *Electromagnetic Wave Theory*. 2nd ed. John Wiley & Sons, Inc.: New York, NY, 1990.

107. Tearney GJ, Bouma BE, Boppart SA, Golubovic B, Swanson EA, Fujimoto JG. Rapid acquisition of *in vivo* biological images by use of optical coherence tomography. Opt. Lett. 21:1408-1410, 1996.

108. Yasa ZA, Amer NM. A rapid-scanning autocorrelation scheme for continuous monitoring of picosecond laser pulses. Opt. Comm. 36:406-408, 1981.

109. Ballif J, Gianotti R, Chavanne P, Walti R, Salathe RP. Rapid and scalable scans at 21 m/s in optical low-coherence reflectometry. Opt. Lett. 22:757-759, 1997.

110. Su CB. Achieving variation of the optical path length by a few millimeters at millisecond rates for imaging of turbid media and optical interferometry: A new technique. Opt. Lett. 22:665-667, 1997.

111. Kwong KF, Yankelevich D, Chu KC, Heritage JP, Dienes A. 400-Hz mechanical scanning optical delay line. Opt. Lett. 18:558-560, 1993.

112. Weiner AM, Heritage JP, Kirschner EM. High-resolution femtosecond pulse shaping. J. Opt. Soc. Am. B 5:1563-1572, 1988.

113. Weiner AM, Leaird DE, Patel JS, Wullert JR. Programmable femtosecond pulse shaping by use of a multielement liquid-crystal phase modulator. Opt. Lett. 15:326-328, 1990.

114. Tearney GJ, Bouma BE, Fujimoto JG. High-speed phase- and group-delay scanning with a grating-based phase control delay line. Opt. Lett. 22:1811-1813, 1997.

115. Fork RL, Brito Cruz CH, Becker PC, Shank CV. Compression of optical pulses to six femtoseconds by using cubic phase compensation. Opt. Lett. 12:483-485, 1987.

116. Saleh BEA, Teich MC. *Fundamentals of Photonics*. John Wiley & Sons, Inc.: New York, NY, 1991.

117. Izatt JA, Hee MR, Owen GM, Swanson EA, Fujimoto JG. Optical coherence microscopy in scattering media. Opt. Lett. 19:590-592, 1993.

118. Bail M, Hausler G, Herrmann JM, Kiesewetter F, Lindner MW, Schultz A. Optical coherence tomography by spectral radar for the analysis of human skin. Society of Photo-Optical Instrumentation Engineers-Biomedical Optics, San Jose, CA, February 8-14, 1997.

119. Bail M, Eigensee A, Hausler G, Herrmann JM, Lindner MW. 3D imaging of human skin - optical *in vivo* tomography and topology by short coherence interferometry. Society of Photo-Optical Instrumentation Engineers-Biomedical Optics, San Jose, CA, February 8-14, 1997.

120. Ammon G, Andretzky P, Bohn G, Hausler G, Herrmann JM, Lindner MW. Optical coherence profilometry (OCP) of human skin *in vivo*. Society of Photo-Optical Instrumentation Engineers-Biomedical Optics, San Jose, CA, February 8-14, 1997.

121. Chinn SR, Swanson EA, Fujimoto JG. Optical coherence tomography using a frequency-tunable optical source. Opt. Lett. 22:340-342, 1997.

122. Passy R, Gisin N, Weid JPvd, Gilgen HH. Experimental and theoretical investigations of coherent OFDR with semiconductor laser sources. J. Lightwave Technol. LT-12:1622-1630, 1994.

123. Glombitza U, Brinkmeyer E. Coherent frequency domain reflectometry for characterization of single-mode integrated optical waveguides. J. Lightwave Technol. LT-11:1377-1384, 1993.

124. Weid JPvd, Passy R, Gisin N. Mid-range coherent optical frequency domain reflectometry with a DFB laser diode coupled to an external cavity. J. Lightwave Technol. LT-13:954-960, 1995.

125. Golubovic B. Study of Near-Infrared Pumped Solid-State Lasers and Applications. PhD Thesis, Department of Electrical Engineering and Computer Science, Massachusetts Institute of Technology, Cambridge, MA, 1997.

126. Born M, Wolf E. *Principles of Optics*. Pergamon Press: Oxford, 1980.

127. Golubovic B, Bouma BE, Tearney GJ, Fujimoto JG. Optical frequency domain reflectometry using rapid wavelength tuning of a Cr^{4+}:forsterite laser. Opt. Lett. 22:1704-1706, 1997.

128. Single Mode Fiber Product Information. Corning, Inc., Opto-Electronics Group: Corning, NY, 1992.

129. Schmitt JM, Knuttel A. Model of optical coherence tomography of heterogeneous tissue. J. Opt. Soc. Am. A 14:1231-1242, 1997.

130. Beiser L, Johnson RB. Scanners. In *Handbook of Optics, Vol. 2*, Bass M, Editor. McGraw Hill, Inc.: New York, 1995.

131. Boppart SA, Tearney GJ, Bouma BE, Brezinski ME, Fujimoto JG, Swanson EA. Method and Apparatus for Forward-Directed Optical Scanning Instruments for the Acquisition of Optical Images and Delivery of Optical Radiation. Patent. Massachusetts Institute of Technology, U.S.A., 1997.

132. Boppart SA, Bouma BE, Pitris C, Tearney GJ, Fujimoto JG. Forward-imaging instruments for optical coherence tomography. Opt. Lett. 22:1618-1620, 1997.

133. Ryan JM, Milner SM, Cooper GJ, Haywood IR. Field surgery on a future conventional battlefield: Strategy and wound management. Ann. Royal Coll. Surg. England 73:13-20, 1991.

134. Haus HS. *Waves and Fields in Optoelectronics*. Prentice-Hall: Englewood Cliffs, 1984.

135. The Piezo Book. Burleigh Inc., 1991.

136. SELFOC Product Guide. NSG America, Inc.: Somerset, NJ, 1996.

137. LeCarpentier GL, Motamedi M, McMath LP, Rastegar S, Welch AJ. Continuous wave laser ablation of tissue: Analysis of thermal and mechanical events. IEEE Trans. Biomed. Engr. 40:188-200, 1993.

138. Hopkins HH. Optical principles of the endoscope. In *Endoscopy*, Berci G, Editor. Appleton-Century-Crofts: New York, NY. pp. 3-26, 1976.

139. Technical Notes. NSG America, Inc.: Somerset, NJ, 1996.

140. Nissen SE, Gurley JC, Booth DC, DeMaria AN. Intravascular ultrasound of the coronary arteries: Current applications and future directions. Am. J. Card. 69:18H-29H, 1992.

141. Potkin BN, Bartorelli AL, Gessert JM, Neville RF, Almagor Y, Roberts WC, Leon MB. Coronary artery imaging with intravascular ultrasound. Circulation 81:1575-1585, 1990.

142. Tearney GJ, Boppart SA, Bouma BE, Brezinski ME, Weissman NJ, Southern JF, Fujimoto JG. Scanning single-mode fiber optic catheter-endoscope for optical coherence tomography. Opt. Lett. 21:1-3, 1996.

143. Tearney GJ, Bouma BE, Boppart SA, Brezinski ME, Southern JF, Swanson EA, Fujimoto JG. Endoscopic optical coherence tomography. IEEE Lasers and Electro-Optics Society Annual Meeting, LEOS '96, Boston, MA, November 18-21, 1996.

144. Tearney GJ, Brezinski ME, Boppart SA, Bouma BE, Weissman N, Southern JF, Swanson EA, Fujimoto JG. Catheter-based optical imaging of a human coronary artery. Circulation 94:3013, 1996.

145. Finet G, Maurincomme E, Tabib A, Crowley RJ, Magnin I, Roriz R, Beaune J, Amiel M. Artifacts in intravascular ultrasound imaging: Analysis and implications. Ultrasound in Med. & Biol. 19:533-547, 1993.

146. Boppart SA, Brezinski ME, Bouma BE, Tearney GJ, Fujimoto JG. Investigation of developing embryonic morphology using optical coherence tomography. Dev. Biol. 177:54-63, 1996.

147. Turnbull DH, Bloomfield TS, Baldwin HS, Foster FS, Joyner AL. Ultrasound backscatter microscope analysis of early mouse embryonic brain development. Proc. Natl. Acad. Sci. USA 92:2239-2243, 1995.

148. White JG, Amos WB, Fordham M. An evaluation of confocal versus conventional imaging of biological structures by fluorescence light microscopy. J. Cell. Biol. 105:41-48, 1987.

149. Webb WW, Wells KS, Sandison DR, Strickler J. Criteria for quantitative dynamical confocal fluorescence imaging. In *Optical Microscopy for Biology,* Herman B, Jacobson K, Eds. Wiley-Liss: New York. pp. 73-108, 1990.

150. Jester JV, Andrews PM, Petroll WM, Lemp MA, Cavanagh HD. *In vivo*, real-time confocal imaging. J. Elec. Microsc. Tech. 18:50-60, 1991.

151. Nieuwkoop PD, Faber J. *Normal Table of Xenopus Laevis.* Garland Publishing, Inc.: New York, NY, 1994.

152. Boppart SA, Brezinski ME, Tearney GJ, Bouma BE, Fujimoto JG. Imaging developing neural morphology using optical coherence tomography. J. Neurosci. Meth. 70:65-72, 1996.

153. Olson EN, Srivastava D. Molecular pathways controlling heart development. Science 272:671-676, 1996.

154. Konig K, So PTC, Mantulin WW, Gratton E. Cellular response to near-infrared femtosecond laser pulses in two-photon microscopes. Opt. Lett. 22:135-137, 1997.

155. Konig K, Liang H, Berns MW, Tromberg BJ. Cell damage in near-infrared multimode optical traps as a result of multiphoton absorption. Opt. Lett. 21:1090-1092, 1996.

156. Burke AC, Nelson CE, Morgan BA, Tabin C. *Hox* genes and the evolution of vertebrate axial morphology. Development 121:333-346, 1995.

157. Boppart SA, Tearney GJ, Bouma BE, Southern JF, Brezinski ME, Fujimoto JG. Noninvasive assessment of the developing *Xenopus* cardiovascular system using optical coherence tomography. Proc. Natl. Acad. Sci. USA 94:4256-4261, 1997.

158. American Society of Echocardiography Committee on Standards. Recommendations for quantitation of the left ventricle by two-dimensional echocardiography. J. Amer. Soc. Echocardiogr. 2:358-367, 1989.

159. Schmidt KG, Silverman NH, Van Hare GF, Hawkins JA, Cloez J-L, Rudolph AM. Two-dimensional echocardiographic determination of ventricular volumes in the fetal heart. Circulation 81:325-333, 1990.

160. Stewart WJ, Rodkey SM, Gunawardena S, White RD, Luvisi B, Klein AL, Salcedo E. Left ventricular volume calculation with integrated backscatter from echocardiography. J. Am. Soc. Echocardiogr. 6:553-563, 1993.

161. Wang XJ, Milner TE, Nelson JS. Characterization of fluid flow velocity by optical Doppler tomography. Opt. Lett. 20:1337-1339, 1995.

162. Chen Z, Milner TE, Dave D, Nelson JS. Optical Doppler tomographic imaging of fluid flow velocity in highly scattering media. Opt. Lett. 22:64-66, 1997.

163. Chen Z, Milner TE, Srinivas S, Wang X. Noninvasive imaging of *in vivo* blood flow velocity using optical Doppler tomography. Opt. Lett. 22:1119-1121, 1997.

164. Wang X-J, Milner TE, Chen Z, Nelson JS. Measurement of fluid-flow-velocity profile in turbid media by the use of optical Doppler tomography. Appl. Opt. 36:144-149, 1997.

165. Yazdanfar S, Kulkarni MD, Izatt JA. High resolution imaging of *in vivo* cardiac dynamics using color Doppler optical coherence tomography. Opt. Express 1:424-431, 1997.

166. Boppart SA, Bouma BE, Pitris C, Southern JF, Brezinski ME, Fujimoto JG. *In vivo* cellular optical coherence tomography imaging: Implications for the early diagnosis of neoplasms. Nature Med. Submitted, 1998.

167. Dunn AK, Smithpeter C, Welch AJ, Richards-Kortum R. Sources of contrast in confocal reflectance imaging. Appl. Opt. 35:3441-3446, 1996.

168. Beuthan J, Minet O, Helfmann J, Herrig M, Muller G. The spatial variation of the refractive index in biological cells. Phys. Med. Biol. 41:369-382, 1996.

169. Maier J, Walker S, Fantini S, Franceschini M, Gratton E. Possible correlation between blood glucose concentration and the reduced scattering coefficient of tissues in the near infrared. Opt. Lett. 19:2062-2064, 1994.

170. Brunsting A, Mullaney P. Differential light scattering from spherical mammalian cells. Biophys. J. 14:439-453, 1974.

171. Liu H, Beauvoit B, Kimura M, Chance B. Dependence of tissue optical properties on solute-induced changes in refractive index and osmolarity. J. Biomed. Opt. 1:200-211, 1996.

172. Vitkin I, Woolsey J, Wilson B, Anderson R. Optical and thermal characterization of natural (*sepia oficinalis*) melanin. Photochem. and Photobio. 59:455-462, 1994.

173. Ishimaru A. *Wave Propagation and Scattering in Random Media, Vol. 1.* Academic Press: New York, NY, 1978.

174. Clivaz X, Marquis-Weible F, Salathe RP, Novak RP, Gilgen HH. High-resolution reflectometry in biological tissues. Opt. Lett. 17:4-6, 1992.

175. Gilbert SF. *Developmental Biology.* 4th ed. Sinauer Assoc., Inc.: Sunderland, MA, 1994.

176. Stratton J. *Electromagnetic Theory.* McGraw-Hill Book Co.: New York, 1941.

177. Bohren CF, Huffman DR. *Absorption and Scattering of Light by Small Particles.* John Wiley and Sons: New York, 1983.

178. Anderson RR, Parrish JA. The optics of human skin. J. Investig. Derm. 77:13-19, 1981.

179. Chance B. *Photon Migration in Tissues.* Plenum Press: New York, 1988.

180. Profio AE, Doiron DR. Transport of light in tissue in photodynamic therapy of cancer. Photochem. Photobiol. 46:591-599, 1987.

181. Cheong WF, Prahl SA, Welch AJ. A review of the optical properties of biological tissues. IEEE J. Quant. Elect. 26:2166-2187, 1991.

182. Jacques SL, Alter CA, Prahl SA. Angular dependence of HeNe laser light scattering by human dermis. Lasers Life Sci. 1:309-334, 1987.

183. Wray S, Cope M, Delpy DT, Wyatt JS, Raynolds EOR. Characterization of the near infrared absorption spectra of cytochrome aa3 and haemoglobin for the non-invasive monitoring of cerebral oxygenation. Biochimica et Biophysica Acta 933:184-192, 1988.

184. Hee MR. Biological Imaging with Low Coherence Optical Interferometry. MS Thesis, Department of Electrical Engineering and Computer Science, Massachusetts Institute of Technology, Cambridge, MA, 1992.

185. Hee MR, Izatt JA, Jacobson JM, Fujimoto JG. Femtosecond transillumination optical coherence tomography. Opt. Lett. 18:950-952, 1993.

186. Hee MR, Huang D, Swanson EA, Fujimoto JG. Polarization-sensitive low-coherence reflectometer for birefringence characterization and ranging. J. Opt. Soc. Amer. B 9:903-908, 1992.

187. de Boer JF, Milner TE, van Gemert MJC, Nelson JS. Two-dimensional birefringence imaging in biological tissue by polarization-sensitive optical coherence tomography. Opt. Lett. 22:934-936, 1997.

188. Thomsen S, Pearce JA, Cheong W-F. Changes in birefringence as markers of thermal damage in tissues. IEEE Trans. Biomed. Eng. BME-36:1174-1179, 1989.

189. Mang TS, McGinnis C, Liebow C, Nseyo UO, Crean DH, Dougherty TJ. Fluorescence detection of tumors. Cancer 71:269-276, 1993.

190. Van Wissen B, Eisenberg C, Debey P, Pennehouat G, Auger J, Bomsel-Helmreich O. *In vitro* DNA fluorescence after *in vitro* fertilization (IVF) failure. J. Assist. Repro. Gen. 9:564-571, 1992.

191. Warnakulasuriya KA, Johnson NW. Sensitivity and specificity of OraScan toluidine blue mouthrinse in the detection of oral cancer and precancer. J. Oral. Pathol. Med. 25:97-103, 1996.

192. Haugland RP. *Handbook of Fluorescent Probes and Research Chemicals.* 6th ed. Molecular Probes, Inc.: Eugene, OR, 1996.

193. Rajadhyaksha M, Grossman M, Esterowitz D, Webb RH, Anderson RR. *In vivo* confocal scanning laser microscopy of human skin: Melanin provides strong contrast. J. Invest. Dermatol. 104:946-952, 1995.

194. Kollias N, Baqer A. Spectroscopic characteristics of human melanin *in vivo*. J. Invest. Derm. 85:38-42, 1985.

195. Wolbarsht ML, Walsh AJ, George G. Melanin, a unique biological absorber. Appl. Opt. 20:2184-2186, 1981.

196. Kramer K, Elam JO, Saxton GA, Elam WN. Influence of oxygen saturation, erythrocyte concentration, and optical depth upon the red and near-infrared light transmittance of whole blood. Am. J. Physiol. 165:229-246, 1951.

197. Lee VS, Tarassenko L. Absorption and multiple scattering by suspensions of aligned red blood cells. J. Opt. Soc. Am. A. 8:1135-1141, 1991.

198. Lindberg LG, Oberg PA. Optical properties of blood in motion. Opt. Engin. 32:253-257, 1993.

199. Ninomiya M, Fujii M, Niwa M, Sakamoto K, Kanai H. Physical properties of flowing blood. Biorheology 25:319-328, 1988.

200. Russ JC. *The Image Processing Handbook.* 2nd ed. CRC Press: Ann Arbor, MI, 1995.

201. Bolle RM, Vemuri BC. On three-dimensional surface reconstruction methods. IEEE Trans. Pattern Anal. Mach. Intell. 13:1-13, 1991.

202. Lorensen WE, Cline HE. Marching Cubes: A high resolution 3D surface reconstruction algorithm. Computer Graphics 21:163-169, 1987.

203. Dobrezyneki A. Personal Communication, 1995.

204. Wied GL, Bartels PH, Bibbo M, Dytch HE. Image analysis in quantitative cytopathology and histopathology. Human Path. 20:549-571, 1989.

205. Tearney GJ, Brezinski ME, Southern JF, Bouma BE, Boppart SA, Fujimoto JG. Optical biopsy in human gastrointestinal tissue using optical coherence tomography. Am. J. Gastroenterology 92:1800-1804, 1997.

206. Schmitt JM. Array detection for speckle reduction in optical coherence microscopy. Phys. Med. Biol. 42:1427-1439, 1997.

207. Liedtke CE, Gahm T, Kappei F, Aeikens B. Segmentation of microscopic cell scenes. Analytical Quant. Cytol. Histol. 9:197-211, 1987.

208. Abmayr W, Mannweiler E, Oesterle D, Deml E. Segmentation of scenes in tissue sections. Analytical Quant. Cytol. Histol. 9:190-196, 1987.

209. Melzer A, Schmidt A, Kipfmuller K, Gronemeyer D, Seibel R. Technology and principles of tomographic image-guided interventions and surgery. Surg. Endosc. 11:946-956, 1997.

210. Grimson WEL, Ettinger GJ, White SJ, Lozano-Perez T, Wells III WM, Kikinis R. An automatic registration method for frameless stereotaxy, image-guided surgery, and enhanced reality visualization. IEEE Trans. Med. Imaging 15:129-140, 1996.

211. Brezinski ME, Tearney GJ, Boppart SA, Swanson EA, Southern JF, Fujimoto JG. Optical biopsy with optical coherence tomography, feasibility for surgical diagnostics. J. Surg. Res. 71:32-40, 1997.

212. Cotran RS, Kumar V, Robbins SL. *Robbins Pathologic Basis of Disease.* 5th ed, Schoen FJ, Editor. W.B. Saunders Co.: Philadelphia, PA, 1994.

213. American Cancer Society. Cancer Statistics 1998. CA: A cancer journal for clinicians 48:6-29, 1998.

214. Chandler WF, Knake JE, McGillicuddy JE, Lillehei KO, Silver TM. Intraoperative use of real-time ultrasonography in neurosurgery. J. Neurosurg. 57:157-163, 1982.

215. Gooding GAW, Boggan JE, Weinstein PR. Characterization of intracranial neoplasms by CT and intraoperative sonography. Am. J. Neuroradiol. 5:517-520, 1984.

216. Kaye AH, Morstyn G, Apuzzo MLJ. Photoradiation therapy and its potential in the management of neurological tumors. J. Neurosurg. 69:1-14, 1988.

217. Taphoorn MJ, Heimans JJ, Kaiser MC, de Slegte RG, Crezee FC, Valk J. Imaging of brain metastases: Comparison of computerized tomography (CT) and magnetic resonance imaging (MRI). Neuroradiol. 31:391-395, 1989.

218. Enzmann DR, Wheat R, Marshall WH, Bird R, Murphy-Irwin K, Karbon K, Hanbery J, Silverberg GD, Britt RH, Shuer L. Tumors of the central nervous system studied by computed tomography and ultrasound. Radiology 154:393-399, 1985.

219. Jeannesson P, Manfait M, Jardillier JC. A technique for laser Raman spectroscopic studies of isolated cell populations. Anal. Biochem. 129:305-309, 1983.

220. Mizuno A, Hayashi T, Tashibu K, Maraishi S, Kawauchi K, Ozaki Y. Near-infrared FT-Raman spectra of the rat brain tissues. Neurosci. Lett. 141:47-52, 1992.

221. Poon WS, Schomacker KT, Deutsch TF, Martuza RL. Laser-induced fluorescence: Experimental intraoperative delineation of tumor resection margins. J. Neurosurg. 76:679-686, 1992.

222. Hansen DA, Spence AM, Carksi T, Berger MS. Indocyanine green (ICG) staining and demarcation of tumor margins in a rat glioma model. Surg. Neurol. 40:451-456, 1993.

223. Svaasand LO, Ellingsen R. Optical properties of human brain. Photochem. Photobiol. 38:293-299, 1983.

224. Eggert HR, Blazek V. Optical properties of human brain tissue, meninges, and brain tumors in the spectral range of 200 to 900 nm. Neurosurgery 21:459-464, 1987.

225. Boppart SA, Brezinski ME, Pitris C, Fujimoto JG. Optical coherence tomography for neurosurgical imaging of intracortical melanoma. Neurosurgery. Submitted, 1998.

226. Dunn A, Richards-Kortum R. Three-dimensional computation of light scattering from cells. IEEE J. Selected Topics in Quant. Elec. 2:898-905, 1996.

227. Zuniga JR, Labanc JP. Advances in microsurgical nerve repair. J. Oral Maxillofac. Surg. 51 (suppl 1):62-68, 1993.

228. Zajtchuk R, Sullivan GR. Battlefield trauma care: Focus on advanced technology. Military Med. 160:1-7, 1995.

229. Terris DJ, Fee WE. Current issues in nerve repair. Arch. Otolaryngol. Head Neck Surg. 119:725-731, 1993.

230. Boppart SA, Bouma BE, Pitris C, Tearney GJ, Southern JF, Brezinski ME, Fujimoto JG. Three-dimensional optical coherence tomography for microsurgical diagnostics. Radiology. In Press, 1998.

231. Wyrick JD, Stern PJ. Secondary nerve reconstruction. Microsurgery 8:587-598, 1992.

232. Brezinski ME, Tearney GJ, Bouma BE, Boppart SA, Hee MR, Swanson EA, Southern JF, Fujimoto JG. Imaging of coronary artery microstructure with optical coherence tomography. Am. J. Card. 77:92-93, 1996.

233. Brezinski ME, Tearney GJ, Weissman NJ, Boppart SA, Bouma BE, Hee MR, Weyman AE, Swanson EA, Southern JF, Fujimoto JG. Assessing atherosclerotic plaque morphology: Comparison of optical coherence tomography and high frequency intravascular ultrasound. Heart :397-403, 1997.

234. Fujimoto JG, Boppart SA, Tearney GJ, Bouma BE, Pitris C, Brezinski ME. High resolution *in vivo* intraarterial imaging with optical coherence tomography. Circulation. Submitted, 1998.

235. Zhong-wei C, Dong-yue Y, Di-Sheng C, Eds. *Microsurgery.* Springer Verlag: New York, NY, 1982.

236. Culbertson JH, Rand RP, Jurkiwicz MJ. Advances in microsurgery. Adv. Surg. 23:57-88, 1990.

237. Runowicz CD. Office laparoscopy as a screening tool for early detection of ovarian cancer. J. Cell. Biochem. 23 (Suppl.):238-242, 1995.

238. Boppart SA, Pitris C, Brezinski ME, Fujimoto JG. High-resolution optical coherence tomography imaging of laparoscopically-accessible gynecological tissue. Surg. Laparosc. Submitted, 1998.

239. Nisolle M, Donnez J. Peritoneal endometriosis, ovarian endometriosis, and adenomyotic nodules of the rectovaginal septum are three different entities. Fert. and Steril. 68:585-596, 1997.

240. Kjerulff KH, Erickson BA, Langenberg PW. Chronic gynecological conditions reported by US women: Findings from the National Health Information Survey, 1984 to 1992. Am. J. Public Health 86:195-199, 1996.

241. Eskenazi B, Warner ML. Epidemiology of endometriosis. Obstet. Gyn. Clin. N. Amer. 24:235-258, 1997.

242. American Cancer Society. Cancer Statistics 1997. CA: A cancer journal for clinicians 47:9, 1997.

243. Scully RE. Pathology of ovarian cancer precursors. J. Cell. Biochem. 23 (Suppl.):208-218, 1995.

244. Tortolero-Luna G, Mitchell MF. The epidemiology of ovarian cancer. J. Cell. Biochem. 23 (Suppl.):200-207, 1995.

245. Holcomb GW, Tomita SS, Haase GM, Dillon PW, Newman KD, Applebaum H, Wiener ES. Minimally invasive surgery in children with cancer. Cancer 76:121-128, 1995.

246. Childers JM, Balserak JC, Kent T, Surwit EA. Laparoscopic staging of Hodgkin's lymphoma. J. Laparoendosc. Surg. 3:495-499, 1993.

247. Vassallo P, Edel G, Roos N, Naguib A, Peters PE. *In-vitro* high-resolution ultrasonography of benign and malignant lymph nodes. Invest. Radiol. 28:698-705, 1993.

248. Boppart SA, Brezinski ME, Pitris C, Fujimoto JG. High-resolution subsurface imaging of lymphoid tissue for pediatric laparoscopy. Ped. Res. Submitted, 1998.

249. Botet JF, Lightdale C. Endoscopic ultrasonography of the upper gastrointestinal tract. Radiologic Clin. N. Amer. 30:1067-83, 1992.

250. Spivak H, Hunter JG. Endoluminal surgery. Surg. Endosc. 11:321-325, 1997.

251. Wilson BC, Patterson MS. The physics of photodynamic therapy. Phys. Med. Biol. 31:327-360, 1986.

252. Phillips RW, Wong RKH. Barrett's esophagus. Gastroentereology Clin. N. Amer. 20:791-815, 1991.

253. Spechler SJ. Gastroesophageal reflux disease and other disorders of the esophagus. In *Pathophysiology of Gastrointestinal Diseases,* Chopra S, May RJ, Editors. Little, Brown and Company: Boston, MA. pp. 37-70, 1989.

254. Izatt JA, Kulkarni MD, Wang H-W, Kobayashi K, Sivak MV. Optical coherence tomography and microscopy in gastrointestinal tissues. IEEE J. Selected Topics in Quant. Elect. 2:1017-1028, 1996.

255. Chancellor MB, Liu J, Rivas DA, Karasick S, Bagley DH, Goldberg BB. Intraoperative endo-luminal ultrasound evaluation of urethral diverticula. J. Urol. 153:72-75, 1995.

256. Tearney GJ, Brezinski ME, Southern JF, Bouma BE, Boppart SA, Fujimoto JG. Optical biopsy in human urologic tissue using optical coherence tomography. J. Urol. 157:1915-1919, 1997.

257. Parker SL, Tong T, Balden S, Wingo PA. Cancer statistics 1996. CA 46:5-27, 1996.

258. Shimizu H, Ross RK, Bernstein L, Yatani R, Henderson BE, Mack TM. Cancers of the prostate and breast among Japanese and white immigrants in Los Angeles County. Br. J. Cancer 63:963-966, 1991.

259. Sagalowsky AI, Wilson JD. Hyperplasia and carcinoma of the prostate. In *Harrison's Principles of Internal Medicine, 13th Edition,* Isselbacher KJ, Braunwald E, Wilson JD, Martin JB, Fauci AS, Kasper DL, Editors. McGraw-Hill, Inc.: New York, NY. pp. 1862-1865, 1994.

260. Clarke HS. Benign prostatic hyperplasia. Am. J. Med. Sci. 314:239-244, 1997.

261. Hanbury DC, Sethia KK. Erectile function following transurethral prostatectomy. Br. J. Urol. 75:12-13, 1995.

262. Toth CA, Birngruber R, Boppart SA, Hee MR, Fujimoto JG, DiCarlo CD, Swanson EA, Cain CP, Narayan DG, Noojin GD, Roach WP. Argon laser retinal lesions evaluated *in vivo* by optical coherence tomography. Amer. J. Ophthalmol. 123:188-198, 1997.

263. Toth CA, Narayan DG, Boppart SA, Hee MR, Fujimoto JG, Birngruber R, Cain CP, DiCarlo CD, Roach WP. A comparison of retinal morphology viewed by optical coherence tomography and by light microscopy. Arch. Ophthalmol. 115:1425-1428, 1997.

264. Roach WP, Toth CA, Narayan DG, Winter KP, Noojin GD, DiCarlo CD, Boppart SA, Hee MR, Birngruber R, Fujimoto JG, Cain CP. The retinal response to picosecond laser pulses of varying energy and spot size. Invest. Ophthalmol. Vis. Sci. Submitted, 1998.

265. Charschan SS. *American National Standard for Safe Use of Lasers*. The Laser Institute of America: Orlando, FL, 1993.

266. Rossant J, Hopkins N. Of fin and fur: Mutational analysis of vertebrate embryonic development. Genes & Dev. 6:1-13, 1992.

267. Thomsen S. Pathologic analysis of photothermal and photomechanical effects of laser-tissue interactions. Photochem. Photobiol. 53:825-835, 1991.

268. Welch AJ, van Gemert MJC. *Optical-Thermal Response of Laser-Irradiated Tissue*. Plenum Press: New York, NY, 1995.

269. Schober R, Ulrich F, Sander T, Durselen H, Hessel S. Laser-induced alteration of collagen substructure allows microsurgical tissue welding. Science 232:1421-1422, 1986.

270. Henriques FC, Moritz AR. Studies of thermal injury in the conduction of heat to and through skin and the temperatures attained therein: A theoretical and experimental investigation. Am. J. Pathol. 23:531-549, 1947.

271. Kennedy PK. A first-order model for computation of laser-induced breakdown thresholds in ocular and aqueous media: Part I-theory. IEEE J. Quant. Elect. 31:2241-2249, 1995.

272. Kennedy PK, Boppart SA, Hammer DX, Rockwell BA, Noojin GD, Roach WP. A first-order model for computation of laser-induced breakdown thresholds in ocular and aqueous media: Part II-comparison to experiment. IEEE J. Quant. Elect. 31:2250-2257, 1995.

273. Lin W-C, Motamedi M, Welch AJ. Dynamics of tissue optics during laser heating of turbid media. Appl. Opt. 35:3413-3420, 1996.

274. Pettit GH, Ediger MN, Weiblinger RP. Dynamic optical properties of collagen-based tissue during ArF excimer laser ablation. Appl. Opt. 32:488-493, 1993.

275. Horecker BL. The absorption spectra of hemoglobin and its derivatives in the visible and near infrared regions. J. Biol. Chem. 48:173-184, 1943.

276. Tan OT. *Management and Treatment of Benign Cutaneous Vascular Lesions*. Lea & Febiger: Philadelphia, PA, 1992.

277. Tan OT, Morrison P, Kurban AK. 585 nm for treatment of portwine stains. Plast. Reconstr. Surg. 86:1112-1117, 1990.

278. Mclean AJ. The Bovie electrosurgical current generator: Some underlying principles and results. Arch. Surg. 18:1863-1867, 1929.

279. Wu TG, Lu ZY. Comparison betweeen laser and electrical ablation of ventricle in dogs: Hemodynamic, pathologic and electrocardiographic observations. J. Tongji Med. Univ. 12:237-242, 1992.

280. Phillips DR. A comparison of endometrial ablation using the Nd:YAG laser or electrosurgical techniques. J. Am. Assoc. Gynecol. Laparosc. 1:235-239, 1994.

281. Soffa AJ, Markel MD, Converse LJ, Massa KL, Bogdanske JJ, Dillingham MF. Treatment of inflammatory arthritis by synovial ablation: A comparison of the holmium:YAG laser, electrocautery, and mechanical ablation in a rabbit model. Lasers Surg. Med. 19:143-151, 1996.

282. Cowles RS, Kabalin JN, Childs S, Lepor H, Dixon C, Stern B, Zabbo A. A prospective randomized comparison of transurethral resection to visual laser ablation of the prostate for the treatment of benign prostate hyperplasia. Urol. 46:155-160, 1995.

283. Bosch JLHR. Urodynamic effects of various treatment modalities for benign prostatic hyperplasia. J. Urol. 158:2034-2044, 1997.

284. Holtgrewe HL, Mebust WK, Dowd JB, Cockett AT, Peters PC, Proctor C. Transurethral prostatectomy: Practice aspects of the dominant operation in American urology. J. Urol. 141:248-253, 1989.

285. Mulligan ED, Lynch TH, Mulvin D, Greene D, Smith JM, Fitzpatrick JM. High-intensity focused ultrasound in the treatment of benign prostatic hyperplasia. Br. J. Urol. 79:177-180, 1997.

286. Nawrocki JD, Bell TJ, Lawrence WT, Ward JP. A randomized controlled trial of transurethral microwave thermotherapy. Br. J. Urol. 79:389-393, 1997.

287. Costello AJ, Bowsher WG, Bolton DM, Braslis KG, Burt J. Laser ablation of the prostate in patients with benign prostatic hypertrophy. Br. J. Urol. 69:603-608, 1992.

288. Covarrubias L, Nashida Y, Terao P, D'Eustachio P, Mintz B. Cellular DNA rearrangements and early developmental arrest caused by DNA insertion in transgenic mouse embryos. Mol. Cell. Biol. 7:2243-2247, 1987.

289. Dove WF. Molecular genetics of *Mus musculus*: Point mutagenesis and millimorgans. Genetics 116:5-8, 1987.

290. Rinchik EM, Russell LB. Germ-line deletion mutations in the mouse: Tools for intensive functional and physical mapping of regions of the mammalian genome. In *Genome Analysis*, Davies K, Tilghman S, Editors. Cold Springs Harbor Laboratory Press: Cold Springs Harbor, NY, 1990.

291. Olson EN, Martin JF, Schneider MD. *Cardiovascular Medicine*. Willerson JT, Cohn JN, Editors. Churchill Livingstone: New York, NY, 1995.

292. Sive HL, Draper BW, Harland RM, Weintraub H. Identification of a retinoic acid-sensitive period during primary axis formation in *Xenopus laevis*. Genes & Dev. 4:932-942, 1990.

293. Papalopulu N, Clarke JDW, Bradley L, Wilkinson D, Krumlauf R, Holder N. Retinoic acid causes abnormal development and segmental patterning of the anterior hindbrain in *Xenopus* embryos. Development 113:1145-1158, 1991.

294. Yasui H, Nakazawa M, Morishima M, Miyagawa-Tomita S, Momma K. Morphological observations on the pathogenetic process of transposition of the great arteries induced by retinoic acid in mice. Circulation 91:2478-2486, 1995.

295. Wang GM, Schwetz BA. An evaluation system for ranking chemicals with teratogenic potential. Teratogenesis Carcinog. Mutagen. 7:133-139, 1987.

296. Finnell RH. Phenytoin-induced teratogenesis: A mouse model. Science 211:483-484, 1981.

297. Holmes L. Personal Communication, 1996.

298. Kaiser J. Deformed frogs leap into spotlight at health workshop. Science 278:2051-2052, 1997.

299. Blaustein AR, Hoffman PD, Hokit DG, Kiesecker JM, Walls SC, Hays JB. UV repair and resistance to solar UV-B in amphibian eggs: A link to population declines? Proc. Natl. Acad. Sci. USA 91:1791-1795, 1994.

300. Kiesecker JM, Blaustein AR. Synergism between UV-B radiation and a pathogen magnifies amphibian embryo mortality in nature. Proc. Natl. Acad. Sci. USA 92:11049-11052, 1995.

301. Wilson T. *Confocal Microscopy.* Academic Press: California, 1990.

302. Ramanujam N, Mitchell MF, Mahadevan A, Warren S, Thomsen S, Silva E, Richards-Kortum R. *In vivo* diagnosis of cervical intraepithelial neoplasia using 337-nm-excited laser-induced fluorescence. Proc. Natl. Acad. Sci. USA 91:10193-10197, 1994.

303. Ramanujam N, Mitchell MF, Mahadevan A, Thomsen S, Malpica A, Wright T, Atkinson N, Richards-Kortum R. Spectroscopic diagnosis of cervical intraepithelial neoplasia (CIN) *in vivo* using laser-induced fluorescence spectra at multiple excitation wavelengths. Lasers Surg. Med. 19:63-74, 1996.

304. Herrmann JM, Pitris C, Bouma BE, Boppart SA, Fujimoto JG, Brezinski ME. High resolution imaging of normal and osteoarthritic cartilage with optical coherence tomography. Arthritis. Submitted, 1998.

305. Hammer DX, Noojin GD, Thomas RJ, Clary CE, Rockwell BA, Toth CA, Roach WP. Intraocular laser surgical probe for membrane ablation by laser-induced breakdown. Appl. Opt. 36:1684-1693, 1997.

Statement of Animal Care and Tissue Use

The animals used in this thesis research were cared for and maintained under the established and approved protocols of the Committee on Animal Care, Massachusetts Institute of Technology, Cambridge, MA.

The protocol for the use of discarded human tissue has been approved by the Committee on the Use of Human Subjects, Massachusetts General Hospital, Boston, MA.

List of Figures

List of Tables

Frequently used Abbreviations

ANSI, American National Standards Institute
BPH, benign prostatic hypertropy
CCD, charge-coupled device
CT, computed tomography
CM, confocal microscopy
CW, continuous wave
Cr, chromium
ET, ejection time
EDD, end diastolic dimension
ESD, end systolic dimension
FFT, fast Fourier transform
FOV, field of view
FT, filling time
FWHM, full width half maximum
fMRI, functional magnetic resonance imaging
GRIN, gradient index
GVD, group velocity dispersion
HR, heart rate
H & E, hematoxylin and eosin
IR, infrared
IVUS, intravascular ultrasound
KLM, Kerr-lens modelocked
MRI, magnetic resonance imaging
MPE, maximum permissible exposure
MFP, mean free path
MIS, minimally invasive surgery
NBT, nitrophenyl ditetrazolium salt
NOSSD, non-overlapping spot size diameters
N/C, nuclear-to-cytoplasmic
NA, numerical aperture
OCDR, optical coherence domain reflectometry
OCM, optical coherence microscopy
OCT, optical coherence tomography
OFDR, optical frequency domain reflectometry
OTDR, optical time domain reflectometry
PZT, lead zirconate titanate
PSF, point spread function
RF, radio-frequency
REDF, rare earth doped fiber
SPM, self-phase modulation
SNR, signal-to-noise
SLD, super-luminescent diode
$Ti:Al_2O_3$, titanium:sapphire